Mécanisme d'accélération d'une flamme de prémélange hydrogène/air et effets sur les structures

Roberta Scarpa

Centre Val de Loire UNIVERSITÉ Spirit of the Loire Valley

UNIVERSITÉ D'ORLÉANS

UNIVERSITE D'ORLEANS

ÉCOLE DOCTORALE ÉNERGIE, MATÉRIAUX, SCIENCES DE LA TERRE ET DE L'UNIVERS

Institut de Combustion Aérothermique Réactivité et Environnement

Thèse présentée par :

Roberta SCARPA

soutenue le : **19 décembre 2017**

pour obtenir le grade de : **Docteur de l'Université d'Orléans**

Discipline : **Énergetique**

Mécanisme d'accélération d'une flamme de prémélange hydrogène/air et effets sur les structures

THÉSE dirigée par :

Nabiha CHAUMEIX	Directeur de Recherche, CNRS-Orléans

RAPPORTEURS :

Mikhail KUZNETSOV	Docteur, Karlsruhe Institute of Technology
Christophe PROUST	Directeur de Recherche, INERIS

JURY :

Laurent CATOIRE	Professeur, ENSTA ParisTech, Président du jury
Nabiha CHAUMEIX	Directeur de Recherche, CNRS-Orléans
Etienne STUDER	Ingénieur, CEA Paris-Saclay
Mikhail KUZNETSOV	Docteur, Karlsruhe Institute of Technology
Christophe PROUST	Directeur de Recherche, INERIS
Ratiba ZITOUN	Maître de Conférence, Université de Poitiers

Acknowledgments

This research work was performed at the Commissariat à l'Énergie Atomique, Paris-Saclay. I would like to thank the Thermo-hydraulics and Fluid Dynamics Unit (STMF) of the Nuclear Energy Division (DEN) for giving me the opportunity to learn and to work side by side with prominent scientists and internationally renowned researchers.

I would like to thank my thesis director, Dr. Nabiha Chaumeix, for her support and guidance. Her advice, suggestions and recommendations have been precious to me and for the success of this work.

I want to express my sincere gratitude to Etienne Studer, my supervisor and mentor. He challenged and encouraged me. His undeniable passion for his work has been for me a true source of motivation.

I am grateful to all members of the jury for taking part in my PhD dissertation. Special thanks go to Professor Christophe Proust and Dr. Mikhail Kuznetsov for being part of the reading committee: their comments and feedback have been of great value to me.

I would like to thank Sergey Kudriakov for our fruitful and constructive discussions and for sharing with me his undoubted optimism. I must also thank Benjamin Cariteau for his technical expertise and supervision.

Surely, I have to thank the technical staff of the LIEFT laboratory; in particular, Jean-Luc Wildloecher and Olivier Norvez, for their technical advice and most importantly for their skills in fixing all kind of problems, and Véronique Lechopied, for her kindness. Without their help this work would not have been possible.

Moreover, I would like to spend few words to thank my colleagues, with whom I shared these three-years experience: Constantin Ledier, Lucia Sargentini and Gianluca Artini, for being such good friends, Frédéric Dabbene, for his eloquence, Sonia Benteboula and Gilles Bernard-Michel, for the coffee-time conversations, Jean-Paul Magnaud, for his words of wisdom, and Jean-Paul Garandet, for his advice and encouragement. I would like to thank all those researchers, post-docs, PhD students and undergraduate students which I had the opportunity to meet and to discuss with. In particular, I want to thank the ICARE team of the CNRS-Orléans for the fruitful discussions.

Eventually, I would like to thank AirLiquide and EDF (Électricité de France) for their support to this research work, as well as ANR (Agence Nationale de la Recherche) and the Mithygéne project (project reference number 11-RSNR-0015 [68]) for supporting the activities on combustion generated loads and their effects on structures.

Said so, I would like to dedicate this thesis work to my partner, for being heartening and supportive, and to all my relatives.

Contents

List of Figures

List of Tables

Nomenclature

Latin Letters

a	Number density of molecules	$[1/m^3]$
A	Pre-exponential factor of Arrhenius law	[-]
A	Flame surface area	$[m^2]$
AIBC	Adiabatic isobaric transformation	
AICC	Adiabatic isochoric transformation	
B_{FS}	Dimensionless parameter for fluid-solid coupling	[-]
BR	Blockage ratio	[-]
BWR	Boiling Water Reactors	
c	Generic variable	
c_p	Specific heat capacity at constant pressure	[J/(kg K)]
c_s	Speed of sound	[m/s]
c_v	Specific heat capacity at constant volume	[J/(kg K)]
C_v	Molar heat capacity	[J/(mol K)]
CC	Chimiemetal shock sensor	
CJ	Chapman-Jouguet	
d	Internal tube diameter	[m]
D	Detonation velocity	[m/s]
D	Tube inner diameter	[m]
$\mathcal{D}$	Bending stiffness	[Nm]
D_k	Mass diffusion coefficient of the species k	$[m^2/s]$
Da	Damköhler number	[-]
DDT	Deflagration-to-Detonation Transition	
D-L	Darrieus-Landau	
DOF	Degrees Of Freedom	
e	Specific internal energy	[J/kg]
E	Internal energy	[J]
E	Young's modulus	[Pa]
E_a	Activation energy	[J]
f	Frequency	[Hz]
F	Generic load	[N]
FA	Flame Acceleration	
FEM	Finite Element Method	
FN	Natural frequency	[Hz]
FSI	Flame Structure Interaction	
G	Shear modulus	[Pa]
GC	Gas Chromatograph	

h	Specific enthalpy	[J/kg]
h	Cylinder thickness	[m]
H	Enthalpy	[J]
I	Light intensity	[W/m^2]
IR	Infra-Red	
$\boldsymbol{j_k}$	Diffusion flux of the chemical species k	[kg/(m^{2}s)]
$\boldsymbol{j_q}$	Heat flux	[W/m^2]
k	Wave number	[1/m]
k	Turbulence kinetic energy	[J/kg]
k	Spring elastic constant	[N/m]
K	Karlovitz stretch factor	[-]
Ka	Karlovitz number	[-]
$l*$	Extinction length for bending effects	[m]
L_m	Markstein characteristic length	[m]
L_T	Integral turbulence length scale	[m]
LDV	Laser Doppler Velocimetry	
Le	Lewis number	[-]
m	Axial mode number	[-]
m	Mass	[kg]
m	Bending moment per unit length for plates	[N]
M	Mach number	[-]
M	Flexural moment per unit length	[N]
Ma	Markstein number	[-]
MIE	Minimum ignition energy	[J]
n	Reaction order	[-]
n	Radial mode number	[-]
N	Force per unit length	[N/m]
NPP	Nuclear Power Plant	
NPT	Nominal Pressure and Temperature	
p	Pressure	[Pa]
Pe	Peclet number	[-]
PIV	Particle Image Velocimetry	
PLIF	Planar Laser Induced Fluorescence	
PMT	Photomoltiplier tube	
PP	Kistler pressure sensor	
Pr	Prandtl number	[-]
q	Non-dimensional heat release	[-]
Q	Heat release	[J/kg]
Q	Force per unit length	[N/m]
R	Universal gas constant	[J/(mol K)]
R	Radius	[m]
R_{fl}	Curvature radius of the flame front	[m]
Re	Reynolds number	[-]
s	Absorption cross section	[m^2]
S	Inter-space between obstacles	[m]
Sc	Schmidt number	[-]
SSEXHY	Structure Subjected to an EXplosion of HYdrogen	

S_L	Laminar burning velocity	[m/s]
S_T	Turbulent flame velocity	[m/s]
SWACER	Shock Wave Amplification by Coherent Energy Release	
t	Time	[s]
T	Temperature	[K]
T	Oscillation period	[s]
TCD	Thermal Conductivity Detector	
TMI	Three Miles Island	
TR	Tube section	
u	Axial displacement	[m]
u	Generic uncertainty	
UV	Ultra-Violet	
$\boldsymbol{U}$	Velocity field	[m/s]
v	Azimuthal displacement	[m]
V	Volume	[m^3]
V	Voltage	[V]
w	Radial displacement	[m]
W	Molecular weight	[kg/mol]
x	Spatial coordinate	[m]
X	Molar fraction	[-]
y	Spatial coordinate	[m]
Y	Mass fraction	[-]
ZND	Zel'dovich Neuman and Döring	

Greek Letters

α	Incident angle	[rad]
α	Thermal diffusivity	[m^2/s]
β	Zel'dovich number	[-]
γ	Heat capacity ratio	[-]
Γ	Gamma function	
δ	Bias in the position of the flame front	[m]
δ_{ij}	Kronecker delta	
δ_K	Turbulent eddies length	[m]
δ_L	Laminar flame thickness	[m]
δ_T	Turbulent flame thickness	[m]
Δ	Difference	
Δ	Distance from the shock wave to equilibrium conditions	[m]
ϵ	Turbulence dissipation rate	[W/kg]
$\boldsymbol{\epsilon}$	Hooke strain tensor	[m]
ζ	Tangential coordinate of the flame front	[m]
θ	Acceleration rate	[s]
ϑ	Dimensionless acceleration rate	[-]
Θ	Dimensionless activation energy	[-]
κ	Shear coefficient	[-]
κ	Surface curvature for a plate	[1/m]

λ	Thermal conductivity	[W/(m K)]
λ	Detonation cell width	[m]
λ	Wave length	[m]
μ	Dynamic viscosity	[Pa s]
ν	Kinematic viscosity	[m^2/s]
ν	Poisson's ratio	[-]
π	Non-dimensional pressure	[-]
Π_j	Exitaction parameter	[-]
ρ	Density	[kg/m^3]
ρ	Curvature radius for a plate	[m]
σ	Non-dimensional density / expansion ratio	[-]
$\boldsymbol{\sigma}$	Hooke stress tensor	[Pa]
τ	Characteristic time	[s]
τ	Gas transmittance	[-]
$\boldsymbol{\tau}$	Internal stress tensor	[Pa]
ϕ	Equivalence ratio	[-]
ϕ	Dynamic amplification factor	[-]
Φ	Diameter	[m]
φ	Bending angle	[rad]
φ_q	Eigenmodes	[-]
χ	Thermal diffusivity	[m^2/s]
ω	Production rate	[1/s]
ω_q	Eigenfrequencies	[Hz]
Ω	Rate of growth	[1/s]

Subscripts

$2D$	Two-dimensional
$2D$axi	Two-dimensional axisymmetric
b	Burnt gas
CS	Clanet and Searby
def	Deflagration
f	Flame
g	Gas
k	Chemical species
L	Laminar
ox	Oxidizer
r	Radial direction
s	Solid
st	Stoichiometric condition
u	Unburnt gas
T	Turbulent
z	Axial direction
θ	Azimuthal direction

Mathematical Operators

$\nabla\cdot$ Divergence
∇ Gradient
Δ Laplacian

Introduction

Context and motivations

In case of severe accident, in-core metal-water reactions due to fuel temperature increase lead to massive release of hydrogen into the containment of Light Water Reactors. The highly compartmentalization of these buildings makes non-condensable gases to accumulate in clouds. With ease, a flammable atmosphere can locally be achieved. Eventually, the explosion of such a cloud may jeopardize the integrity of the containment.
The likelihood of such events has found an evidence in the notorious accident of Three Miles Island in 1979 and, more recently, at the Fukushima Daiichi NPP, in 2011.
At TMI a relatively frequent incident, the loss of normal feedwater to the steam generators, degenerated in a severe accident because of the fatal combination of erroneous evaluations by the operators and careless plant management [112]. Skipping the detailed sequence of the event, during the first sixteen hours of the accident, core uncovery occurred on several occasions before the operators were capable of recovering a correct core cooling. As a consequence, it has been calculated that about 50% of the zirconium in the core reacted with water to produce hydrogen (without considering the production of hydrogen by water radiolysis). The hydrogen cloud leaked from the primary circuit through the relief valve (which was stuck open) led to an explosion in the reactor containment about 10 hours from the initiating event. The explosion did not damage the containment and the essential safety equipment; nevertheless, a pressure spike of about 0.2 MPa was recorded by the instrumentation.
A different scenario occurred at the Fukushima Daiichi NPP on the 11th of March 2011 [4]. Here, the initiating event was a station blackout led by a strong earthquake and the following tsunami. In addition, the flooding caused the unavailability of the emergency diesel generators for the Units 1 to 4. The total loss of electrical power for several hours led to the loss of core cooling and eventually to core damage. Leakage from the containment to the reactor building caused the migration of hydrogen, together with volatile fission products, into the reactor building. As a result, two hydrogen explosions in the reactor buildings of Units 1 and 3 occurred.
Both these accidents proved the importance of a correct management of the risk of hydrogen explosions for the safety of nuclear reactors.
The dynamics of combustion reactions is strongly influenced by boundary conditions: confined geometries tend in fact to promote flame acceleration. Under certain circumstances, the overpressure generated by the lead shock ahead of the flame may cause structural failure. To deal with these safety issues empirical criteria have been developed in the early 2000s [47, 27] to discern possible flame acceleration or deflagration-to-detonation transition (DDT) scenarios. These criteria have proved to be powerful means in best esti-

mate studies for the selection of the most relevant situations for which flame acceleration takes place.

Thanks to the recent improvements in computer capabilities, numerical models have been developed over the last decades in order to perform large scale simulation [143, 54]. Here, the main challenge lays in the resolution of combustion micro-scales: several orders of magnitude separate, in fact, combustion characteristic lengths ($\sim 0.1 - 1$ mm) from typical mesh sizes adopted for containment safety analysis (~ 0.01 m for 2D simulations to 0.1 for 3D ones). As a result, in large scale simulations combustion phenomena are under-resolved. Algebraic combustion models are, therefore, implemented to offset the unresolved terms in the set of balance equations. Nowadays, efforts are made to increase model predictivity pushing towards the use of detailed kinetics and Direct Numerical Simulations [69]. Still, as pointed out in [114], when complex chemical schemes are used, the applicability of DNS is reduced to very small fluid domains due to the need of resolving stiff gradients. Therefore, the improvement of large scale models for containment safety analysis remains of great importance. Nevertheless, the predictivity of these models is still an open issue. Hasslberger et al. [65] showed that the implementation of an Adaptive Mesh Refinement scheme could be a starting point to improve large scale numerical simulations accuracy.

The main purpose of large scale combustion simulations is to provide velocity and acceleration fields, together with local combustion overpressures, for the evaluation of the dynamic load acting on structures. This information is in fact crucial for safety analysis. As pointed out previously, in case of severe accident, the containment of a nuclear reactor is the last barrier to avoid fission products release into the environment. Therefore, its integrity should not be jeopardized by excessive loads. Moreover, the availability of those safety features important for accident management and mitigation should be ensured over the entire duration of the accident. The hydrodynamic force acting on a freestanding object depends not only on the pressure field but also on the flow velocity [133], via the drag force and inertia. Hence, the importance of a fine characterization of flame and shock wave propagation in confined geometries.

Starting from the study of the impact of blast waves, simple models were developed to predict the structural response to explosive loading [13]. The extensive works of Duffey and colleagues on impulsive loads [49] and those of Shepherd and colleagues on gaseous detonation loads [16, 124], brought to the development of new methodology for the assessment of the effects on dynamically loaded structures. Recently, efforts have been made to take into account the structure deformations in combustion simulations. An example is given in [80], where numerical simulations are performed coupling a gas dynamics code with a finite element one.

In this perspective, an R&D program is currently ongoing at CEA Paris-Saclay for the implementation of Fluid-Structure Interaction models in EUROPLEXUS code. The need for verification and validation of these models against experiments has pushed the CEA to design a middle-scale facility for the analysis of combustion generated loads. SSEXHY facility (Structure Subjected to an EXplosion of HYdrogen) is one of many experimental facilities of the Floréal Platform devoted to the studies on hydrogen risk in nuclear and chemical plants.

It is worth noticing that chemical and process industries, dealing with hydrogen transformation and storage, present similar safety issues. Recently, a renewed interest in hydrogen

safety has developed thanks to the spreading use of fuel cells in the automotive (and transport) industry. Many countries worldwide are supporting hydrogen as an alternative fuel to improve air quality and to reduce CO2 emissions. On the 24th of October 2017, R. Harding wrote in the Financial Times: « Japan wants the Tokyo Olympics of 2020 to run on hydrogen ».

Objectives

In the present work, experimental campaigns have been performed with the aim of better understanding the underlying mechanisms of premixed hydrogen/air flame acceleration in obstructed tubes. The main purpose is to provide further details for the improvement of large scale combustion models and, in particular, to determine which parameters play a key role in the flame acceleration process.
Experiments are performed in a circular tube with closed ends, 5 m long, with an internal diameter of 12 cm. An array of equally distributed annular obstacles was placed inside the tube in order to perturb the flame in its propagation. This configuration is chosen to represent the compartments of a reactor containment with a simplified 1D model. Moreover, FA in obstructed tubes has been widely studied in the literature [90, 47, 82, 39] over the past decades, giving us a wide and rich reference database for the comparison. Two experimental campaigns are carried out: the objective is to analyze the effects of the initial pressure and the nitrogen dilution on the mechanisms of flame acceleration, since both these parameters are relevant to severe accident scenarios in nuclear reactors containments.
Additionally, in order to provide more detailed data for the improvement and the validation of numerical models, a feasibility study on a new diagnostic technique to track the flame front position along the tube is performed. The purpose is to obtain a finer representation of the flame velocity profile with respect to the one obtained with classical combustion diagnostics.
Finally, an additional device was specifically designed to the study of the effect of combustion generated loads. This module, placed at the end of the combustion tube, allow to investigate the deformation and the failure mechanism of stainless steel specimens. In the present study, preliminary analyses on the structural response of different specimens to dynamic loads are performed with the aims of defining the setup of the facility and providing reference results for future experimental campaigns.

Methodological approach

The thesis is structured in five main parts, each one divided in different chapters.
Part I is a review of the state of the art on the dynamics of combustion, the flame acceleration mechanisms and the mechanical response of structures under transient loads. In Chapter 1 the balance equations for combustion and flame propagation are provided, with a particular focus on the Hugoniot equation and the Chapman-Jouguet theory. Chapter 2 contains an overview of the phenomenology of deflagration and detonation, highlighting the key parameters for each phenomenon. A focus on the criteria for flame acceleration in obstructed tubes is given in Chapter 3. The analytical formulations for the mechanical

response of shells and plates under static and dynamic loads are provided in Chapter 4.
In **Part II**, the experimental facility SSEXHY is described. Chapter 5 contains a description of the combustion tube for flame acceleration studies and the module for the analysis of combustion generated loads on structures. The setup of an experiment, from the gas injection procedure to the characterization of the flammable mixture, is detailed in Chapter 6. Chapters 7 and 8 provide an outline of the instrumentation used for combustion diagnostics and of the signal post-processing methods, respectively.
Part III presents the experimental results on flame acceleration and is broken down in three chapters. A discussion on the repeatability and reproducibility of the experiments is given in Chapter 9. Chapters 10 and 11 present the effects of the initial pressure and the nitrogen-to-oxygen ratio on flame acceleration process.
The feasibility study on a new technique for flame front tracking measurements is provided in **Part IV**: it consists in performing time-resolved IR absorption measurements by doping the fresh mixture with an alkane.
Part V is focused on the responses of simple structures under different loading conditions: Chapter 13 deals with the results obtained applying a static load on a circular plate with clamped edges; Chapter 14 presents a preliminary analysis of dynamic loads applied to circular plates and cylindrical shells, in order to provide a starting point for the future experimental campaign.
Finally, conclusions are drawn in Chapter 14.3. Here, on-going activities and future works are also outlined.

Part I

State of the Art

Chapter 1

Fluid dynamics of combustion

1.1 Conservation equations for a reactive system

If we consider a gaseous reactive system, composed by K different chemical species, the governing equations are [77, 138, 81]:

1. the continuity equation
$$\frac{\partial \rho}{\partial t} + \nabla \cdot (\rho \boldsymbol{U}) = 0 \tag{1.1}$$

2. the species-mass conservation equations
$$\frac{\partial}{\partial t}(\rho Y_k) + \nabla \cdot (\rho \boldsymbol{U} Y_i) = -\nabla \cdot (\boldsymbol{j_k}) + \rho \omega_k \quad k = 1, \ldots, (K-1) \tag{1.2}$$

3. the momentum equation
$$\frac{\partial}{\partial t}(\rho \boldsymbol{U}) + \nabla \cdot \rho \boldsymbol{U}\boldsymbol{U} = -\nabla p - \nabla \cdot \boldsymbol{\tau} \tag{1.3}$$

4. the energy equation (in terms of total enthalpy)
$$\frac{\partial}{\partial t}(\rho h_t) + \nabla \cdot (\rho \boldsymbol{U} h_t) = \nabla \cdot \left(-\boldsymbol{j_q} - \sum_{k=1}^{K} h_k \boldsymbol{j_k} \right) + \nabla \cdot (\boldsymbol{\tau} \cdot \boldsymbol{U}) + \frac{\partial p}{\partial t} \tag{1.4}$$

5. the ideal-gas equation of state
$$p = \rho R T \sum_{k=1}^{K} \frac{Y_k}{W_k} \,. \tag{1.5}$$

In equations (1.1)-(1.5) body forces are neglected.
Here, the unknown variables of the system are the thermodynamic variables, i.e. temperature T, pressure p and density ρ, the three components of the velocity field, $\boldsymbol{U}$, and the $(K-1)$ species mass fractions Y_k. The total number of the variables (and equations) is therefore equal to $[3 + 3 + (K-1)] = K + 5$.

The mass fractions of the species k is related to the mole fraction X_k via its molecular weight W_k :

$$Y_k = \frac{W_k}{W} X_k \tag{1.6}$$

where $k = 1, \ldots, K$ and $W = \sum_{k=1}^{K} X_k W_k$.
In equations (1.1)-(1.5), t is the time, $\boldsymbol{j_k}$ is the diffusion flux of the species k, ω_k is the production rate, $\boldsymbol{\tau}$ is the internal stress tensor, $\boldsymbol{j_q} = -\lambda \nabla T$ is the heat flux where λ is the mixture thermal conductivity, h_k denote the mass-based constant-pressure enthalpy and R denotes the universal gas constant.
According to Fick's law, the diffusion flux of the species k can be written as:

$$\boldsymbol{j_k} = -\rho D_k \nabla Y_k \,. \tag{1.7}$$

For a viscous fluid (that follows the Newtonian laws of viscosity), the components of internal stress tensor τ_{ij} is defined as:

$$\tau_{ij} = \mu \left(\frac{\partial U_i}{\partial x_j} + \frac{\partial U_j}{\partial x_i} \right) - \frac{2}{3} \mu (\nabla \cdot \boldsymbol{U}) \delta_{ij} \tag{1.8}$$

where $\delta_{ij} = 1$ for $i = j$ and $\delta_{ij} = 0$ for $i \neq j$.
For inviscid flows, equation (1.3) becomes:

$$\frac{\partial}{\partial t}(\rho \boldsymbol{U}) + \nabla \cdot \rho \boldsymbol{U}\boldsymbol{U} = -\nabla p \tag{1.9}$$

that correspond to Euler equation in absence of body forces.

1.2 Mono-dimensional propagation of a flame front

Let us consider a non-viscous fluid propagating in a tube of infinite length with uniform cross-section [81, 22]. By making the following hypotheses:

1. steady-state flow;
2. one-dimensional flow;
3. no body forces;
4. adiabatic conditions (no heat losses or external heat addition);

balance equations (1.1), (1.3) and (1.4) can be written in the form:

$$\begin{aligned} \frac{\mathrm{d}}{\mathrm{d}x}(\rho U) &= 0 \\ \frac{\mathrm{d}}{\mathrm{d}x}(p + \rho U^2) &= 0 \\ \frac{\mathrm{d}}{\mathrm{d}x}(\rho h_t U) &= 0 \,. \end{aligned} \tag{1.10}$$

Energy balance equation can be simplified as:

$$\frac{\mathrm{d}(\rho h_t U)}{\mathrm{d}x} = h_t \underbrace{\frac{\mathrm{d}(\rho U)}{\mathrm{d}x}}_{=0} + \frac{\mathrm{d}h_t}{\mathrm{d}x}(\rho U) = 0 \tag{1.11}$$

therefore, $h_t = \text{const}$. The total enthalpy can be rewritten as the sum of the enthalpy h and the dynamic pressure $U^2/2$:

$$h_t = h + \frac{U^2}{2}\,. \tag{1.12}$$

Thus, integrating balance equations (1.10) across a single discontinuity that separates the unburnt and the burnt gases, the following system of equation is obtained:

$$\begin{aligned} \rho_u U_u &= \rho_b U_b \\ p_u + \rho_u U_u^2 &= p_b + \rho_b U_b^2 \\ h_u + \frac{U_u^2}{2} &= h_b + \frac{U_b^2}{2}\,, \end{aligned} \tag{1.13}$$

where with subscript u and b we denote the unburnt and burnt gases, respectively.
Coupling continuity and momentum equations in (1.13), we get:

$$p_b - p_u = -(\rho_u U_u)^2 \left(\frac{1}{\rho_b} - \frac{1}{\rho_u}\right)\,. \tag{1.14}$$

Equation (1.14) is generally referred to as the Rayleigh-line. It corresponds to a straight-line in the plane $(1/\rho, p)$:

$$p \propto \frac{1}{\rho}$$

whose slope is equal to $-(\rho_u U_u)^2$.
Eventually, if we couple the Rayleigh-line (equation (1.14)) with the energy equation (1.13), we obtain the Hugoniot-Rankine relation:

$$h_b - h_u = \frac{1}{2}(p_b - p_u)\left(\frac{1}{\rho_b} + \frac{1}{\rho_u}\right)\,. \tag{1.15}$$

Possible solutions of the Hugoniot equation

For a designated mixture (Δh^0 is known) and for a given value of $(1/\rho_u, p_u)$, it is possible to plot Hugoniot curve in the $(1/\rho, p)$ diagram. The curve that represents the final state of the burnt mixture is called the Crussard adiabatic.
Even if Hugoniot curve represents all the possible solutions of the Hugoniot equation (1.15), physically there is a branch of solutions that is not valid. The validity regions can be estimated taken into account equations (1.13) and computing the velocities for the unburnt and burnt mixtures:

$$U_u = \frac{1}{\rho_u}\left(\frac{\Delta p}{\frac{1}{\rho_u} - \frac{1}{\rho_b}}\right)^{\frac{1}{2}} \tag{1.16a}$$

$$U_b = \frac{1}{\rho_b}\left(\frac{\Delta p}{\frac{1}{\rho_u} - \frac{1}{\rho_b}}\right)^{\frac{1}{2}}\,. \tag{1.16b}$$

From relations (1.16), we can deduce that:

$$\frac{1}{\rho_u} > \frac{1}{\rho_b}, \text{if } \Delta p > 0 \tag{1.17a}$$

$$\frac{1}{\rho_u} < \frac{1}{\rho_b}, \text{if } \Delta p < 0 \tag{1.17b}$$

Hugoniot curve description

In Figure 1.1 the symbol I designates the initial state of the unburnt mixture, characterized by the values $(1/\rho_u, p_u)$. The bold black line is the Hugoniot curve for the burnt mixture (or Crussard adiabatic), described by equation (1.15). The line that connect points I and B represents an adiabatic isochoric transformation (AICC) that occurs at $U = \infty$ and for which the internal energy is conserved ($e_u = e_b$). In this case we deal with an infinite fast reaction, i.e. an explosion, whose final temperature, T_{AICC}, an pressure, p_{AICC}, are completely defined by thermodynamics considerations [128]:

$$\begin{aligned} \Delta E &= (\Delta H_r^0 - \Delta n R T_u) + \int_{T_u}^{T_b} \sum_j n_j C_{v,j}(T')\,\mathrm{d}T' = 0 \\ V_u &= V_b \\ p_b V_b &= n_b R T_b \end{aligned} \tag{1.18}$$

where $j = 1 \ldots N$ is the number of chemical species in the products.

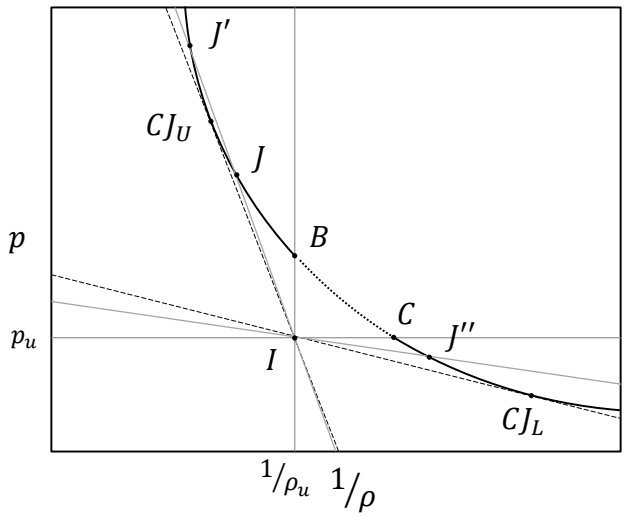

Figure 1.1: Hugoniot-Rankine curve of pressure against specific volume.

Line $\overline{IC}$ represents instead an adiabatic isobaric transformation (AIBC) at $U = 0$. In this case enthalpy is conserved ($h_u = h_b$). The flame temperature, T_b, can be evaluated from the following equation:

$$\Delta H = \Delta H_r^0 + \int_{T_u}^{T_b} \sum_j n_j C_{p,j}(T')\,\mathrm{d}T' = 0\,. \tag{1.19}$$

Points B and C denote the limiting values in the Hugoniot curve for which equation (1.15) has physical meaning: in the left region of the plot delimited by the line $\overline{IB}$ condition (1.17a) is satisfied (detonation region), while condition (1.17b) is verified only in the region under the line $\overline{IC}$ (deflagration region).
The final status of the combustion reaction can be graphically determined by the intersection of the Rayleigh line with the Hugoniot curve (points J, J' and J'' in Figure 1.1). In the limiting cases in which the Rayleigh line is tangent to the Hugoniot curve, two points are determined, called Chapman-Jouguet points (CJ_U and CJ_L).
From Figure 1.1 is also possible to infer that, in the detonation region, where the pressure of the burnt mixture is greater than that of the unburnt mixture, the slope of the Rayleigh line is much steeper than in the case in which $p_b < p_u$ (deflagration region). This means that the steeper the slope, the faster the chemical reaction.

Chapman-Jouguet Theory

The model developed by Chapman (1899) and Jouguet (1905) is based on the definition of a minimum velocity for the detonation regime [128]. This minimum velocity corresponds to the slope of the Rayleigh line tangent to the Crussard adiabatic in point CJ_U in Figure 1.1 (Upper Chapman-Jouguet point). If $U > U_{CJ}$, two distinct solutions are possible:

1. strong detonation ($p_b > p_{CJ}$);

2. weak detonation ($p_b < p_{CJ}$).

Weak detonations have no physical meaning (see [122]) and they are not experimentally observed.
For the determination of the Chapman-Jouguet velocity, U_{CJ}, we refer to the nomenclature used in [122]. In Figure 1.2, a schematic representation of the wave front is presented. $D = U_{CJ}$ is the velocity of the gas entering the front, i.e. the detonation velocity, while $D - u_3$ is the velocity of the burnt gas. In point U, $D \equiv U_{CJ}$. In the Chapman-Jouguet theory the thickness of the combustion reaction is negligible, i.e. fronts I and II coincide. In CJ theory, the detonation is viewed as one unique discontinuity.

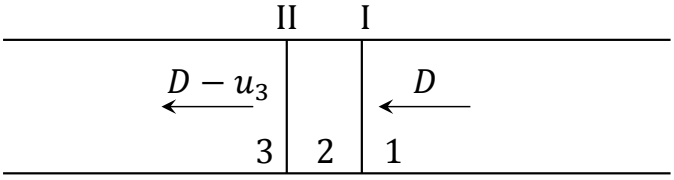

Figure 1.2: Schematic representation of a plain detonation wave in a tube of uniform cross-section.

A plain detonation wave in a tube of uniform cross section is described by the following balance equations:

$$\text{m:} \quad D\rho_1 = (D-u_3)\rho_3 \tag{1.20a}$$

$$\text{qm:} \quad D^2\rho_1 + p_1 = (D-u_3)^2\rho_3 + p_3 \tag{1.20b}$$

$$\text{e:} \quad c_{v,1}T_1 + Q + \frac{p_1}{\rho_1} + \frac{D^2}{2} = c_{v,3}T_3 + \frac{p_3}{\rho_3} + \frac{(D-u_3)^2}{2} \tag{1.20c}$$

coupled with the equation of state for perfect gas:

$$p = \rho RT\,.$$

If we consider non-dimensional pressure, $\pi_3 = p_3/p_1$, and density, $\sigma_3 = \rho_1/\rho_3$, and we assume that the gas undergoes a perfect polytropic transformation with constant γ, equations (1.20) can be simplified in the following way:

$$D^2 = \left(\frac{\pi_3 - 1}{1-\sigma_3}\right)\left(\frac{p_1}{\rho_1}\right) \tag{1.21a}$$

$$(D-u_3)^2 = \sigma_3^2 \frac{\pi_3 - 1}{1-\sigma_3} \tag{1.21b}$$

$$\frac{p_1}{\rho_1} = \sigma_3^2 D^2 \tag{1.21c}$$

$$\pi_3 = \frac{\kappa\sigma_3 + \frac{2\gamma Q}{c_{s1}^2}}{\kappa\sigma_3 - 1} \tag{1.21d}$$

where:

$$\gamma = \frac{c_p}{c_v} \qquad \kappa = \frac{\gamma+1}{\gamma-1} \qquad c_{s1}^2 = \frac{\gamma p_1}{\rho_1}\,.$$

Equation (1.21d) represents the Hugoniot-Rankine equation (1.15) in a non-dimensional form.
To close the system and evaluate the detonation velocity, another condition is necessary. This relation is achieved by imposing the equivalence between the slope of the Rayleigh line passing through U and the tangent in U at the adiabatic Crussard curve. To simplify the computation of $\frac{\mathrm{d}\pi_3}{\mathrm{d}\sigma_3}$, we consider the polytropic adiabatic ($\pi/\sigma^\gamma = \text{const}$) instead of the Hugoniot curve, since they are tangent in U:

$$\frac{\pi_3 - 1}{1-\sigma_3} = \frac{\gamma\pi_3}{\sigma_3}\,. \qquad \text{[Jouguet condition]} \tag{1.22}$$

Equations (1.21),(1.22) allow the computation of all the quantities characterizing a detonation.
Moreover, if we multiply equation (1.22) by σ_3^2, we get:

$$(D-u_3)^2 = c_{s3}^2$$

it means that combustion products depart from the detonation front at sonic velocity.

Eventually, if the Mach number ($M^2 = D^2/c_{s1}^2$) is introduced into the equations, we obtain:

$$\sigma_3 = \frac{1+\gamma M^2}{M^2(1+\gamma)} \tag{1.23a}$$

$$\pi_3 = 1 + \frac{\gamma}{1+\gamma}(M^2-1)\,. \tag{1.23b}$$

Imposing $q = Q/c_vT$ and substituting equation (1.23a) in (1.21d), we get:

$$M^2 = \frac{D^2}{c_{s1}^2} = \left(1+\frac{\gamma+1}{\gamma}q\right) \pm \sqrt{\left(1+\frac{\gamma+1}{\gamma}q\right)^2 + 2\frac{\gamma+1}{\gamma}q}\,.$$

The detonation solution is the one with the + symbol. Moreover, for $q \gg 1$:

$$M^2 \simeq 2\frac{\gamma+1}{\gamma}q \Rightarrow D^2 \simeq 2(\gamma^2-1)Q\,.$$

For a stoichiometric mixture of H_2/air , $U_{\mathrm{CJ}} = D \simeq 1977$m/s.
Eventually, the CJ deflagration speed can be evaluated according to [37]:

$$U_{\mathrm{CJ,def}} = c_{su}\left(1+\frac{\gamma(\gamma-1)}{2(\gamma+1)}\right)\sqrt{2\frac{\sigma-1}{\gamma+1}}\,. \tag{1.24}$$

Equation (1.24) defines the upper limit of flame velocity for deflagrations with high energy release.

1.3 Conclusions

In the present chapter, thermodynamic quantities typical of gas combustion were defined. The attention was focused in particular to those parameters that are used to analyze experimental results, such as

1. the adiabatic isochoric pressure p_{AICC},
2. the adiabatic isobaric temperature T_b,
3. CJ detonation speed U_{CJ},
4. CJ deflagration speed $U_{\mathrm{CJ,def}}$,
5. etc...

These quantities depend only on the thermochemical properties of the gas mixture and on the energy release during the physical transformation, i.e. the chemical reaction. In the next chapter, combustion propagation mechanisms will be discussed. Mass and heat transfer across the reaction front will be solved in parallel with chemical kinetics in order to determine the combustion burning rate and flame propagation characteristics.

Chapter 2

Flame propagation

2.1 Deflagration

In this chapter we will point the attention on the lower part of the Hugoniot-Ranking diagram 1.1, below the lower C-J point L. In this zone combustion reactions are characterized by low propagation velocities in the order of 10 m/s (subsonic speed). In case of deflagration, the reaction propagates thanks to mass and heat transfer across the flame front.
Once the mixture is ignited, a smooth flame front is generated. Depending on the geometry and on the fundamental properties of the flammable mixture, laminar flames can be perturbed and wrinkled. This distortion is due to the formation of a turbulent flow ahead the flame front. Moreover the flame front may incur to several instabilities that accentuate flame distortion. As the flame is wrinkled and bended, its surface strongly increases. This rapid change in the burning rate induce the flame to propagate faster then a laminar one. Usually turbulent velocities are almost ten times greater than laminar ones.
In the present chapter we will try to summarize the most relevant aspects of both laminar and turbulent combustion of premixed gases, focusing on flame propagation mechanisms.

2.1.1 Laminar flames

With the term laminar flame we denote those deflagrations characterized by slow burning velocities in a medium with a laminar flow. This type of flames are usually initiated by a weak source of energy. Since laminar flames propagates at subsonic speed compressible effect can be neglected in both the unburnt and the burnt gases.
Writing the system of balance equations for an almost isobaric transformation between burnt and unburnt gases considering that ignition has happened at a closed end of the vessel ($U_b = 0$), we obtain a simplified expression of the conservation equations [128]:

$$\rho_u(U_u - V_F) = -\rho_b V_F \tag{2.1a}$$

$$p_u + \rho_u(U_u - V_F)^2 = p_b + \rho_b V_F^2 \tag{2.1b}$$

$$h_u + \frac{(U_u - V_F)^2}{2} + Q = h_b + \frac{V_F^2}{2} \tag{2.1c}$$

where V_F is the apparent velocity of the flame front. If we introduce the velocity of the flame front relative to the fresh mixture, $S_L = V_F - U_u$, in the equation for the conservation

of mass, we get:

$$V_F = \frac{\rho_u}{\rho_b} S_L = \sigma S_L \,. \tag{2.2}$$

The laminar burning velocity, S_L^0, that is equal to S_L for unstretched flames, is a characteristic property of the combustible mixture that depends on the chemical and physical properties of the mixture itself. Several models have been proposed during the last century to determine the value of the laminar burning velocity, S_L^0. In the following paragraphs we will review these models starting from the theory of Mallard and Le Chatelier [97] dating back to 1883.

Thermal theory of Mallard and Le Chatelier

In Mallard and Le Chatelier theory the flame thickness comprises two distinguished regions: a preheating one, where the fresh gas is heated by conduction, and a reaction one where the gas has a temperature greater than the ignition temperature and combustion takes place. A schematic representation of the temperature profile across the flame thickness is shown in Figure 2.1. Exhaustive explanations of this model are presented in [22, 81].

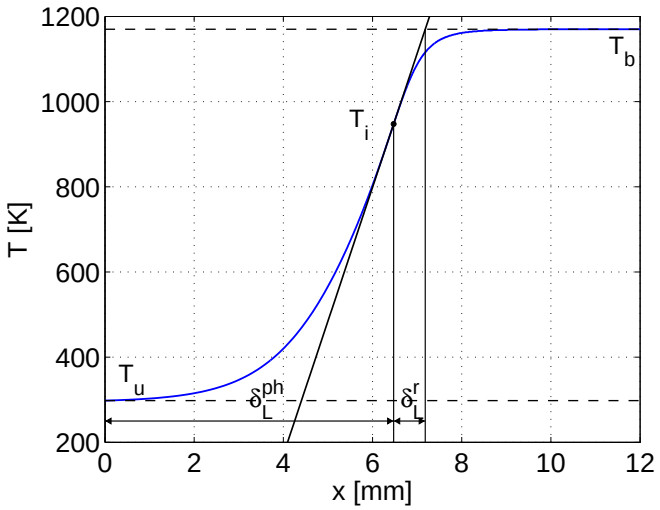

Figure 2.1: Temperature profile across the flame thickness for a 11% hydrogen/air mixture: δ_L^{ph} is the thickness of the preheating zone and δ_L^r is the thickness of the reaction zone.

Let us consider a flat stationary flame-front with a low Mach hypothesis on the flow ($U = -S_L^0$) in which heat flux is described by Fourier's law for heat conduction:

$$\rho c_p U \frac{dT}{dx} - \frac{d}{dx}\left(\lambda \frac{dT}{dx}\right) = q\omega \,. \tag{2.3}$$

To solve equation (2.3) and get the temperature profile, we split the problem in two parts: we first solve the equation in the preheating zone and than we use this solution as boundary condition for the reaction zone.

Preheating zone. In this zone the temperature of the unburnt gas rises from T_u to T_i, the ignition temperature. Temperature conservation equation (2.3) can be simplified since no reactions take place in this zone ($\omega = 0$):

$$\left.\frac{dT}{dx}\right|_{x\to-\infty} = 0 \tag{2.4a}$$

$$T(x \to -\infty) = T_u \tag{2.4b}$$

$$\rho c_p U \frac{dT}{dx} = \frac{d}{dx}\left(\lambda \frac{dT}{dx}\right) \tag{2.4c}$$

By integrating equation (2.4c) in the range $T_u < T < T_i$, we obtain:

$$T(x) - T_u = (T_i - T_u) e^{\frac{\rho c_p U}{\lambda} x}\,. \tag{2.5}$$

Reaction zone. In the reaction zone we can make the hypothesis that the tangent at the temperature profile is constant and equal to that one of the preheating zone in $T = T_i$:

$$\frac{T_b - T_i}{\delta_L^r} = \frac{\rho c_p U}{\lambda}(T_i - T_u) \tag{2.6}$$

where δ_L^r is the thickness of the reaction zone. If we assume that the average reaction rate is proportional to S_L^0/δ_L^r, keeping in mind that $U = -S_L^0$, we obtain a formulation for S_L^0:

$$(S_L^0)^2 = \frac{T_b - T_i}{T_i - T_u}\frac{\lambda}{\rho c_p}\frac{\langle\omega\rangle}{k} \tag{2.7}$$

where k is the proportionality constant between $\langle\omega\rangle$ and S_L^0/δ_L^r.
From equation (2.7) we can eventually infer that

$$S_L^0 \propto \sqrt{\chi\langle\omega\rangle} \tag{2.8}$$

where χ is the thermal diffusivity defined as $\chi = \lambda/(\rho c_p)$. This is one of the most noticeably result of Mallard and Le Chatelier.
Eventually, since the reaction rate is proportional to p^{n-1}, where n is the reaction order, we have $S_L^0 \propto \sqrt{p^{n-2}}$.

Theory of Zeldovich, Frank-Kamenetsky and Semenov

Zeldovich, Frank-Kamenetsky and Semenov extended the theory of Mallard and Le Chatelier coupling the energy balance equation to the species-conservation equation [81].
The hypotheses at the basis of this model are:

1. the ignition temperature is close to the adiabatic temperature of the flame, $T_i \simeq T_b$;
2. constant pressure;
3. constant ratio between reactants moles and products moles;
4. constant λ and c_p;

5. constant Lewis number (Le $= \chi/D$) ;

6. one-dimensional, steady-state flame propagation.

Conservation equations for the general k-th species can then be written as:

$$\underbrace{X_k \frac{d}{dx}(\rho U)}_{=0} + \rho U \frac{dX_k}{dx} = \rho D \frac{d^2 X_k}{dx^2} - \omega \tag{2.9a}$$

$$\rho c_p u \frac{dT}{dx} = \lambda \frac{d^2 T}{dx^2} + q\omega \,. \tag{2.9b}$$

In the adimensional form (Shvab-Zeldovich formulation), equations (2.9) are similar if Le $= 1$.
By considering the Arrhenius law, $\omega \propto A e^{-E_a/(RT_b)}$, The solution of the problem, in terms of laminar burning velocity, depends on the reaction order:

- 0-order reaction

$$S_L^0 = \sqrt{\frac{2\lambda}{c_p \rho_u} \frac{1}{a_u} \left(\frac{RT_b^2}{E_a(T_b - T_u)} \right) A e^{-\frac{E_a}{RT_b}}} \,; \tag{2.10}$$

- n-order reaction

$$S_L^0 = \sqrt{\frac{2}{\rho_u} \frac{\bar{\lambda}}{\bar{c}_p^{n+1}} c_{pu}^n a_u^{n-1} \left(\frac{T_u}{T_b} \right)^n \left(\frac{N_r}{N_p} \right)^n \mathrm{Le}^n \left(\frac{RT_b^2}{E_a(T_b - T_u)} \right)^{n+1} A e^{-\frac{E_a}{RT_b}}} \,. \tag{2.11}$$

In equation (2.11) we have introduced for the preheating zone an average heat capacity, $\bar{c_p}$, an average thermal conductivity, $\bar{\lambda}$ and the number density of reactant molecules, a_u.
In both equations (2.10) and (2.11) appears Zeldovich non-dimensional number:

$$\beta = \frac{E_a(T_b - T_u)}{RT_b^2} \,. \tag{2.12}$$

Eventually, for simplicity, let's consider equation (2.10) (zero-order reaction); since $a_u \propto p$ and $\rho_u \propto p$, $S_L \propto \sqrt{p^{-2}}$ that is coherent with the formulation obtained by Mallard and Le Chatelier ($S_L \propto \sqrt{p^{n-2}}$).

Multi-radicals kinetics models

The further increase in computers capability made it possibles to solve the problem of a propagating laminar flame adopting detailed chemical kinetics and heat transfer mechanisms. Several softwares are now available to compute thermodynamic, transport and kinetic parameters associated with laminar combustion. Among them, we can cite CHEMKIN-II [74] and COSILAB [77].

Laminar flame thickness

Another important parameter for the characterization of laminar flames is the laminar flame thickness. In literature several definitions have been proposed for computing this quantity. Here, in this section, we will present the most widely used.
Let's first consider the model proposed by Mallard and Le Chatelier. As shown in Figure 2.1, the total thickness of the laminar flame is given by the sum of the length of the preheating zone, δ_L^{ph}, and that of the reaction zone, δ_L^r:

$$\delta_L = \delta_L^{ph} + \delta_L^r \simeq \delta_L^r + \delta_L^r \frac{T_i - T_u}{T_b - T_i} = \delta_L^r \frac{T_b - T_u}{T_b - T_i} \,. \tag{2.13}$$

Considering equations (2.6) and (2.7), we get:

$$\delta_L = \frac{T_b - T_u}{T_b - T_i} \left[\frac{(T_b - T_i) k \lambda}{(T_i - T_u) \langle \omega \rangle \rho c_p} \right]^2 \,. \tag{2.14}$$

The thermal thickness can also be evaluated by considering the thermal balance between the burnt and the unburnt gases ($\delta_L^h \rho_u S_L^0 \simeq \rho_b \chi(T_b)$):

$$\delta_L^h \simeq \frac{\chi(T_b)}{\sigma S_L^0} \,, \tag{2.15}$$

where $\chi(T_b)$ is the thermal diffusivity evaluated at $T = T_b$.
The ratio between the thickness of the preheating and that of the reaction zone can be expressed through the Zeldovich number, β:

$$\delta_L^r = \frac{\delta_L^h}{\beta} \simeq \frac{\chi}{S_L^0} \beta \,. \tag{2.16}$$

For high activation energy β is greater than unity and δ_L^r is much smaller than δ_L^h, i.e the chemical reaction is extremely confined. The flame thickness is then only dependent on the thermal properties of the mixture. Actually, this is true only if $\mathrm{Le} > 1$, otherwise the diffusion of species at the flame front is the predominant phenomenon. In this case the flame thickness is influenced by the molar diffusion coefficient of the limiting component, D_l. For a reactive mixtures, the effective Lewis number [3] is usually taken into account:

$$\mathrm{Le}_{\mathrm{eff}} = 1 + \frac{(\mathrm{Le}_e - 1) + (\mathrm{Le}_l - 1) A}{1 + A} \tag{2.17}$$

where $A = 1 + \beta(\phi' - 1)$. In equation (2.17), subscripts, l and e refer to the limiting and exceeding components respectively, while ϕ' corresponds to the equivalence ratio for rich mixtures or to its reciprocal for lean mixture:

$$\phi' = \begin{cases} \phi & \text{if } \phi > 1 \\ 1/\phi & \text{if } \phi < 1 \end{cases}$$

The fuel-to-oxidizer equivalent ratio is defined as:

$$\phi = \frac{m_{\mathrm{fuel}}/m_{\mathrm{ox}}}{(m_{\mathrm{fuel}}/m_{\mathrm{ox}})_{\mathrm{st}}} \tag{2.18}$$

where m is the mass and the subscript st stands for the stoichiometric condition.
In the case of turbulent combustion (detailed in Chapter 2.1.3) it is preferred to adopt the kinematic viscosity to define the flame thickness (momentum, heat and mass transfer analogy, $\mathrm{Sc} = \mathrm{Pr} = 1$):

$$\delta_T \simeq \mathrm{Pr}\delta_L \simeq \frac{\nu}{S_L^0}\,. \tag{2.19}$$

Another definition of the flame thickness was proposed by [114]:

$$\delta_L^{th} = \frac{T_b - T_u}{\frac{dT}{dx}|_{max}}\,. \tag{2.20}$$

Equation (2.20) requires the computation of the temperature profile across the flame. The final temperature of the burnt gas, T_b, is the adiabatic flame temperature computed considering the thermochemistry equilibrium between fresh and burnt gases (see equation (1.19)).
All the definitions for the laminar flame thickness above described are summarized in Table 2.1.

Table 2.1: Laminar flame thickness

Model	**Definition**	**Comments**
Mallard	$\delta_L = \frac{T_b - T_u}{T_b - T_i}\left[\frac{(T_b - T_i)k\chi}{(T_i - T_u)\langle\omega\rangle}\right]^2$	Total laminar flame thickness.
Thermal theory	$\delta_L^h = \frac{\chi}{\sigma S_L^0}$	Equivalent to δ_L if the heat transfer is the predominant phenomenon.
Diffusive theory	$\delta_L^h = \frac{D_l}{S_L^0}$	Equivalent to δ_L if the mass transfer is the predominant phenomenon.
Reaction zone	$\delta_L^r = \frac{\delta_L^h}{\beta}$	Length of the zone where the chemical reaction is confined.
Poinsot	$\delta_L^{th} = \frac{T_b - T_u}{\frac{dT}{dx}\|_{max}}$	Precise estimation of the total laminar flame thickness. A numerical computation is required.

2.1.2 Flame instabilities

In previous chapters we have assumed that the flame front is planar, with the normal to the surface that is parallel to the tube axis. It has been observed experimentally that a premixed laminar flame could incur several instabilities that distort its surfaces making flame propagation dynamics to vary [128]. In this section we will describe briefly the different types of instabilities of a flame front.

Darrieus-Landau instabilities

The limits of stability of a laminar flame front under small perturbation have been studied independently by Darrieus [42] and Landau [87] in the 1940s. These investigations pointed out that a planar front is intrinsically unstable following the expansion of the burnt gas. Darrieus and Landau developed their analysis considering the flame front as a discontinuity in the yz-plane coordinates. Since for laminar flames the velocity is far lower then

the speed of sound, the gas can be assumed as incompressible and inviscid, thus governed by the linearized Euler equations [88]. A small perturbation periodic in y-direction and in time is then added to the flame front having the form $\zeta(y,t) = Ae^{iky-\Omega t}$, where k is the wave number, Ω is the rate of growth and A is the initial amplitude.
By solving Euler equations for the perturbed pressure and velocity field, we obtain an equation for Ω:

$$(\sigma+1)\Omega^2 + 2k\sigma S_L^0\Omega + k^2\sigma(S_L^0)^2(1-\sigma) = 0 \tag{2.21}$$

Equation (2.21) presents a real and positive solution, which describes the intrinsic instability of the flame front:

$$\Omega = kS_L^0\frac{\sigma}{1+\sigma}\left(\sqrt{1+\sigma-\frac{1}{\sigma}}-1\right) \tag{2.22}$$

Moreover, from equation (2.22) is possible to infer that the flame front is unstable for a perturbation of any wavelength as the rate of growth is proportional to k.
As pointed out in [88], such instability would promote the formation of a spontaneous turbulence of the flame. Actually, experimental results have shown that D-L instability appears only if Reynolds numbers associated to unburnt and burnt gases are very large. Only in this case the viscosity of the fluid does not intervene stabilizing the front. Moreover, the applicability of the approach above described is limited to the case in which the flame thickness is small compared to the wavelength. In fact, if the wavelength is small, the flame front is strongly corrugated and the hypothesis of infinitely thin flame is no more valid.

Diffusive instabilities

Another important factor for flame stabilization is the Lewis number, $\mathrm{Le} = \chi/D_L$. If the heat flux prevails over the diffusive flux ($\mathrm{Le} > 1$), the velocity of the unburnt gas increases at the concave parts of the flame front (facing the fresh mixture), where heat exchange between the two gas phases is promoted [88]. In the convex zones the velocity of the unburnt gas tends to decreases, then smoothing the wrinkles and flattening the flame front, whit a stabilizing effect.
On the opposite side, when the Lewis number is lower than the unity, the diffusive flux of the limiting component tends to emphasize the formation of crests and throats in the flame front thus increasing flame wrinkling [38].

Flame stretching instabilities

The influence of the curvature of the flame front on the combustion rate has been studied by Markstein [98] in 1951.
Unlike Darrieus and Landau, whose model was based on the assumption of a constant burning velocity with $u_u = S_L^0$ and $u_b = \sigma S_L^0$, Markstein proposed to introduce a dependence of burning velocity on the curvature of the flame front [99] through a linear relation:

$$S_L = S_L^0\left(1+\frac{L_m}{R_{fl}}\right) \tag{2.23}$$

where R_{fl} is the radius of the curvature of the flame front and L_m is referred as 'Markstein characteristic length' and it is proportional to the thermal thickness of the flame, δ_L^h. Defining the curvature as positive when the flame front is convex toward the burnt gas (stabilizing effect for positive L_m), equation (2.23) can be rewritten as:

$$S_L = S_L^0 \left(1 - L_m \frac{\partial^2 \zeta}{\partial y^2}\right) \tag{2.24}$$

By substituting relation (2.24) in equations (2.21), we obtain another expression for Ω [128], whose solution presents in this case both stable and unstable ranges of wave numbers. The critical wave number, corresponding to the transition between the these ranges, can be computed by imposing $\Omega = 0$:

$$k_c = \frac{1}{2} \frac{\sigma - 1}{\sigma L_m} \,. \tag{2.25}$$

For perturbations of the flame front with $k > k_c$, the flame front is stable, otherwise wrinkles are amplified. Moreover, if we impose $L_m = 0$, we get the same solution of Darrieus and Landau, described by equation (2.22), while, as already mentioned, for $L_m > 0$ we get a stabilizing effect.
The Markstein number, Ma, defined as the proportionality coefficient between L_m and δ_L, depends on both Zeldovich and Lewis numbers, as following [128]:

$$\mathrm{Ma} = \frac{1}{\mathrm{Le}} \left[1 + \frac{\beta}{2}(\mathrm{Le} - 1)\right] \,. \tag{2.26}$$

According to equation (2.26), the sign of Ma depends on the product $\beta(\mathrm{Le} - 1)$: for $\beta(\mathrm{Le} - 1) > -2$, $\mathrm{Ma} > 0$, while for $\beta(\mathrm{Le} - 1) < -2$, $\mathrm{Ma} < 0$. Experimentally, it has been noted that for positive Ma, flame stretch leads to a decrease of the burning velocity, stabilizing flame wrinkling. On the contrary, for lean hydrogen-air flames, with a negative Ma, a distinct unstable behavior was observed [27]. The product $\beta(\mathrm{Le} - 1)$ plays also an important role in thermal-diffusion flame instabilities. In fact, the lower limit for flame stability corresponds to:

$$\beta(\mathrm{Le} - 1) = -2 \,. \tag{2.27}$$

Other instabilities

When a flame is subjected to an acceleration process, like in a obstacle-laden tube, the propagation is influenced by other types of instabilities, such as Kelvin-Helmholtz, Rayleigh-Taylor and Richtmeyer-Meshkov instabilities [128, 38].
The K-H instabilities appear as shear velocity arises at the interface between two fluids of different densities. As a result, the discontinuity surface is periodically wrinkled. When a lighter fluid is accelerated towards a heavier fluid, R-T instabilities are developed. Moreover, this type of instability is amplified by the effect of the gravity force when a flame propagates upwards. R-M instabilities occur when two fluids with different densities are rapidly accelerated, as, for example, after a shock wave transit. While D-L instabilities are significant only in the early stages of flame propagation, the above mentioned instabilities become important during the following acceleration phase, promoting turbulence.
Acoustic instabilities are characteristic of slow flames in enclosures without obstacles [38]. Experiments performed by [132] suggested that this type of instabilities could be also important in obstacle-laden tubes.

2.1.3 Turbulent flames

As mentioned in section 2.1.2, a laminar propagating planar front can undergo the action of instabilities that fold and wrinkle its surface. Once the flame front becomes more chaotic, we can observe a transition from a laminar quiescent regime to a turbulent regime. This is due to the interaction between turbulent eddies in the fresh gas ahead of the flame and the flame front.
In the following paragraphs we will adopt the notation proposed by Reynolds to describe a turbulent flow. According to Reynolds' theory each variable can be decomposed in an average contribution and a fluctuating part having a zero time average [116, 6]:

$$c(t) = \bar{c}(t) + c'(t) \tag{2.28a}$$

$$\bar{c}(t) = \frac{1}{\Delta t}\int_{t-\Delta t/2}^{t+\Delta t/2} c(\tau)\, d\tau \tag{2.28b}$$

$$\int_{t-\Delta t/2}^{t+\Delta t/2} c'(\tau)\, d\tau = 0\,. \tag{2.28c}$$

Turbulence intensity can be estimated considering the square root of the quadratic average of velocity fluctuations, $\sqrt{\bar{U'^2_x} + \bar{U'^2_y} + \bar{U'^2_z}}$. Hereafter we will call the quantity $\sqrt{\bar{U'^2_k}}$ random mean square velocity, $U'_{k,rms}$, or simply U'_k (that should not be confused with definition (2.28c)).
Turbulent Reynolds number represents the ratio between the kinetic energy associated to eddies and the energy dissipated by viscous forces:

$$\mathrm{Re}_T = \frac{k^{1/2} L_T}{\nu}\,. \tag{2.29}$$

Turbulence kinetic energy, k, is linked to the velocity fluctuations via the following relationship:

$$k = \frac{1}{2}(\bar{U'^2_x} + \bar{U'^2_y} + \bar{U'^2_z}) = \frac{3}{2} U'^2_{rms}\,. \tag{2.30}$$

L_T is the integral turbulence length scale and it characterizes the scale of the largest eddies (maximum distance over which a fluctuating component of velocity is still correlated, i.e. $\bar{U'_k}(\boldsymbol{r_1})\bar{U'_k}(\boldsymbol{r_2}) \neq 0$ for $\overline{\boldsymbol{r_1 r_2}} \leq L_T$). For high Reynolds number it holds:

$$L_T \propto \frac{k^{3/2}}{\epsilon} \tag{2.31}$$

where ϵ is the turbulence dissipation rate ($\epsilon = -dk/dt$). Other important parameters for the characterization of a turbulent flow are the Kolmogorov length, time and velocity scales, that describe the behavior of the smallest eddies. In fact, while large eddies transfer turbulence kinetic energy from the main flow to the smaller structures (energy cascade), the smallest eddies are responsible for the dissipation of the turbulence kinetic energy.
After having recalled all the most important aspects of a turbulent flow, we will point our attention on the interaction between a turbulent flow and a propagating reaction front. The different aspects of the turbulent combustion will be described in the following paragraphs.

Turbulent combustion regimes: Borghi diagram

In a laminar combustion the characteristic time of the chemical reaction, τ_r ($\tau_r = \delta_L^r / S_L^0$), is much shorter than the time associated to flow fluctuation, τ_m; chemistry is, then, not influenced by any changes in the flow pattern. The opposite occurs when $\tau_r > \tau_m$ [60]. In this case, even a low-intensity turbulent flow tends to modify the almost planar laminar front making it more wrinkled. The further increase of the surface area of the flame, thanks to the formation of wrinkles, leads to and increase of the burning rate, thus to a rapid augmentation of the flame speed. This phenomenon, in turn, tends to increase the level of turbulence, leading to a self-sustaining mechanism. When the turbulence is so intense that the flame front becomes fragmented, the combustion reaction can extinguish. Depending on velocity fluctuations and on turbulence length scale, it is possible to distinguish different turbulent regimes. These combustion regimes are presented in Figure 2.2, that represents Borghi's diagram [21, 22, 2].

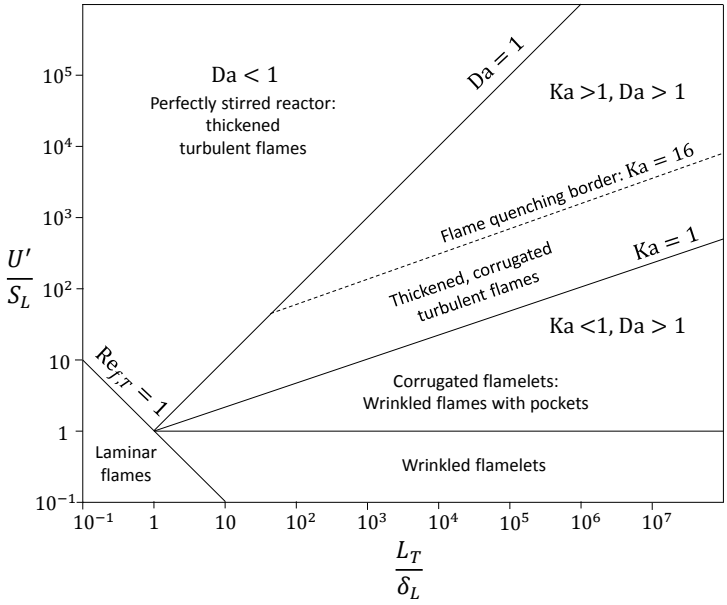

Figure 2.2: Borghi's diagram of combustion regimes [2].

In the ordinates axis we can find the ratio between U', the random mean square velocity, and the laminar flame speed, S_L; while in the abscissas axis there is the ratio between the turbulence integral length scale, L_T, and the laminar flame thickness, δ_L. In the logarithmic plot each regime is separated by straight lines, given by constant Reynolds, Damköhler and Karlovitz numbers, whose slopes are defined by the following expressions:

$$\mathrm{Re}_{f,T} = \frac{U' L_T}{\nu} = \left(\frac{U'}{S_L}\right)\left(\frac{L_T}{\delta_L}\right) \text{ (cf. equation (2.19))} \tag{2.32}$$

$$\mathrm{Da} = \frac{\tau_T}{\tau_r} = \left(\frac{U'}{S_L}\right)^{-1}\left(\frac{L_T}{\delta_L}\right) \tag{2.33}$$

$$\mathrm{Ka} = \frac{\tau_r}{\tau_K} = \left(\frac{U'}{S_L}\right)^{3/2}\left(\frac{L_T}{\delta_L}\right)^{-1} \tag{2.34}$$

where we have assumed $k^{1/2} = U'$.

For small value of L_T/δ_L and U'/S_L ($\mathrm{Re}_{f,T} < 1$), turbulence is too weak to interfere with the combustion process, thus the flame propagates in a laminar regime, characterized by a thick thermal flame length. As both L_T/δ_L and U'/S_L increase, several regimes are possible. Lets describe each region of the plot in details, focusing on the transition from a regime to another:

- $\mathrm{Re}_{f,T} > 1$, $\mathrm{Ka} < 1$ ($\mathrm{Da} > 1$)
  In this region turbulence intensity tends to increase ($\mathrm{Re}_{f,T} > 1$), but the time associated to chemical reactions is still shorter than the characteristic time of turbulent eddies ($\tau_r < \tau_K$). The flow slightly interacts with the flame front stretching and wrinkling it, thus the name *flamelets* to designate these thin and curved flames. When $U'/S_L > 1$, flames become more corrugated, characterized by the presence of reactant pockets in the burnt gas.

- $\mathrm{Ka} > 1$, $\mathrm{Da} > 1$
  Chemical reactions are influenced by the motion of the smallest eddies ($\tau_r > \tau_K$) and the flame becomes thicker (*thickened flames*). As Ka increases, the flame front is subjected to a fragmentation (reactant pockets expand, cooling the region where chemical reactions take place). If the flame is severely stretched, flame quenching becomes possible.

- $\mathrm{Re}_{f,T} > 1$, $\mathrm{Da} < 1$
  When $\tau_r \gg \tau_T$, large eddies promote the mixing inside the whole volume and no flame structure exists. Generally, this regime is referred to as *perfectly stirred reactor*.

If we consider a flame propagating in a confined volume characterized by a fixed geometry, such as a duct, we can make the hypothesis that L_t is constant. In this case, as the flame accelerate, turbulence intensity increases and the flame passes through almost all the regimes early mentioned. In Borghi's diagram this transformation is represented by a vertical line at $L_T/\delta_L = \text{const}$: L_T depends almost only on the geometry, that do not vary, while δ_L is defined by the chemical properties of the fresh mixture [38].
As mentioned above, if the flame is highly stretched, flame quenching could appear. Flame quenching has been observed to happen in the region of the Borghi's diagram characterized by higher Ka. It has also been noted that the Lewis number of reactants intervene in promoting this process: the larger the value of Le, the greater is the influence of flame straining [2].
In [1] two criteria for flame quenching have been formulated on the basis of the experimental data available at that time on fan-stirred combustion bombs:

$$K \cdot \mathrm{Re}_{f,T}^{-1/2} > 0.079 \quad \text{for} \quad \mathrm{Re}_{f,T} < 300 \tag{2.35a}$$

$$K \cdot \mathrm{Le} > 1.5 \quad \text{for} \quad \mathrm{Re}_{f,T} > 300\,. \tag{2.35b}$$

Karlovitz stretch factor, K, embodies the influence of strain on flame shape, in terms of the variation of the surface area A:

$$\begin{aligned} K &= \frac{1}{A}\frac{dA}{dt} \\ &= \left(\frac{U'}{S_L}\right)\left(\frac{\delta_L}{\lambda}\right) \end{aligned} \tag{2.36}$$

where λ is the Taylor length scale. By imposing $\lambda/L_T = C\mathrm{Re}_{f,T}^{-1/2}$, we obtain a relationship between Karlovitz stretch factor K and Karlovitz number Ka. Abdel-Gayed and Bradley [1] suggested for the numerical constant C the value $\sqrt{40.4}$; thus equation (2.36) yields:

$$K = 0.157\,\mathrm{Ka}\,. \tag{2.37}$$

A detailed comparison between different quenching criteria is presented in [101]. Here the experimental data of [1] are compared with the analytical model of [115] and numerical simulation results. Three features can be stressed out:

1. eddies at Kolmogorov scales are not able to quench a flame (they are dissipated by viscosity too fast to interact with the flame);

2. numerical simulations performed by [101] give results similar to the single-eddy criterion proposed by [115], that can be expressed as (in similarity to equation (2.35b)):

$$Ka = 16 \quad \text{for} \quad \mathrm{Re}_{f,T} > 250\,; \tag{2.38}$$

3. for low Reynolds number ($\mathrm{Re}_{f,T} < 250$) quenching is more likely to happen because of thermal losses then flame stretching.

Equation (2.38) is presented in Figure 2.2 with a dashed line [128].
The problem of thermal quenching has been studied analytically by Dorofeev in [45]. By assuming that the flame front is characterized by the presence of nearly spherical mixed reactants/products pockets ($Ka > 1$) and by imposing the thermal equilibrium of these pockets, the author derives a critical condition between thermal quenching and re-ignition of mixed pockets:

$$\left(\frac{\Delta}{\delta_L}\frac{1}{\mathrm{Ka}}\right)^{\frac{2}{3}} \frac{\sigma^2\beta^2\left(\frac{\beta}{2}-1\right)^n e^{1-\frac{\beta}{2}}}{6\mathrm{Le}^n\Gamma_{n+1}\varkappa} = 1 \tag{2.39}$$

where Δ is the average pockets radius, $\Gamma_{n+1} = \int_0^\infty x^n e^{-x}\,dx$ is the Gamma function and $\varkappa$ is a constant that depends on the Prandtl number.
The size of the mixed pockets depends on the turbulent regime. If turbulent eddies are smaller than the laminar flame thickness, then mixed pockets can not be formed since small eddies are rapidly dissipated by viscous effects. Thus, the smallest size of the pockets is on the order of magnitude of δ_L. The opposite happens when $\Delta > \delta_K$, where δ_K is the length of the turbulent eddies; in this case turbulence is not fast enough to provide effective mixing of reactants and products. The size of the pockets is then limited in the range $\delta_L < \Delta < \delta_K$. Let's now focus on the two limiting cases $\Delta \simeq \delta_L$ and $\Delta \simeq \delta_K$. In the first case, equation (2.39) becomes

$$\mathrm{Ka}^{2/3} = \frac{\sigma^2\beta^2\left(\frac{\beta}{2}-1\right)^n e^{1-\frac{\beta}{2}}}{6\mathrm{Le}^n\Gamma_{n+1}\varkappa}\,. \tag{2.40}$$

Equation (2.40) identify a straight line parallel to Ka = 1. Above this line, small mixed pockets are thermally quenched. Moreover, the critical value of Ka for thermal quenching, Ka^*, depends on thermo-chemical properties of the mixture: small values of β and Le or high value of σ and n promote flame stability (upward translation of the critical curve), while highly unstable (highly fragmented) flames occur in the opposite case.

For $\Delta \simeq \delta_K$, the ratio Δ/δ_L is equal to Ka. Equation (2.39) can be rewritten as

$$1 = \frac{\sigma^2 \beta^2 \left(\frac{\beta}{2} - 1\right)^n e^{1-\frac{\beta}{2}}}{6\mathrm{Le}^n \Gamma_{n+1} \varkappa} \,. \tag{2.41}$$

In this case, no turbulence parameter appears in the equation that describes the critical condition for mixed pockets' quenching. This means that, for well established turbulent flow (Ka > 1), all pockets are expected to be quenched if the right side of equation (2.41) is lower than 1. As we will see in the forthcoming chapters, equation (2.41) can also be used as a limiting condition for strong flame acceleration.

Turbulent burning velocity

Early investigations on turbulent flame have been performed by Damköhler in 1940s [81]. He found that the velocity of a turbulent flame highly depends on the Reynolds number; for small Reynolds number (Re < 2300), the flame is not influenced by the turbulent flow and the flame speed is equal to the laminar one, while for high Reynolds number the flame speed is proportional to Re. For Re > 6000, turbulent eddies are larger than the flame thickness, making the flame more stretched and wrinkled, but they do not modify the transport properties. The surface area of the flame is thus increased, consequently increasing the combustion rate and the apparent flame speed. Since the surface area is proportional to the velocity fluctuations, which are at the same time proportional to the Reynolds number, Damköhler suggested a simple proportional law to compute the turbulent flame speed:

$$\frac{S_T}{S_L} = A\,\mathrm{Re} + B \,. \tag{2.42}$$

In the intermediate region $2300 <$ Re < 6000, the flow is characterized by a small scale turbulence. In this case eddies dimension is much lower than the flame thickness. The flame is slightly wrinkled but heat and species diffusion processes are enhanced. By assuming an analogy between laminar and turbulent flame propagation, we can hypothesize that

$$S_T = \sqrt{\chi_T \langle w \rangle} \quad \text{(cf. equation (2.8))} \tag{2.43}$$

$$\frac{S_T}{S_L} \simeq \left(\frac{\chi_T}{\chi}\right)^{1/2} \tag{2.44}$$

If $\mathrm{Pr}_T \simeq \mathrm{Pr} \simeq 1$, equation (2.44) becomes

$$\frac{S_T}{S_L} \simeq \left(\frac{\nu_T}{\nu}\right)^{1/2} \simeq 0.1\mathrm{Re}^{1/2} \tag{2.45}$$

where it has been assumed $\nu_T/\nu = 0.01$Re (pipe flow).
Equation (2.45) perfectly fits Damköhler experiments on Bunsen-burners, but it is not valid as $\nu_T \to 0$, since in this case $S_T \to 0$ instead of S_L.
A similar approach has been adopted by Shelkin [121]. Unlike Damköhler, Shelkin has also highlighted the importance of time scale associated to a turbulent flow. For small turbulent scale, he considered that mixing processes are influence by both turbulent and

molecular diffusivities. Stressing the fact that in this regime the most relevant time scale is the one associated with chemical reaction, equation (2.44) becomes

$$\begin{aligned} S_T &\simeq \sqrt{\frac{\chi_T + \chi}{\tau_r}} \\ &\simeq \sqrt{\frac{\chi}{\tau_r}}\sqrt{1 + \frac{\chi_T}{\chi}} \\ &\simeq S_L\sqrt{1 + \frac{\chi_T}{\chi}}\,, \end{aligned} \tag{2.46}$$

thus the solution of the problem of the lower asymptote.
For larger turbulence scales, we can assume that the mixing coefficient entirely depends on turbulent properties, thus $\chi_T \propto L_T U'$. Time scales are also deeply influenced by turbulence. Thus

$$S_T \simeq \sqrt{\frac{\chi_T}{\tau_T}} \propto \sqrt{\frac{L_T U'}{\frac{L_T}{U'}}} \propto U' \tag{2.47}$$

From equation (2.47) it is possible to infer that the turbulent flame speed does not depend on the chemical nature of the mixture. Shelkin's arguments then proved the validity of equation (2.42) for high velocity fluctuations ($U' >> S_L$).
Shelkin has also proposed a geometrical approach to describe the influence of surface augmentation on flame speed. In this analysis, each wrinkle is compared to a cone, whose base is perpendicular to flame propagation direction. The base radius is supposed to be equal to $L_T/2$ while the height h is on the order of $L_T U'/S_L$. The ratio between the turbulent speed and the laminar one can be assumed to be proportional to the ratio of the flame surfaces with and without turbulence. Thus

$$\left(\frac{S_T}{S_L}\right)^2 \simeq 1 + B\left(\frac{U'}{S_L}\right)^2 \tag{2.48a}$$

$$\simeq 1 + B\kappa^2\left(\frac{U}{S_L}\right)^2 \tag{2.48b}$$

where B is a constant, U the mean flow velocity and κ is the Von Karman constant ($U' = \kappa U$). Of high importance is the fact that equation (2.48) can be adopted for any turbulence scale.
Another historical approach for the estimation of the turbulent flame speed is the one of Summerfield and colleagues [129]. Rearranging equation (2.45), it is possible to obtain the following similarity relation:

$$\frac{S_T \delta_T}{\nu_T} = \frac{S_L \delta_L}{\nu}\,. \tag{2.49}$$

On experimental basis the ratio $S_L\delta_L/\nu$ is found to be 10, thus

$$S_T = 10\frac{\nu_T}{\delta_T}\,. \tag{2.50}$$

The turbulent speed can then be estimated only on the basis of turbulent viscosity and turbulent flame thickness.
Other examples from the litterature for the formulation of S_T are given in Table 2.2 (n.b. the list is not exhaustive).

Table 2.2: Turbulent burning velocity

Definition	Reference	Note
$S_T \propto U' \mathrm{Da}^{1/4} = U' \left(\frac{S_L}{U'} \frac{L_T}{\delta_L}\right)^{1/4}$	[152]	Note that for $U' \to 0$, $S_T \to 0$ instead of $S_T \to S_L$ as expected.
$\frac{S_T}{S_L} = 1 + 0.8 \left(\frac{U'}{S_L}\right)^{0.55} \left(\frac{L_T}{\delta_L}\right)^{0.15} \mathrm{Le}^{-0.3}$	[24]	
$\frac{U_T}{U_L} = 1.61 \left(\frac{r}{L_T}\right)^{0.333} \left(\frac{U'}{S_L}\right)^{0.526} \mathrm{Le}^{-0.140}$	[61]	Experimental correlation derived for hydrogen/air spherical flames with $X_{\mathrm{H2}} = 0.16 - 0.28$ and $r/L_T = 0.4 - 1.2$. U_T and U_L are the apparent flame velocities ($U_L = \sigma S_L$) and r is the flame radius.

2.2 Detonation

In this chapter we will point the attention towards the mechanisms associated with the detonation of a premixed mixture. Starting from the theory of Chapman-Jouget with a mono-dimensional detonation wave structure where gasdynamics are governed solely by the thermodynamics of the mixture (as detailed in Chapter 1.3), several improvements have been done in order to establish a model capable of predicting the 3D character of the detonation wave.
The first step forward has been made in the early 1940s with the ZND model, an extension of the classical C-J theory where shock wave and reaction front are coupled. In this perspective, the shock wave, moving at the detonation velocity, modifies the thermodynamic state of the gas immediately behind the shock wave, thus influencing the thermochemistry of the reaction.
The turning-point in understanding the mechanisms governing the detonation has been marked in the 1960s. Thanks to the smoked-foil technique, Denisov and Troshin [43] proved that self-sustaining propagating detonation waves present a multidimensional structure, with an unstable leading shock that is composed by numerous curved shock sections, convex toward the incoming flow [122, 145, 127, 81].

2.2.1 ZND model

In the Chapman-Jouget model, described in Chapter 1.3, the chemical reaction was considered to be coincident with the shock wave (see Figure 1.2). No characteristic time scales for reaction are evoked to consider the delay for the reaction to take place nor the time to reach completion [26]. As an extension of the C-J theory, Zel'dovich [150], von Neuman [146] and Döring [44] have independently assumed that detonation structure consists of a mono-dimensional steady planar shock wave, moving at the detonation velocity, followed by a finite length reaction zone typically larger than the shock one. The adiabatic compression associated with the shock wave heats the reactants to a temperature at which the combustion rate is sufficient to sustain a propagation of the flame at the shock wave velocity. Thus, differently from the case of planar deflagration, the propagation of the flame front is no more governed by heat and mass transfers.
Figure 2.3 shows the variation of physical properties through a detonation wave in the

ZND model. In the region between the lines denoted with the numbers 1 and 1′, the fast increase of pressure and temperature is due to the adiabatic compression. State 1′ defines the so-called von Neuman spike. Immediately behind the shock, thermodynamic properties profiles become more flatten; this is linked to the fact that the combustion rate, following the Arrhenius law, varies slowly. For this reason the region 1′-1″ is called 'induction zone'. As the reaction rate increases (region 1″-2), the energy released makes the temperature rise, while pressure decreases. The velocity of the flow downstream of the shock accelerates towards the C-J velocity (the Mach number tends to 1 at the equilibrium state). At point 2 the reaction is completed and the thermodynamic properties reach the equilibrium values. Generally, the induction length is defined as the distance between the shock and the point at which the temperature increasing rate has its maximum (maximum heat release) [123, 38]. Other definitions can be found in the literature related to the distance needed to reach a fraction of the Mach number [123].

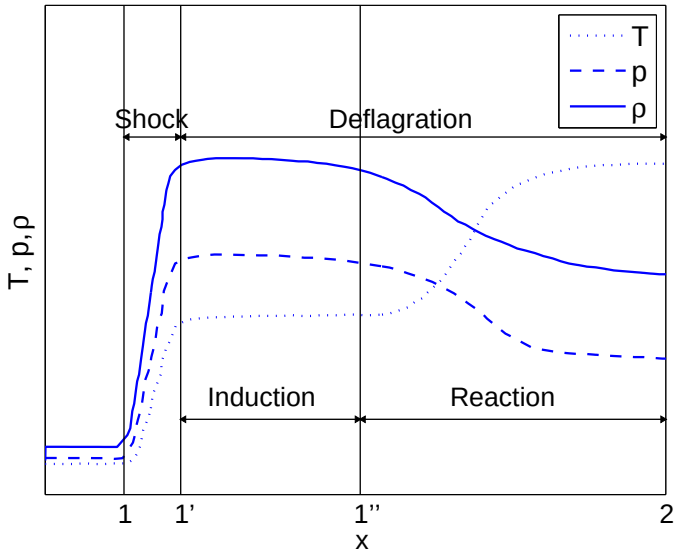

Figure 2.3: ZND wave structure: variation of physical properties through a detonation wave [81].

2.2.2 Multi-dimensional cellular detonation

In the early Sixties, deeper investigations on gas detonation have been performed to better understand the unstable behavior of detonation waves observed experimentally. Experimental results proved that detonations waves, in contrast to the classical theory of steady, one-dimensional, planar waves, present a strong three-dimensional structure. Transverse waves lead to the formation of a cellular pattern generated by triple-points trajectories. A triple-point is formed when an planar shock wave reflects on a surface with an angle of incidence. In this case two other waves are formed: the reflected ones and the so-called Mach stem, a shock wave perpendicular to the surface that moves parallel to the surface. The point in which these three waves intersect coincides with the triple-point. Transverse waves can be created following a perturbation of the flame front, that is, as already mentioned, intrinsically unstable [122, 145].

The collision of two transverse waves generates a strong shock wave whose intensity diminishes in time. While passing through a single cell this shock wave behaves like a decaying blast wave: as the strength of the wave diminishes, the temperature behind the leading shock also decreases thus increasing the distance between the shock and reaction front until the collision of two transverse waves happens again forming the following detonation cell. The resulting leading shock is then characterized by a periodically discontinuous profile as described in [63]. Strehlow and Crooker [127] used smoked foils to record the detonation structure of stoichiometric hydrogen/oxygen mixtures diluted with argon. The cellular structure is clearly visible in these pictures; a multiheaded detonation front propagating along the tube can also be distinctly recognized.
An important parameter to take into account while dealing with detonation processes is the width of the detonation cell, λ. The cell size is a fundamental property of a mixture and it gives an idea of the mixture sensitivity to detonation initiation. Plotting λ as a function of the equivalence ratio, a classical U-shaped curve is obtained with a minimum value at the stoichiometry [64, 136, 40, 17]. According to the experimental data of [63] for hydrogen/air mixture at NPT initial conditions, the cell size increases from $\lambda = 1.5$ cm at the stoichiometric composition to $\lambda = 1.03$ m for $\phi = 0.37$ (lean mixture) and $\lambda = 1.35$ m $\phi = 5.55$ (reach mixture). It has also been shown experimentally that λ decreases in increasing the initial pressure [79].
As suggested by Shelkin and Troshin [122], the cell size can be calculated from the induction distance, since they are directly proportional. Westbrook and Urtiew [148] and Shepherd [123] have independently developed detailed kinetic models to compute induction lengths for hydrogen/air mixtures. In both models 1D gasdynamic equations and chemical reaction kinetics are integrated from the von Neuman state. The proportionality constant between the computed induction length and the experimental value of λ at the stoichiometry was found to be equal to 22 in Shepherd's model and 20 in Westbrook's one. As pointed out in [63], Westbrook's model tends to overestimate λ for lean mixture by a factor of 30, while Shepherd's results overestimate or underestimate the experimental data by no more then a factor of 2. More recently Gavrikov and colleagues [57] have proposed a simple model to determine the cell width from characteristic reaction zone width, taking into account the multidimensional structure of real detonation. The mean deviation of calculated values from the experimental data is about 50%.
In [27] an analytical function has been proposed to fit experimental data. The following expression allows to compute the detonation cell width (λ [cm]) as a function of the dry hydrogen concentration (A [% vol]), the initial temperature (B [K]), the steam concentration (C [% vol]) and the initial pressure (D [MPa]):

$$\log_{10}(\lambda) = \left(a - m + \left(\frac{b}{\left(A - \frac{k}{B}\right)^f} + h(A - gB)^2 + i(A - gB) \right) (1 + dC + eBC^2) \frac{j}{B} \right) \cdot \cdot (D - c) \left(\frac{1}{0.1 - c} + n(D - 0.1) \right) + m \quad (2.51)$$

Lowercase letters in equation (2.51) refer to the constant values listed in the following

table:

$a = -1.1333$	$b = 4.59807 \cdot 10^{1}$	$c = -1.5765 \cdot 10^{-1}$	$d = 4.65429 \cdot 10^{-2}$
$e = 3.59620 \cdot 10^{-7}$	$f = 9.97468 \cdot 10^{-1}$	$g = -2.66646 \cdot 10^{-2}$	$h = 8.74995 \cdot 10^{-4}$
$i = -4.07641 \cdot 10^{-2}$	$j = 3.31162 \cdot 10^{2}$	$k = -4.18215 \cdot 10^{2}$	$m = 2.38970$
$n = -8.42378$			

The standard deviation associated to equation (2.51) is $1.72128 \cdot 10^{-1}$. Figure 2.4 shows the cell size obtained with equation (2.51) for dry hydrogen/air mixtures.

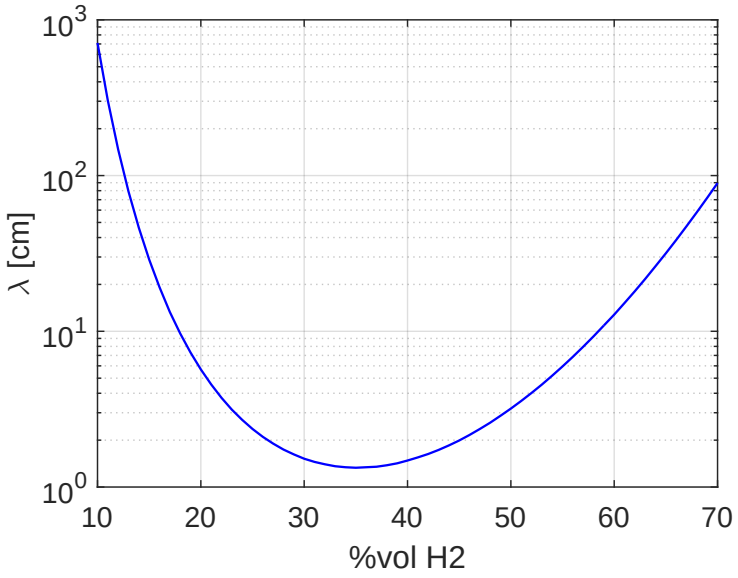

Figure 2.4: Detonation cell size vs hydrogen content for dry hydrogen/air mixtures at 300 K and 0.1 MPa initial temperature and pressure. Results are obtained from equation (2.51).

2.2.3 Onset of detonation

Direct initiation and DDT

For reactive mixtures inside the detonability region, detonation can be achieved (1) thanks to powerful ignition sources such as solid explosives or (2) following flame acceleration to sufficiently high speed capable of triggering the transition to detonation. The first case is called direct initiation or blast initiation since the onset of the detonation is the blast wave generated by the igniter. The critical energy needed to generate a multi-headed detonation at CJ velocity strongly depends on the igniter characteristics, such as its nature and geometry. In the case of an unconfined spherical detonation transmitted by a confined planar detonation, the critical energy was found to be proportional to λ^3 (surface energy model of Lee and colleagues [63]).
On the other hand, for the deflagration-to-detonation transition (DDT), the ignition source does not influence the transition process. As it will be explained later in Chapter 3 this kind of mechanism is more likely to happen in confined geometries with rough

walls since turbulence and flame shock interaction play a key role in the acceleration process [106]. From this perspective σ-criterion for flame acceleration, that will be described in Chapter 3, can be used as a necessary condition for DDT [27].

SWACER mechanism

In 1970s, it has been suggested that a single underlying mechanism is responsible for the onset of detonation. The first approach was made by Zel'dovich [151] with the induction time gradient mechanism. If a coherence between the chemical energy release from the flame and the gasdynamic process occurs, the compression wave is gradually amplified into a strong shock wave that can auto-ignite the mixture leading to DDT [38]. Since this mechanism foresees the synchronization of the chemical energy release with the shock wave as it propagates through the mixture, it has subsequently been called SWACER (Shock Wave Amplification by Coherent Energy Release) in analogy to the LASER technique (Light Amplification by Stimulated Emission of Radiation) [91].
The SWACER mechanism may be responsible for a wide range of detonation initiation observations including [27]:

1. direct detonation initiation due to the temperature gradient behind the leading shock;

2. detonation initiation due to shock focusing;

3. DDT in tube caused by temperature gradient in the boundary layer or between a fast flame and the leading shock;

4. DDT due to pre-compression at the end of a channel by a slow flame;

5. DDT in rough or obstacle-filled tubes; jet initiation caused by temperature and concentration gradients in the flame/vortex structure;

6. DDT in multi-phase system resulting from the temperature relaxation caused by particles.

2.2.4 Detonability limits

As defined in [63], detonability limits of a reactive mixture are the critical conditions for the propagation of self-sustained detonation. Both mixture properties and boundary conditions are evoked in the above definition.
For this reason different criteria can be found in literature depending on the degree of confinement of the experimental facilities. As a matter of fact, in small tubes heat and momentum losses through the walls play an important role in governing flame propagation mechanisms, thus strongly influencing the detonation limits. On the other hand, for larger scales, heat and momentum losses can be neglected.
A clear example on how the degree of confinement can influence detonation limits for homogeneous hydrogen/air clouds (pressure, temperature and concentration are homogeneous in the cloud) is presented in Figure 2.5. Here the minimum cloud dimension for self-sustained detonation propagation is shown as a function of the mixture composition

for powerful ignition sources (direct initiation) [64]. Three curves can be distinguished in the graph:

curve 1 refers to fully confined detonations in tubes. The line corresponds to the limit $\lambda = 1.7d$ defined by Moen and colleagues [107] for the onset of single-head spin detonation.

curve 2 represents the limit for geometries with one degree of confinement ($h_{cloud} = h_c/2 = 5\lambda$[1] as defined by Mitrofanov and Soloukhin [63] for two-dimensional channels).

curve 3 refers to fully unconfined detonations (see equation (2.53): $D_{cloud} = d_c/2 = 6.5\lambda$).

Note that in the notation above used, to which we will refer hereinafter, uppercase D denotes the hydraulic diameter of tubes or clouds, while lowercase d refers to the unobstructed diameter of the channel. For 2D geometries the characteristic length is indicated with h.
According to Figure 2.5, the minimum cloud dimension at the stoichiometry varies from 7.5 mm to 10 cm, depending on the degree of confinement. For fully unconfined detonation the minimum cloud thickness for 13% hydrogen is expected to be 8 m. This means that detonation of very lean (or highly rich) mixtures can be successfully achieved only in large scale experiments.
Considering circular tubes with smooth walls, several criteria have been proposed in the form $\lambda/D \leq 1$. The most common one is the $\lambda = \pi D$ criterion, proposed by Kogaro and Zeldovich. The physical explanation of this criterion have been given by Lee [63], who compared the characteristic chemical time (λ/c) to the acoustic vibration time in the detonation cell ($\pi D/c$). The validity of the criterion has been proved experimentally for strong source initiation. For weak initiation sources a more reactive mixture is needed to trigger the detonation transition: in smooth tubes a mixture is expected to detonate if $\lambda \simeq D$.
These formulations are particularly useful to estimate the minimum tube diameter, D^*, for which a defined mixture is susceptible to detonate:

$$D^* \simeq \begin{cases} \lambda/\pi & \text{for direct initiation} \\ \lambda & \text{for DDT} \end{cases} \tag{2.52}$$

While dealing with weak initiation sources, criteria are usually expressed in the form $D/\lambda \geq \alpha$, where the value of α depends on the particular geometrical configuration [27]. A type of geometry widely studied in literature consists of a long obstacle-laden tube whose open end is connected with a large chamber. This configuration is used to observe the transmission of confined detonations into unconfined environments. Experimental campaigns [64] have corroborated the validity of the criterion suggested by Mitrofanov

[1]The experimental facility of [64] consists in a circular tube connected to a larger volume. The detonation is induced through an explosive charge at the extremity of the tube; here the detonation front propagates as a planar wave until it reaches the chamber, where it becomes spherical. As suggested by Lee, in this configuration the critical cloud dimension can estimated from the channel size by imposing the conservation of energy at the surface, i.e. $D_{cloud} = d_c/2$.

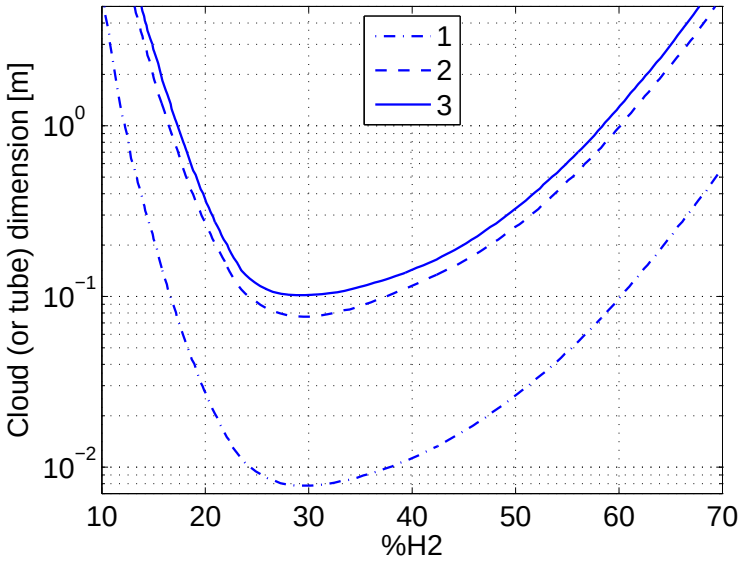

Figure 2.5: Minimum cloud dimensions for self-sustained detonation propagation for hydrogen/air mixtures [64]: (1) fully confined detonation; (2) one degree of confinement; (3) zero degree of confinement.

and Soloukhin (1965) for the minimum tube diameter required for the transition from planar detonation to spherical detonation:

$$d_c \simeq 13\lambda \tag{2.53}$$

A theoretical demonstration of this empirical correlation has been performed by Lee by comparing the characteristic time for gas expansion in the unconfined volume, t_q, to the time required for the detonation wave to propagate at a distance equal to 2Δ, t_p. The length 2Δ corresponds to the minimum distance from the detonation kernel so that detonation propagation is not affected by gasdynamic perturbations (note that Δ is defined as the distance from the shock wave to equilibrium condition at C-J velocity) . If $t_p \geq t_q$, the detonation is self-sustained. The critical condition $t_p \simeq t_q$ gives:

$$\frac{2\Delta}{U_{CJ}} \simeq \frac{d_c}{2c_b}\,. \tag{2.54}$$

If we assume that $2c_b \simeq U_{CJ}$, we get $d_c \simeq 2\Delta$. Taking the average value of Δ from the measurements performed by Vasiliev et al. (1971) ($\Delta = 3 \div 10\lambda$ so $\Delta_{\text{avg}} = 6.5\lambda$), we obtain $d_c \simeq 13\lambda$, thus confirming equation (2.53).
For obstructed tubes or channels, detonability limits are usually computed on the basis of the two following criteria [27]:

$$d \geq \lambda \tag{2.55}$$

$$L \geq 7\lambda \tag{2.56}$$

where d is the unobstructed height of the tube (for circular tubes with annular obstacles it coincides with the obstacle's internal diameter) while L is a characteristic geometrical

size define as:

$$L = \frac{S+D}{2}\frac{1}{1-\frac{d}{D}} = \frac{S+D}{2}\frac{1}{1-\sqrt{1-\mathrm{BR}}} \tag{2.57}$$

where S is the inter-space between two obstacles and BR is the ostacle blockage ratio defined as:

$$\mathrm{BR} = \frac{\pi D^2 - \pi d^2}{\pi D^2} = 1 - \left(\frac{d}{D}\right)^2 . \tag{2.58}$$

Definition (2.57) has a singularity for $d/D \to 1$; thus for small blockage ratio (BR $= 1-(d/D)^2 < 0.1$), L is usually taken as the average value of S and D.
The criteria defined by equations (2.55) and (2.56) can be used in a complementary way since the first one refers to a critical unobstructed diameter (largely used for long tube with obstacles) while the second one to a minimum macroscopic size for which the detonation of a sensitized mixture can originate and develop (self-sustained propagation).
An example of the application of L/λ-correlation for the determination of flame acceleration (σ-criterion) and DDT limits for hydrogen/air/steam mixtures is given in [27]. Here, the more conservative DDT limits have been estimated imposing $\lambda = 2$ m, that corresponds to the largest value of cell size for which a detonation has been reported in HDT facility test at Sandia National Laboratories. According to [27] DDT is possible in rooms with $L \simeq 10$ m (DDT limits are not only given in terms of mixture composition but they are also scale-dependent).
Eventually, another important thing to underline is that all the empirical criteria above described are necessary and not sufficient conditions for detonation or DDT.

2.3 Conclusions

In this chapter an overview on the main phenomena characterizing flame propagation was made. Key parameters for deflagration and detonation were identified.
The main properties governing laminar deflagration are the laminar burning velocity S_L^0 and the laminar flame thickness δ_L. They can be determined by solving mass, momentum and energy conservation equations for a mono-dimensional, adiabatic, freely propagating flame. Analytical models for one-step reactions are available in the literature (equations(2.7) and (2.10)). Nowadays, numerical simulations allow the implementation of multiradical models: detailed kinetics mechanisms can be implemented in computer codes to determine thermodynamic, transport and kinetic parameters associated with laminar combustion.
The laminar flame thickness can be dermined according to the definitions given in Table 2.1.
Premixed laminar flames could incur several instabilities that distort the flame front surface, affecting propagation dynamics. Experimentally, it was foud that thermo-diffusive instabilities play an important role in flame dynamics for lean hydrogen air mixtures (cf. criterion (2.27)). Turbulence acts on the flame front wrinkling it; this effect leads to an increase of the surface area of the flame and as a consequence of its propagation velocity. Different experimental correlations for the turbulent burning velocity can be found in the literature (cf. Table 2.2).
If the mixture is sufficiently reactive, detonation may occur. In 1970s the SWACER mechanism, which could explain the onset of detonation in a wide range of experiments,

has been suggested: if a synchronization between the chemical energy release and the shock wave propagation occur, the compression strength is amplified until reaching the auto-ignition of the mixture, leading to DDT. The detonability limits for a reactive mixture were proved to be strongly dependent on the degree of confinement, i.e. on the ratio between the characteristic geometrical size of a tube or chamber and the detonation cell width λ (ref. criteria (2.55) and (2.56) for obstructed ducts). The latter depends only on the mixture properties and is a key parameter to determine its sensitivity to detonation. Flame acceleration mechanisms and, in particular, the criteria for strong acceleration are discussed the next chapter.

Chapter 3

Flame acceleration in obstructed tubes

For premixed flammable mixture in obstructed tubes with closed ends, different phases can be distinguished in the propagation process of fast flames. Each phase is characterized by a peculiar phenomenology: some of them are only dependent on thermo-dynamics, while others are strongly affected by boundary conditions, gas-dynamics and kinetics of combustion.
At first, close to the low-energy ignition source, a laminar flame starts developing and propagation is governed by molecular transport of gaseous species and heat, with negligible compressible effects. This flame can undergoes Darrieus-Landau and thermal-diffusive instabilities, leading to the development of a cellular structure and the subsequent increase of the flame surface. As a consequence, flame accelerates and the confinement created by the tube forces burnt gases to stretch in the direction of propagation. The interaction with the boundary layer and the obstacles leads to the formation of eddies in the fresh gases ahead of the flame and the increase of turbulence on the flame front.
As the flame accelerates, a leading shock wave is formed ahead of the flame. During this phase, the acceleration process is sustained by two mechanisms [69]: the increased temperature following gas compression and the increased density of the reacting fuel entering in the flame front. Therefore both the reactivity and the amount of fresh gas participating to the reaction increase. According to the double discontinuity theory, the dynamics of the shock wave and its interaction with the reaction wave strongly influence FA and DDT processes.
In this chapter an overview of these phenomena, based on the available literature, is presented.

3.1 Propagation regimes

Flame propagation in obstacle-laden tubes can evolve according to four different regimes, as described by Lee at al. [90]. For obstructed tubes with annular obstacles, an abrupt transition is observed from one regime to another with a sudden change in the propagation mechanism [33]. In spite of the more recent findings on the subject (see for example [37, 48, 82, 27, 33, 39, 75]), the definitions given in [90] remain an important reference from a qualitative point of view.
Regimes are classified according to the magnitude of the flame velocity, measured at the end of the tube. Experiments were performed in steel tubes of different diameters

and ranging from 11 m to 17 m in length. Annular obstacles with blockage ratios BR= $0.28 - 0.44$ spaced one diameter apart were used. Tested fuels include H_2, CH_4, C_2H_2, C_2H_4 and C_3H_8 with air as oxidant.

Quenching regime

In the quenching regime, the flame accelerates at first and then extinguish itself after propagation past a certain number of orifice plates. This kind of propagation can be considered as the successive ignition of a sequence of combustion chambers separated by the orifice plates. Quenching occurs when the hot jet of product gases fails to cause ignition. Two main causes were found to be at the origin of the quenching phenomenon by Thibault et al. [134]:

1. if the Δp is negligible, i.e. for laminar flames, quenching is controlled by the competition between the rate of heat release due to combustion and the heat losses at the wall ("Peclet" domain). The critical diameter corresponds to the quenching distance for laminar flames.

2. for higher values of Δp, quenching is caused by the cooling due to the rapid entrainment of cold unburnt gas mixture in the reaction zone. Therefore q critical diameter for flame quenching can be determined by the comparison between the characteristic chemical time and the turbulent mixing time.

From similar considerations on flame extinction due to mixture cooling by pockets of unburnt gas in the reaction zone, a criterion for quenching, defined by equation (2.39), was obtained by Dorofeev [45].

Choking regime

When the conditions for quenching are not met, the flame keeps accelerating until reaching a final steady-state value. In this case, flame propagation is controlled by the combined effect of wall friction and heat addition which drive the flow to sonic conditions.
Experimental results in [90] and [33] showed that the flame velocity reached in "choked" conditions is independent from tube diameter, blockage ratio and the initial accelerating phase and can be directly determined from the thermodynamic properties of the mixture. From the modeling of the accelerating flame as a double discontinuity (reaction wave and shock wave are no longer coincident as in the CJ theory) Chue [37] derived an analytical expression for the CJ deflagration velocity (see equation (1.24)). According to [37], this velocity corresponds to the propagation velocity of a choked flame. In consistency with Lee's findings, equation (1.24) is only dependent on the thermodynamic properties of the mixture.
The choking regime is typical of tubes with annular obstacles that define a pattern of consecutive combustion chambers. In fact, this regime is not observed with different obstacles configuration. For example, in the experiments performed by Chao et al. [33] inside a square tube with an obstacle array of staggered vertical rods, a smooth transition from slow turbulent flames to quasi-detonation velocities was observed.

Quasi-detonation

For the transition from "choking regime" to detonation, the denotation cell size λ represents an important characteristic length scale. As mentioned in Chapter 2.2, the lower limit for the detonation to occur in smooth tubes is $D/\lambda \geq 1$; for tubes with large blockage ratios, instead, the limit is found to be $D/\lambda \geq 13$. As a consequence, transition to detonation in obstacles-laden tubes can occur if the diameter is inside these limits.
In this regime, however, the detonation velocity can be significantly below U_{CJ} due to the severe momentum losses caused by the obstacles. In fact, even when transition to detonation occurs, detonation velocities in the range 20%-50% U_{CJ} have been observed. This regime has been defined as "quasi-detonation". According to [75], a quasi-detonation may occur if the collision of transverse shock waves, produced by a detonation initiation at the obstacle face, results in a local explosion in the tube centerline. An intermittent detonation propagation is therefore observed. Otherwise, if ignition of the gas at the obstacle face does not occur, a chocked flame regime is observed. The limit between these two propagation regimes was found to be $d/\lambda = 2$.

Detonation

As mentioned in Chapter 2.2, steady-state detonations in the CJ regime were observed for tube diameters higher than 13λ. More details about the detonability limits are given in Chapter 2.2.

3.2 Criteria for FA

One of the first explanations for flame acceleration was proposed by Shchelkin [121, 122]. Shchelkin's theory was based on the assumption that flame acceleration is governed by strong turbulent flow in the unburnt gas ahead of the flame, characterized by a turbulent Reynolds number:

$$\mathrm{Re}_f = \frac{UD}{\nu} > 2300 \tag{3.1}$$

where U is the flow velocity ahead of the flame. Equation (3.1) is a necessary (but not sufficient) condition for flame acceleration.
The above criterion, however, did not explain FA and DDT in smooth tubes with no-slip condition at the wall. The explanation of this phenomenon was found in the appearance of turbulence in the upstream flow due to the thermal expansion of the burnt gas. This criterion can be expressed in the form of a comparison between the time necessary for a perturbation of the flame surface to cover a volume of burnt gas and the time of combustion:

$$\frac{R}{c_{sb}} \geq \frac{\delta}{S_L} \tag{3.2}$$

where R is the tube radius. Equation (3.2) was found to be consistent with experiments for $\mathrm{Re} = RS_L/\nu > 10^4$. If the condition expressed by equation (3.2) is verified, any perturbations arising in the combustion zone are not smoothed out over the flame surface before any fundamental changes in the flame zone occur.

In the early 2000s, Dorofeev and colleagues [48, 82, 47] proposed a criterion for FA based on the analysis of a wide database of experiments performed in obstructed tubes and ducts with different hydraulic diameters and blockage ratios.
It was found that, for large turbulent scales, the acceleration process is not influenced by the boundary conditions, but depends mainly on the expansion ratio σ. This result is in accordance with the pioneer work of Shchelkin, who defined a criterion for DDT based on the piston effect induced by the density difference across the reactive wave:

$$0.6 < C_P C_K(\sigma - 1) < 2 \tag{3.3}$$

where $C_P = 2 - 3$ is a coefficient that takes into account the shape of gas flow profile in the tube and C_K is the von Karman constant ($C_K = 0.05$ for smooth tubes, $C_K = 0.1$ for rough tubes).
The FA criterion developed at the Kurchatov Institute can be expressed in the following form:

$$\sigma \geq \sigma^* \tag{3.4}$$

where σ^* is defined as the lower limit for FA. Therefore, if $\sigma < \sigma^*$, the flame is not expected to accelerate. Criterion (3.4) identifies a necessary but not sufficient condition for flame acceleration.
The value of σ^* was determined from the analysis of the experimental results. The distinction between accelerating flames (fast regimes) and slow or quenched ones was based on the following definitions:

$$\begin{array}{ll} \frac{U_F}{c_{sb}} \geq 0.5 & \text{Fast regimes} \\ \frac{U_F}{c_{sb}} < 0.5 & \text{Slow regimes.} \end{array} \tag{3.5}$$

Kuznetsov et al. [82] found that:

1. for $\frac{L_T}{\delta_L} > 100$, large turbulent scales, the potential for FA depends only on the mixture composition:
$$\sigma^* = 3.75 \pm 0.25 \tag{3.6}$$
2. while for $\frac{L_T}{\delta_L} < 100$, a much higher piston effect is required for effective flame acceleration.

In fact, by referring to the Borghi's diagram of Figure 2.2, a small value of the ratio L_T/δ_L corresponds to more unstable flames: if the ratio U'/S_L is only slightly increased, the transition from a combustion regime to another may occur. Note that, the ratio L_T/δ_L may also be seen as a Peclet number (balance between advection and diffusion phenomena).
Here, the integral length scale of turbulence is defined as a function of the obstacles blockage ratio [82]:

$$L_T = \begin{cases} h = \frac{D}{2}\left(1 - (1 - \mathrm{BR})^{1/2}\right) & \text{for BR} \leq 0.1 \\ D & \text{for } 0.3 \leq \mathrm{BR} \leq 0.6 \\ d = D\,(1 - \mathrm{BR})^{1/2} & \text{for BR} \geq 0.9 \end{cases} \tag{3.7}$$

where h is the obstacle height ($(D - d)/2$).

In the concluding remarks, Dorofeev et al. [48] suggested that other parameters, such as the Zeldovich number and the Lewis number may play an important role in defining the limits for effective FA. As a matter of fact, further studies [27, 47] showed that for hydrogen/air mixtures with negative Markstein number ($\beta(\mathrm{Le}-1) < -2$), σ^* depends on the dimensionless activation energy $\Theta = E_a/RT_u$ as:

$$\sigma^* = 0.9 \cdot 10^{-5}\Theta^3 - 0.0019\Theta^2 + 0.1807\Theta + 0.2314\,. \tag{3.8}$$

A similar formulation for σ^* was also derived by Malet [96]:

$$\sigma^* = 0.075\beta(\mathrm{Le}-1) + 4.38\,. \tag{3.9}$$

From its earlier definition, the σ criterion was found to be an effective tool to identify different combustion scenarios. For example, some applications to reactor containment analysis are presented in Chapter 6 of [27].
It is worth noticing that the criterion for quenching (already mentioned in a previous section) obtained by Dorofeev [45] and expressed by equation (2.41) also identifies a lower limit for flame acceleration: for high turbulent flow (Ka>1), if the second term of equation (2.41) is greater than one, a strong acceleration is expected. Importantly, only fundamental combustion parameters appears in equation (2.41).
A theoretical criterion for FA up to DDT was also proposed by Bradley et al. [25]. Their approach is based on the definition of a minimum turbulent velocity for which a leading shock wave is formed ahead of the flame. Pressure and therefore temperature are increased right ahead of the flame front promoting the the acceleration process. The turbulent velocity is expressed as a function of the Karlovitz turbulent stretch factor, K, and the effective rms turbulent velocity acting on the flame front, U'_K:

$$\left(\frac{S_T}{S_L}\right)_{\mathrm{th}} = u_{\mathrm{th}}\frac{U'_K}{U'}\left(\frac{K}{0.25}\left(\frac{S_L L_T}{\nu}\right)^{1/2}\right)^{2/3} \tag{3.10}$$

where u_{th} is the theoretical ratio between the turbulent burning velocity and the effective rms velocity acting on the flame front.
Formulation (3.10) was corrected on the basis of experimental results. The minimum turbulent velocity for which a leading shock wave is formed ahead of the flame is therefore defined by:

$$\left(\frac{S_T}{S_L}\right)_{\mathrm{th}} b\left(\frac{K}{K_{ql}}\right)^{1/4} = \left(\frac{S_T}{S_L}\right)_{\mathrm{exp}} \tag{3.11}$$

where $b = 0.8 - 3$ and K_{ql} is the Karloviz stretch factor for flame localized quenching. Therefore, as obtained by Dorofeev [45], high values of K are associated with strong flame acceleration ($K \propto \mathrm{Ka}$, ref. equation (2.37)).
In this case, turbulent parameters and geometry play an important role in defining the limits for flame acceleration. As a matter of fact, in equation (3.11), the effects of duct size and obstacle blockage ratio are included in L_T (see equation (3.7)).

3.3 Analytical models for flame propagation

Up to the early 2000s, the interest was mainly focused on the asymptotic flame speed. The need for more accurate data for the validation of numerical models has pushed towards

more instrumentation. In this view, middle scale experiments were instrumented to follow flame propagation all along the tube. The use of visualization modules coupled with high speed camera allowed also to have access to more detailed information on the flame surface. From an analytical point of view, models have been developed to characterize flame propagation from the early beginning to the steady-state condition.
One of the first analytical approach to describe flame propagation in tubes was developed by Clanet and Searby [41]. Their study was mainly focused on the early stages of flame acceleration in smooth tubes, that is characterized by a finger shaped flame that propagates with an exponential growth in a non-compressible fluid. As the flame touches the tube inner wall the flame front tends to flatten until it becomes concave with a characteristic tulip shape.
The term "tulip flame" appeared for the first time in literature in 1959, in the paper of Salamandra and colleagues [119] to designate those flames propagating along half-open tubes whose shape changes while approaching the tube walls. Nevertheless, the phenomenon of the inversion of the flame front curvature in the early stages of burning has been observed since the end of 18th Century by Mallard and Le Chatelier.
An accurate bibliographical review on this phenomenon is presented in [41]. Several hypotheses have been proposed to explain this inversion in the direction of progression of the flame, evoking the importance of the interaction between the propagating flame and the boundary layer at wall [118], the flame quenching at the walls [50] as well as the appearance of Taylor instabilities [62].
In [41] Clanet and Searby have derived a simple geometrical model to describe this phenomenon on the basis of the experimental results. By making the assumption that viscous and acoustic effects do not influence the initial stages of tulip flame formation, the trajectory of the flame tip can then be predicted by imposing the equivalence between the variation in time of the burnt gas volume and the fresh gas burning rate as:

$$R\frac{dx_f}{dt} = 2S_L\sigma x_f \tag{3.12}$$

The solution of equation (3.12) in time is:

$$\frac{x_f}{R} = \exp\left(\frac{t-t'}{\theta}\right), \quad \theta = \frac{R}{2\sigma S_L}. \tag{3.13}$$

where t' is the transition time from the hemispherical shape to the finger shape.
From equation (3.13), we find that the propagation of the flame tip is described by an exponential time-law with a characteristic time of growth, θ, that is a function of the expansion ratio, the laminar burning velocity and the tube radius. In dimensionless terms, the growth rate can be rewritten as $\vartheta_{CS} = 2\sigma$.
The theory of Clanet and Searby was recently revisited by Bychkov and colleagues [29]. In contrast with Shchelkin's belief that only turbulent flames were expected to accelerate up to detonation, Bychkov and colleagues [31] developed an analytical model for laminar flame acceleration on the basis of previous works on micro-propulsion. According to them, laminar flames with large density drop propagating in a closed-end tube with no-slip condition at the walls are supposed to accelerate. In this case turbulence plays only a supplementary role during the acceleration process (it is no more a prerequisite to flame acceleration). The model foresees a planar infinitely thin flame front moving parallel to

flow in a 2 dimensions geometry. D-L instabilities are not taken into account since, as mentioned in Chapter 2.1.2, their contribution is significant only in the early stage of flame acceleration. The model of [31] was adapted to cylindrical tubes by Akkerman and colleagues [5].
Analytical and numerical models of flame acceleration in smooth tubes with no-slip condition at the wall were also developed by Liberman et al. [95]. Here, flame propagation was characterized from the early beginning (exponential acceleration due to flame stretching at the boundary) to the formation of a strong shock wave in the upstream flow, that leads to DDT.
The acceleration of a premixed flame in a tube with repeated obstacles was theoretically described by [32] under the hypothesis of incompressible flow in the unburnt and burnt mixture. One of the main assumptions of this model was that flame acceleration is driven by a powerful jet-flow created by the delayed burning between the obstacles. This mechanism was found to be stronger than the classical Shchelkin scenario of flame acceleration due to no-slip condition at the walls. By considering a square channel (2D geometry) with tightly placed thin obstacles the following equation for the flame tip propagation was obtained:

$$x_f = R\sqrt{1-\mathrm{BR}}\frac{\sigma}{\sigma-1}\left(\exp\left(\frac{\vartheta_{2D}S_L}{R}t\right)-1\right) \tag{3.14}$$

$$U_f = \frac{\vartheta_{2D}S_L}{R}x_f + \sigma S_L \tag{3.15}$$

where x_f is the flame tip position and U_f its velocity. Note that, for $t \to 0$, $U_f \to \sigma S_L$. The dimensionless acceleration rate was found to be a function of the blockage ratio: $\vartheta_{2D} = (\sigma-1)/\sqrt{1-\mathrm{BR}}$. Equation (3.14) was found to be in good agreement with experimental results of Johansen and Ciccarelli [71]. This model is valid only in the initial phase of acceleration since the flame is assumed to be laminar and mono-dimensional both in the tube and between the obstacles.
By developing flame propagation equation in 2D axisymmetric geometry, an increased acceleration rate was obtained [141]:

$$\vartheta_{2D\mathrm{axi}} = 2\frac{\sigma-1}{\sqrt{1-\mathrm{BR}}}\left(1+\frac{1}{2(\sigma-1)}\right) = 2\left(1+\frac{1}{2(\sigma-1)}\right)\vartheta_{2D} \tag{3.16}$$

The models described above are valid only in first stages of flame acceleration where the fluid can be considered as incompressible. As the flame velocity increases this hypothesis is no longer valid. The extension of the model in the limit of small compression ($M \ll 1$) was developed by Valiev et al. [140]. A first order expansion in M was used to include gas compression effects:

$$\frac{dU_f}{dt} = \frac{S_L}{R}\vartheta U_f\left(1-\alpha M\frac{U_f}{S_L}\right) \tag{3.17}$$

$$\frac{U_f}{S_L} = \frac{\sigma\exp\left(\frac{\vartheta S_L}{R}t\right)}{1+\alpha M\exp\left(\frac{\vartheta S_L}{R}t\right)} \tag{3.18}$$

As a result, gas compression tends to slow down the acceleration process. Nevertheless, equation (3.18) provides only a qualitative representation of the flame acceleration process:

at the beginning the flame accelerates exponentially (M=0); then a constant acceleration phase takes place; finally the velocity reaches a saturation value equal to $U_{\mathrm{CJ,def}}$. The coefficient α is thus $c_s/U_{\mathrm{CJ,def}}$.
The role of compressibility in the process of flame acceleration in 2D obstructed channels was also investigated in [30]. The model for the planar case described in [32] was adapted to take into account compressible effects. By considering the flow ahead of the flame as isentropic, and solving the Euler equation for $M \ll 1$, the following equation is obtained:

$$\frac{dx_f}{dt} = -M\frac{\psi\vartheta_{2D}^2 S_L}{R^2}x_f^2 + \frac{\vartheta_1 S_L}{R}x_f + \sigma_1 S_L \tag{3.19}$$

where $\psi = (\gamma-1) + 1/(\sqrt{1-\mathrm{BR}})$, $\sigma_1 = \sigma - M(\gamma-1)(\sigma-1)^2$, $\vartheta_1 = \vartheta_{2D}(1-\zeta M)$ and $\zeta = 2(\gamma-1)(\sigma-1) + \sigma/\sqrt{1-\mathrm{BR}}$. In the limit $M = 0$, equation (3.19) reduces to equation (3.14). Also in this case gas compression has a moderating effect on flame acceleration (the non-linear term of equation (3.19)is negative). The analytical formulation is in good agreement with numerical simulations for low value of the ratio x_f/R. On the other hand, as the velocity of the flame tip increases, equation (3.19) tends to overestimate the moderating effect.
For the sake of completeness, in Table 3.1 the analytical expression for the acceleration rate ϑ for the different models are listed.

Table 3.1: Analytical expression for the non-dimensional acceleratiom rate ϑ

Model	**Acceleration rate**
Clanet and Searby, 1996	$\vartheta_{CS} = 2\sigma$
Bychkov et al., 2008	$\vartheta_{2D} = (\sigma-1)/\sqrt{1-\mathrm{BR}}$
Valiev et al., 2010	$\vartheta_{2D\mathrm{axi}} = 2\left(1+\frac{1}{2(\sigma-1)}\right)\vartheta_{2D}$
Bychkov et al., 2010	$\vartheta_1 = \vartheta_{2D}(1-\left(2(\gamma-1)(\sigma-1)+\frac{\sigma}{\sqrt{1-\mathrm{BR}}}\right)M)$

An additional parameter used in the literature to describe flame acceleration mechanisms is the so-called "run-up distance" [144, 46, 126]. This quantity identifies the path needed for the flame to reach a given velocity. This velocity is, however, not univocally defined in the literature: for example for Veser et al. [144] the discriminating velocity is the speed of sound in the burnt gas, while for Silvestrini et al. [126] it corresponds to $0.5U_{\mathrm{CJ}} \simeq U_{\mathrm{CJ,def}}$. In [144], Veser et al. provided a semi-empirical formulation for the determination of the run-up distance X_S based on the geometrical description of flame stretching due to the obstacles:

$$U_f = S_T(\sigma-1)\frac{x}{R}\left(\frac{1-\mathrm{BR}}{1+b\mathrm{BR}}\right). \tag{3.20}$$

By making the assumption that $S_T \simeq 10S_L$ and by imposing $U_f = c_{sb}$, we get:

$$\frac{X_s}{R} = \frac{a}{10}\left(\frac{1-\mathrm{BR}}{1+b\mathrm{BR}}\right)\frac{c_{sb}}{S_L(\sigma-1)}, \tag{3.21}$$

where a and b are empirical coefficient. For $0.3 < \mathrm{BR} < 0.75$, it was found $a = 2$ and $b = 1.5$ (with an uncertainty of $\pm 25\%$). By rewriting equation (3.15) as:

$$\frac{x_f}{R} = \frac{\sqrt{1-\mathrm{BR}}}{(\sigma-1)S_L}\left(\frac{dx_f}{dt} - \sigma S_L\right) \tag{3.22}$$

we can underline a strong similarity between equation (3.20) and the analytical model proposed by Bychkov et al. [32].

3.4 Conclusions

In the present chapter the mechanisms of flame propagations have been discussed. The main purpose was to provide an overview of the experimental correlations and analytical models available in the literature for the description of the different phenomena characterising flame propagation.
A section was devoted to the description of the criteria for flame acceleration, which are currently used in safety studies to identify the most hazardeous scenarios.
Finally, analytical models for the description of the flame velocity evolution in time were illustrated. Here, the main parameter influencing flame propagation is the acceleration rate. A summary of the different expressions for the dimensionless acceleration rate is given in Table 3.1. The comparison with experimental results and numerical simulations showed that these analytical models are able to predict the early stages of flame acceleration, where gas compression is low. As the flame velocity gets closer to the speed of sound, these models provide only a qualitative representation of the phenomenon.

Chapter 4

Mechanical response to combustion generated loads

Depending on flame propagation regimes and structure characteristics, the combustion generated loads on structures may vary from quasi-static to dynamic ones. In case of deflagration, low speed turbulent flames cause a slow pressurization of the combustion chamber. The resulting pressure load is maintained for such a sufficiently long period that they can be considered as quasi-static [135]. For combustion in closed volumes, the maximum pressure corresponds to Adiabatic Isochoric Complete Combustion (AICC), that can be determined from thermodynamic equilibrium conditions. This gives a conservative estimation of the structural load since (1) the combustion chamber is supposed to be adiabatic and (2) the limiting species (respectively, fuel for lean mixtures and oxidizer for rich mixtures) is supposed to be completely consumed during the combustion. This second assumption fails near the flammability limits, since locally the flame may quench. Therefore, pockets of unburnt mixture can then survive to combustion [45]. This is for example the case of very lean hydrogen/air mixture, as shown experimentally in [82], in which the energy released by the exothermic combustion reaction is not likely to compensate thermal losses at the boundary.
Detonations are instead characterized by supersonic waves and they result in a non-uniform dynamic structural loading. For steady-state detonation, locally the mechanical response of the structure can be determined by considering the dynamic load resulting from a mono-dimensional Chapman-Jouguet detonation. For a long tube with closed ends, the maximum pressure is achieved in correspondence to the tube end, where the detonation wave is reflected. As previously, thermodynamic equilibrium codes can be used for CJ state characterization. The reflected pressure can be estimated from equation (4.1), according to [135]:

$$\frac{p_2}{p_1} = \left(\frac{2\gamma}{\gamma+1}\right)\left[\left(\frac{U_2}{C_1}\right)\left(\frac{\gamma+1}{4}\right) + \left(\left[\left(\frac{U_2}{C_1}\right)\left(\frac{\gamma+1}{4}\right)\right]^2 + 1\right)^{1/2}\right]^2 - \left(\frac{\gamma-1}{\gamma+1}\right) \quad (4.1)$$

where the states 1 and 2 refer to incident shock and the reflected one respectively, $U_2 = V_1 - V_2$ is the reflected shock particle velocity and $C_1 = \left(\frac{\gamma RT_1}{\mathrm{MW}}\right)^{1/2}$. In this case U_2 is equal to the CJ velocity and γ, MW and T are evaluated at the CJ condition.
In case of flame acceleration and deflagration-to-detonation transition (DDT) in long

tube with closed ends, the pressure load acting on structures varies strongly in time. In the first phase, the gas ahead of the flame is precompressed by the leading shock wave; then, as the run-up distance for DDT is attained, an over-driven detonation is achieved. As shown by Kuznestov [86], the distance at which the detonation takes place strongly influences the pressure load time history. Cumulative effects of shock waves reflection and detonation occurrence make the problem more and more complex from the point of view of the structural response.
In the present Chapter a brief review on structure response to static and transient pressure loads is presented. A particular attention is paid to the elastic response of internally loaded pipes and plates. For an isotropic, homogenous and elastic material, internal stresses and strain are related via Hooke's law:

$$\boldsymbol{\sigma} \propto \boldsymbol{\epsilon} \tag{4.2}$$

where $\boldsymbol{\sigma}$ is the stress tensor and $\boldsymbol{\epsilon}$ is the strain tensor. Relation (4.2) is valid throughout the material elastic range, that is bounded by the yield stress, σ_{YS}. The yield stress is defined as the value of the stress that corresponds to $\epsilon = 0.2\%$. In this range, displacements do not induce permanent deformations on the structure. If the stress exceeds the value of σ_{YS}, stress and strain are no longer proportional. For stainless steel, strain-rate models are usually considered in the plastic region to correlate the two quantities:

$$\frac{\sigma^{\mathrm{dyn}}}{\sigma^{\mathrm{static}}} = f(\dot{\epsilon})\,. \tag{4.3}$$

Ductile steels tend to absorb energy while deforming. Following this stretching process, important levels of strain may be reached before rupture occurs. Due to the complexity of the problem, finite element methods (FEM) are usually addressed to model plastic response and structure failure. Strain hardening, material inhomogeneities and pre-existing flaws can then be included in model to predict structure deformation in the plastic regime. Influence of crack growth in tubes under gaseous detonation was investigated both experimentally [34] and numerically [105]. Moreover, dynamic deformations in the plastic regime are strongly affected by the load time history.

4.1 Fluid-structure interaction

The propagation of a shock wave in a confined volume is influenced by the rigidity of the vessel walls [28]. When a shock wave travels into a pipe, it may induce changes in its geometry. Depending on wall stiffness, the structure may oscillate around a fixed position or deform. In case of plastic deformation, part of the energy released by the shock wave is absorbed by the structure.
Let us consider for example a shock wave that hits normally the end wall of a duct. If the wall is rigid, the pressure load of the reflected wave can be evaluated according to equation (4.1). On the other hand, if the wall is flexible or even ductile, the reflected shock wave is less energetic then that one predicted by equation (4.1).
In fluid-structure interaction analysis, gaseous explosions in closed semi-rigid volumes are example of weak fluid-solid coupling. Nevertheless this coupling can not be neglected if accurate records of pressure load time history are important for the prediction of the structure deformation.

In gas-filled pipe, fluid-solid coupling is usually judged via the dimensionless parameter B_{FS} [125], defined as:

$$B_{\mathrm{FS}} = \left(\frac{c_{sg}}{c_{ss}}\right)^2 \left(\frac{\rho_g}{\rho_s}\right) \left(\frac{2R}{h}\right) \tag{4.4}$$

where R is the tube radius, h its thickness, c_s is speed of sound while subscripts g and s refer to gas and solid respectively. For thin-walled tubes filled with air, $B_{\mathrm{FS}} \simeq 10^{-5}$. For $B_{\mathrm{FS}} \ll 1$, the tube can be considered as rigid and the fluid-solid system can be decoupled. Therefore, structure deformations can be determined directly by considering the pressure variation in the gas as a boundary condition (as described in Chapter 4.2.3).
In equation (4.4), we have considered only waves propagating at the gas sound speed (acoustic waves). If a strong shock wave is formed, a better estimation of B_{FS} can be obtained by substituting c_{sg} with the velocity of the shock wave U (U_{CJ} is case of detonation). The value of B_{FS} therefore increases and fluid-solid coupling becomes stronger.
The effect of fluid compressibility on the dynamic response of free-standing plates was investigated by Kambouchev et al. [73]. More recently, Chennamsetty et al. [36] studied numerically and experimentally the effect of normal and oblique shock wave on Hastelloy plates. Numerical simulations of the dynamic behavior of the specimen were performed by taking into account fluid-structure coupling. In both these two works, the reduced amplitude of the reflected pressure wave provided by the FSI effect was highlighted.
The mitigating effect of bendable walls in decreasing the maximum combustion pressure was also observed by Kotchourko et al. [80]. Numerical simulations were performed coupling the gas dynamic code COM3D with the finite element code ABAQUS. Numerical results thus obtained were in good agreement with experimental data from [85].

4.2 Cylindrical shells

The structural response of cylindrical and spherical vessels to internal impulsive loads was largely studied by Duffey and colleagues, at Sandia Laboratories and Los Alamos National Laboratories. Comprehensive reviews of their works are presented in [18, 49, 125]. Material plastic deformation mechanisms and failure criteria derived at Los Alamos National Laboratories were implemented in ASME code for the design of impulsively loaded pressure vessels [9]. These criteria were derived from studies on material vessels response to high explosives. Although magnitude and time history of blast loads differ considerably from those typical of gas explosions, Duffey's results may be used as reference for material plastic response to impulsive loads.
Extensive investigations on gaseous detonation loads were performed by Shepherd and colleagues, at the California Institute of Technology [15, 16, 124, 125]. Particular attention was paid to detonation shock waves propagating in long tubes with closed ends. Theoretical and experimental results in terms of structure dynamic response were compared to those obtained in the case of impulsive loads [49] in the limit of strong detonation waves.
In the present paragraph we recall first the linear elastic theory of shells [137] and then we present the structure response of cylindrical vessels to transient loads.

4.2.1 Linear elastic theory of shells

According to [137], a shell is a tridimensional body characterized by a defined curvature of the middle plane in the unloaded configuration. The linear theory of thin shell can be applied only to solids with uniform thickness having an aspect ratio that meets the following condition:

$$\left.\begin{array}{l}\frac{h}{2R_y}\\ \frac{h}{2R_z}\end{array}\right\} \leq 0.1 \tag{4.5}$$

where h is the thickness of the shell while R_y and R_z are the curvatures in the y and z directions respectively. For a cylinder, condition (4.5) reduces to $h/(2R) < 0.1$, where R is the radius of the mid-surface. Relation (4.5) implies that shell cross sections can be assumed as rectangular. With this hypothesis, in case of uniform stress distribution along the thickness, no bending moments are generated. If condition (4.5) is not verified, Lamé's equations for thick cylinders should be preferred[1].
Due to the reduced thickness, only the the mid-surface, $r = R$, is taken into account for the balance equations. Moreover, only loads perpendicular to the surface and bending ones are considered. With the notation presented in Figure 4.1, from the equilibrium of the forces acting on a slice of cylinder in r and θ directions, we get:

$$R\frac{\partial Q_z}{\partial z} + N_\theta - pR = 0 \tag{4.6}$$

$$\frac{\partial M_z}{\partial z} = Q_z \tag{4.7}$$

[1] In a thick walled cylinder shear stress through the cross section can no longer be neglected. In a plane stress configuration for a cylinder with infinite length and open ends ($\sigma_z = 0$), the equilibrium equation is:

$$\frac{\mathrm{d}\sigma_r}{\mathrm{d}r} + \frac{\sigma_r + \sigma_\theta}{r} = 0\,.$$

Since the radial and tangential strains are defined as:

$$\epsilon_r = \frac{\mathrm{d}u}{\mathrm{d}r} = \frac{1}{E}(\sigma_r - \nu\sigma_\theta)$$
$$\epsilon_\theta = \frac{u}{r} = \frac{1}{E}(\sigma_\theta - \nu\sigma_r)$$

the above equation can be rewritten as:

$$\frac{\mathrm{d}^2u}{\mathrm{d}r^2} + \frac{1}{r}\frac{\mathrm{d}u}{\mathrm{d}r} - \frac{u}{r^2} = 0$$

whose solution depends on the boundary conditions. By imposing that the stress at the inner/outer radius equals the internal/external pressure, $\sigma_r(r_i) = -p_i$ and $\sigma_r(r_e) = -p_e$, we find Lamé's equations for the stress tensor:

$$\sigma_r(r) = C_1 + \frac{C_2}{r^2} \quad C_1 = \frac{p_i^2 r_i^2 - p_e^2 r_e^2}{(r_e^2 - r_i^2)}$$
$$\sigma_\theta(r) = C_1 - \frac{C_2}{r^2} \quad C_2 = \frac{r_e^2 r_i^2 (p_e - p_i)}{(r_e^2 - r_i^2)}$$

If the cylinder has closed ends, then the longitudinal stress is:

$$\sigma_z = \frac{p_i^2 r_i^2 - p_e^2 r_e^2}{(r_e^2 - r_i^2)} = C_1\,.$$

where we have supposed that the load has only a radial component: $\boldsymbol{p} = (p_r, p_\theta, p_z) = (p, 0, 0)$.
Thus, substituting equation (4.7) in (4.6), we obtain[2]:

$$\frac{\partial^2 M_z}{\partial z^2} + \frac{N_\theta}{R} - p = 0\,. \tag{4.9}$$

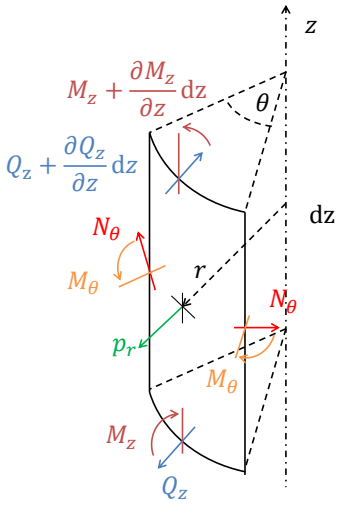

Figure 4.1: Balance of external and internal forces on a slice of cylinder $R\mathrm{d}\theta\mathrm{d}z$ under uniform pressure $p = p_r$.

Since shell cross section can be considered as rectangular, we can substitute the radial coordinate r with a Cartesian coordinate x, that identifies the shell thickness. If we denote with u, v and w the displacements along z, θ and x directions respectively, the deformation of the shell is described as:

$$\epsilon_z(x) = \frac{\partial u}{\partial z} - x\frac{\partial^2 w}{\partial z^2} \tag{4.10a}$$

$$\epsilon_\theta(x) = \frac{w}{R} \tag{4.10b}$$

$$\gamma_{z\theta}(x) = 0 \tag{4.10c}$$

where we have imposed that $x \ll R$ and we have assumed $v = 0$ and $\frac{\partial \circ}{\partial \theta} = 0$ for axial symmetry conditions.

[2]We can note that, if flexural effects are neglected, equation (4.9) reduces to:

$$N_\theta = pR$$

The membrane state of tension for a thin cylinder with closed ends is described by:

$$\sigma_\theta = \tfrac{pR}{h}\,, \quad \sigma_r = p\,, \quad \sigma_z = \tfrac{pR}{2h} \tag{4.8}$$

For an elastic homogenous material, the components of the stress tensor are:

$$\sigma_z(x) = \frac{E}{1-\nu^2}\left(\epsilon_z(x) + \nu\epsilon_\theta(x)\right) \tag{4.11a}$$

$$\sigma_\theta(x) = \frac{E}{1-\nu^2}\left(\epsilon_\theta(x) + \nu\epsilon_z(x)\right) . \tag{4.11b}$$

Substituting equations (4.10) in (4.11) and integrating $\sigma_z(x)$ and $\sigma_\theta(x)$ along the thickness, the stress resultants N_z, M_z, N_θ and M_θ are defined as:

$$N_z = \frac{Eh}{1-\nu^2}\left(\frac{\partial u}{\partial z} + \nu\frac{w}{R}\right) = 0 \tag{4.12}$$

$$M_z = \frac{Eh^3}{12(1-\nu^2)}\frac{\partial^2 w}{\partial z^2} \tag{4.13}$$

$$M_\theta = \nu\frac{Eh^3}{12(1-\nu^2)}\frac{\partial^2 w}{\partial z^2} \tag{4.14}$$

$$N_\theta = Eh\frac{w}{R} \tag{4.15}$$

where we have imposed $N_z = 0$ due to the fact that $p_z = 0$.
The equilibrium equation (4.9) can be rewritten as:

$$\frac{\partial^4 w}{\partial z^4} + \frac{12(1-\nu^2)}{h^2R^2}w = \frac{12(1-\nu^2)}{Eh^3}p \tag{4.16}$$

or, by imposing $z' = z/R$:

$$\frac{\partial^4 w}{\partial (z')^4} + 12(1-\nu^2)\left(\frac{R}{h}\right)^2 w = 12(1-\nu^2)\frac{pR^4}{Eh^3} . \tag{4.17}$$

In case $p = 0$, the solution of equation (4.17) gives:

$$w(z') = A_1\exp(-\alpha z')\sin(\alpha z' + \Psi_1) + A_2\exp\left(-\alpha\left(\frac{H}{R} - z'\right)\right)\sin\left(\alpha\left(\frac{H}{R} - z'\right) + \Psi_2\right) \tag{4.18}$$

where $\alpha^4 = \frac{3R^2(1-\nu^2)}{h^2}$, while A_1, A_2, Ψ_1 and Ψ_2 can be determined by imposing the boundary conditions. Therefore, the flexural moment is given by the following expression:

$$\begin{aligned} M_z(z') = 2\frac{Eh^3}{12(1-\nu^2)}\frac{\alpha^2}{R^2}\left(-A_1\exp(-\alpha z')\sin(\alpha z' + \Psi_1) + \right. \\ \left. + A_2\exp\left(-\alpha\left(\frac{H}{R} - z'\right)\right)\sin\left(\alpha\left(\frac{H}{R} - z'\right) + \Psi_2\right)\right) \end{aligned} \tag{4.19}$$

According to equation (4.19), bending effects at the boundary decrease exponentially, with a decay rate $\alpha' = \alpha/R$. Thus, we can define an extinction length l^* for which flexural effects cancel:

$$l^* = \frac{3}{\alpha'} . \tag{4.20}$$

For stainless steels with $\nu = 0.3$, $l^* \simeq 2.33\sqrt{hR}$. More generally, the parameter α' (or its reciprocal) is frequently used as scale parameter for the length of cylindrical shells.

4.2.2 Vibration modes

Resonance frequencies of a thin pulsating cylinder were derived by Gibert et al. in [59], for a tube with aspect ratio $H/R \simeq 1$, where H is the length of the cylinder. By making the assumption that the pulsation modes of the cylinder (solid of revolution) can be written in the form:

$$X_{nm}(z,\theta) = \begin{cases} w_{nm}(z)\cos(n\theta) \\ v_{nm}(z)\sin(n\theta) \\ u_{nm}(z)\cos(n\theta) \end{cases} \tag{4.21}$$

the following equilibrium equation is obtained:

$$\frac{EhR^3}{n^4(1-\nu^2)}\frac{\partial^4 w}{\partial z^4} + \frac{(n^2-1)Eh^3}{12(1-\nu^2)R^3}w + \rho hR\left(1+\frac{1}{n^2}\right)\frac{\partial^2 w}{\partial t^2} = 0\,. \tag{4.22}$$

The first term of equation (4.22) takes into account membrane stresses while bending stresses appear in the second term of equation (4.22). The third term is obtained considering only the displacement in time along radial and circumferential directions.
By taking the Fourier transformation, equation (4.22) can be rewritten in the form:

$$\frac{\partial^4 w}{\partial (z/H)^4} - k^4 w = 0\,, \tag{4.23}$$

where

$$k^4 = n^4\frac{\rho}{E}(1-\nu^2)\left(1+\frac{1}{n^2}\right)\left(\frac{H^2}{R}\right)^2(\omega^2-\omega_{\theta n}^2) \tag{4.24}$$

$$\omega_{\theta n} = \left(\frac{E}{12(1-\nu^2)\rho}\right)^{1/2}\frac{n^2-1}{R\left(1+\frac{1}{n^2}\right)^{1/2}}\frac{h}{R}\,. \tag{4.25}$$

The solution of equation (4.23), coupled with the boundary conditions at $z = 0$ and $z = H$, allows us to determine the values of k_m for which the structure resonates, where m is the axial mode number (for simply supported shell $k_m = m\pi$). Pulsation modes can be written in the form:

$$\omega_{nm}^2 = \omega_{\theta n}^2 + \omega_{zmn}^2 \tag{4.26}$$

$$\omega_{nm}^2 = \frac{E}{R^2\rho(1-\nu^2)\left(1+\frac{1}{n^2}\right)}\left(\left(\frac{n^2-1}{\sqrt{12}}\frac{h}{R}\right)^2 + \left(\frac{k_m R}{nH}\right)^4\right)\,. \tag{4.27}$$

Resonance frequencies f_{n1} of a stainless steel with $\nu = 0.3$ can be computed by referring to the abaci presented in [59]:

$$f_{n1} = \frac{\omega_{n1}}{2\pi} = b\left(n, \frac{H}{2R}, \frac{h}{R}\right)\frac{1\cdot 10^{-3}}{2\pi R}\sqrt{\frac{E}{\rho}}\,. \tag{4.28}$$

Here, the values of b are given as a function n for different values of the ratios $H/(2R)$ and h/R.

For a cylindrical shell of infinite length, the ovaling component of the pulsation mode $\omega_{\theta n}$ can be evaluated through equation (4.25) for $n \geq 2$. Radial and axial modes can be computed, according to [19], by the following expression:

$$\omega_{n0} = \frac{\lambda_{n0}}{R}\sqrt{\frac{E}{\rho(1-\nu^2)}} \tag{4.29}$$

where $\lambda_{n0} = n\sqrt{\frac{1-\nu}{2}}$ with $n = 1, 2, 3\ldots$ for the axial mode, while $\lambda_{n0} = \sqrt{1+n^2}$ with $n = 0, 1, 2\ldots$ for the radial mode. Thus for a cylinder with infinite length the axial pulsation mode does not depend on the cylinder length. The dependance on the shell thickness appears only in the circumferential mode $\omega_{\theta n}$. The natural frequency f_{00} can be computed as:

$$f_{00} = \frac{1}{2\pi R}\sqrt{\frac{E}{\rho(1-\nu^2)}}\,. \tag{4.30}$$

Fundamental frequencies for cylindrical shells with different boundary conditions are tabulated in [19].

4.2.3 Transient loads

From the study of the impact of blast waves, simple models were developed to predict the structural response to explosive loading [13]. The simplest approach use in hazard analysis consists in considering the structure as a single-degree-of-freedom system. The dynamic response of the elastic oscillator is:

$$m\frac{\mathrm{d}^2x}{\mathrm{d}t^2} + kx = f(t) \tag{4.31}$$

where m is the mass, k is the spring elastic constant, x the structure displacement and $f(t) = p(t)S$ is the blast load $p(t)$ acting on the oscillator surface S. An exponential decay law is used to describe the load:

$$f(t) = f_{\max}\exp\left(-\frac{t}{\tau_{\text{load}}}\right) \tag{4.32}$$

where $f_{\max} = p_{\max}S$ and τ_{load} is the load characteristic time. If we impose as initial condition that displacement and velocity are zero, the solution of equation (4.31) is:

$$\frac{x(t)}{(f_{\max}/k)} = \frac{(\omega\tau_{\text{load}})^2}{1+(\omega\tau_{\text{load}})^2}\left(\frac{\sin(\omega t)}{\omega\tau_{\text{load}}} - \cos(\omega t) + \exp\left(-\frac{t}{\tau_{\text{load}}}\right)\right) \tag{4.33}$$

where $\omega = \sqrt{m/k}$ is the natural pulsation of the structure. By plotting the dimensionless maximum displacement $\frac{x_{\max}}{(f_{\max}/k)}$ against the product $\omega\tau_{\text{load}}$, we find that the solution presents two asymptotes:

$$\frac{x_{\max}}{(f_{\max}/k)} = 2 \quad \text{for large values of} \omega\tau_{\text{load}} \tag{4.34a}$$

$$\frac{x_{\max}}{(f_{\max}/k)} = \omega\tau_{\text{load}} \quad \text{for very small values of} \omega\tau_{\text{load}} \tag{4.34b}$$

The first asymptote (4.34a) corresponds to a quasi-static loading process. For a quasi-static load, the maximum deflection is twice the value of the static deflection ($x^{\text{static}} = f_{\max}/k$). Moreover, the deformation depends only on the value of the peak pressure, $p_{\max}$, and on the structural stiffness, k.
For small values of the product $\omega\tau_{\text{load}}$, the deformation is directly proportional to the impulse $I = f_{\max}\tau_{\text{load}}$. Asymptote (4.34b) thus bounds the region of pure impulsive loads. In the region between the two asymptotes, the full time history of the loading process needs to be taken into account to evaluate the maximum structure displacement.
Now, if we apply the 1 DOF model described above to a cylinder of infinite length, equation (4.31) can be rewritten in the form [124]:

$$\frac{\partial^2 w}{\partial t^2} + \omega^2 w = \frac{p(t)}{\rho h} \tag{4.35}$$

where the tube oscillation frequency $f = \omega/2\pi$ is given by equation (4.30). With this hypothesis, only the radial expansion of the cylinder is considered, while axial bending effects are neglected. Also in this case we can express the maximum dynamic deformation as a function of the static structure response to the peak load:

$$\epsilon_{p_{\max}}^{\text{dyn}} = \phi\left(\frac{\tau_{\text{load}}}{T}\right)\epsilon_{p_{\max}}^{\text{static}} \tag{4.36}$$

where $\epsilon_{p_{\max}}^{\text{dyn}}$ is the hoop strain for a dynamic load and $\epsilon_{p_{\max}}^{\text{static}}$ is the hoop strain computed considering a static load at $p = p_{\max}$. Dynamic and static strains are therefore related through a dynamic amplification factor, ϕ, that depends on the duration of the pulse τ_{load} and on the structure oscillation period $T = 1/f$. With this notation, the impulsive load region is identified by the value $\tau_{\text{load}}/T < 1/4$. The dynamic amplification factor increases with increasing load pulse duration and for a rectangular pulse it can be evaluated from equation (4.34b) :

$$\phi = 2\pi\frac{\tau_{\text{load}}}{T}\,. \tag{4.37}$$

In the limiting case $\tau_{\text{load}} > 0.4T$, $\phi = 2$ and the tube deformation can be estimated directly from the value of the dynamic pressure peak $p_{\max}$, as previously:

$$\epsilon_{p_{dm}}^{\text{dyn}} = 2\epsilon_{p_{dm}}^{\text{static}} = 2\frac{R(1-\nu^2)}{hE}p_{dm}\,. \tag{4.38}$$

In equation (4.38), the hypothesis of membrane loads in a thin cylindrical shell was made. Since, the wave transit time through the shell thickness[3] is usually much lower than the oscillation period, longitudinal waves through the thickness can be neglected [124]. The thin shells (plates) approximation remains valid.
A first approach to solve analytically the problem of a shock wave loading by taking into account both radial and axial deformations was proposed by Tang [131]. According to [15],

[3]The wave transit time through the shell thickness τ_{wave} can be estimated as:

$$\tau_{wave} = \frac{h}{c_{sl}}$$

where c_{sl} is the longitudinal speed of sound of the shell material.

equations (4.6) and (4.7) were rewritten in order to take into account the dynamic response of the structure (translational and rotary inertia) and the transverse shear deformation:

$$\frac{\partial Q_z}{\partial z} - \frac{N_\theta}{R} + \Delta p = \rho h \frac{\partial^2 w}{\partial t^2} \tag{4.39a}$$

$$\frac{\partial M_z}{\partial z} - Q_z = \rho h^3 \ddot{\psi} \tag{4.39b}$$

$$\frac{\partial N_z}{\partial z} = \rho h \ddot{u} \tag{4.39c}$$

where $\psi = \partial w_b / \partial z$ is the rotation, $w = w_s + w_b$ the total displacement, given by the sum of the shear displacement w_s and the bending displacement w_b, and Δp is the pressure difference across the shell thickness.
The following parameters are introduced:

$$U_d = \sqrt{\frac{E}{\rho(1-\nu^2)}} \tag{4.40}$$

$$U_s = \sqrt{\frac{\kappa G}{\rho}} \tag{4.41}$$

$$\bar{\eta} = \frac{\sqrt{12}}{h}(z - Ut) \tag{4.42}$$

$$\xi = \frac{h}{R\sqrt{12}} \tag{4.43}$$

$$\Pi_j = \frac{(p_j - p_{\mathrm{atm}})R^2}{Eh^2} \quad \text{with } j = 1 \ldots 3 \tag{4.44}$$

where U_d is the dilatational wave velocity, U_s is the shear wave velocity, κ is the shear coefficient and $G = E/2(1+\nu)$ the shear modulus. The excitation parameter Π_j is used to make the load dimensionless.
By defining the dimensionless displacements $\bar{w} = w/h$, $\bar{u} = u/h$ and $\bar{\psi} = \psi/\sqrt{12}$, the equilibrium equation can be written in the form:

$$A_4 \frac{\partial^4 \bar{w}_b}{\partial \bar{\eta}^4} + A_2 \frac{\partial^2 \bar{w}_b}{\partial \bar{\eta}^2} + A_0 \bar{w}_b = F(\bar{\eta}) \tag{4.45}$$

The coefficients A_4, A_2 and A_0 of equation (4.45) are given by:

$$A_4 = \left(\left(\frac{U}{U_d}\right)^2 - 1\right)\left(\left(\frac{U}{U_s}\right)^2 - 1\right) \tag{4.46}$$

$$A_2 = \left(\frac{U}{U_d}\right)^2 \left(1 + \xi^2 \left(\frac{U_d}{U_s}\right)^2\right) - \xi^2(1-\nu^2)\left(\frac{U_d}{U_s}\right)^2 \tag{4.47}$$

$$A_0 = \xi^2 \left(1 + \frac{\nu^2}{\left(\frac{U}{U_d}\right)^2 - 1}\right) . \tag{4.48}$$

The dimensionless load $F(\bar{\eta})$ corresponds to the sum of a step function and an exponential decay law [16]:

$$F(\bar{\eta}) = \xi^2(1-\nu^2)(\Pi_1 + (\Pi_3 - \Pi_1)(1 - H(\bar{\eta}))) + \xi^2(1-\nu^2)((\Pi_2 - \Pi_3)(1 - H(\bar{\eta})) \exp\left(\frac{\bar{\eta}}{\bar{\eta_0}}\right) \tag{4.49}$$

where $H(\bar{\eta})$ is the step function, $\bar{\eta_0} = Ut^*\sqrt{12}$ and t^* is the characteristic load time (by fitting experimental data, it was found $t^* \simeq t_{CJ}/3$, with $t_{CJ} = z/U_{CJ}$).
$F(\bar{\eta})$ represents the pressure profile typical of a gaseous detonation with $p_{\max} = p_{CJ}$ (exponential approximation of the Taylor-Zeldovich model):

$$p(z,t) = \begin{cases} p1 & 0 < t < t_{CJ} \\ (p_2 - p_3)\exp\left(-\frac{t-t_{CJ}}{t^*}\right) + p_3 & t_{CJ} \leq t < \infty \end{cases} \tag{4.50}$$

where p_1 is the initial pressure of the fresh gas (state 1), $p_2 = p_{CJ}$ is the maximum pressure, $p_3 = p_{CJ}\left(\frac{c_3}{c_{CJ}}\right)^{2\gamma/(\gamma-1)}$ is the pressure at the state 3 (at the end of the expansion wave), $c_3 = \frac{\gamma+1}{2}c_{CJ} - \frac{\gamma-1}{2}U_{CJ}$.
The pressure history defined by equation (4.50) is shown in Figure 4.2 for a stoichiometric hydrogen/air mixture ($p_{CJ} = 15.58$ bar, $U_{CJ} = 1977$ m/s and $\tau_{\text{load}} = 0.1$ ms).

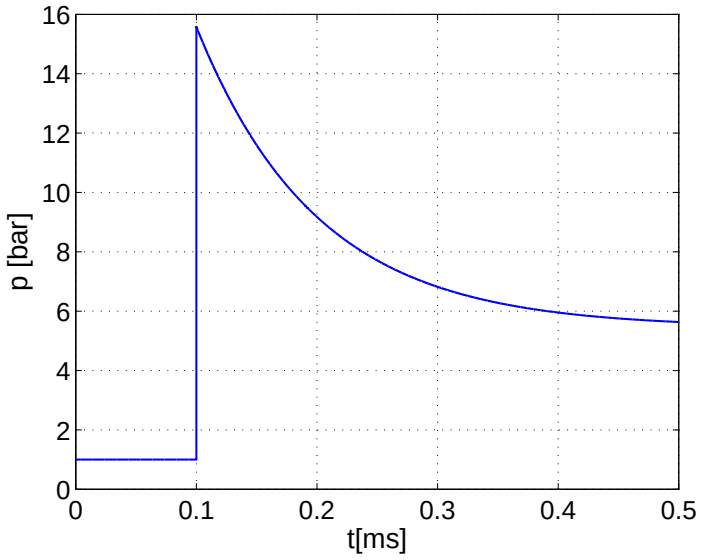

Figure 4.2: Pressure history of a planar steady detonation according to equation (4.50) (exponential approximation of the Taylor-Zeldovich model) for a stoichiometric hydrogen/air mixture.

From the solution of the homogeneous part of equation (4.45), four critical velocities can

be found:

$$U_{c0} = \left(\frac{E^2 h^2}{3\rho^2 R^2 (1-\nu^2)} \right)^{1/4} \tag{4.51}$$

$$U_{c1} = U_s \tag{4.52}$$

$$U_{c2} = U_{db} = \sqrt{\frac{E}{\rho}} = U_d \sqrt{1-\nu^2} \tag{4.53}$$

$$U_{c3} = U_d \tag{4.54}$$

$$\tag{4.55}$$

where U_{db} is the dilatational wave speed in a bar. If the velocity of the shock wave equals one of the critical velocities, $U = U_{ci}$ with $i = 0, 1, 2, 3$, the solution diverges (linear exitation model without damping). An important thing to note is that the shell thickness appears only in U_{c0}.
Therefore, for the solution of equation (4.45) five cases can be distinguished depending on the value of the shock wave velocity. According to [16], the two most relevant cases are the subcritical case ($0 < U < U_{c0}$) and the supercritical one ($U_{c0} < U < U_s$). In the first case the solution is oscillatory with an oscillation amplitude that decreases exponentially as the distance from the detonation front increases. In the second case, the solution is purely oscillatory and two different pulsation frequencies can be distinguished in the main wave and in the precursor one.
More recently, a transient solution of Tang's model was derived by Beltman et al. [16]. A time-dependent solution has the advantage to give more realistic predictions as the velocity approaches the critical value, where the structure response is predicted to be infinite. In Beltman's model transverse shear and rotary inertia are neglected. Thus, the structural response of a cylinder under transient loads can be evaluated from equation (4.16) by adding the contribution due to the inertia of the structure:

$$\frac{\partial^4 w}{\partial z^4} + \frac{12(1-\nu^2)}{h^2 R^2} w + \frac{12\rho(1-\nu^2)}{E h^2} \frac{\partial^2 w}{\partial t^2} = \frac{12^2}{h^3} F(z,t) \tag{4.56}$$

where $F(z,t)$ is temporal formulation of equation (4.49), in which the variable $\bar{\eta}$ is substituted by $(z - Ut)$.
The solution of equation (4.56) was found by writing the radial displacement as the sum of eigenmodes φ_q:

$$w(z,t) = \sum_{q=1}^{\infty} b_q(t) \varphi_q(z)\,. \tag{4.57}$$

Equation (4.56) therefore becomes:

$$\ddot{b_q} + \omega_q^2 b_q = \frac{12 U_d^2}{h} \int_0^H \varphi_q F(z,t)\,\mathrm{d}z\,. \tag{4.58}$$

By imposing the boundary conditions, the eigenmodes can be determined. The integration of equation (4.58) allows then to determine b_q. The eigenfrequencies ω_q are:

$$\omega_q^2 = \frac{U_d^2 h^2}{12} \left(k_q + \frac{12^2 \xi^2 (1-\nu^2)}{h^4} \right) \tag{4.59}$$

where k_q depends on the boundary conditions.
Furthermore, Beltman and colleagues [15, 16] traced the value of the amplification factor (equation (4.36)) versus the velocity of the detonation wave. Experiments performed within the GALCIT shock tube are compared to the analytical solutions obtained with Tang and Beltman models. Experimentally, the maximum value for ϕ was found near the value of the critical velocity U_{c0}. As mentioned above, Tang's model is not accurate in correspondence to the critical velocities for which displacements are infinite. Nevertheless, far from the critical velocity U_{c0}, the value of the amplification factor predicted by Tang's model approaches unity for subcritical velocities and the value 2 for supercritical velocities. Beltman's model, on the other hand, gives a more realistic prediction of the maximum value of the amplification factor, capturing well the experimental results.
Moreover, for supercritical velocities these findings ($\phi \to 2$) are in good agreement with equation (4.38) derived from the 1 DOF model for impulsive loads. The main difference between the 1 DOF model and the shock wave model is that, while for first one $\phi_{\max} = 2$, the second one predict higher values of ϕ in correspondence to the critical velocity ($\phi_{\max} \simeq 3 - 4$), as observed experimentally.
The transient model of Beltman was improved by Mirazei et al. [104] by adding the effects of rotary inertia and shear deformation for a finite length thin shell with simple supports. With respect to the prevoius one, this model was found to be more accurate in predicting both the critical velocity and the amplification factor.

4.3 Circular plates with clamped edge

The problem of a circular plate with clamped edge uniformly loaded is widely studied in the literature. Analytical solutions are available for the elastic region of the stress-strain diagram supposing that the material is perfectly homogeneous and that its behavior agrees with the Hooke's law [137]. Non-linear solutions were also developed to cover a wider spectrum of plate deformations [147].
A complete review on impulsively loaded clamped plates is presented in [108, 109]. All the works discussed in [108, 109] deal with plastic deformation and failure of thin plates subjected to high explosives, blast waves and underwater explosions. Further studies on impulsive loads were recently published [12, 10].

4.3.1 Linear elastic theory of plates

Kirchhoff theory of thin plates can be applied to those solids that have two over three predominant dimensions [137]. If we denote with z the coordinate identifying the thickness, then the deformation of the plates is defined by an inflection in the xz and yz planes. Due to the reduced thickness, only the elastic surface (i.e. the mid- surface, $z = 0$) is taken into account for the balance equations. Moreover, only loads perpendicular to the surface and bending ones are considered. The model is based on the following hypotheses:

1. plate's material is homogeneous and plate's thickness h is constant and it does not change during a deformation;

2. plate's material obeys to Hooke's law for plane stress;

3. when unloaded, the plane $z = 0$ is not deformed;

4. the displacement, w, in the z direction is small compared to the diameter of the plate (small bending angles);

5. plate cross sections must remain plain.

In case of axis-symmetric load, the stress tensor, in polar coordinates, is given by:

$$\boldsymbol{\sigma} = \begin{bmatrix} \sigma_r & 0 & \tau_{rz} \\ 0 & \sigma_\theta & 0 \\ \tau_{rz} & 0 & 0 \end{bmatrix} \tag{4.60}$$

where is $\tau_{r\theta} = \tau_{\theta z} = \tau_{\theta r} = \tau_{z\theta} = 0$ imposed to keep the symmetry of the problem. σ_z can be neglected since it is equal to zero at the intrados while it is equal to the applied load at the extrados, whose value is much lower than the stress components.
The deformation of the plate is then described by the strain vector (ϵ_r, ϵ_θ), whose components are defined as:

$$\epsilon_r = \frac{z}{\rho_r} = -z\frac{d^2w}{dr^2} \tag{4.61a}$$

$$\epsilon_\theta = \frac{z}{\rho_\theta} = -\frac{z}{r}\frac{dw}{dr} \tag{4.61b}$$

where w denotes the displacement in the z direction. Since $\sigma_z = 0$, the bending moments per unit of length [N·m/m] can be related to the surface curvatures κ_r and κ_θ as in case of pure bending:

$$m_r = \mathcal{D}\left(\kappa_r + \nu\kappa_\theta\right) = \mathcal{D}\left(\frac{1}{\rho_r} + \nu\frac{1}{\rho_\theta}\right) = -\mathcal{D}\left(\frac{d^2w}{dr^2} + \frac{\nu}{r}\frac{dw}{dr}\right) \tag{4.62a}$$

$$m_\theta = \mathcal{D}\left(\kappa_\theta + \nu\kappa_r\right) = \mathcal{D}\left(\frac{1}{\rho_\theta} + \nu\frac{1}{\rho_r}\right) = -\mathcal{D}\left(\frac{1}{r}\frac{dw}{dr} + \nu\frac{d^2w}{dr^2}\right) \tag{4.62b}$$

where we have made the hypotheses that $r \simeq \rho_\theta\varphi$ while $dr = \rho_r d\varphi$. Here the bending angle is defined as $\varphi = -(dw/dr)$. Equations (4.62) represent plates constitutive equations. Bending stiffness (or isotropic plate rigidity), $\mathcal{D}$, is defined as follows:

$$\mathcal{D} = \frac{Eh^3}{12(1-\nu^2)}\,. \tag{4.63}$$

Now let us consider a slice of plate, as shown in Figure 4.3. From the rotational equilibrium in the rz-plane we get:

$$\left(m_r + \frac{\partial m_r}{\partial r}dr\right)(r + dr)d\theta - m_r r\,d\theta + t_r r\,d\theta\,dr - 2m_\theta dr\frac{\theta}{2} = 0 \tag{4.64}$$

while the translational equilibrium gives:

$$2\pi r t_r = \pi r^2 p\,. \tag{4.65}$$

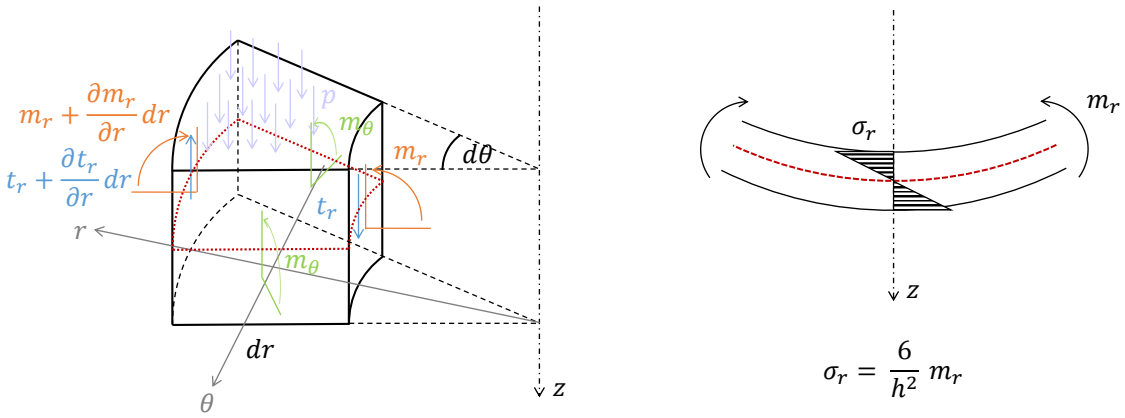

Figure 4.3: Balance of external and internal forces on a slice of plate $h dr d\theta$ under uniform pressure.

Substituting equation (4.65) into equation (4.64), we get:

$$\frac{\partial(m_r r)}{\partial r} - m_\theta = -\frac{r^2 p}{2}\,. \tag{4.66}$$

Taking into account the constitutive equations (4.62), it is possible to rewrite equation (4.66) as:

$$\frac{d}{dr}\left(\frac{1}{r}\frac{d(r\varphi)}{dr}\right) = -\frac{pr}{2D}\,. \tag{4.67}$$

The solution of equation (4.67) is obtained imposing the boundary conditions, i.e. fixed edge for $r = R$ and axis-symmetric conditions for $r = 0$:

$$\varphi(0) = 0 \tag{4.68a}$$
$$\varphi(R) = 0 \tag{4.68b}$$
$$w(R) = 0\,. \tag{4.68c}$$

Thus, we obtain:

$$w = \frac{p}{64\mathcal{D}}(R^2 - r^2)^2 \tag{4.69a}$$
$$\varphi = \frac{pr}{16\mathcal{D}}(R^2 - r^2)\,. \tag{4.69b}$$

The maximum displacement in z direction is found to be at $r = 0$:

$$w(0) = \frac{pR^4}{64D}\,. \tag{4.70}$$

The moment distribution along the radius is obtained substituting equation (4.69) into (4.62):

$$m_r = \frac{p}{16}(R^2(1+\nu) - r^2(3+\nu)) \tag{4.71a}$$
$$m_\theta = \frac{p}{16}(R^2(1+\nu) - r^2(1+3\nu))\,. \tag{4.71b}$$

As proved in Chapter 2.13 of [137], equations derived in the present paragraph can be applied with sufficient accuracy if the deflections of plate from its initial plane are small in comparison with the thickness of the plate. Way has shown in [147] that for clamped circular plates the above described theory is applicable for maximum deflections less then 0.4 of the thickness. For such deflections the error in the deflection is less than 10%. For larger deflections, non-linear effects must be taken into account.
A solution of the problem for "large deflections" ($0.5 < \frac{w}{h} < 1$) is presented in [147]. The solution was obtained taking into account a power series decomposition for the lateral displacement w.
The problem of large deflections of a uniform thickness, circular isotropic elastic membrane clamped at its boundary and subjected to uniform lateral loading was first studied by Hencky [66] in 1915. The membrane solution is obtained by imposing a no-slip condition at the edge (zero radial displacement, $u(R) = 0$ and $u(0) = 0$). The membrane deflection at the center is given by the following formula:

$$\frac{w(0)}{h} = \frac{3}{4}\left(\frac{(1-\nu^2)pR^4}{Eh^4}\right)^{\frac{1}{3}} . \tag{4.72}$$

A revisited solution of Hencky problem is presented in [55]. Here the solution for a uniform lateral loading ($\boldsymbol{p} = (0, 0, p_z)$) is compared to the case with a uniform pressure load ($\boldsymbol{p} = p\boldsymbol{I}$).
Li and colleagues [94] have recently included non-linear effects to the elastic theory presented above. A strain model was added to the middle plane in order to take into account the stretching effect of the neutral plane when its central deflection is larger then the plate thickness. A cubic equation for $w(0) = w_0$ was so found:

$$w(r) = w_0\left(1 - \left(\frac{r}{R}\right)^2\right)^2 \tag{4.73}$$

$$w_0 = \frac{pR^4}{64\mathcal{D}}\left(\frac{1}{1 + \left(\frac{0.4442}{(1-\nu^2)}\frac{w_0^2}{h^2}\right)}\right) . \tag{4.74}$$

Therefore, w_0 is no longer proportional to the load intensity p while the rigidity of the plate is greater than that one predicted by the pure bending theory. A cubic solution for w_0 is also proposed by Eaton and al. [51]. Here, a built-in residual strain appears in the expression for the membrane central displacement.
A comparison among the different formulations cited above for circular plate deformation in the elastic region are shown in Figure 4.4. Moreover, from 4.4, we can see that if the plate deflection reaches approximately one and half the plate thickness, membrane forces takes over the bending ones.

4.3.2 Vibration modes

Let us now consider the bending movement of the plate in time [59]. We suppose that the plate neutral plane displacement $w = w(r, t)$ is small compared to the plate thickness. The more general formulation of the equilibrium equation (4.67) in cylindrical coordinates

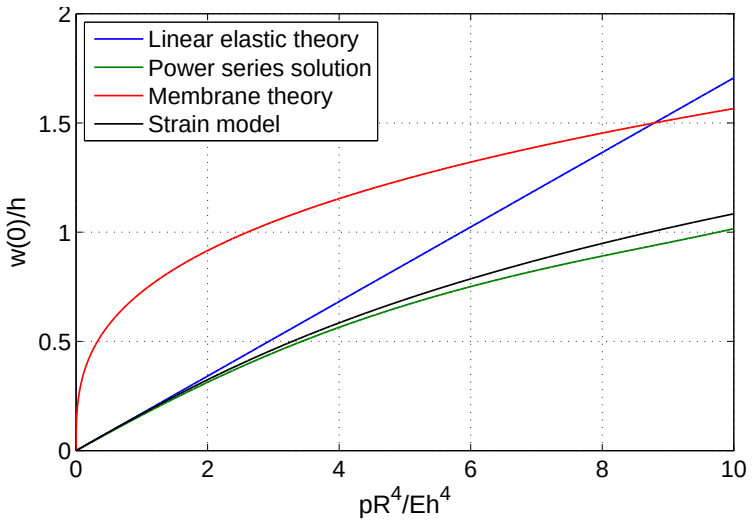

Figure 4.4: Non-dimensional maximum deflection for a circular plate with clamped edge: comparison of the results obtained with the linear theory (equation (4.70)), the power series solution (Way's solution), the membrane theory (internal stress, equation (4.72)) and the strain model (equation (4.73)) for $\nu = 0.3$.

is:

$$\mathcal{D}\left(\frac{\partial^2}{\partial r^2}+\frac{1}{r}\frac{\partial}{\partial r}+\frac{1}{r^2}\frac{\partial^2}{\partial\theta^2}\right)^2 w+\rho h\frac{\partial^2 w}{\partial t^2}=0\,. \tag{4.75}$$

Since the circular plate is a revolution solid, the normal modes of vibration can be expressed in the form:

$$W_{nm}=W_{nm}(r)f(\theta) \tag{4.76}$$

where $f(\theta)$ is a sinusoidal function in the form $\cos(n\theta)$ or $\sin(n\theta)$.
For the simple case $n=0$, the equilibrium equation (4.75) can be rewritten as (Fourier transformation):

$$\mathcal{D}\left(\frac{\mathrm{d}^2}{\mathrm{d}r^2}+\frac{1}{r}\frac{\mathrm{d}}{\mathrm{d}r}\right)^2 W-\rho h\omega^2 W=0\,. \tag{4.77}$$

The solution of equation (4.77) is a linear combination of Bessel functions J_0 and I_0:

$$X(r)=aJ_0\left(\lambda\frac{r}{R}\right)+bI_0\left(\lambda\frac{r}{R}\right) \tag{4.78}$$

where $\left(\frac{\lambda}{R}\right)^4=\frac{\rho h\omega^2}{\mathcal{D}}$, while coefficients a and b can be computed by imposing the boundary conditions. The boundary conditions for a clamped plate are $X(r=R)=0$ and $\frac{\mathrm{d}X}{\mathrm{d}r}|_{r=R}=0$. λ_{0m} are the solution of equation:

$$J_0(\lambda)I_1(\lambda)+J_1(\lambda)I_0(\lambda)=0\,. \tag{4.79}$$

Oscillation frequencies are given by $f_{0m}=\omega_{0m}/(2\pi)$. The fundamental frequency f_{01} is:

$$f_{01}=\frac{\lambda_{01}^2}{4\pi R^2}\sqrt{\frac{Eh^2}{3\rho(1-\nu^2)}} \tag{4.80}$$

where $\lambda_{01}=3.2$.

For $n \neq 0$, the solution is also a function of the θ angle. In this case the oscillation frequencies for a plate with clamped edge are:

$$f_{nm} = \frac{\lambda_{nm}^2}{4\pi R^2}\sqrt{\frac{Eh^2}{3\rho(1-\nu^2)}} \tag{4.81}$$

where the values of λ_{nm} for $n = 0, 1, 2$ and $m = 1, 2, 3$ are listed in Table 4.1

Table 4.1: Tabulated values for the coefficient λ_{nm} of equation (4.81) for $n = 0, 1, 2$ and $m = 1, 2, 3$.

λ_{nm}^2	$m=1$	$m=2$	$m=3$
$n=0$	10.21	21.22	34.84
$n=1$	39.78	60.84	84.58
$n=2$	88.90	120.08	153.81

For different boundary conditions (free edge, simply supported, etc.), the values of plate natural frequencies are tabulated in [19].

4.3.3 Transient loads

Plate response to transient loads can be evaluated in first approximation with the single-degree-of-freedom model (equation (4.35)) described in Chapter 4.2.3. For thin plates with clamped edge, the natural frequency is given by equation (4.80).
Also in this case we can distinguish two loading regimes: the pure impulsive regime and the quasi-static one. For pure impulsive loads, the maximum central deflection can be determined directly from the load impulse. A complete list of theoretical expressions for the maximum plate displacement is summarized in [108]. From experimental observations, the following relation between the central deflection and the load pulse I was proposed [109]:

$$\frac{w_0}{h} = 0.425\frac{I}{\pi R h^2(\rho\sigma_{\mathrm{YS}})^{1/2}} \tag{4.82}$$

where σ_{YS} is the static yield stress. If the load is not impulsive nor quasi-static, plate deformation depends on the load time history and it has to be derived by the solution of 1 DOF model.
In case of perfectly planar wave, the shock load $p = p(t)$ depends only on time. With this assumption, we expect that only radial mode are excited. This is also the case of axisymmetric loads $p = p(r, t)$. If the shock wave is not planar $p = p(r, \theta, t)$, then circumferential modes must be taken into account. Therefore, for a more accurate solution, the general formulation for the equilibrium equation of a thin plate should be taken into account:

$$\mathcal{D}\left(\frac{\partial^2}{\partial r^2} + \frac{1}{r}\frac{\partial}{\partial r} + \frac{1}{r^2}\frac{\partial^2}{\partial\theta^2}\right)^2 w + \rho h\frac{\partial^2 w}{\partial t^2} = p(r,\theta,t)\,. \tag{4.83}$$

Recently, an experimental and numerical study on blast waves acting on steel square plates has been performed by Aune et al. [11]. In this study, a shock tube was used

to generate the load. The capabilities of shock tubes to create impulsive loading were studied before by [7]. Experimental results show a dynamic elastoplastic response of the plate, with a strong increase of the central deflection in correspondence with the shock wave reflection. Secondary and tertiary reflections seem to have negligible effect on plate deflection. Moreover, fluid-structure interaction effects were investigated by comparing pressure records from the experiments with rigid massive walls with those ones with deformable plates.

4.4 Conclusion

In this chapter, a review of analytical models, proposed in the literature, for the mechanical response of thin shells and plates under static and transient loads were presented. Particular attention was paid to quasi-static loads from slow deflagrations and to impulsive loads generated by gaseous detonations. The foregoing analytical expressions provide a basis for both experimental and numerical results. They can also be used as a reference for the design of impulsively loaded pressure vessels. In particular, in the frame of this work, we will refer to these theoretical models in Chapter 14 to perform pre-test analysis on the mechanical response of the experimental facility SSEXHY, described below.
For more complex transient loading with multiple shock reflections, such as in case of flame acceleration and deflagration-to-detonation in complex geometries, numerical simulations need to be performed. Non-linear effects and material plastic behavior can also be included in the numerical model for a more realistic prediction of the structural response.
Eventually, in this chapter we have mentioned the role of the fluid-structure interactions. In case of detonations, the load can be considered as pure impulsive and the structure response can be determined directly from the load impulse. In this limiting case, structure mechanics and fluid dynamics can be decoupled. In other words, it is assumed that the time needed by structure to deform is usually much greater than the characteristic time of the detonation process. On the other hand, for lower flame speeds, for which the shock wave ahead of the flame is not self-sustained, changes in the surrounding geometry may cause significant effects in gas dynamics in terms of pressure peaks and combustion propagation. This effects are more pronounced as the structure stiffness decreases. Therefore, experiments performed within shock tubes are only relevant to investigate detonation-like impulsive loads. However, to study the impact of fast flames before the transition to detonation, experiments in combustion tubes seem to be of more relevance.
Moreover, as shown by Kuznestov [86], depending on the structure stiffness and natural frequency, accelerated flames can be in certain cases more penalising in terms of structural loads than steady-state detonation waves. In case of DDT induced by the interaction between the reflected shock wave and the reactive front, detonation occurs in a pre-compressed medium; the resulting structural damages are therefore more important.

Part II

Experimental set-up

Chapter 5

Description of the experimental facility

This chapter is devoted to the general description of the experimental facility SSEXHY. The apparatus is a modular structure composed of multiple sections that can be easily connected to and disconnected from each other. It is mainly formed by two parts: (1) a combustion tube for the characterization of flame propagation mechanisms and (2) a module for the study of the dynamic response of structures to combustion generated loads. While the combustion tube can be operated as a single self-standing experimental device, for the FSI module to be operational, it is required that the module is connected to the combustion tube.

5.1 Combustion tube for flame acceleration

The combustion tube features a stainless steel obstructed duct designed to study the acceleration mechanisms of premixed hydrogen/air flames. The tube includes four interchangeable sections connected by flanges. Each section is 1310 mm long with an internal diameter of 120 mm. Hereinafter, sections are denoted with the acronym TRi00 with $i = 1, 2, 3, 4$. The design pressure of the tube is 100 bar. For safety reasons, at least three over the four sections should be connected to form the combustion tube while performing an experiment. The total length, l_{tot}, of the tube can therefore vary between 3930 mm and 5240 mm. Two blank flanges are used to seal the combustion tube at its extremities. A picture of the experimental device is shown in Figure 5.1.

5.1.1 Gas injection and venting system

Gas injection lines are connected to one end-flange via an isolation valve. At the center of this flange, a threaded hole houses an automotive spark plug. Mixture ignition is provided by the electrical discharge between the two electrodes of the plug[1].
On the other extremity, venting lines ensure burnt gas evacuation from the combustion tube at the end of the experiment. A primary vacuum pump is also connected at both sides of the tube. A schematic of the combustion tube is shown in Figure 5.2.

[1]The energy released by an ordinary spark plug is around 25 mJ [113]. The minimum ignition energy (MIE) for a stoichiometric hydrogen/air dry mixture is 0.019 mJ. A typical U-shape curve was experimentally drawn by Lewis et al. [93] for the MIE as a function of the hydrogen content. For very lean mixtures the MIE is around 1 mJ.

Figure 5.1: Picture of the combustion tube. Here, the device is composed by three sections (TR400, TR200 and TR300).

Gas injection procedures are controlled throughout three static pressure sensors with different operating ranges: a vacuum gauge (P1) in the range 0-133 mbar, a pressure transmitter (P2) in the range 0-1000 mbar, and a third sensor (P3) covering the range 0-5 bar. The main characteristics of these transducers are summarized in Table 5.1. Injection procedures and flammable mixture characterization are further discussed in Chapter 6.

Table 5.1: Static pressure transducers

	P1 CERAVAC CTR90	**P2** KELLER PA25HTT	**P3** WIKA IS-21-S
type	absolute	absolute	relative
range	$0 \cdots 100$ Torr	$0 \cdots 1$ bar abs	$-1 \cdots +5$ bar g
output	$0 \cdots 10$ V	$4 \cdots 20$ mA	$4 \cdots 20$ mA
accuracy	0.2% reading	$5.2 \cdot 10^{-3}$ bar	$5.2 \cdot 10^{-3}$ bar

5.1.2 Sampling system and recirculation loop

Once hydrogen and air are injected inside the tube, a non-homogeneous mixture is formed (see Chapter 6). Homogenization is then promoted by a gas recirculation pump (BÜHLER P2.74 ATEX pump). The mixture is forced to recirculate into an external loop for about 30 minutes before reaching the homogeneous condition. This period of time was calibrated from pre-tests using helium instead of hydrogen and measuring the local concentration with thermal conductivity gauges, as described in Chapter 6.2.
Two taps are available for gas sampling at the recirculation loop connections to the tube wall (see Figure 5.2).

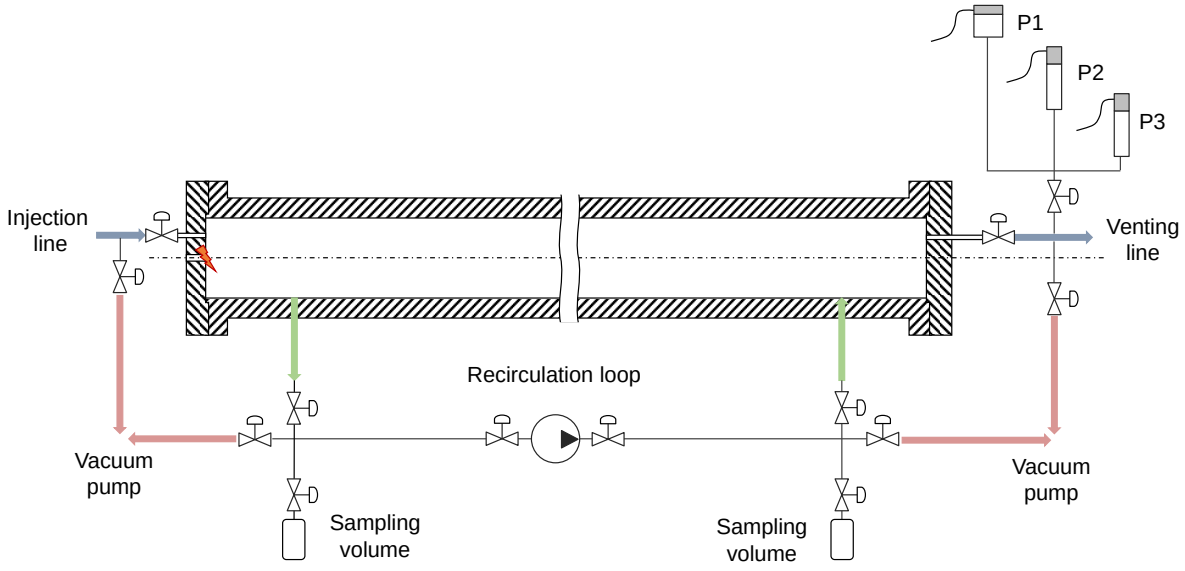

Figure 5.2: Injection and venting system of the combustion tube and external recirculation loop.

5.1.3 Tube internals: obstacles array

An array of equally spaced annular obstacles are placed inside the tube with the aim of promoting turbulence at the wall. Two obstacle blockage ratios (i.e. the ratio between the area obstructed by the obstacle and the tube cross section area) are available ranging from 0.3 to 0.6.
The structure supporting the obstacles is formed by three thin threaded rods. The stainless steel annular obstacles (5 mm thick) have three holes, 120° spaced from each other, for rods insertion. Obstacles are 120 mm spaced from each other, resulting in a 125 mm uniform pitch, as shown in Figure 5.3. According to [39], this corresponds to the optimal configuration for annular obstacles in terms of potential for flame acceleration.

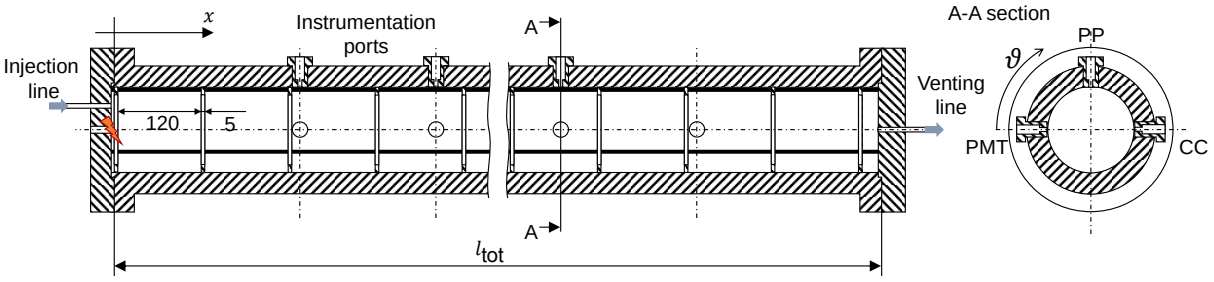

Figure 5.3: Schematic of the combustion tube (obstacle blockage ratio BR= 0.3). Lengths are given in mm. PMT, photomultiplier tube; PP, pressure sensor; CC, shock sensor.

Obstacles surface, as well as tube inner wall, was thermally treated with black oxides to prevent light reflection. The accuracy of optical measurements is therefore increased.

5.1.4 Accesses for instrumentation diagnostics

Along the tube wall, several ports are available for the diagnostics. In Table 5.2, longitudinal and circumferential coordinates of these accesses are listed according to the tube section. Here, the origin $x = 0$ corresponds to the inner surface of the flanged junction of each section, while the origin of ϑ is shown in Figure 5.3.

Table 5.2: Instrumentation ports location along the combustion tube axis. x, longitudinal coordinate; ϑ, circumferential coordinate. The symbol $\times$ denote the presence of the instrumentation port at corresponding position.

	TR100		TR200		TR300		TR400	
x [mm]	$\vartheta = 0, \pi$	$\vartheta = \frac{\pi}{2}$	$\vartheta = 0, \pi$	$\vartheta = \frac{\pi}{2}$	$\vartheta = 0, \pi$	$\vartheta = \frac{\pi}{2}$	$\vartheta = 0, \pi$	$\vartheta = \frac{\pi}{2}$
265	$\times$	-	$\times$	$\times$	$\times$	-	$\times$	$\times$
460	$\times$	-	$\times$	-	$\times$	$\times$	$\times$	$\times$
655	$\times$	$\times$	$\times$	$\times$	$\times$	-	$\times$	$\times$
850	$\times$	-	$\times$	-	$\times$	$\times$	$\times$	$\times$
1045	$\times$	-	$\times$	$\times$	$\times$	-	$\times$	$\times$

Moreover, the threaded central holes of the two end-flanges can be used to house special bolts equipped with sapphire windows. In this case, the spark plug is relocated.
A cross sectional view of the tube (A – A section) in Figure 5.3 shows the standard position of the sensors:

- horizontally, at $\vartheta = 0$, the optical accesses of the photomultiplier tubes (PMT) for flame time-of-arrival measurements;
- on the vertical position, at $\vartheta = \pi/2$, the dynamic pressure sensors (PP);
- facing the PMT, at $\vartheta = \pi$, the piezoelectric shock sensors (CC).

A more detailed description of these sensors is provided later on, in Chapter 7.

5.2 Module for the dynamic response of structures to combustion generated loads

To investigate the effect of combustion loads on structures, the combustion tube described above is coupled with a supplementary module, the FSI module, designed for this purpose. The connection between the combustion tube and the FSI module occurs at the end-flange of the tube. Here, the end sealing flange is replaced by an intermediate flange that ensure the coupling. The intermediate flange also serves as support for the testing specimens. Moreover, it hosts the connections for nitrogen injection and venting lines (to inert FSI module atmosphere). It has an outer diameter of 895 mm and an internal diameter of 120 mm, that allows the perfect continuity with the combustion tube internal wall. The connection of the flange to the tube is made though the use of a series of bolts located at $\Phi = 215$. A second series of bolts on the outer ring ensure the connection to the safety

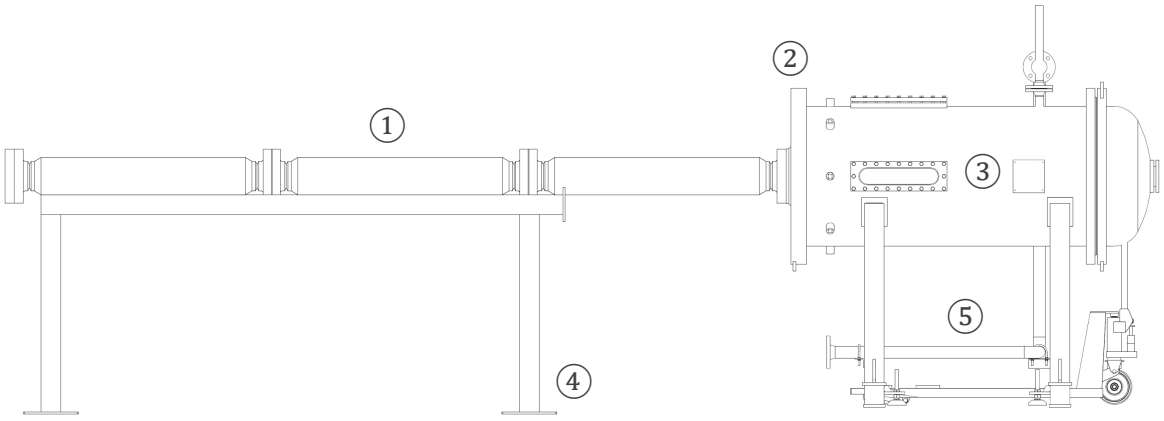

Figure 5.4: Schematic view of the experimental device for the study of structure response to combustion originated loads: (1) combustion tube; (2) intermediate flange; (3) safety dome; (4) frame for tube anchoring; (5) movable frame for safety dome handling.

dome of the FSI module. A schematic view of the coupling between the combustion tube (in the configuration with 3 sections) at the FSI module is shown in Figure 5.4.
The FSI module is composed by the following interconnected parts:

1. intermediate flange;
2. adapter or support (optional) for the specimen to test;
3. stainless steel specimen;
4. counter-flange for specimen fixation;
5. safety dome.

Afterwords, a detailed description of module internals is presented.

5.2.1 Description of the specimens

Three types of stainless steel specimens can be installed in SSEXHY facility:

1. small circular plates;
2. big circular plates;
3. cylinders.

Specimens material

Specimens are made of 304L austenitic stainless steel. Together with the 316L SS, the 304L SS is one of the most commonly used steel in the nuclear industry. In fact, this low carbon stainless steel minimizes carbide precipitation during welding procedures, making it suitable for severe corrosion environments. Some example of nuclear equipment made

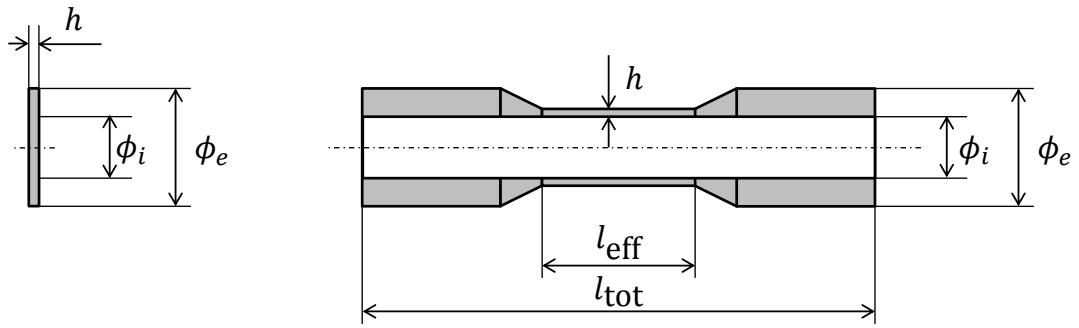

(a) Circular plate. **(b)** Cylinder.

Figure 5.5: Schematic view of the specimens.

of 304L SS are accumulator tanks, reactor internals, heat exchangers, pool liners for spent fuel storage and casks for spent fuel transport. Moreover, several studies have been performed on the dynamic behavior of this type of stainless steel at the mechanical division of the CEA.
Mechanical properties of the SS 304L are listed in Table 5.3.

Table 5.3: SS AISI 304L properties (cold worked). E, Young modulus; ν, Poisson coefficient;ρ, density; $\sigma_{0.2\%} = \sigma_{\text{YS}}$, 0.2% yield strength at room temperature; $\sigma_{1\%}$, strength at 1% elongation; σ_{m}, rupture strength; c_{sl}, longitudinal speed of sound.

E [GPa]	ν	ρ [kg/m^3]	$\sigma_{0.2\%}$ [MPa]	$\sigma_{1\%}$ [MPa]	σ_{m} [MPa]	c_{sl} [m/s]
200	0.3	7930	180	218	500	5790

Specimens dimensions

Specimens' characteristic dimensions are given in Table 5.4. Here, the notation refers to Figure 5.5.
Once installed in the facility, the circular plate is clamped at the edge. The clamped area

Table 5.4: Characteristic dimensions of the specimens. All dimensions are given in mm.

	Small plates		**Big plates**		**Cylinders**
h	0.5	1	1	2	2
Φ_i	120	120	200	200	120
Φ_e	175	175	285	285	150
l_{eff}	–	–	–	–	300
l_{tot}	–	–	–	–	1000

S_c extends from the external diameter Φ_e up to the the diameter Φ_i, $S_c = \pi(\Phi_e^2 - \Phi_i^2)/4$. Therefore, the plate area that is exposed to pressure loads is $S_p = \pi\Phi_i^2/4$.
A schematic view of the cylindrical specimen is shown in Figure 5.5b. The internal diameter of the cylinder is equal to the internal diameter of the combustion tube $\Phi_i = 120$ mm. At the extremities the cylinder is 15 mm thick, while in the central region the thickness is gradually reduced to 2 mm, to limit local stresses originated by geometrical inconguences. The effective length of the 2 mm thick region of the cylinder is 300 mm and it correspond to the effective testing zone of the specimen.
At its extremities, the cylinder is stiffer. The rigidity was locally increased to bare the stresses induced by the constraints at the border and to ensure its correct placement on the facility. If bending forces are generated at the border after fixing the cylinder on its support, internal stresses are gradually dumped along the cylinder length. The extinction length, l^*, of the bending effects can be evaluated according to equation (4.20). By taking $R = 135$ mm and $h = 15$ mm, $l^* \simeq 105$ mm. Without pressure loads, therefore, the central testing zone should not be affected by any residual stresses arising from cylinder fixation.
Once the geometry of the specimen are defined, we can compute the pressure load associated to the yield strength σ_{YS}. Tresca or Von Mises yield criteria can be used to evaluate this quantity:

$$\sigma_T = \max\left\{|\sigma_{11} - \sigma_{22}|, |\sigma_{22} - \sigma_{33}|, |\sigma_{33} - \sigma_{11}|\right\} \tag{5.1}$$

$$\sigma_{VM} = \sqrt{\frac{1}{2}\left((\sigma_{11} - \sigma_{22})^2 + (\sigma_{22} - \sigma_{33})^2 + (\sigma_{33} - \sigma_{11})^2 + 6(\sigma_{23}^2 + \sigma_{31}^2 + \sigma_{12}^2)\right)} \tag{5.2}$$

where σ_{ij} are the components of the stress tensor $\boldsymbol{\sigma}$. For a plane state of tension (thin plates), equations (5.1) and (5.2) reduce to:

$$\sigma_T = \max\left\{|\sigma_r - \sigma_\theta|, |\sigma_r|, |\sigma_\theta|\right\} \tag{5.3}$$

$$\sigma_{VM} = \sqrt{\sigma_r^2 - \sigma_r\sigma_\theta + \sigma_\theta^2} \tag{5.4}$$

Usually pressure vessels design criteria meet the Tresca criterion since it is more conservative. Once σ_T (or σ_{VM}) is computed, the failure by yeld is supposed to occur when

$$\sigma_T(p) \geq \sigma_{\mathrm{YS}}\,. \tag{5.5}$$

In Table 5.5, the minimum pressure that meets criterion (5.5) is given.

5.2.2 Specimens fixation

In order to fix the specimen to the combustion tube, three different supporting structures are available, according to the type of specimen to test. At one side the adapter is fixed to the intermediate flange, while at the other side the end-flange has a groove to accommodate the specimen. Specimen edges are then clamped between the adapter end-flange and a counter-flange. The sealing is ensured by two flat gaskets at each side that extent over the whole clamped area S_c.

Table 5.5: Pressure load associated to the yield strength. Plates state of tension is described by equation (4.71). Cylinders state of tension is given by equation (4.8).

	Small plates		**Big plates**		**Cylinders**
h [mm]	0.5	1	1	2	2
R [mm]	60	60	100	100	60
p_T [MPa]	0.0167	0.0667	0.0240	0.0960	6.0000
p_{VM} [MPa]	0.0188	0.0750	0.0270	0.1080	7.1657

Small plate adapter

Small circular plates can be installed directly between the intermediate flange and the counter-flange. The counter-flange is a ring with an internal diameter equal to $\Phi_i = 120$ mm.
It is possible to extend the length of the combustion tube inside the safety dome of the FSI module by using a cylindrical adapter (see Figure 5.6a). This adapter features a thick stainless steel flanged tube 500 mm long with an inner diameter $\Phi_i = 120$ mm. As previously, the circular plate is installed at the end-flange. On the adapter wall four ports are available for instrumentation diagnostics: two are located at 167 mm from the first flange and two at 333 mm. The two ports at the same location along the tube axis are 90° spaced to each other.

Big plate adapter

In order to test circular plates with different diameters, a flanged conical adapter 500 mm long is used (see Figure 5.6b). The internal diameter of this adapter increases smoothly from 120 mm to 200 mm at the plate fixation point. A ring counter-flange with $\Phi_i = 200$ mm is used to clamp the plate. As for the cylindrical adapter, four instrumentation housings are available on the adapter wall.

Cylinder support

The cylinder specimen is clamped between the intermediate flange and the counter-flange. In this case the counter-flange is blank to confine the explosion. The blank counter-flange is supported by eight studs tighten to the intermediate bride. A slight pre-compression is applied on the flat gaskets to seal the assembly. To avoid specimen displacement from its location in case of large deformation, two retaining plates, hold by the studs, surround the cylinder (in normal configurations, they are not in contact with it). A 3D view of cylinder support system is shown in Figure 5.7. An instrumentation port is located at the center of the counter-flange, dedicated to dynamic pressure monitoring.

5.2.3 Safety dome

The FSI module is enclosed by a safety dome. It is a stainless steel pressure vessel with a nominal diameter of 700 mm and a total length of 1800 mm, design for a nominal pressure

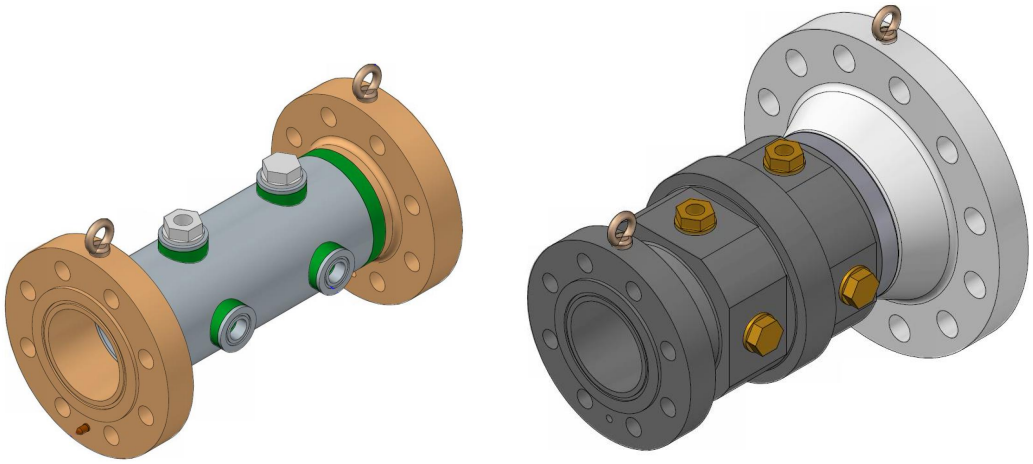

(a) Small plate adapter **(b)** Big plate adapter

Figure 5.6: 3D view of the adapters used to fix circular plates on the combustion tube.

of 8 bar. The dome has multiple functions:

1. to contain possible missiles that can be generated and ejected following specimens failure and fragmentation;
2. to provide an inert atmosphere surrounding the specimens (the dome is filled with nitrogen);
3. to avoid pressure differences across specimen thickness during venting and filling procedures;
4. to provide optical accesses on the specimens (in order to use optical diagnostics to characterize specimens deformation in time);
5. to provide electrical ports for the different diagnostics connections.

To avoid any direct impact between specimen fragments and the dome, the internal wall of the dome is shielded by a deformable sheet metal.
The optical access to the specimen is provided by three glass windows:

- two lateral rectangular windows with a visualization area of 400×80 mm;
- one circular window on the convex end of the dome, facing the dome axis, with $\Phi 80$ mm diameter.

The two rectangular windows are located 275 mm from the intermediate flange and 90° spaced to each other. They provide the direct optical access to the testing zone of the cylindrical specimen (the distance between two consecutive studs of the cylinder holding system ensure the cylinder visualization through the windows).
A pressure transducer is installed on the dome to record the static pressure during filling and venting procedure. It allows to manage the pressure differences between the combustion tube and the dome during these phases in order to avoid excessive pressure

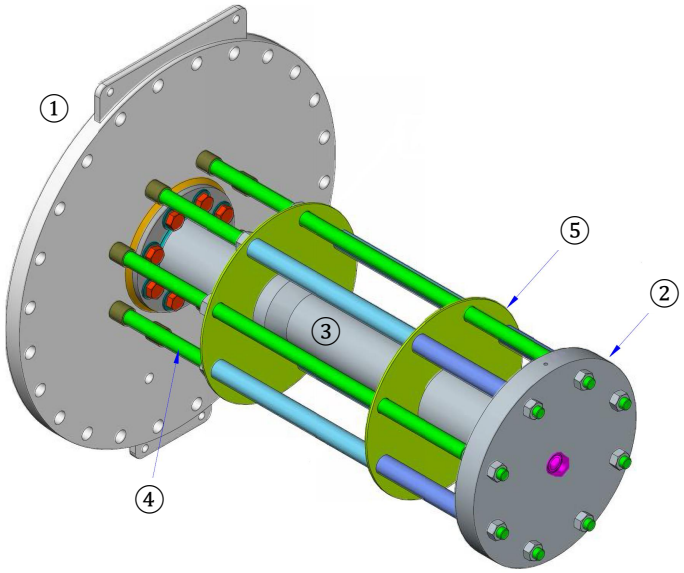

Figure 5.7: 3D view of the cylinder support system: (1) intermediate flange; (2) counter-flange; (3) cylindrical specimen; (4) counter-flange supporting stud; (5) specimen retaining plate.

loads on the specimens (avoiding plastic deformations of the specimen raising from the establishment of a Δp across the specimen thickness).
Since the end-flange of the combustion tube is replaced by the FSI module, gas venting lines are now connected to the last available intrumentation port of the combustion tube.

Chapter 6

Experiment setup

In the present chapter, the setup of an experiment is described. The procedures detailed below are required to set the boundary and initial conditions of the experiment.

6.1 Gas injection procedure

Once the initial conditions of the experiment are established, i.e. initial pressure and hydrogen concentration, the method of partial pressures is used to prepare the desired mixture inside the tube. Hydrogen concentration can be varied inside flame propagation limits, covering the whole spectrum of possible mixtures from lean mixtures to rich ones, including stoichiometric conditions. Since the combustion tube is designed for a nominal pressure of 100 bar, experiments can be performed at an initial pressure greater than the ambient one.
Prior to gas injection, the combustion tube, the injection lines and, eventually, the recirculation loop are set under primary vacuum ($p_\mathrm{v} \simeq 2$ mbar). First hydrogen and then synthetic air (21% O2 – 79% N2) are injected inside the tube from two separate tanks. Three pressure transmitters allow controlling the injection. If the recirculation pump is used (see Chapter 6.2) the recirculation loop is connected to the tube and filled with the mixture; otherwise, the tube is isolated by closing the isolation valves and the recirculation loop is by-passed even during the gas injection phase.
Air and hydrogen molar fractions can be computed through the following relations:

$$X_{\mathrm{H_2}} = \frac{p_{\mathrm{H_2}}}{p_\mathrm{tot}} \tag{6.1a}$$

$$X_\mathrm{air} = \frac{p_\mathrm{air}}{p_\mathrm{tot}} = 1 - X_{\mathrm{H_2}}\,. \tag{6.1b}$$

According to Dalton's law, hydrogen partial pressure is determined by subtracting the primary vacuum pressure p_v from the pressure measured after hydrogen injection $p_{\mathrm{H_2}}^\mathrm{inj}$:

$$p_{\mathrm{H_2}} = p_{\mathrm{H_2}}^\mathrm{inj} - p_\mathrm{v} \tag{6.2}$$

It is worth noticing that the residual gas contained in the tube is supposed to be composed only by air (any traces of water vapour remaining after the drying process are not considered in the evaluation).

A MATLAB® routine was coded to manage the filling process with the possibility to switch from a pressure transmitter to another, according to the pressure range (Figure 6.1).

6.2 Mixture homogenization process

Since hydrogen and air are injected at different times, a concentration gradient is formed along the tube axis. If the initial pressure of the test, p_{tot}, is between 0.4 and 2.8 bar abs, which corresponds to the recirculation pump operating pressure range, the mixture is forced to recirculate into the external loop (as described in Chapter 5) until a homogeneous concentration is obtained.
On the other hand, if $p_{\text{tot}} > 2.8$ bar, the recirculation loop is by-passed and the gas mixing process depends only by passive phenomena (residual inertia of the air jet and molecular diffusion).
The methods used to determine the period needed for gas homogenization is described in the following paragraphs.

6.2.1 Homogenization time with recirculation pump

Knowing the nominal pump flow rate, Q_{pump}, the time needed to recirculate the total volume of the mixture inside the tube is:

$$\Delta t_{\text{pump}} = \frac{V_{\text{tube}} + V_{\text{loop}}}{Q_{\text{pump}}}\,, \tag{6.3}$$

where $V_{\text{tube}} = 59$ L is the volume of the combustion tube (with 4 sections) and $V_{\text{loop}} \simeq 1$ L is the volume of the recirculation loop.
The flow rate of the BÜHLER P2.74 pump was determined at atmospheric pressure through the use of the SENSIDYNE GILIBRATOR2 flow calibration system. An average flow rate of 12.5 l/min (750 l/h) was measured when the pump was not connected to the recirculation loop (no pressure losses). Once the pump is connected to the loop, the flow rate decreases up to 9.2 l/min. According to flow curve given by the pump manufacturer, the flow rate has its maximum at the atmospheric pressure, while it drops as pressure is increased or decreased.
In first approximation, we assumed that mixture homogenization is achieved once the pump has circulated for at least three times the whole volume of mixture: $\Delta t_{\text{hom}} = 3\Delta t_{\text{pump}}$. At atmospheric pressure, $\Delta t_{\text{hom}} \simeq 20$ min.
Preliminary tests were performed to confirm the estimation of Δt_{hom}. In these tests helium was used instead of hydrogen. The evolution in time of the local concentration of helium was measured with thermal conductivity gauges located at both ends of the tube. The sampling volumes (see Figure 5.2) were replaced by two cavities (with a free volume of almost $2\,10^{-5}\,\text{m}^3 = 2\,\text{cl}$) housing a mini-katharometer for mixture characterization.
A katharometer is an electrically heated filament in a temperature-controlled cell [142]. As a sample of gas flows through the detector, its thermal conductance causes a decrease in the effective thermal resistance between the sensitive area of the sensor and the ambient. Since the output signal (the difference in voltage at the ends of the filament) depends on

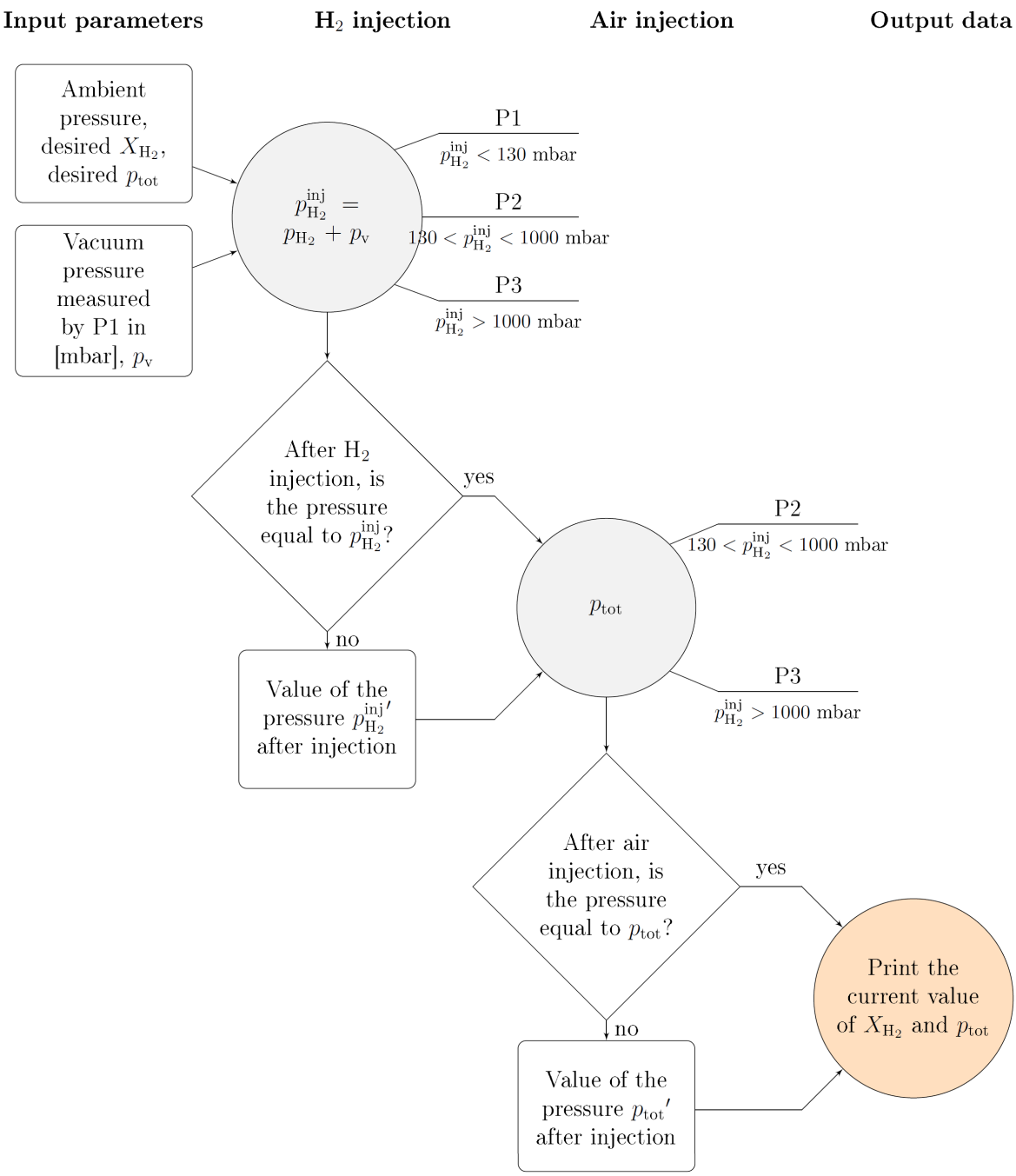

Figure 6.1: Flow chart summarizing a MATLAB® script for mixture calibration during gas injection.

the conductivity of the surrounding gas (i.e. on the helium/air percentage), these sensors allow us to determine the composition of the gas mixture.
In order to provide the worst configuration for the mixing process, the combustion tube was composed of 4 sections (for a total length of 5240 mm) and the obstacles blockage ratio was equal to 0.6.
In Figure 6.2, the homogenization process recorded by both katharometers is shown for two tests at different initial pressure: (a) $p_{\mathrm{tot}} = 1000$ mbar and (b) $p_{\mathrm{tot}} = 2000$ mbar.
While the mixture is circulating along the loop, the two katharometers record the local change of the mixture composition. The recirculation pump is kept working for a period of time equal to $3\Delta t_{\mathrm{pump}}$. In Figure 6.2b, we can clearly see the suction effect of the pump on the katharometer output signal (gas flow rate influences thermal conductivity gauges measurements) until the pump is switched off and the fluid is back at rest.
On the basis of these preliminary results, we have estimated that a period of time $\Delta t = 30$ minutes is long enough to guarantee the mixture homogenization at any value of p_{tot}, for which the recirculation pump can be used, and for any geometrical configuration of the tube.

6.2.2 Homogenization time without recirculation pump

If the initial pressure of the experiment is greater than 2.8 bar abs (maximum pump operating pressure), the recirculation pump cannot be used and the recirculation loop is isolated from the tube. Therefore, the homogenization process depends on:

1. jet induced turbulence, during and just after the injection phase;
2. the molecular diffusion of the binary gas, in a second phase when the gas is at rest.

Experimentally, the homogenization time was found to be in the order of 4 hours. The first phase, governed by turbulent convection, strongly contributes to mixture homogenization. By neglecting this contribution and considering only the molecular diffusion as driving force, the homogenization time would be much longer.
The evolution in time of the helium molar fraction along the tube can be estimated from the convection diffusion equation (1.2) [120]:

$$\rho_{\mathrm{He}} \frac{\partial X_{\mathrm{He}}}{\partial t} + \rho_{\mathrm{He}} \boldsymbol{u} \cdot (\nabla X_{\mathrm{He}}) = \rho_{\mathrm{He}} \nabla \cdot (D_{\mathrm{He}} \nabla X_{\mathrm{He}}) \tag{6.4}$$

where ρ_{He} is helium density, $\boldsymbol{u}$ is the velocity field and $D_{\mathrm{He}} = 2 \cdot 10^{-5}\,\mathrm{m}^2/\mathrm{s}$ is the molecular diffusivity. Two distinct physical phenomena are involved in equation (6.4): the turbulent convection and the molecular diffusion. If the fluid is at rest, $\boldsymbol{u} = 0$, gas mixing is promoted only by the molecular diffusion.
In first approximation, we can assume that the diffusion phenomenon is mono-dimensional: $X_{\mathrm{He}} = X_{\mathrm{He}}(x, t)$, where x is the tube longitudinal coordinate. As initial condition, a cosinusoidal distribution of helium along the tube is considered:

$$X_{\mathrm{He}}(x, t = 0) = X^0_{\mathrm{He}} \left(1 - a \cos \left(\pi \left(\frac{x}{L} + \frac{1}{2} \right) \right) \right) \tag{6.5}$$

where X^0_{He} is the average helium content inside the tube at $t = 0$, L is the total length of the tube ($L = l_{\mathrm{tot}}$) and the longitudinal coordinate varies in the range $-L/2 \leq x \leq L/2$.

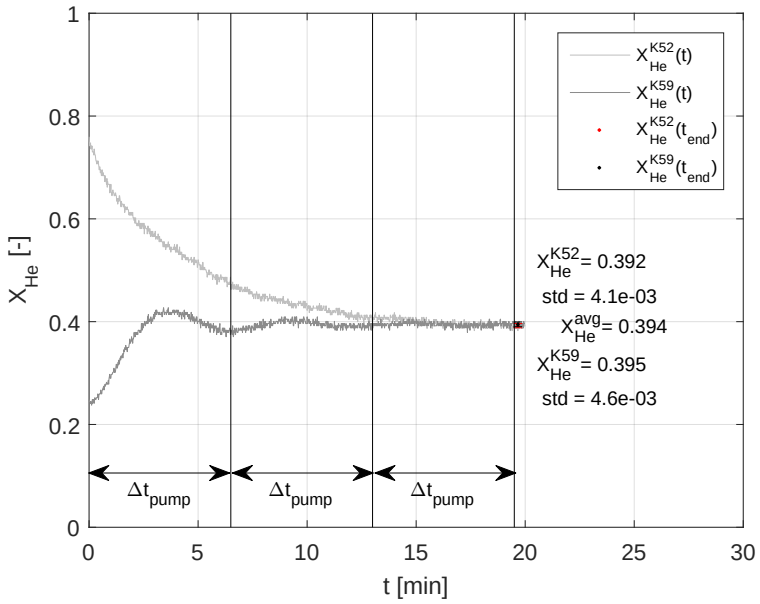

(a) $p_{\mathrm{tot}} = 1000$ mbar.

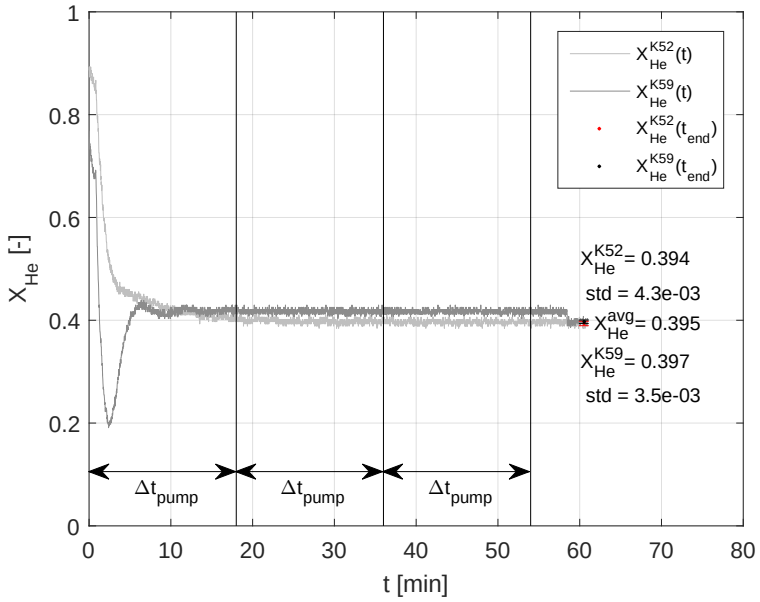

(b) $p_{\mathrm{tot}} = 2000$ mbar.

Figure 6.2: Homogenization process recorded by the two katharometers, K52 and K59. Helium molar fraction for the two experiments was equal to 0.4.

The coefficient a was determined in order to have an initial distribution similar to the one measured experimentally. With reference to Figure 6.2a, where

$$\begin{cases} X^0_{\mathrm{He}} = 0.4 \\ |X^{\mathrm{K59}}_{\mathrm{He}}(t=0) - X^{\mathrm{K52}}_{\mathrm{He}}(t=0)| \simeq 0.4 \end{cases}$$

the coefficient a was set equal to 0.5. The initial profile thus obtained is presented in Figure 6.3a.
The method of separation of variables is then used to obtain the analytical solution of equation (6.4) :

$$X_{\mathrm{He}}(x,t) = X^0_{\mathrm{He}} \left(1 - a\cos\left(\pi\left(\frac{x}{L} + \frac{1}{2}\right)\right)\exp\left(-\left(\frac{\pi}{L}\right)^2 D_{\mathrm{He}} t\right)\right) \tag{6.6}$$

The result, presented in Figure 6.3b, gives an estimation of the homogenization time from pure molecular diffusion. By denoting with τ_{hom} the decay constant:

$$\tau_{\mathrm{hom}} = \frac{1}{\left(\frac{\pi}{L}\right)^2 D_{\mathrm{He}}}$$

we can assume that the mixture is homogeneous when $t = 3\tau$. From this condition, we have $\Delta t^{\mathrm{diffusion}}_{\mathrm{hom}} = 116$ hours, or 4.8 days. Therefore, by neglecting the contribution of the turbulent convection after gas injection, the homogenization process would be much slower than the one observed experimentally.

6.3 Characterization of the flammable mixture

Once the binary gas is injected inside the tube, the uncertainty on the mixture composition depends on the accuracy of the pressure transmitters controlling the injection phase.
In order to guarantee a high experimental repeatability, it is necessary to calibrate accurately the binary mixture. Moreover, since several combustion phenomena present an abrupt change for particular mixture composition, we would like to discriminate the composition of the binary mixture within a 0.5% span. For example, in obstacle laden tubes, 11 %vol hydrogen/air flames are supposed to accelerate up to the Chapman-Jouguet deflagration velocity; on the other hand, for leaner mixtures with $9 - 10\%$ hydrogen, the flame can be quenched.

6.3.1 Accuracy of the pressure measurements

According to equations (6.1) and (6.2), hydrogen molar fraction is computed on the basis of the hydrogen partial pressure and the mixture total pressure. Therefore, any errors in these measurements during the injection process strongly affect the mixture composition. Pressure uncertainties can be estimated considering the sensor accuracy and the calibration error. The accuracy of pressure transmitters is shown in Table 5.1. The effect of the propagation of uncertainties, i.e. the influence of pressure measurements errors in the mixture composition, has been evaluated according to the standards defined in [70]. The

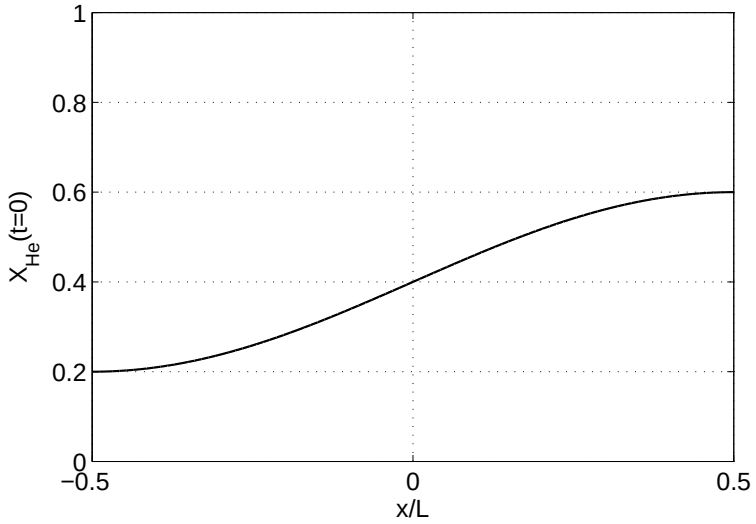

(a) Helium initial distribution from equation (6.5) with $X^0_{\mathrm{He}} = 0.4$.

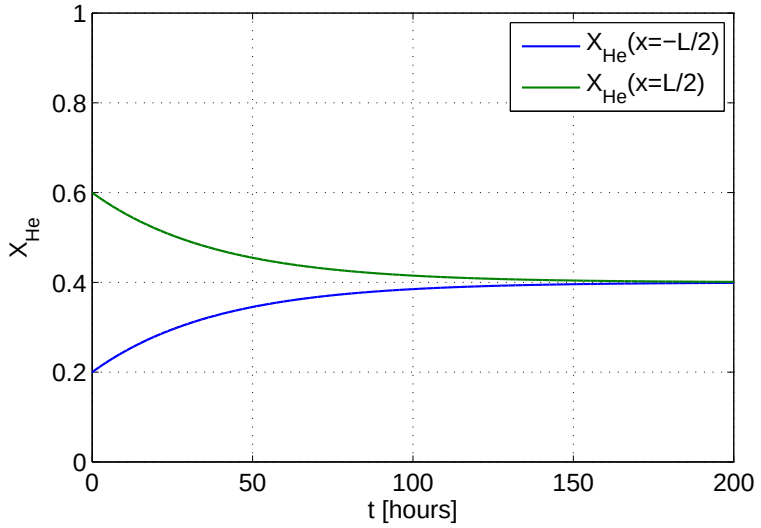

(b) Evolution in time of helium molar fraction at the two extremities of the tube (equation (6.6)).

Figure 6.3: Homogenization process governed only by molecular diffusion.

combined uncertainty u_c can be computed with the following expression[1]:

$$u_c(y) = \sqrt{\sum_{i=1}^{n} \left[\frac{\partial f}{\partial x_i}\right]^2 \cdot u^2(x_i)}\,, \tag{6.7}$$

where $y = f(x_1, x_2, \cdots, x_n)$ and $u(x_i)$ is the uncertainty of the independent variable x_i. In our case, y is the molar fraction given by the MATLAB® routine after the injection: $X_{\mathrm{H_2}}^{\mathrm{inj}} = \frac{p_{\mathrm{H_2}}^{\mathrm{inj}} - p_{\mathrm{v}}}{p_{\mathrm{tot}}}$, while the independent variables are the pressure measurements, p_{v}, $p_{\mathrm{H_2}}^{\mathrm{inj}}$ and p_{tot}. With these substitutions, we get:

$$u_c^{\mathrm{p}}(X_{\mathrm{H_2}}^{\mathrm{inj}}) = \frac{1}{p_{\mathrm{tot}}}\sqrt{u^2(p_{\mathrm{H_2}}^{\mathrm{inj}}) + u^2(p_{\mathrm{v}}) + (X_{\mathrm{H_2}}^{\mathrm{inj}} \cdot u(p_{\mathrm{tot}}))^2}\,, \tag{6.8}$$

where the superscript p in $u_c^{\mathrm{p}}(X_{\mathrm{H_2}}^{\mathrm{inj}})$ stands for pressure measurements induced error.
From equation (6.8), we can infer that the combined uncertainty depends on $X_{\mathrm{H_2}}^{\mathrm{inj}}$ and p_{tot} as well as on the accuracy of the pressure transmitter(s) chosen to measure p_{v}, $p_{\mathrm{H_2}}^{\mathrm{inj}}$ and p_{tot}. For example, if we use the CERAVAC CTR90 (P1) to measure the vacuum pressure, while the KELLER PA25HTT (P2) for helium and air injections, we get:

$$\begin{aligned} u_c^{\mathrm{p}}(X_{\mathrm{H_2}}^{\mathrm{inj}}) &= \frac{1}{p_{\mathrm{tot}}}\sqrt{u_{\mathrm{P2}}^2 + u_{\mathrm{P1}}^2 + (X_{\mathrm{He}}^{\mathrm{inj}} \cdot u_{\mathrm{P2}})^2} \\ &= \frac{1}{p_{\mathrm{tot}}[\mathrm{bar}]}\sqrt{2.7 \cdot 10^{-5}(1 - (X_{\mathrm{H_2}}^{\mathrm{inj}})^2) + 4 \cdot 10^{-6} p_{\mathrm{v}}^2[\mathrm{bar}]}\,. \end{aligned} \tag{6.9}$$

In Table 6.1 the results obtained from equation (6.9) for different hydrogen molar fractions are listed. Here we have supposed that $p_{\mathrm{v}} = 3 \cdot 10^{-3}$ bar and $p_{\mathrm{tot}} = 1$ bar.

Table 6.1: Uncertainty $u_c^{\mathrm{p}}(X_{\mathrm{H_2}})$ on the mixture composition as a function of $X_{\mathrm{H_2}}^{\mathrm{inj}}$ (equation (6.9)). $p_{\mathrm{v}} = 3 \cdot 10^{-3}$ bar and $p_{\mathrm{tot}} = 1$ bar

$X_{\mathrm{H_2}}^{\mathrm{inj}}$	$u_c^{\mathrm{p}}(X_{\mathrm{H_2}}^{\mathrm{inj}})$
0.1	$5.22 \cdot 10^{-3}$
0.2	$5.30 \cdot 10^{-3}$
0.3	$5.42 \cdot 10^{-3}$
0.4	$5.60 \cdot 10^{-3}$
0.5	$5.81 \cdot 10^{-3}$
0.6	$6.06 \cdot 10^{-3}$
0.7	$6.34 \cdot 10^{-3}$
0.8	$6.65 \cdot 10^{-3}$

From the combined uncertainty, it is possible to compute the expanded uncertainty, u_e^{p}, such as:

$$u_e^{\mathrm{p}}(X_{\mathrm{H_2}}^{\mathrm{inj}}) = k\, u_c^{\mathrm{p}}(X_{\mathrm{H_2}}^{\mathrm{inj}})\,, \tag{6.10}$$

[1] Equation (6.7) is valid only if $x_1, x_2, \cdots, x_n$ are independent variables, otherwise the correlation term (covariance) cannot be neglected.

where k depends on the desired confidence level. Since $u_c^{\mathrm{p}}(X_{\mathrm{H_2}}^{\mathrm{inj}})$ is a function of three independent variables (independent pressure observations), the central limit theorem allows us to adopt a normal distribution for the variance. Therefore, for a confidence level of 95.45%, $k = 2$. The confidence interval thus obtained can be expressed as

$$X_{\mathrm{H_2}}^{\mathrm{inj}} - u_e^{\mathrm{p}}(X_{\mathrm{H_2}}^{\mathrm{inj}}) \leq X_{\mathrm{H_2}} \leq X_{\mathrm{H_2}}^{\mathrm{inj}} + u_e^{\mathrm{p}}(X_{\mathrm{H_2}}^{\mathrm{inj}})\,.$$

As a result, the uncertainty on the mixture composition is quite important and it is not compatible with our requirements.
Moreover, in the present discussion we have neglected the following sources of errors:

- instruments digit precision;
- the variation of the ambient pressure during the day (note that we have taken the value of the atmospheric pressure provided by the weather station in CEA-Saclay as the reference for the ambient pressure);
- the dead volume associated to the recirculation pump, between the pump isolation valves.

The latter is due to the fact that we do not take into account the volume of air between the two isolation valves of the recirculation pump to compute the composition of the gas mixture. This dead volume has been estimated to be $\simeq 10$ ml. By neglecting the dead volume, we introduce an error in the order of $V_{\mathrm{pump}}/(V_{\mathrm{tube}} + V_{\mathrm{loop}}) \simeq 2 \cdot 10^{-4}$ (supposing that the air contained in V_{pump} is at the same pressure of the mixture in the tube).
To conclude this paragraph, we need to mention the human error associated to valves operation during the injection phase (valves are manually operated on the basis of pressure values displayed in the monitor). This is the reason why, in the MATLAB® script for injection process (see Figure 6.1), an optional adjusting phase was added.

6.3.2 Verification of the mixture composition

To prove the reliability of our procedure for gas injection, a series of preliminary tests were performed replacing hydrogen with helium, in order to measure the mixture content with thermal conductivity gauges, as explained in Chapter 6.2. Helium concentration measured at the end of the homogenization phase is then compared to the value obtained from the partial pressure method.

Uncertainty in katharometers measurements

Katharometers measurements of helium concentration in air are affected by a bias that depends mainly on two causes: the standard uncertainty associated with the arithmetic mean of the readings ($\sigma(X_{\mathrm{He}}^{\mathrm{K}i})$, where i is the katharometer number: $i = 52, 59$), and the calibration error.
The calibration process has been performed in CALIGA facility. This facility is equipped with BROOKS™ flow-meters, that can be used to generate a calibration mixture. The uncertainty related to the full scale error of these instruments affects the composition of the calibration mixture. In the range $0.1 < X_{\mathrm{He}} < 0.8$, $u_{\mathrm{BROOKS}}(X_{\mathrm{He}})/X_{\mathrm{He}} = 1.40 \cdot 10^{-2}$.

The uncertainty associated with the polynomial regression, $u_{\mathrm{pr}}(X_{\mathrm{He}})$, is equal to $3.00 \cdot 10^{-4}$ for both sensors.
Eventually, the total contribution can be computed as the sum of the estimated variances:

$$u_c^{\mathrm{K}}(X_{\mathrm{He}}^{\mathrm{K}i}) = \sqrt{(\sigma(X_{\mathrm{He}}^{\mathrm{K}i}))^2 + (u_{\mathrm{BROOKS}}(X_{\mathrm{He}}^{\mathrm{K}i}))^2 + (u_{\mathrm{pr}}(X_{\mathrm{He}}^{\mathrm{K}i}))^2}\,. \tag{6.11}$$

Again, we can define a confidence interval around the arithmetic mean of katharometer measurements $X_{\mathrm{He}}^{\mathrm{K}\#}$ in which we have the 95% chance of finding the measurand X_{He}: $[X_{\mathrm{He}}^{\mathrm{K}i} - u_e^{\mathrm{K}}(X_{\mathrm{He}}^{\mathrm{K}i}); X_{\mathrm{He}}^{\mathrm{K}i} + u_e^{\mathrm{K}}(X_{\mathrm{He}}^{\mathrm{K}i})]$. $u_e^{\mathrm{K}}(X_{\mathrm{He}}^{\mathrm{K}i})$ is determined by multiplying $u_c^{\mathrm{K}}(X_{\mathrm{He}}^{\mathrm{K}i})$ by a proper coverage factor k, that for a normal distribution is equal to 2.

Comparison of the results

Since $X_{\mathrm{He}}^{\mathrm{K}i}$ and $X_{\mathrm{He}}^{\mathrm{inj}}$ are both biased, in order to compare these quantities, we need to take into account the related uncertainties. A graphic representation of this comparison is shown in Figure 6.4.

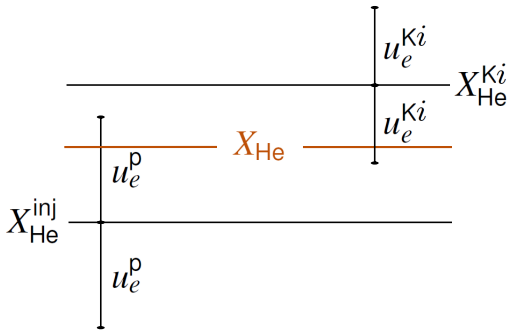

Figure 6.4: Comparison between $X_{\mathrm{He}}^{\mathrm{inj}}$ and $X_{\mathrm{He}}^{\mathrm{K}i}$.

The results of the two measurements are compatible if:

$$u(\Delta) > \Delta\,, \tag{6.12}$$

where Δ is the absolute value of the difference between the two values $X_{\mathrm{He}}^{\mathrm{K}i}$ and $X_{\mathrm{He}}^{\mathrm{inj}}$, while $u(\Delta)$ is the associated uncertainty. Since the two measurement techniques are independent and the coverage factor is the same, $u(\Delta)$ can be computed as follows[2]:

$$u(\Delta) = \sqrt{(u_e^{\mathrm{p}}(X_{\mathrm{He}}^{\mathrm{inj}}))^2 + (u_e^{\mathrm{K}}(X_{\mathrm{He}}^{\mathrm{K}i}))^2}\,. \tag{6.13}$$

Even if relation (6.12) is satisfied, there could still be a degree of inhomogeneity inside the tube: for example, gas may stagnate in some points along the circuit. To compare the results of the two techniques (partial pressure measurements and katharometers ones), it

[2]The same method can be used to decide if the mixture is homogeneous or not. In this case the quantities that we need to compare are the two katharometer measurements $X_{\mathrm{He}}^{\mathrm{K}52}$ and $X_{\mathrm{He}}^{\mathrm{K}59}$. Defining $\Delta' = X_{\mathrm{He}}^{\mathrm{K}52} - X_{\mathrm{He}}^{\mathrm{K}59}$, we can state that a gaseous mixture is homogeneous if

$$u(\Delta') > \Delta'\,.$$

is, therefore, more convenient to compute the average value of the readings of the two katharometers:

$$X_{\mathrm{He}}^{\mathrm{avg}} = \frac{X_{\mathrm{He}}^{\mathrm{K52}} + X_{\mathrm{He}}^{\mathrm{K59}}}{2} \tag{6.14a}$$

$$u_c^{\mathrm{K}}(X_{\mathrm{He}}^{\mathrm{avg}}) = \frac{1}{2}\sqrt{(u_c^{\mathrm{K52}})^2 + (u_c^{\mathrm{K59}})^2}\,. \tag{6.14b}$$

Nine tests were performed for different helium concentrations ($X_{\mathrm{He}} = 0.01$, 0.2, 0.4, 0.5). The initial pressure was varied in the range $0.6 - 2$ bar. The test matrix is presented in Table 6.2.

Table 6.2: Test matrix.

Test #	$X_{\mathrm{He}}^{\mathrm{inj}}$	p_{tot}
1	0.012	1001.1
2	0.202	999.5
3	0.204	1000.7
4	0.202	999.5
5	0.403	600.4
6	0.400	1003.2
7	0.402	2008.9
8	0.501	1000.7
9	0.502	1002.6

The uncertainty in the mixture composition obtained from pressure measurements was computed according to equations (6.8) and (6.9). On the other hand, the uncertainty associated to the katharometers measurements was computed with equation (6.11). Table 6.3 summarizes the results for the nine test cases. As shown in the last column of Table 6.3, criterion (6.12) is satisfied for all the test cases.

Discussion

To summarize, in the present chapter we have compared the measurements of the mixture composition taken with two different and independent techniques in order to prove the reliability of our procedure for gas injection. The obtained results are in good agreement and both measurements are proven to be comparable.
Nevertheless, according to fifth column of Table 6.3, once injected, the mixture is known in a interval of the order of $\pm 2 \cdot 10^{-2}$ with a 95% level of confidence. The accuracy thus achieved is not adequate for our purposes. As above mentioned, we would like to know the composition of the mixture within an interval of $5 \cdot 10^{-3}$ in order to further discriminate, during flame acceleration experiments, those mixtures susceptible to accelerate from those that are quenched. For this reason, a gas-chromatographic analysis of mixture samples is foreseen to better characterize the initial condition of flame acceleration experiments.

Table 6.3: Comparison between Helium molar fraction measurements: $X_{\mathrm{He}}^{\mathrm{inj}}$ and $X_{\mathrm{He}}^{\mathrm{avg}}$

Test #	$X_{\mathrm{He}}^{\mathrm{inj}}$	$X_{\mathrm{He}}^{\mathrm{avg}}$	Δ	$u_e^{\mathrm{p}}(X_{\mathrm{He}}^{\mathrm{inj}})$	$u_e^{\mathrm{K}}(X_{\mathrm{He}}^{\mathrm{avg}})$	$u(\Delta)$	$u(\Delta) - \Delta$
1	0.012	0.009	$3.00 \cdot 10^{-3}$	$4.00 \cdot 10^{-3}$	$6.27 \cdot 10^{-3}$	$7.44 \cdot 10^{-3}$	$4.44 \cdot 10^{-3}$
2	0.202	0.206	$4.00 \cdot 10^{-3}$	$1.06 \cdot 10^{-2}$	$1.12 \cdot 10^{-2}$	$1.54 \cdot 10^{-2}$	$1.14 \cdot 10^{-2}$
3	0.204	0.202	$2.00 \cdot 10^{-3}$	$1.06 \cdot 10^{-2}$	$1.22 \cdot 10^{-2}$	$1.62 \cdot 10^{-2}$	$1.42 \cdot 10^{-2}$
4	0.202	0.199	$3.00 \cdot 10^{-3}$	$1.06 \cdot 10^{-2}$	$1.13 \cdot 10^{-2}$	$1.55 \cdot 10^{-2}$	$1.25 \cdot 10^{-2}$
5	0.403	0.391	$1.20 \cdot 10^{-2}$	$1.87 \cdot 10^{-2}$	$1.73 \cdot 10^{-2}$	$2.55 \cdot 10^{-2}$	$1.35 \cdot 10^{-2}$
6	0.400	0.394	$6.00 \cdot 10^{-3}$	$1.12 \cdot 10^{-2}$	$1.76 \cdot 10^{-2}$	$2.09 \cdot 10^{-2}$	$1.49 \cdot 10^{-2}$
7	0.402	0.395	$7.00 \cdot 10^{-3}$	$5.58 \cdot 10^{-3}$	$1.79 \cdot 10^{-2}$	$1.88 \cdot 10^{-2}$	$1.18 \cdot 10^{-2}$
8	0.501	0.492	$9.00 \cdot 10^{-3}$	$1.16 \cdot 10^{-2}$	$2.18 \cdot 10^{-2}$	$2.47 \cdot 10^{-2}$	$1.57 \cdot 10^{-2}$
9	0.502	0.495	$7.00 \cdot 10^{-3}$	$1.16 \cdot 10^{-2}$	$2.21 \cdot 10^{-2}$	$2.50 \cdot 10^{-2}$	$1.80 \cdot 10^{-2}$

6.4 Mixture gas-chromatographic analysis

At the end of the homogenization process, the flammable mixture is sampled and analyzed via gas chromatography. The analysis are performed in a Agilent 490 μGC equipped with a thermal conductivity detector (TCD). Argon is used as carrier gas. This allows detecting helium, oxygen, nitrogen, hydrogen and methane in a single GC module.
To handle the gas samples, two sampling volume were designed. Each volume features a stainless steel cylinder with a leak tight piston activated by a lead screw (see Figure 6.5). The cylinders are also equipped with an isolation valve in order to connect and disconnect them from the recirculation loop (as shown in Figure 5.2). The moving piston and the pressure gauge installed on the gas chromatograph inlet (as shown in Figure 6.5) allow controlling the GC inlet pressure. Gas analysis are then performed at constant pressure, ensuring a linear response of the instrument.

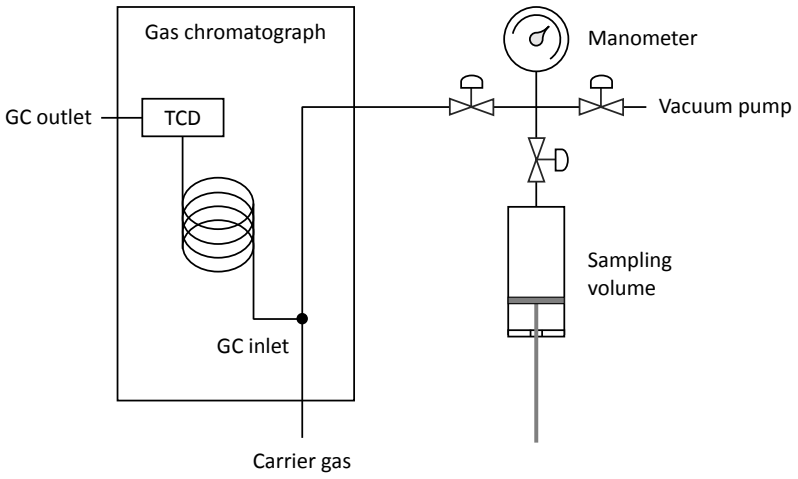

Figure 6.5: Schematic view of the system for gas chromatography.

Pre-calibrated mixtures are used to calibrate the sensor output. The relative uncertainty on the chemical species I in the calibrated mixtures depends on its molar fraction X_{I}, as

follows:

- if $X_{\mathrm{I}} > 25\%$, $u_e(X_{\mathrm{I}})/X_{\mathrm{I}} = 0.1\%\mathrm{rel}$;
- if $X_{\mathrm{I}} \leq 25\%$, $u_e(X_{\mathrm{I}})/X_{\mathrm{I}} = 0.5\%\mathrm{rel}$.

The extended uncertainty $u_e(X_{\mathrm{I}})$ is given with a coverage factor $k = 2$.
The result of the gas chromatographic analysis is usually given as the average value over 10 measurements of the same sample ($X_{\mathrm{I}}^{\mathrm{avg}}$). The related uncertainty is given by the square root of quadratic sum of the standard deviation of these measurements and the calibration error, as:

$$u_e^{\mathrm{GC}}(X_{\mathrm{I}}) = 2\sqrt{(\sigma(X_{\mathrm{I}}^{\mathrm{avg}}))^2 + \left(\frac{u_e(X_{\mathrm{I}})}{2}\right)^2}. \tag{6.15}$$

As an example, the results obtained from the analysis of a H_2/N_2 binary gas with 15% vol hydrogen are shown in Table 6.4.

Table 6.4: Gas chromatographic analysis of a H_2/N_2 binary gas with 15% vol hydrogen. Values are given in %vol.

$X_{\mathrm{H_2}}^{\mathrm{avg}}$	$\sigma(X_{\mathrm{H_2}}^{\mathrm{avg}})$	$u_e(X_{\mathrm{H_2}})/X_{\mathrm{H_2}}$	$u_e^{\mathrm{GC}}(X_{\mathrm{H_2}})$	$u_e^{\mathrm{GC}}(X_{\mathrm{H_2}})/X_{\mathrm{H_2}}$
15.033	0.013	0.500	0.079	0.527%

As a result, the requirements defined in Chapter 6.3 are matched: in the range $0.10 < X_{\mathrm{H_2}} < 0.15$ the absolute uncertainty on the mixture composition is lower than 0.001. The initial composition of the flammable mixture (before ignition) is given by the gas chromatographic analysis. The fundamental properties of flammable mixture, such as the laminar flame speed or the laminar flame thickness, can be computed according to this value.

6.5 Conclusions

In light of these results, the flammable mixture is prepared according to the injection procedures summarized in the flow chart 6.1. It allows achieving an hydrogen concentration in the mixture within a limited range. After gas injection hydrogen and air are not homogeneously distributed along the tube. The homogeneous condition is reached after $\simeq 30$ min in case of active mixing or after 4 hours for passive mixing.
Once the homogenization process is fulfilled, two samples of gas are taken at the tube extremities to be chemically analyzed. Gas chromatographic analysis are performed to properly set the initial and boundary conditions of the experiment.

Chapter 7

Combustion diagnostics

Once the mixture is ignited, pressure evolution and flame propagation in time are monitored by a series of sensors distributed along the combustion tube (see Figure 5.3). Combustion diagnostics features:

1. dynamic pressure sensors;

2. shock sensors;

3. photomultiplier tubes.

Output signals are recorded via a National Instruments^{TM} high performance data acquisition unit (NI PXIe-1078). Five acquisition cards PXI-5105 with 8 channels (analog input, 60 MHz maximum acquisition frequency, 12 bit a/d conversion) are used. Cards synchronization and triggering are managed via LabVIEW environment. The ignition spark is used as reference signal to trigger the acquisition cards.

7.1 Pressure sensors

Up to ten dynamic pressure sensors can be installed in the upper part the combustion tube wall. Three types of Kistler piezo-electric sensors were tested ($0 - 250$ bar pressure range): 601A, 6001 and 7001. Types 601A and 6001 feature a high natural frequency (FN= 150 kHz); the 6001 present a better resistance to high temperatures up to 350 °C. The 7001 has a lower natural frequency (FN= 70 kHz), but at the same time its sensitivity is higher (the diameter of the sensitive area of the 7001 sensor is 9.5 mm, while the diameter of 601A and 6001types is 5.55 mm).
A flush mounting nut is used to plug the 601A and 6001 types on the facility, while 7001 sensors are recessed mounted. In the recessed mounting position, the sensor is less sensitive to thermal radiation. On the other hand, the volume of gas close to the sensor can act as a resonance cavity, affecting the sensor main output signal. To reduce thermal effects on the Kistler sensors that are flush mounted (601A and 6001), an aluminum thin foil was used to shield the sensitive area (the effectiveness of this shielding technique was proven at ICARE laboratory of the CNRS-Orléans).
Kistler 5018 charge amplifier units are used to convert the charge signal from the sensors into an output voltage.

7.2 Shock sensors

Chimiemetal piezo-electic sensors allow the detection of a shock wave in the unburnt gas. Thanks to their fast response (3 ns pulse rise time and 2.5 MHz natural frequency), they are usually employed for time-of-flight measurements of shock waves. Moreover, they can be used to extrapolate the velocity of the pressure wave ahead of the flame in a more accurate way because of their small sensitive area (2 mm diameter).
Shock sensors are made of a ceramic piezo-electric brass-coated polarized crystal. These sensors are not calibrated and strongly affected by the radiation emitted by the burnt gas. As a result, once the flame passes by the sensor, the piezo-electric crystal responds with a strong current pulse. Their use is therefore restricted to the detection of the shock waves ahead the flame, in the unburnt gas.

7.3 Photomultiplier tubes

15 Hamamatsu R11568 photomultiplier tubes (PMT) can be installed along combustion tube wall in order to measure the axial velocity of the flame front propagating along the tube. These detectors collect the UV light emitted by $OH^\bullet$ radicals located at the reaction front within a very narrow solid angle. As the flame tip passes through the PMT solid angle, a negative voltage is recorded. This signal allows us to extrapolate the time-of-arrival of the flame tip, monitoring flame propagation along the tube axis, as further detailed in Chapter 8.2.1.
Hydroxyl radicals can be considered as a burnt gases marker: they are formed following the dissociation of H_2O_2 molecules as the combustion temperature increases, as shown in Figure 7.1. These radicals are then chemi-excited via the reaction [58]:

$$H + OH + OH = H_2O + OH^\bullet$$

The emission band of $OH^\bullet$ ($306 < \lambda_{OH^\bullet} < 310$ nm) presents a strong head at 306.4 nm, that corresponds to de-exitation process from the $A^2\Sigma$ state to the ground state $X^2\Pi$. Two other strong heads appear at 306.7 and 309 nm. Photons emitted via chemiluminescence are collected by a photomultiplier tube that amplifies the signal before being recorded through an acquisition card.
In the present chapter the operation principle of a PMT is described. The system housing the detector and the optimization of the optical path are also discussed.

7.3.1 Photomultiplier tube description

Hamamatsu R11568 PMT guarantee an ultra-fast response (2.2 ns pulse rise time) and, at the same time, an extremely high sensitivity [72]. Behind the frontal grid that limits the effective sensitive area of the PMT, we can find the photo-cathode, where the incident light photons are converted into low-energy electrons.
Once photoelectrons are produced, they are amplified by a cascade of secondary emissions at the dynodes. An external voltage source must be connected to the PMT in order to provide the proper voltage gradient between each dynode. PMT gain and thus the output signal amplitude are directly proportional to the supply voltage.

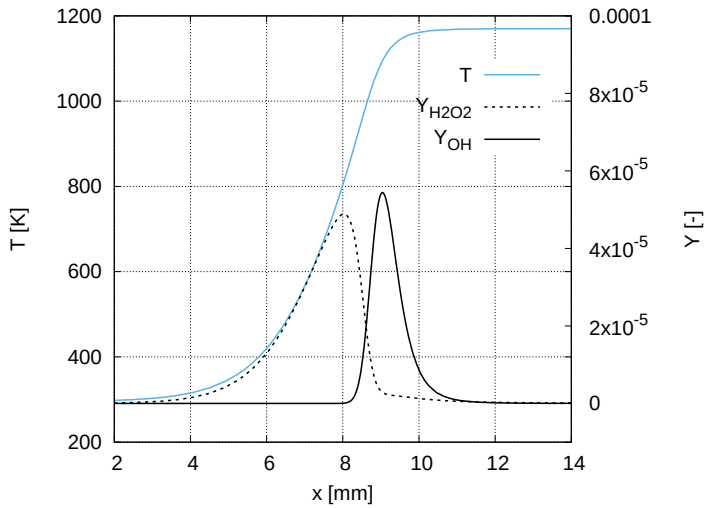

Figure 7.1: Zoom on the temperature and species profiles across the flame thickness for a 11%vol hydrogen in air mixture. 1D flame propagation simulation performed with PREMIX code.

Even when the tube is operated in a completely dark state, a small amount of current (anode dark current) persists in the photomultiplier tube. The resulting noise strongly influences the lower limit for light detection (see Chapter 8.2.1).
As schematically shown in Figure 7.2, the photomultiplier tube is inserted in a carter connected to the combustion tube via a stainless steel adapter. This adapter is designed to host the quartz window and the optical arrangement for light path optimization (see Chapter 7.3.2) and at the same time to hermetically seal the combustion tube.
This assembly ensures a stable position of the PMT during the flame acceleration experiments, and it also protects the PMT from the vessel inner atmosphere as well as from the outer environment. O-rings are used to seal carter connections in order to avoid any incoming light from the outside.

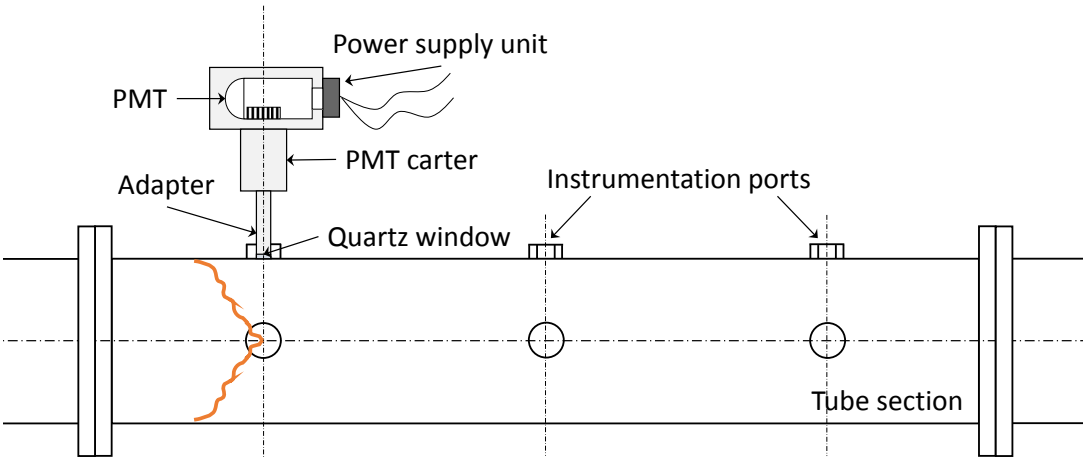

Figure 7.2: Traversal view of a tube section with PMT setup.

7.3.2 PMT optical path

As already mentioned, the PMT is normally kept at dark. In this condition, if no light comes from the acceleration tube, only the anode dark current is recorded.
When a combustion reaction takes place inside the tube, a quasi-axis-symmetrical reaction front is formed. While propagating along the axis, the flame crosses PMTs optical axes (see Figure 7.2). The light emitted by $OH^{\bullet}$ radicals is then collected by the PMT and a strong current pulse is sent to the anode.
The photons collected by the PMT are those which are emitted inside the solid angle facing PMT sensitive area. In order to focus the measurement right on the tube axis, an optical path was designed with the aim of (1) minimizing rays incident angle and (2) exploiting the whole sensitive area of the PMT. The optical system thus obtained is shown in Figure 7.3. Starting from the quartz window of the adapter we can find two diaphragms with a $\Phi = 3$ mm central hole, separated by a $\Phi 9 \times 66$ mm annular spacer, two divergent lenses and a UV filter (EDMUND Optics bandpass filter on 307.1 nm with a 10 nm FWHM). A the end of the path there is the PMT sensitive area (8×24 mm).

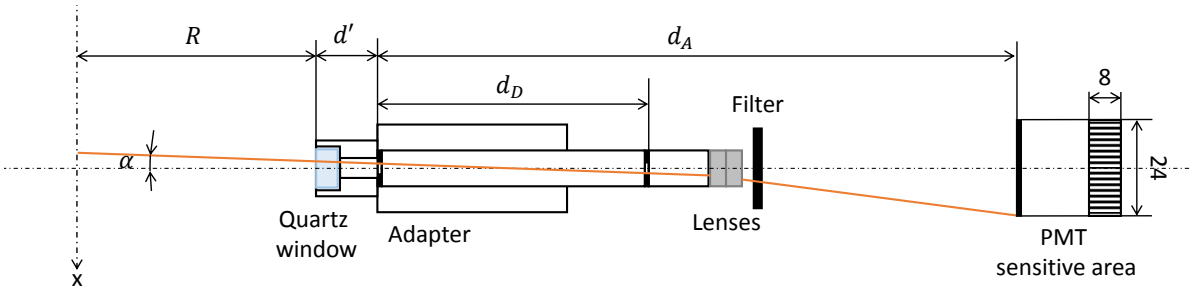

Figure 7.3: Optical path of a ray of light. α, maximum incidence angle without any reflections on metal surfaces; $R = 60$ mm, combustion tube internal radius; $d_D = 70$ mm, distance between the external surfaces of the diaphragms; $d' = 16$ mm, distance between the quartz window surface and the first diaphragm; $d_A = 160$ mm, distance from the first diaphragm and the PMT sensitive area.

Figure 7.3 also presents the maximum incident angle α for an UV ray to pass through the optical path without being reflected before targeting the PMT sensitive area. The amplitude of this angle is limited by diaphragms inner diameter, Φ_D, and depends also on the distance between them, d_D, as follows:

$$\alpha = \arctan\left(\frac{\Phi_D}{d_D}\right) = \arctan\left(\frac{3}{70}\right) = 2.45^{\circ} \tag{7.1}$$

This angle introduces a bias in the position of the flame front: photons emitted by $OH^{\bullet}$ radicals with an angle α with respect to the optical path axis are detected before the flame intersects the optical path axis. According to Figure 7.3, this bias can be computed throughout the following expression:

$$\delta = \frac{\Phi_D}{2} + \left[(R + d')\frac{\Phi_D}{d_D}\right] = 4.76\,\text{mm}. \tag{7.2}$$

Equation (7.2) gives the value of the error made when the PMT sensitive area is placed horizontally, i.e. when PMT axis is parallel to the combustion tube axis. When the PMT

is in vertical position (the larger side of the sensitive area is placed vertically), the error introduced on the flame position decreases, as shown in Figure 7.4.

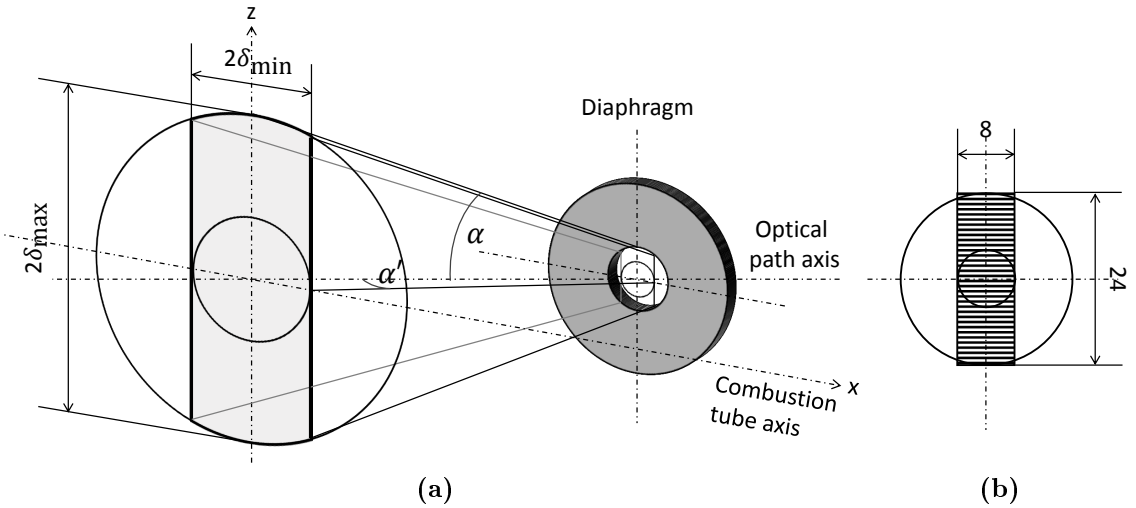

Figure 7.4: Evaluation of the bias in the position of the flame on the combustion tube axis. (a) Projection of PMT sensitive area on the vertical plane passing through the combustion tube axis. (b) Projection of the diaphragm inner diameter on PMT sensitive area due to the diverging effect of the lenses.

Figure 7.4a represents the projection of the PMT sensitive area on combustion tube axis (gray surface). It takes into account the shadow effect of the diaphragms and the divergent effect of the lenses. If we focus our attention to the right hand picture, two circles have been sketched on the sensitive area: the first one has a diameter of 24 mm while the second one has 8 mm diameter. The largest one corresponds to the projection of the diaphragm inner diameter on the sensitive area due to the divergent effect of the lenses: rays of light coming from the tube can reach only the surface enclosed inside this circle. Once this circle is projected on the tube axis with an angle α, the $2\delta_{\max}$ diameter circle is generated. $\delta_{\max}$ is given equation (7.2) and it corresponds to the error in the position of the flame tip on the z-direction in picture 7.4b.
The error along x-direction is, on the other hand, quite smaller. It can be computed by projecting the $\Phi = 8$ mm circle, that delimits the smaller side of the PMT sensitive area, on the tube axis. As before, the incidence angle α' can be used to compute $\delta_{\min}$. Since the $\Phi = 8$ mm circle corresponds to the case with a diaphragm of $\Phi'_D = 1$ mm, α' can be evaluated as follows:

$$\alpha' = \arctan\left(\frac{\Phi'_D}{d_D}\right) \arctan\left(\frac{1}{70}\right) = 0.82^\circ\,. \tag{7.3}$$

Substituting the value of α' in equation (7.2), we get $\delta_{\min} = 2.59$ mm.
Therefore, the smaller is the diaphragm inner diameter, the more accurate the PMT measurement. Nevertheless, the intensity of the beam of light strongly decreases. The influence of the diaphragm inner diameter on the PMT signal amplitude is presented more in details in Chapter 8.2.1.
In the more conservative hypothesis, the maximum error on flame tip position would occur if the incident beam was reflected by metal surfaces along the optical path. In this

case, the maximum incidence angle would be almost 10 times larger then α. Nevertheless, since brilliant steel surfaces reflect less than 40% of the incident light at 300 nm [67], the contribution given by photons emitted with an angle of incidence greater than α can be neglected.

Chapter 8

Methods for results analysis

In this chapter the techniques used to analyze experimental results are discussed. We first present the numerical methods for the determination of thermodynamic equilibrium properties and the combustion fundamental properties. Then, the procedure used to post-process combustion diagnostics output signals is described.

8.1 Numerical methods for the evaluation of combustion fundamental properties

In this research work, flame acceleration process in premixed hydrogen/air mixtures is experimentally studied. The bibliographic issues presented in Chapters 2.1.1, 2.1.3 and 3 pointed out a series of combustion properties required to analyze any premixed combustion result. The main goal of this chapter is to describe the method used to compute these properties.
Those parameters that we consider relevant for analyzing the flame acceleration processes are summarized in Table 8.1.
COSILAB v.3 code [77] was used for the numerical computation. Thermodynamic equilibrium properties (defined with the symbol • in Table 8.1) are obtained from 0D Chemical Equilibrium simulations. Detailed reaction mechanism and thermodynamic and transport databases of O'Connaire et al. [110] were used. Temperature and species profiles as well as laminar flame speeds are evaluated from numerical simulations of mono-dimensional freely propagating adiabatic premixed flames. A finite difference approximation is used to reduce the problem (balance equations (1.1)-(1.5)) to a system of algebraic equations. Then a (modified) steady Newton iteration scheme is used to solve the system.
Global activation energy E_a and global reaction order n are computed according to the formulas introduced in Table 8.1. These formulas are derived from the analysis of Zeldovich and Frank-Kamenetski about the 1D fundamental flame velocity of a mixture characterized by a single step Arrhenius chemical reaction [53]. E_a is determined by analyzing the variation of $\ln(\rho_u S_L)$ as a function of $1/T_b$. The adiabatic temperature is varied by diluting the mixture with nitrogen but keeping constant the ratio H_2/O_2. Then, a linear fit is used the to derive E_a. Similarly, to compute the reaction overall order n, the variation of $\ln(\rho_u S_L)$ as a function of $\ln(p)$ is studied. The pressure is varied in the range $0.2 - 4$ atm. A third order polynomial fit is used. Results thus achieved were compared to the

Table 8.1: Combustion properties relevant for analyzing flame acceleration processes. Legend: (•), evaluated from a thermodynamic equilibrium numerical computation; (∗), evaluated from a mono-dimensional premixed flame simulation.

Parameter	Formulation	Definition
σ	(•)	Expansion ratio (ratio of the unburnt to the burnt gas density for an AIBC transformation)
T_b	(•)	Adiabatic flame temperature (AIBC equilibrium temperature)
c_{su}	(•)	Sound speed in the unburnt gas
c_{sb}	(•)	Sound speed in the burnt gas
p_{AICC}	(•)	AICC equilibrium pressure
S_L^0	(∗)	Laminar flame velocity
δ_L^{th}	equation (2.20)	Laminar flame thickness (temperature gradient)
δ_L^h	equation (2.15)	Laminar flame thickness (heat transfer)
$\delta_L^{h'}$	$\sigma\delta_L^h$	Alternative formulation of equation (2.15)
E_a	$\frac{E_a}{R} = -2\frac{\partial \ln(\rho_u S_L)}{\partial(1/T_b)}$	Global activation energy of the one-step reaction mechanism
n	$n = 2\frac{\partial \ln(\rho_u S_L)}{\partial \ln(P)}$	Overall reaction order of the one-step chemical reaction
β	equation (2.12)	Zeldovich number
$\mathrm{Le}_{\mathrm{eff}}$	equation (2.17)	Effective Lewis number
Ma	equation (2.26)	Markstein number
U_{CJ}	(•)	Chapman-Jouguet detonation velocity
p_{CJ}	(•)	Chapman-Jouguet detonation pressure
$U_{\mathrm{CJ,def}}$	equation (1.24)	Chapman-Jouguet deflagration velocity
λ	equation (2.51)	Detonation cell size

literature [53, 130, 89, 96] to confirm their validity.
Moreover, the approach above described for the computation of the combustion properties was verified throughout an inter-laboratories comparison. Three different hydrogen/air mixtures were tested: 11, 13 and 15 vol% H_2, at 1 bar initial pressure and 293 K initial temperature. The composition of the synthetic air was 21 vol% oxygen and 79 vol% nitrogen. Reference data were provided by ICARE laboratory of the CNRS-Orléans (detailed kinetic mechanism of Mével et al. [103]).
From the results provided in Table 8.2, we can conclude that our method (use of the code + kinetic mechanism + thermodynamic and transport database) for the determination of the combustion properties is correct.

8.2 Signal post-processing

In the present chapter the methodology to determine the flame time-of-arrival on the basis of photomultiplier tubes (PMT) signals is described. The uncertainties of the measurement method are also evaluated. In a similar way, an analysis of the piezoelectric signal response and the related post-processing is performed.
The proposed examples refer to experiments performed at room temperature and 1 bar initial pressure. At $t = 0$, the flammable mixture is composed by hydrogen at 11% and

Parameter	11 vol% H_2		13 vol% H_2		15 vol% H_2	
	ICARE	CEA	ICARE	CEA	ICARE	CEA
T_b (K)	1168.2	1168.6	1318.2	1319.1	1465.9	1467.8
σ	3.77	3.77	4.21	4.21	4.63	4.63
S_L^0 (cm/s)	4.22	4.36	11.15	10.41	23.60	23.21
δ_L^{th} (mm)	1.93	1.85	0.96	1.01	0.61	0.61
$\delta_L^{h'}$(mm)	0.72	0.69	0.29	0.31	0.14	0.14

Table 8.2: Validation matrix for some global combustion properties.

air (synthetic air: $20.9\%O_2 - 79.1\%N_2$), homogeneously distributed along the tube. The acquisition frequency f_a may vary between 200 and 300 kHz depending on the number of sensors used during an experiment. This value is fixed for all the sensors.

8.2.1 Flame time-of-arrival

The method to determine the flame time-of-arrival (ToA) is hereinafter discussed. With the term flame time-of-arrival (ToA) we identify the time at which the flame passes through the optical path of a photomultiplier tube. The knowledge of this quantity is crucial for the computation of the flame speed.

Signal analysis in the frequency domain

Once the flame tip passes across the optical path of a PMT, a negative pulse is recorded by the acquisition station. For lean hydrogen/air mixtures, the noise to signal ratio is quite important. As the initial hydrogen content is increased, the number of $OH^\bullet$ in the reaction zone increases, hence the amplitude of PMT output signal increases while the noise to signal ratio decreases, as shown in Figure 8.1.

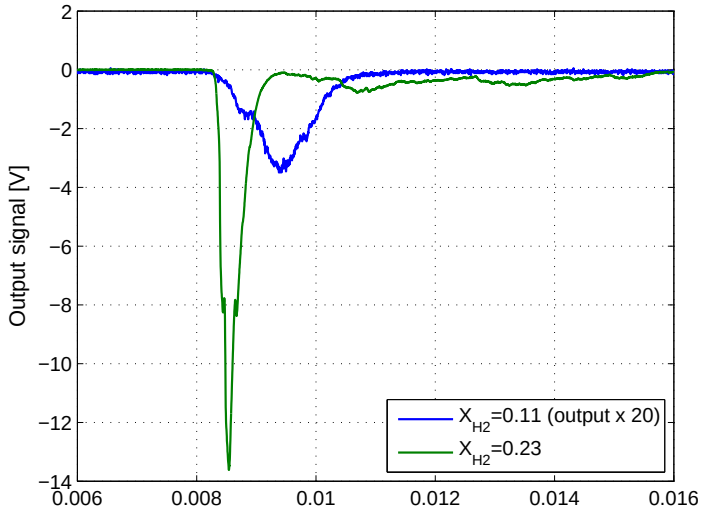

Figure 8.1: PMT response to premixed hydrogen/air flames: 11%vol H_2 vs 23%vol H_2.

To post process PMT signal for very lean mixtures ($X_{H2} = 0.11$), we first proceeded with filtering the signals so that a large part of the noise is removed. A low-pass filter was

used for this purpose with a cutoff frequency high enough to preserve physical oscillations associated to the experiment. Moreover, we opted for a zero-phase forward and reverse digital filter to minimize start up and ending transients, matching initial conditions [100]. The order of the filter is high enough to ensure a sharp front for the cutting window (500th).
A criterion for the choice of the cutoff frequency f_c is therefore required. For our method we suggest to fix a cutoff frequency low enough to dump spurious peaks, but, at the same time, high enough to catch flame oscillations between two subsequent obstacles. As a result, we opted for the following relation to compute the cutoff frequency:

$$f_c \gtrsim f_a = \frac{c_{sb}}{2D} \tag{8.1}$$

where f_a is the frequency of the acoustic waves in the burnt gas, c_{sb} is the speed of sound and $D = 120$ mm is the the distance between two annular obstacles. This frequency thus depends on the initial conditions, i.e. p_{tot} and X_{H_2}, of the experiment. For a hydrogen/air mixture with 11% vol H_2, $f_c \simeq$ 3 kHz. Note that, for the method to be consistent, this frequency must be the same for all the PMT signals along flame path for a given experiment.
Moreover, a further confirmation on the validity of the criterion above discussed is given by the analysis of the signals in the frequency domain. Figure 8.2 shows the single-sided amplitude spectrum $P(f)$ of the PMT response in frequency. Here, we can see that the frequencies that contribute most to the signal are those in the range $f < 1$ kHz. Wave amplitude remains almost constant in the region $1 < f < 3$ kHz while it strongly decreases for $f > 3$ kHz.

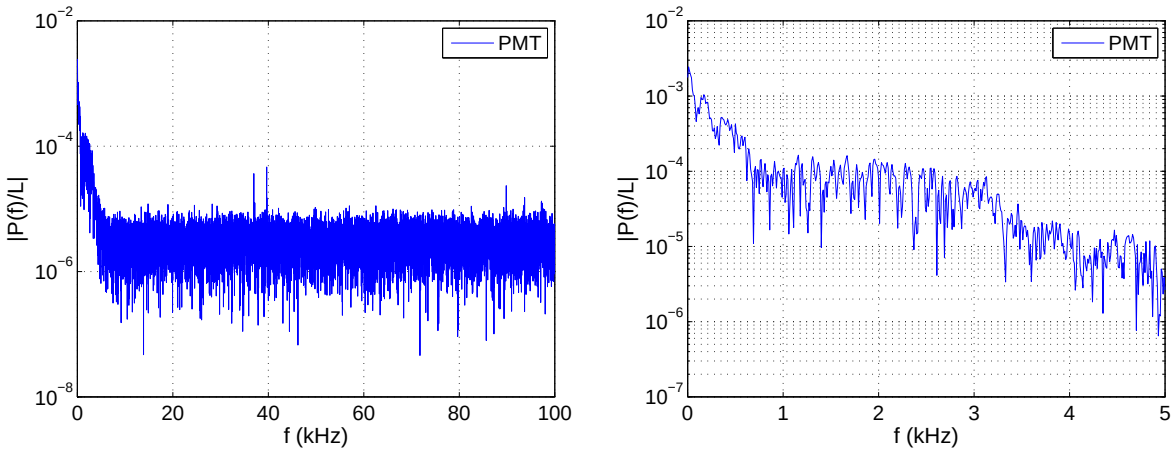

(a) Complete spectrum. **(b)** Zoom on the region $0 < f < 5$ kHz.

Figure 8.2: Single-Sided Amplitude Spectrum $P(f)/L$ (where L is the signal length) of a PMT output signal for a lean hydrogen/air mixture (11 %vol H_2). $f_a = 200$ kHz.

As a result, in Figure 8.3, recorded and filtered signals are shown (here, the cutoff frequency used to filter the signal is $f_c = 3.2$ kHz).

Maximum derivative method

The method to determine flame ToA is graphically shown in Figure 8.4.

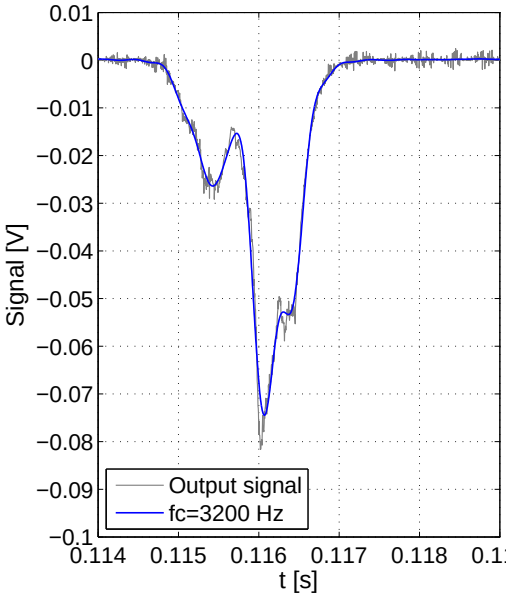

Figure 8.3: PMT output signal. Comparison with the filtered signal ($f_c = 3200$ Hz).

The following procedure is applied on the output signal (filtered signal for very lean mixtures and raw signal for the other cases):

1. First and second derivatives of the signal ($\frac{\mathrm{d}Y}{\mathrm{d}t}$ and $\frac{\mathrm{d}^2Y}{\mathrm{d}t^2}$) are computed.
2. The time t_0 at which the second derivative is equal to zero is determined $\left(\frac{\mathrm{d}^2Y}{\mathrm{d}t^2}(t = t_0) = 0\right)$: in the tY-plane, the abscissa t_0 match the point in which a change of concavity takes place (in other words, it corresponds to the point in which the first derivative of the signal has its maximum).
3. Once the ordered pair $(t_0, Y_0 = Y(t_0))$ is set, the tangent to the curve in (t_0, Y_0) is taken (see left-handed plot of Figure 8.4).
4. Eventually, the time-of-arrival $t_{\mathrm{PM}n}$ (where the index n refers to n-th PMT) is defined as time in which the tangent to the curve intersects the $Y = 0$ line, as shown in the right-handed plot of Figure 8.4.

The physical condition that the ToA measured by the $(n+1)$-th PMT is greater than that one measured by the n-th PMT is imposed to close the algorithm.
In Figure 8.5 the flame time-of-arrival evaluation method is graphically shown for five subsequent PMT.

PMT signal influencing factors

In this paragraph we would like to point out some factors that influence the shape and the amplitude of PMT output signal. As already mentioned in the previous Chapter 7.3 the most important ones are the voltage supply and the diaphragms inner diameter.
First, let us focus on the voltage supply, that is used to drive the high tension at the dynodes. It can be increased within the operating range to retrieve a higher output

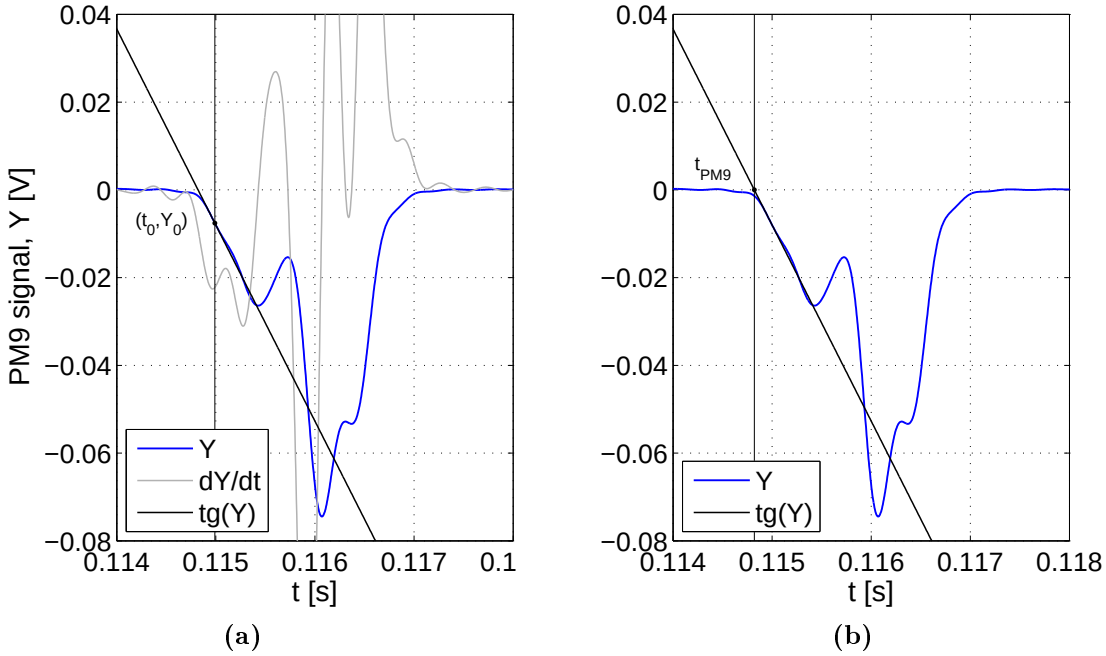

Figure 8.4: Graphic representation of the method used to evaluate the flame time-of-arrival for PMT9. $f_c = 3200$ Hz.

signal. This increase is actually limited to a voltage 20% to 30% lower than the maximum rating. In Figure 8.6a the signal recorded by PM9 is shown for two experiments at the same initial conditions. In one case we supplied 0.8 V to the photomultiplier tube, black solid line, while in the other case, gray solid line, the PMT was supplied with 1 V. As we can see the amplitude of the pic strongly increases with increasing the voltage supply. At the same time, since the flame ToA depends on the shape of the signal, the value of $t_{\mathrm{PM}n}$ differs. For very lean mixtures, for which $OH^{\bullet}$ radicals emission is quite low, PMT are supplied with $1.0 - 1.1$ V; approaching the stoichiometry, the voltage supply is decreased to avoid acquisition card saturation.
In Figure 8.6b the influence of diaphragms hole diameter is shown. As mentioned before, a $\Phi = 1$ mm hole (gray solid line) corresponds to the case in which the PMT sensitive area is enlightened only in the $\Phi = 8$ mm region (see picture 7.4(b)). The sensor is more precise in measuring the position of the flame front but at the same time its output signal is weak and in some cases difficult to post-process. On the other hand, the $\Phi = 3$ mm hole for the diaphragms guarantees the minimum error for the maximum PMT sensitive area irradiation. As we can see in Figure 8.6b, the resulting signal is much stronger than in the previous case. For this reason, the diaphragms currently used in the facility have $\Phi = 3$ mm hole diameter.

8.2.2 Flame speed

The local flame front velocity is defined as the average value of the velocity of the flame tip between two consecutive photomultiplier tubes. It is computed as the ratio between the distance separating two sensors and the difference of the related flame transit times,

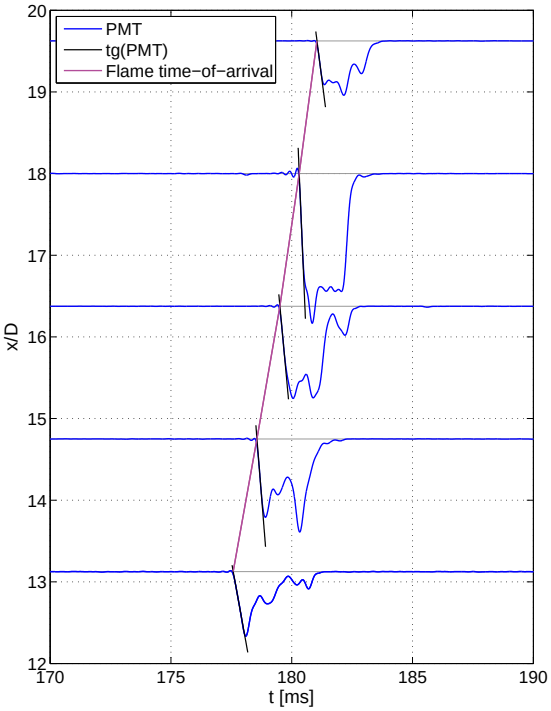

Figure 8.5: Flame tip time-of-arrival diagram for five consecutive PMT located in the second section of the combustion tube (combustion tube in the 3-modules configuration with BR=0.3). Test initial conditions: 11 %vol hydrogen in air and $p_0 = 1$ bar.

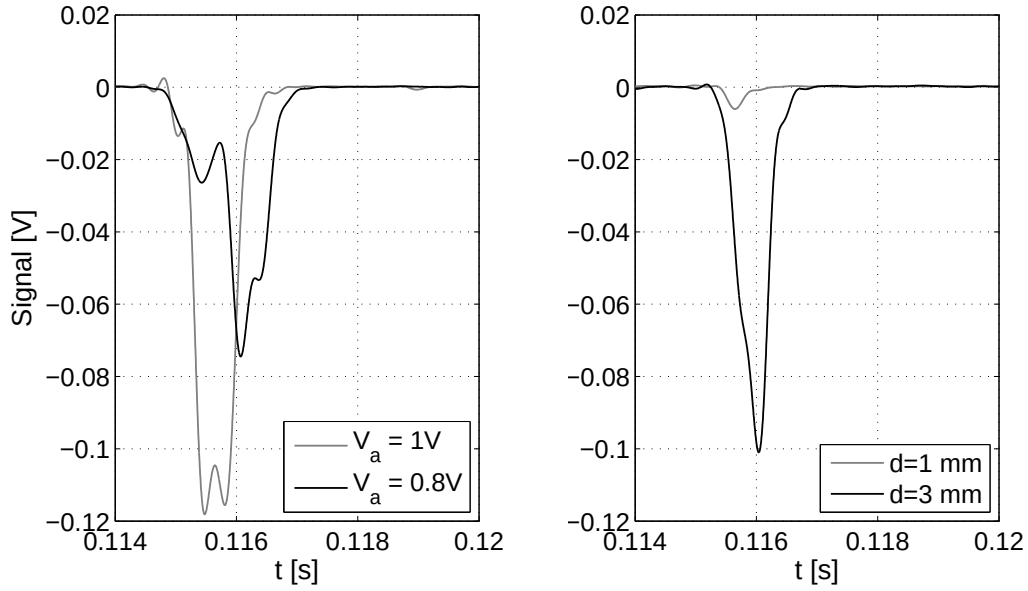

(a) PMT9 output signal variation as a function of voltage supply.

(b) PMT10 output signal variation as a function of the diaphragm inner diameter.

Figure 8.6: PMT output signals. $f_c = 3200$ Hz. Test initial conditions: 11 %vol hydrogen in air and $p_0 = 1$ bar.

as follows:

$$\overline{U}(x) = \frac{\Delta x^{n+1}}{\Delta t^{n+1}} = \frac{x^{n+1} - x^n}{t^{n+1} - t^n} \quad \text{for} \quad x \in [x^n; x^{n+1}]\,. \tag{8.2}$$

Equation (8.2) gives the average value of the velocity in the region $[x^n; x^{n+1}]$. For this reason we have imposed $\overline{U}(x) \equiv U(x^{n+\frac{1}{2}}) = U^{n+\frac{1}{2}}$, where $x^{n+\frac{1}{2}} = \frac{x^n + x^{n+1}}{2}$.

8.2.3 Uncertainty in flame speed computation

The uncertainty related to the flame speed can be evaluated from equation (6.7), according to the error propagation theory [70]. Here, the independent variables are PMT axial positions and flame ToA. Therefore, the variance of the flame tip velocity is:

$$u^2(U^{n+\frac{1}{2}}) = \frac{1}{(\Delta t^{n+1})^2}\left(u^2(x^{n+1}) + u^2(x^n)\right) + (\Delta x^{n+1})^2\left(\frac{u^2(t^{n+1})}{(t^{n+1})^4} + \frac{u^2(t^n)}{(t^n)^4}\right)\,. \tag{8.3}$$

Making the following hypotheses:

$$u(x^{n+1}) \simeq u(x^n) = u(x) \tag{8.4a}$$

$$u(t^{n+1}) \simeq u(t^n) = u(t) \tag{8.4b}$$

equation (8.3) can be rewritten as follows:

$$u^2(U^{n+\frac{1}{2}}) = \frac{2u^2(x)}{(\Delta t^{n+1})^2} + (\Delta x^{n+1})^2 u^2(t)\left(\frac{1}{(t^{n+1})^4} + \frac{1}{(t^n)^4}\right)\,. \tag{8.5}$$

The maximum error in the flame tip position is made when the sensitive area of the PMT is turned of 45° with the vertical axis:

$$u(x) \simeq \delta = \frac{\delta_{min}}{\cos 45^\circ} = 3.66\,\text{mm}\,. \tag{8.6}$$

The time related uncertainty $u(t)$ is the composition of the error associated with the PMT rise time $u(\text{rt})$ and that one introduced by the signal post-processing method:

$$u^2(t) = u^2(\text{rt}) + u^2(t_{\text{PM}n})\,. \tag{8.7}$$

An error propagation analysis has been performed to evaluate how f_c influences the value of $t_{\text{PM}n}$. For lean mixtures, $u(t_{\text{PM}n}) \simeq 1 \cdot 10^{-5}$ s was estimated. For mixtures close to the stoichiometry this value is even smaller since PMT signal peaks are steeper.
Moreover, since $u^2(t) \ll 1$, equation (8.5) reduces to:

$$u^2(U^{n+\frac{1}{2}}) \simeq \frac{2u^2(x)}{(\Delta t^{n+1})^2} \tag{8.8}$$

hence

$$\frac{u(U^{n+\frac{1}{2}})}{U^{n+\frac{1}{2}}} \simeq \sqrt{2}\frac{u(x)}{\Delta x^{n+1}} = \begin{cases} 0.977\% & \text{if}\,\Delta x^{n+1} = 0.530\,\text{m} \\ 2.654\% & \text{if}\,\Delta x^{n+1} = 0.195\,\text{m} \end{cases} \tag{8.9}$$

Therefore, the relative uncertainty on the average velocity is directly proportional to the uncertainty on the flame position $u(x)$ and it depends on the distance between two subsequent PMT.
In Table 8.3 we can find an example of the use of equations (8.2) and (8.5) for the evaluation of the flame speed and the related uncertainty. In Figure 8.7 the velocity profile along the tube axis and the related uncertainty for a 11% H2/air mixture are presented.

Table 8.3: Example of calculation of H2/air flame speed and related uncertainty. Initial conditions of the experiment: $X_{H_2} = 0.11$, $p_0 = 1000$ mbar. The photomultiplier tubes taken into account for the computation are PMT9 and PMT10 ($n = 9$ and $(n+1{=}10)$.

Quantity	**Value**	**SI unit**
x^n	2.160	m
x^{n+1}	2.355	m
t^n	$180.3 \cdot 10^{-3}$	s
t^{n+1}	$181.0 \cdot 10^{-3}$	s
Δx^{n+1}	0.195	m
Δt^{n+1}	$0.730 \cdot 10^{-3}$	s
$\boldsymbol{U^{n+\frac{1}{2}}}$	**267.1**	**m/s**
$u^2(x)$	1.34E-05	m^2
$u^2(\mathrm{rt})$	4.84E-18	s^2
$u^2(t_{\mathrm{PM}}n)$	1.00E-10	s^2
$u^2(t)$	1.00E-10	s^2
$\boldsymbol{u(U^{n+\frac{1}{2}})}$	**7.1**	**m/s**
$\boldsymbol{u(U^{n+\frac{1}{2}})/V^{n+\frac{1}{2}})}$	**2.654**	**%**

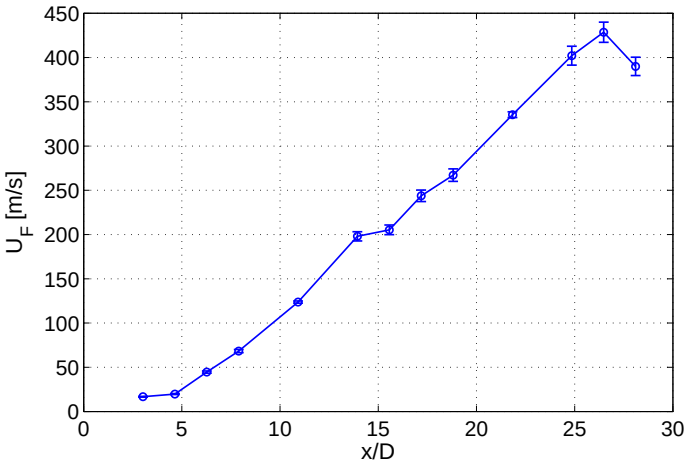

Figure 8.7: Flame tip velocity profile along the tube axis. 11% H2/air mixture and $p_0 = 1$ bar. Combustion tube in the 3-modules configuration with BR=0.3.

8.2.4 Piezoelectric sensors output signals

Similarly to PMT signals, pressure signals can be filtered in order to retrieve only those wavelets that contribute most to the signal. This process allows us to better analyze piezo-electric sensors response in time, from a qualitative point of view. Since the filtering process tends to smooth the signals and to scale down the pressure peaks, both recorded and filtered signals are usually shown to present and discuss the experimental results. Moreover, the filtered signals can be used to determine the shock wave time-of-arrival with the same procedure described in Chapter 8.2.1.

Signal analysis in the frequency domain

In Figure 8.8, the single-sided amplitude spectra of the pressure signals recorded by Kistler sensors during the combustion of a lean hydrogen/air mixture is shown. Frequency response of 601A and 6001 types are presented in Figure 8.8a, while the 7001 is shown in Figure 8.8b. As expected the Kistler 7001 has a peak in correspondence to its natural frequency (FN$\simeq$ 70 kHz). A zoom of Figure 8.8a on the region $f < 5$ kHz is presented in Figure 8.9.

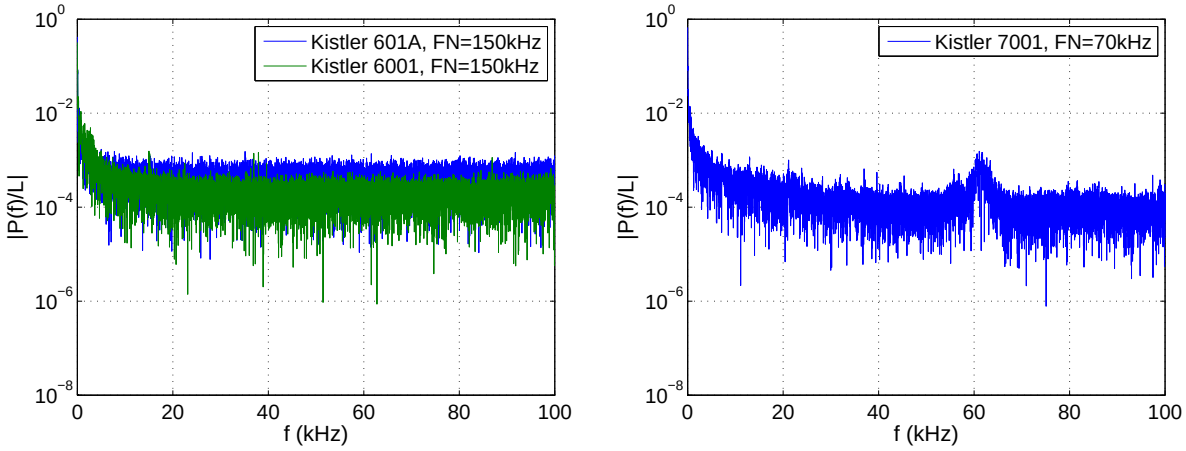

(a) 601A and 6001 Kistler sensors.

(b) 7001 Kistler sensors.

Figure 8.8: Single-sided amplitude spectra of Kistler output signals for a lean hydrogen/air mixture (11 %vol H_2). $f_a = 200$ kHz.

A further upside of the filtering process is shown in Figure 8.10a. The figure presents the output signal and the correspondent filtered signal of a Kistler 7001 sensor (PP7). The analysis of the signal in the frequency domain has shown the presence of several peaks in the region $20 - 30$ kHz, peaks that are not observed in the other pressure sensors. The excitation of these wavelets is probably due to an incorrect fixation of the sensor mounting nut causing the sensor to vibrate. Once the signal is filtered, a time response similar to that one recorded by the adjacent sensors is retrieved (see Figure 8.10a).

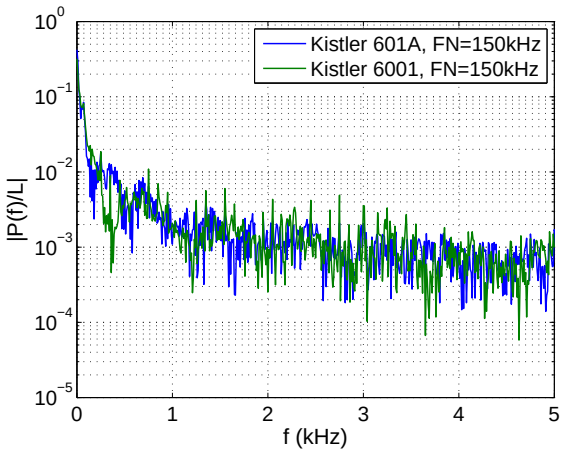

Figure 8.9: Zoom on Kistler 601A and 6001 amplitude spectra.

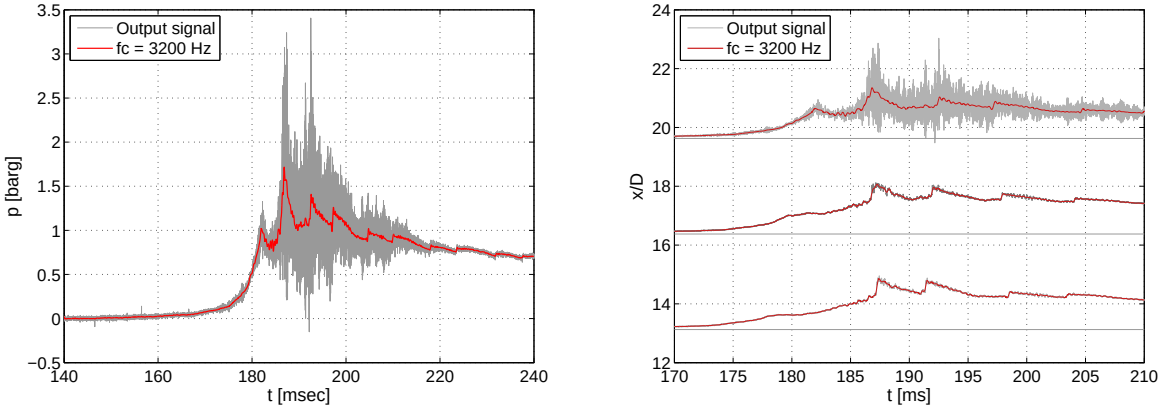

(a) PP7. **(b)** $x-t$ diagram of PP5 PP6 and PP7.

Figure 8.10: Comparison between recorded and filtered ($f_c = 3200$ Hz) pressure signals (Kistler 7001 type) for 11 %vol H_2 in air mixture.

8.3 Conclusions

In the present chapter the methods used to post-process and interpret experimental data were discussed.
First, combustion fundamental properties relevant to results analysis were identified (see Table 8.1). Thermodynamic properties are computed via 0D numerical simulations at the equilibrium state. Laminar burning velocity and temperature and species profiles in the reaction zone are obtained from 1D freely propagating adiabatic premixed flames simulations. Numerical simulations are performed with Cosilab v.3 code.
Then, the methodology used to process combustion diagnostics output signals was detailed. A key quantity for the determination of the flame tip velocity is the flame time-of-arrival or ToA. With the term flame time-of-arrival we identify the time at which the flame passes through the optical path of a photomultiplier tube. The method for the evaluation of the flame ToA was presented, taking into account those factors that may influence PMT output signal.
Once flame ToA is determined, the average velocity of the flame tip between two subsequent sensors can be computed with equation (8.2). The velocity profile along the tube axis can be obtained repeating the computation for $n = 1 \cdots N$, where N is the total number of sensor used for the experiment (normally $N = 14$).
The attention was also focused on the consistency of the method and its limitations in order to evaluate the margin of error of the technique. As a result the uncertainty related to the flame tip velocity can be computed from equation (8.5) (or equation (8.9) for the relative uncertainty).
Eventually, the velocity of the shock wave can be determined in a similar way from Kistler and Chimiemetal piezo-electric sensors output signals.

Part III

Experimental results on flame acceleration

Chapter 9

Repeatability and reproducibility tests

In the present chapter, the experimental results obtained in this study are compared to those from the literature. The aim is to validate our methodological approach in performing flame acceleration experiments. The influence of hydrogen content and obstacle blockage ratio are also discussed. Eventually, tests repeatability is presented for different geometrical configurations and mixtures.
The discussion is limited to the flame tip and shock wave velocity profiles obtained from the post-processing of photomultiplier tubes (PMT) and Kistler sensors (PP) output signals.
Experiments performed by Kuznetsov et al. [82] were chosen as reference data. The reason of this choice lies in the geometrical configuration of the devices used in [82], that are similar to our apparatus. The main judging parameters were duct geometry, obstacle blockage ratio and obstacle spacing. Three combustion tubes were used in [82]. These tubes differ for total length and internal diameter: DRIVER tube, 174 mm inner diameter and 11.5 m total length; FZK tube, 350 mm inner diameter and 12 m total length; and TORPEDO tube, 520 mm inner diameter and 33.5 m total length.
Fundamental combustion properties of the mixtures hereinafter described are listed in Table 9.1. For the same mixture compositions, Table 9.2 lists the criteria (3.4), (2.55) and (2.56) for flame acceleration and deflagration-to-detonation transition. Here, σ^* is computed according to equation (3.6). Values matching the two criteria are highlighted in black, while those value that do not fulfill the criteria are given in gray.

9.1 Obstacle blockage ratio BR=0.3

First, we present the results obtained by placing an array of annular obstacles with blockage ratio BR= 0.3 inside the tube. Moreover, only three over four sections of the tube were used for these experiments. All the experiments were performed at room temperature and initial pressure of 1 bar.
Flame velocity profile along the tube axis for two subsequent shots with 15 %vol hydrogen is shown in Figure 9.1a. Here, error bars correspond to the uncertainty in flame velocity computation, as explained in Chapter 8.2.3. CJ detonation velocity was measured at half of the flame path (Test 13). Then, the detonation is not sustained (excessive heat losses at the baffles) and the flame speed decreases. Note that, according to Table 9.2, both d/λ and L/λ criteria are not met. Even if U_{CJ} was not reached in Test 12, a similar behavior

Table 9.1: Fundamental combustion properties as a function of the hydrogen content for $T_0 = 300$ K and $p_0 = 1$ bar.

vol% H_2	11.0	15.0	23.0	28.5	47.0
ϕ	0.296	0.420	0.715	0.954	2.122
σ	3.720	4.544	6.025	6.791	5.982
c_{su} [m/s]	367.2	375.1	392.5	406.5	464.1
U_{CJ} [m/s]	1340	1524	1812	1959	2154
$U_{\mathrm{CJ,def}}$ [m/s]	617.4	719.9	896.9	997.2	1056
S_L [m/s]	0.046	0.240	1.110	1.851	2.728
$(\sigma - 1)S_L$ [m/s]	0.126	0.849	5.578	10.72	13.59
λ [cm]	303.3	28.89	3.14	1.67	2.36

Table 9.2: σ/σ^*, d/λ and L/λ criteria.

vol% H_2	σ/σ^*	BR = 0.3		BR = 0.6	
		d/λ	L/λ	d/λ	L/λ
11.0	0.99	0.03	0.24	0.03	0.11
15.0	1.21	0.35	2.54	0.26	1.13
23.0	1.61	3.20	23.40	2.42	10.40
28.5	1.81	6.01	43.99	4.54	19.55
47.0	1.60	4.25	31.13	3.22	13.83

was observed with a strong increase of the velocity in the center of the tube, followed by a fast slowdown. The point at which the flame tip velocity has its maximum is however shifted.

Detonation initiation following shock reflection at the obstacles and successive failure due to wave diffraction was also observed by Kellenberger and Ciccarelli [75] for low pressure hydrogen/oxygen flames. Their results showed that, for the same initial conditions, the location for detonation initiation may differ from an experiment to the other, as observed in the present work. Differently from Kellenberger's findings, detonation initiation between obstacles occurs even if $d/\lambda < 1$. This difference may be explained by considering the uncertainty in equation (2.51), used to compute λ.

In Figure 9.1b, experimental results are given in terms of average values over three shots. Error bars identify maximum and minimum values of the shots. Flame acceleration profile is consistent with the one found in [82]. The only difference is that, in our case detonation initiation and failure occur much earlier with respect to [82].

In Figure 9.2 a sensitivity analysis of the mixture composition is shown. Here, the hydrogen content in the mixture was varied in the range $10.9 < X_{\mathrm{H_2}} < 11.2$ %vol. It is important to remind that the composition of the mixture is obtained by taking the arithmetic average over 10 gas-chromatographic analysis of the same sample and that the

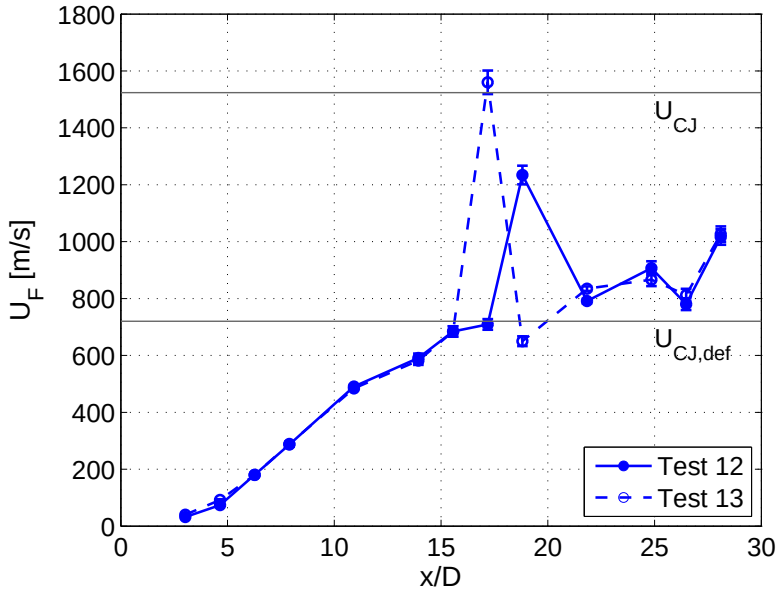

(a) Repeatability study.

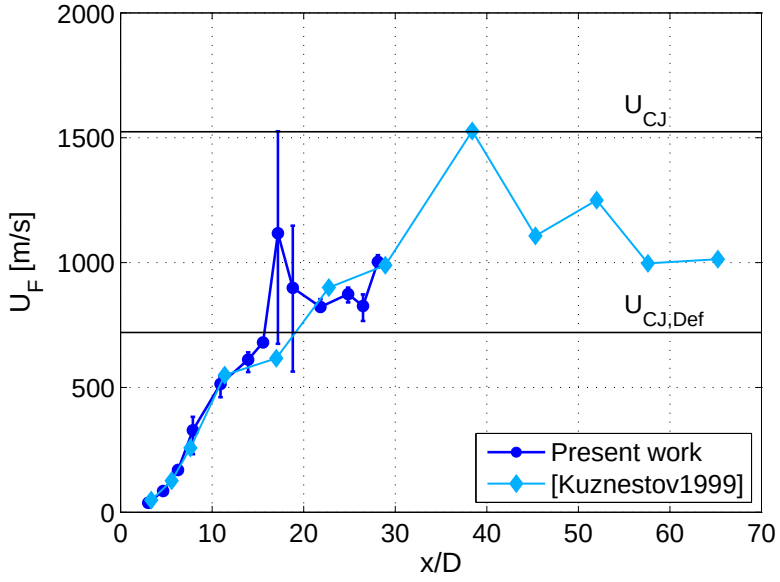

(b) Comparison between the experimental results obtained in the present work and those presented in Kuznetsov et al. [82].

Figure 9.1: Flame speed profile along the tube axis for 15 %vol hydrogen/air mixture with BR= 0.3.

relative uncertainty in the mixture composition is in the order of 0.5% for lean mixtures (for example $X_{H_2} = 10.9 \pm 0.055$ %vol). In Figure 9.2, error bars correspond to the uncertainty in flame velocity computation. Results for the case with $X_{H_2} = 0.109$ are in good agreement with those from [82] ($X_{H_2} = 11$ %vol), except in the region $x/D \simeq 15$ where the velocity obtained in the present work is 20% higher.
A zoom in the initial stage of flame acceleration (Figure 9.2b) shows more clearly the effect of the increase of hydrogen content on flame acceleration. In the early beginning of flame propagation, flame velocity assumes the same value for all the considered cases. Then, the velocity increases quasi-exponentially up to $x/D \simeq 8$. Here, the acceleration rate increases with the hydrogen content. From there on, the increase is globally more linear (with a constant acceleration). At $x/D \simeq 20$ the velocity reaches the value $0.5c_{su}$ (criterion for fast deflagration) and the profile assumes an oscillatory behavior.
Differently from [82], in the present experiments the chocked flame regime is not achieved. The reason lies in the fact that the tube is not long enough to allow flame velocity stabilization around the Chapman-Jouguet deflagration velocity $U_{\mathrm{CJ,def}}$.
The effect of the hydrogen content on flame acceleration is also presented in Figure 9.3. Here, four mixtures with X_{H_2} ranging from 0.11 to 0.47 are tested. Results are given in terms of average values over multiple shots. For sake of clarity, error bands are not included.
The global trend of the flame velocity at the end of the tube is coherent with that one found in the literature, with a maximum velocity that depends on the mixture equivalence ratio. Moreover, a typical U-shape curve was obtained for the run-up distance (see Figure 9.4). Here, we have defined the run-up distance X_S as the distance at which the flame velocity reaches the value of $U_{\mathrm{CJ,def}}$. A linear interpolation between two consecutive measurements was used to determine the intersection between the velocity profile ans the straight line $U_F = U_{\mathrm{CJ,def}}$. In Figure 9.4, the values for the run-up distance obtained from equation (3.21) are also presented with the associated errorbar. To ensure the consistency between experimental and analytical results, in equation (3.21) c_{sb} was replaced with $U_{\mathrm{CJ,def}}$.
The transition to detonation was observed for the 23 %vol and for the 47 %vol hydrogen mixtures. In both cases, DDT criteria expressed by equations (2.55) and (2.56) are met (ref. Table 9.2). In particular, an over-driven detonation was observed for the 23 %vol case while a quasi-detonation was experienced for the rich mixture with 47 %vol hydrogen (note that criterion (2.53) for detonation occurrence independently from the boundary conditions is not fulfilled).

9.2 Obstacle blockage ratio BR=0.6

Figure 9.5 shows the results obtained with an obstacle blockage ratio BR= 0.6 for a 15 %vol hydrogen/air mixture. Present experimental results are given in terms of average values over three shots. Error bars identify maximum and minimum values of the shots. All four sections of the tube were used to perform these experiments. Only 8 photomultiplier tubes were used, located in the first two sections of the tube. The velocity of the shock wave, computed by post-processing Kistler sensors signals, is also shown. As for the previous case, flame acceleration profile matches the profile obtained in [82].
By comparing Figure 9.5 with Figure 9.1a we can clearly see the effect of the obstacle

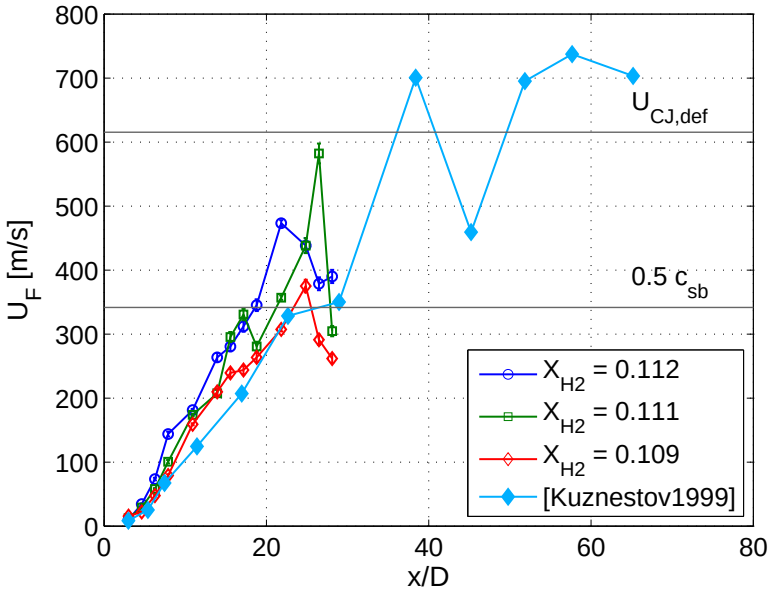

(a) Sensitivity analysis on the mixture composition.

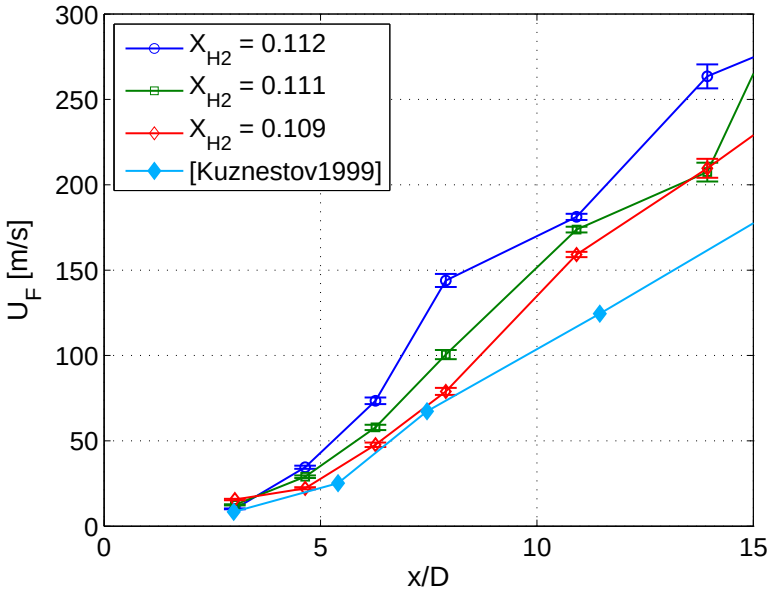

(b) Zoom in the initial stage of flame acceleration.

Figure 9.2: Comparison between the experimental results obtained in the present work and those presented in Kuznetsov et al. [82] for 11 %vol hydrogen/air mixture and BR= 0.3.

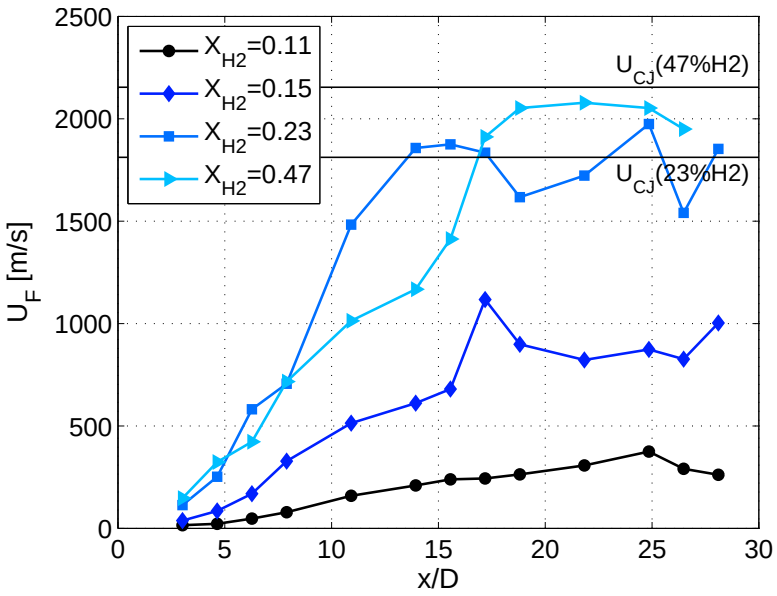

Figure 9.3: Influence of hydrogen content on flame acceleration for BR= 0.3.

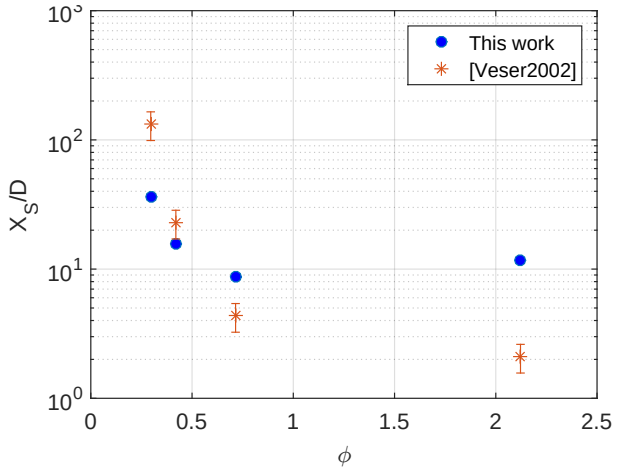

Figure 9.4: Run-up distance vs equivalence ratio for BR= 0.3.

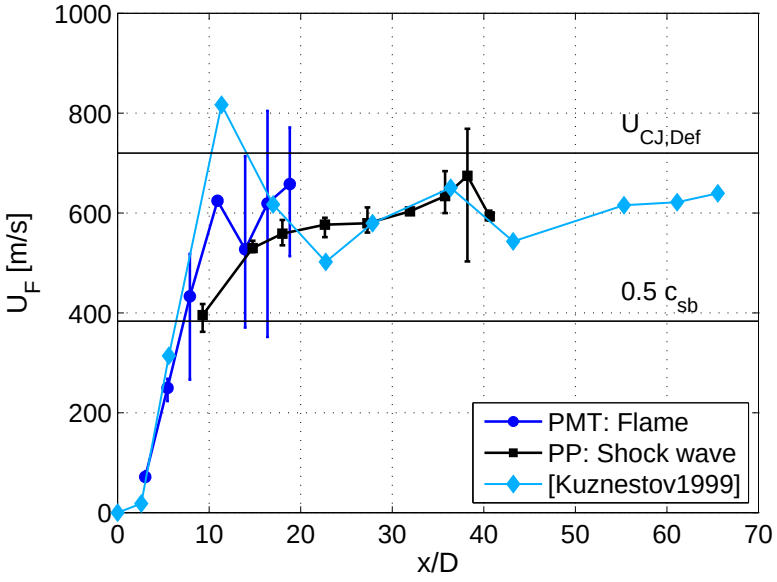

Figure 9.5: Flame velocity and shock wave velocity for 15 %vol hydrogen/air mixture and BR= 0.6.

blockage ratio on flame acceleration profile: with BR=0.6 the Chapman-Jouguet deflagration velocity $U_{\mathrm{CJ,def}}$ is reached much earlier than for the case with BR=0.3.
In Figure 9.6 a repeatability study on 28.5% hydrogen/air mixture is presented. In this case results are not given in term of average value over the shots since the number of photomultiplier tubes for the two experiments was different. A chocked flame regime was observed: the asymptotic velocity of the flame tip is slightly below the CJ deflagration velocity. Even though the criteria for DDT are met (ref. Table 9.2), the transition to detonation was not observed. Therefore, boundary conditions (tube diameter and obstacle blockage ratio) strongly affect flame propagation mechanisms. Moreover, this behavior in the velocity profile may be explained in light of the findings of [75]: if $d/\lambda < 6.5$ and a self-sustained detonation is not formed (shock wave reflection at the obstacle faces fails in generating local explosions), the steady-state conditions are governed only by thermodynamics ($U_F \simeq U_{\mathrm{CJ,def}}$).

9.3 Conclusions

In the present chapter preliminary results obtained with the experimental device described in Chapter 5 are shown. Since the apparatus was used for the first time during the present research work, a first experimental campaign with the main objective of validating the methodological approach was performed. For this campaign, repeatability and reproducibility tests were carried out.
First, experimental results were compared to the existing literature: a good accordance with experiments performed in similar geometrical configurations was found.
In a second phase, some sensitivity studies on mixture concentration and on obstacles blockage ratio were performed. From the analysis of the present experimental results, the characterizing phenomena of the propagation regimes described in Chapter 3 were

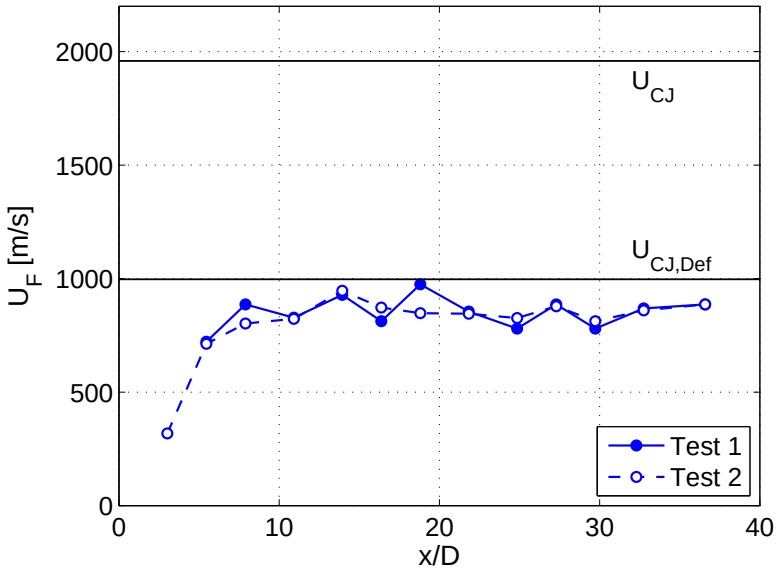

Figure 9.6: Flame velocity for 28.5 %vol hydrogen/air mixture and BR= 0.6.

observed. Results are also consistent with the criteria for flame acceleration and DDT, introduced first in Chapters 3 and 2.2 and expressed in Table 9.2.
On the basis of the obtained results, we can state that the experimental apparatus together with the embedded diagnostics is efficient for the analysis of the flame acceleration mechanisms. In the following chapters a focus on the effect of the initial pressure and the nitrogen concentration on the flame propagation will be treated. Both these parameters play a key role in the nuclear safety with respect to the risk of hydrogen explosion inside the reactor containment.

Chapter 10

Effect of initial pressure on flame acceleration process

The empirical flame acceleration criteria developed in the early 2000s by Dorofeev and colleagues [27, 47] provide effective tools for the analysis of the possible scenarios and it allows the selection of the most relevant situations for which flame acceleration may take place. Nevertheless, most of FA and DDT criteria are based on experimental databases in which explosions were carried out mainly at atmospheric or sub-atmospheric conditions. In case of a severe accident, the high release rate of steam and non-condensable gases into the containment may result in a pressure increase up to 5 bar abs. Therefore, hydrogen explosions are more likely to happen at an initial pressure greater than the atmospheric one.

Previous studies on methane/air mixtures performed by Kuznetsov et al. [83] showed that initial pressure promotes flame acceleration. From the experimental results of Cheng et al. [35] for near stoichiometric hydrogen/propane/air mixtures, it appears that the flame velocity of the binary fuel is only slightly affected by a variation of the initial pressure in the range $0.8 - 1.2$ bar. On the other hand, as the initial pressure is decreased up to 0.5 bar, a decrease of $\simeq 400$ m/s in the maximum velocity is observed.

In the present chapter, the influence of initial pressure p_0 on premixed hydrogen/air flame propagation was experimentally investigated in the SSEXHY facility. For this series of tests, only three section of the combustion tube were used and the selected blockage ratio was BR=0.3. Experiments were performed at initial pressure in the range 0.6-4 bar abs for two lean hydrogen/air mixtures: 11.0 %vol and 15.0 %vol H_2.

At atmospheric conditions, mixtures with 11.0 %vol hydrogen identify the lower limit for FA [47]. This condition is defined by the ratio $\sigma/\sigma^* = 1$ (as specified in Table 9.2). By decreasing the hydrogen content, the mixture is not sufficiently energetic and FA is not sustained. As a result, these flames may be partially or totally quenched depending on the obstacle blockage ratio. The present study may allow to verify the validity of this limit for FA in case of pressure increase.

Additionally, a more reactive and stable mixture was studied (15 %vol H2) in order to provide further elements for the characterization of the different phases of FA, and how they are affected by the variation of the initial pressure.

10.1 Fundamental combustion properties of the investigated mixtures

Fundamental combustion properties of 11 %vol and 15 %vol hydrogen/air mixtures at atmospheric conditions are given in Table 10.1.

Table 10.1: Fundamental combustion properties vs hydrogen content in the mixture at $T_0 = 298$ K, $p_0 = 1$ bar

X_{H2}	11 vol%	15 vol%
T_b [K]	1173.0	1472.1
σ	3.72	4.57
c_{su} [m/s]	366.0	373.8
c_{sb} [m/s]	683.2	767.4
p_{AICC}/p_0	4.55	5.54
p_{CJ}/p_0	8.58	10.6
U_{CJ} [m/s]	1340	1524
$U_{\mathrm{CJ,def}}$ [m/s]	617.4	719.9
S_L^0 [m/s]	0.0462	0.2396
δ_L^{th} [mm]	1.88	0.60
$\delta_L^{h'}$ [mm]	0.66	0.14
E_a/R [K]	11068	19357
n	-0.14	1.09
β	7.04	10.58
$\mathrm{Le_{eff}}$	0.404	0.437
$\beta\,(\mathrm{Le_{eff}} - 1)$	-4.20	-6.0

Hereinafter, the influence of initial pressure on the main combustion parameters are discussed. It is important to remind that the thermodynamics properties σ, c_{su}, p_{AICC}/p_0, p_{CJ}/p_0, U_{CJ} and $U_{\mathrm{CJ,def}}$ are independent on the initial pressure.
Figures 10.1a and 10.1b present the variation of the laminar burning velocity S_L and L_T/δ_L in the range $0.6 < p_0 < 4$ bar abs for 11 %vol hydrogen mixtures. As detailed in Chapter 3, for $L_T/\delta \lesssim 100$, geometry plays an important role in the flame propagation mechanisms. As shown in Figure 10.1, by increasing the initial pressure, the ratio L_T/δ decreases and becomes lower than this threshold value. According to Law [89], for lean mixture the activation energy increases as pressure increases. Since the adiabatic flame temperature is essentially independent on pressure (for $p_0 < 10$ bar), the Zeldovich number is supposed to vary in the same way as the activation energy. Considering that the Lewis number is an invariant of pressure, $\mathrm{Le}(p) = \mathrm{const} = 0.347$ (for very lean hydrogen air mixtures $\mathrm{Le_{eff}} \simeq \mathrm{Le}$), the product $\beta\,(\mathrm{Le} - 1)$ is always negative and lower than the stability threshold value -2. Moreover, by assuming that T_b remains constant, we assume that the speed of sound in the burnt gas is not affected by pressure variations.
In Table 10.2, fundamental combustion parameters for 15 %vol hydrogen mixtures are listed as a function of the initial pressure. Differently from the previous case, for 15 %vol hydrogen mixtures, the ratio L_T/δ_L increases with pressure. According to the experimental results of [79], the detonation cell width λ decreases in increasing the initial pressure.

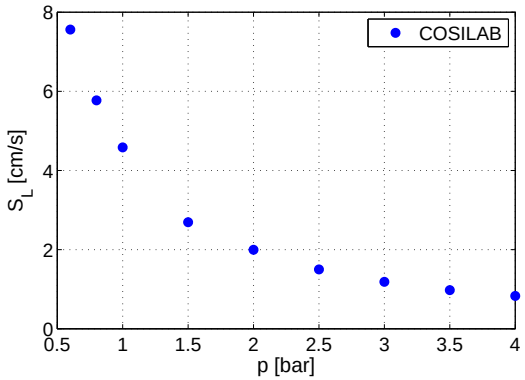

(a) Laminar burning velocity.

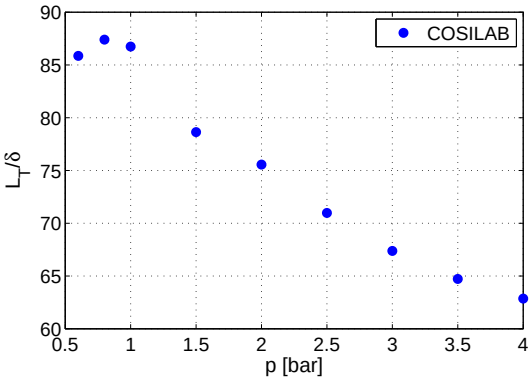

(b) Turbulent length scale over laminar flame thickness

Figure 10.1: Influence of the initial pressure p_0 on fundamental combustion parameters for 11 %vol H2/air mixture ($\phi = 0.296$).

For 15 %vol hydrogen mixtures, this trend is predicted by equation (2.51) up to $p_0 = 2$ bar, where λ reaches a minimum value; for $p_0 > 2$ bar, an increase of the detonation cell width is obtained.

Table 10.2: Fundamental combustion properties as a function of the initial pressure p_0 for 15 %vol hydrogen/air mixture, $T_0 = 300$ K.

p_0 [bar]	0.60	1.00	2.00
S_L [cm/s]	29.48	24.11	16.53
δ_L^{th} [mm]	1.01	0.62	0.38
δ_L^{h} [mm]	0.44	0.32	0.24
L_T/δ_L^h	273.0	375.9	510.2
σS_L [cm/s]	134.0	109.6	75.12
E_a/R [K]	16024	19357	24947
β	8.66	10.5	13.5
$\mathrm{Le_{eff}}$	0.45	0.44	0.42
$\beta(\mathrm{Le_{eff}} - 1)$	−4.77	−5.89	−7.78
λ [cm]	34.42	28.89	23.99

Eventually, we would like to spend few words on the criteria for FA given in Chapter 3. As described above, an increase in the initial pressure results in an increase of the activation energy and in a decrease of the product $\beta(\mathrm{Le} - 1)$. In Table 10.3 a comparison among equations (3.6), (3.9) and (3.8) is given. Data used to compute σ^* are taken from Table 10.2. In the last row, the activation energy is computed according to the expression given in [47]: $\Theta = \Theta(\phi)$; since ϕ is constant, no variation in the value of σ^* are predicted by equation (3.8). On the other hand, by referring to the data presented in Table 10.2, an increase of pressure results in an increase of the value of σ^*. An opposite trend is,

instead, obtained with equation (3.9). Nevertheless, results presented in Table 10.3 must be considered only from a qualitative point of view because of the differences in the values of the activation energy and the Zeldovich number determined in the different studies.

Table 10.3: σ^* as a function of the initial pressure p_0.

p_0 [bar]	0.60	1.00	2.00
σ^* [eq. (3.6)]	3.75	3.75	3.75
σ^* [eq. (3.9)]	4.02	3.94	3.79
σ^* [eq. (3.8)]	5.83	6.34	7.29
σ^* [eq. (3.8) with $\Theta(\phi)$]	4.23	4.23	4.23

10.2 Instrumentation diagnostics location

For the sake of clarity, in Table 10.4 the disposition of the sensors all along the tube is summarized. Here the origin $x = 0$ corresponds to the origin of the fluid domain (see also Table 5.2). For further details on the combustion diagnostics, please refer to Chapter 7.

Table 10.4: Instrumentation configuration.

Location [mm]	**Shock sensors**	**Pressure sensors (type)**	**Photomultiplier tubes**
265			PMT1
460	CC1	PP1 (6001)	PMT2
655	CC2	PP2 (7001)	PMT3
850	CC3	PP3 (6001)	PMT4
1045	CC4	PP4 (601A)	PMT5
1575	CC5	PP5 (7001)	PMT6
1770	CC6		PMT7
1965	CC7	PP6 (7001)	PMT8
2160	CC8		PMT9
2355	CC9	PP7 (7001)	PMT10
2885	CC10		PMT11
3080	CC11	PP8 (7001)	PMT12
3275	CC12		PMT13
3470	CC13	PP9 (7001)	PMT14
3665	CC14		

10.3 Results and discussion

10.3.1 11 %vol hydrogen/air mixture

In Figure 10.2, signals from Test 1 ($X_{H2} = 0.109$ and $p_0 = 0.6$ bar) are presented in a 70 ms time window. In the graph, signals are plotted according to their non-dimensional position x/D along the tube. The thick black lines identify the end of each tube section. Both raw pressure signals (light gray lines) and filtered ones (red lines) are presented in Figure 10.2. For this test PP1, PP3 and PP4 were not thermally shielded. As a result, by comparing their output signals with the ones from PP2, we can note that these sensors undergo a more important thermal load.
PMT output signals are also plotted in black in Figure 10.2. The time-of-arrival diagram of the flame tip, extrapolated from photomultiplier tubes response, is also presented with a blue line. For the sake of clarity, shock sensor output signals are not shown in the graph.
The saw-tooth profile of the pressure signals visible in Figure 10.2 is caused by the shock waves reflecting on the end-flange. According to the present results, for $p_0 \leq 1000$ mbar, a quasi-mono-dimensional leading shock wave is formed. Post-processing pressure signals from Test 1, we found that, after the first reflection at the end of the tube, the shock wave propagates at almost $U_s = 701$ m/s. At each reflection its velocity decreases: $U_s = 655$ m/s after the second reflection, $U_s = 630$ m/s after the third one, $U_s = 594$ m/s after the fourth one and so on. The shock wave is therefore less energetic at each step. As the initial pressure is increased, the leading shock wave can no longer be considered mono-dimensional. As a result, pressure signals are characterized by a multitude of peaks with the same frequency (corresponding to a sound wave traveling along the tube) but different phase (see Figure 10.4a and Figure 10.5a).
The influence of the initial pressure on the flame velocity is shown in Figure 10.3. Test cases were sorted in two groups depending on the hydrogen concentration given by gas-chromatographic analysis: $X_{H2} = 0.109$ in Figure 10.3a and $X_{H2} = 0.111$ in Figure 10.3b. In the first stage of flame acceleration no significant differences with pressure variation are observed. Thus, even if the laminar burning velocity decreases of a factor 9 from 0.6 bar to 4 bar (as shown in Figure 10.1), this seems to have little influence on the first phase of flame acceleration. Therefore other parameters intervene in compensating the decrease in the laminar flame speed, such as Lewis and Zeldovich numbers.
Moreover, as pressure increases, L_T/δ_L becomes lower than 100. According to Borghi's diagram, these flames are more susceptible to slowdown and eventually quench if the turbulence in the gas flow ahead of the flame increases. Nevertheless, in the present study global flame quenching is not observed. As shown in Figure 10.3, the last stage of flame propagation (starting approximately with the 20th obstacle) is characterized by a decrease of flame velocity. This slowdown is more pronounced as the initial pressure increases. At the end of the tube, the flame front is also perturbed by the reflected pressure wave. As the reflected shock interacts with the flame, hydrodynamic forces tend to slow it down. From the literature we know that flame-shock interaction can trigger DDT. This is true for highly reactive mixtures, in which the heat release due to combustion compensate the flame cooldown by the fresh mixture pushed into the reaction zone by the shock wave. In the present tests, as expected, DDT is not observed, since the mixture is not sufficiently reactive (DDT criteria are not satisfied: $d/\lambda < 1$).
The pressure variations recorded by PP6 and PP9 for three tests at different initial pres-

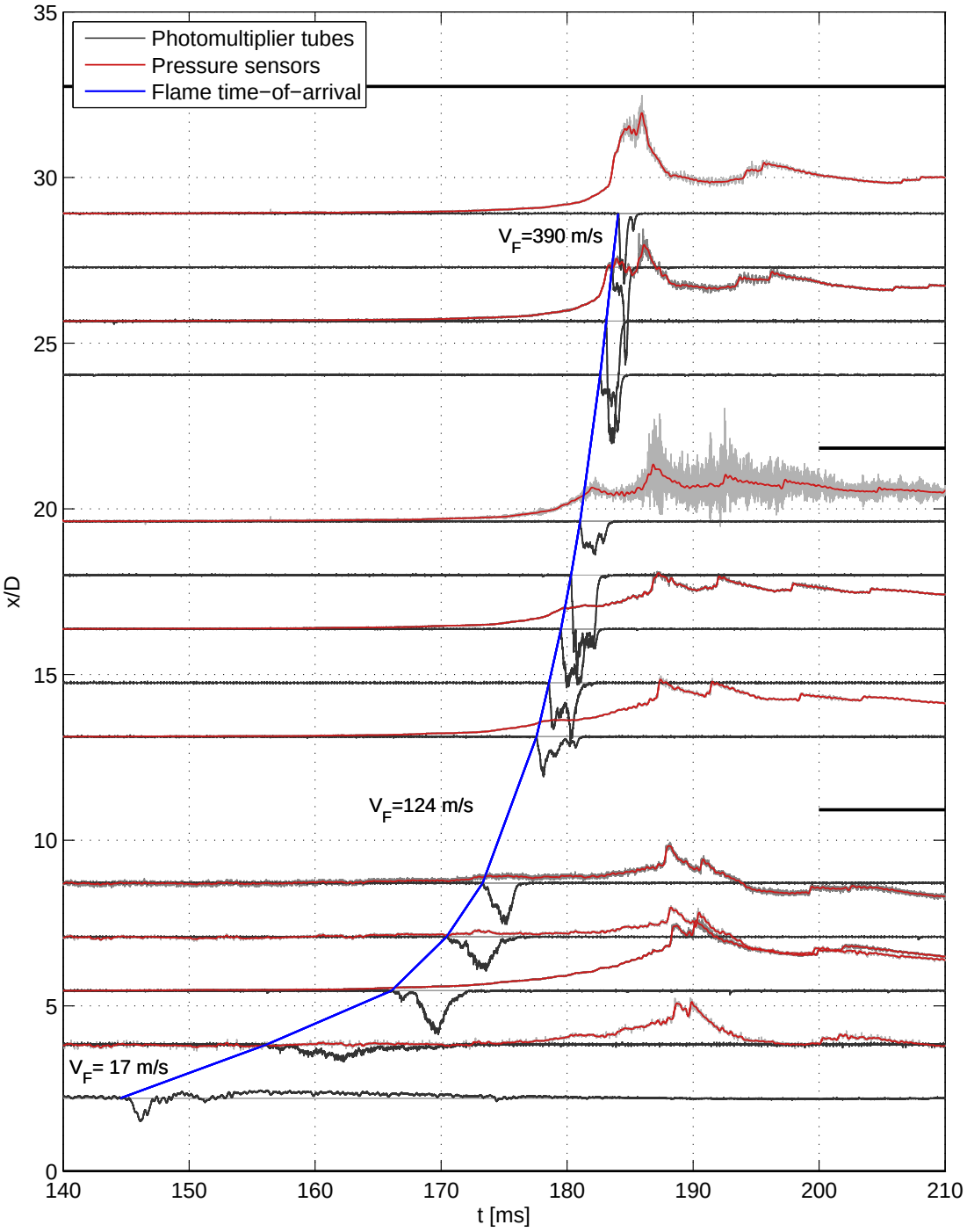

Figure 10.2: Test 1: $p_0 = 600$ mbar and $X_{H2} = 0.109$. Cut-off frequency on pressure sensors output signal $f_c = 3200$ Hz.

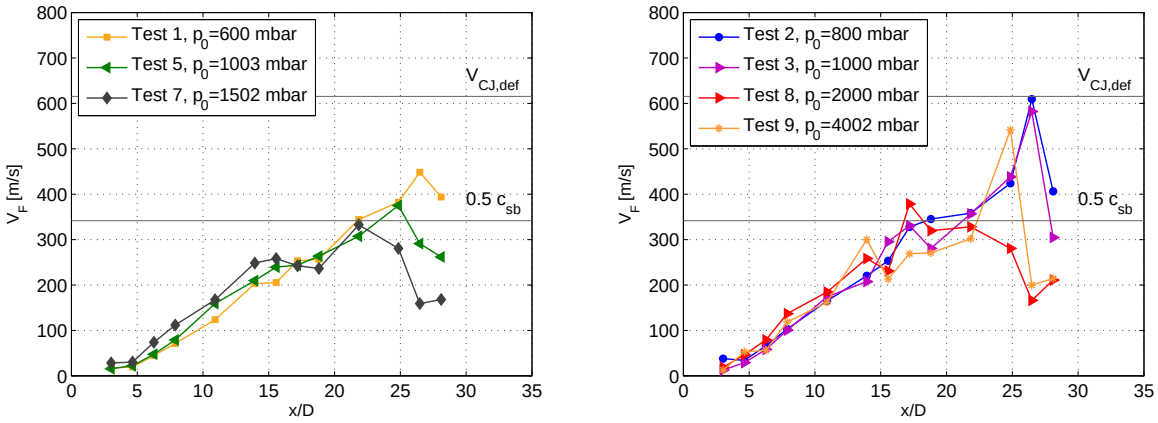

(a) $X_{H2} = 0.109$ **(b)** $X_{H2} = 0.111$

Figure 10.3: Flame tip velocity as a function of the initial pressure.

sure are given in Figure 10.4 and Figure 10.5. Curves are shifted in time on the basis of PMT time-response at the correspondent pressure sensor location. Flame tip ToA is also presented in the graphs with a vertical black line.

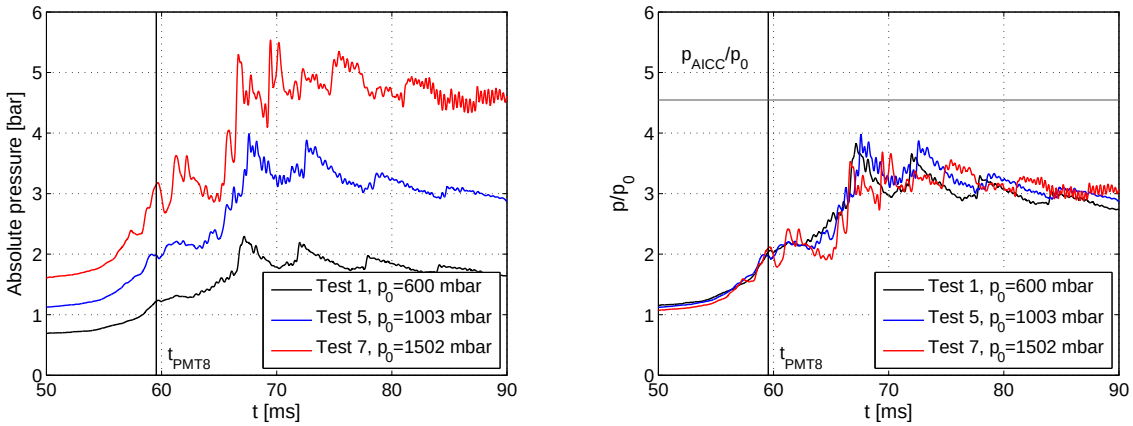

(a) **(b)**

Figure 10.4: Influence of the initial pressure p_0 on the pressure peaks recorded by PP6 (f_c = 3200 Hz) for $X_{H2} = 0.109$: (a) absolute pressure; (b) absolute pressure to initial pressure ratio.

As the initial pressure is increased, the signals show a more oscillating profile. The frequency of these oscillations matches f_a (ref. (8.1)). Therefore, the amplitude of acoustic waves in the burnt gas becomes more important as the initial pressure increases. In Figure 10.4b and Figure 10.5b, the absolute pressure to the initial pressure ratio is presented. Here, we can see that the pressure increase due to the combustion reaction is directly proportional to the initial pressure, as for the case of an adiabatic isochoric complete combustion or for a CJ detonation (transformation governed only by thermo-dynamics). For completeness, the values of the adiabatic isochoric combustion pressure p_{AICC} and of

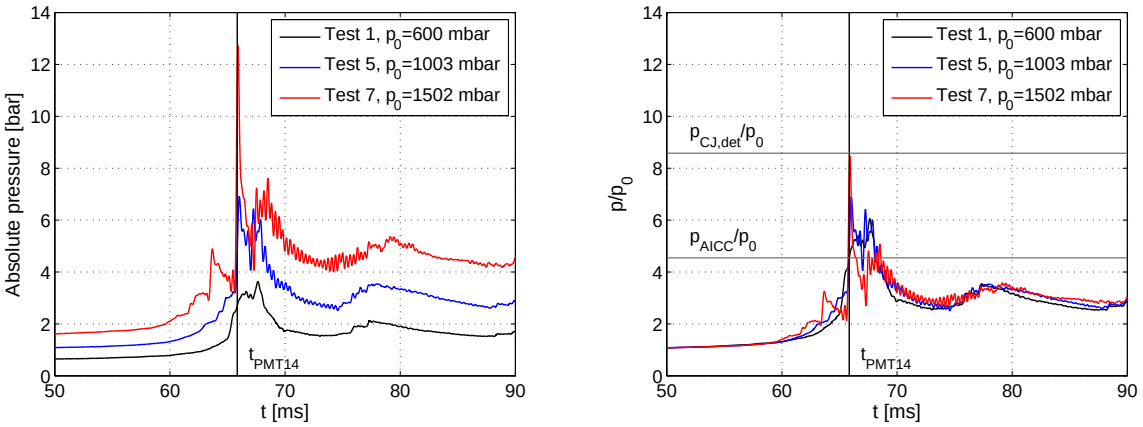

Figure 10.5: Influence of the initial pressure p_0 on the pressure peaks recorded by PP9 (f_c = 3200 Hz) for $X_{H2} = 0.109$: (a) absolute pressure; (b) absolute pressure to initial pressure ratio.

the CJ detonation pressure p_{CJ} are also presented in Figure 10.4b and Figure 10.5b.

10.3.2 15 %vol hydrogen/air mixture

In Figure 10.6 the effect of initial pressure on flame velocity for hydrogen/air mixture with $X_{H2} = 0.15$ is presented. Results are given in terms of average values over two shots. Error bars identify maximum and minimum values of the shots. For $p_0 = 0.6$ and 1 bar, velocity profiles are perfectly superposed up to $x/D = 15$. For p_0 equal to 2 bar, instead, a greater acceleration rate is observed from the early stages of flame propagation. This results in a decrease of the run-up distance.
As pointed out in Table 10.2, the laminar burning velocity and, thus, the apparent initial flame velocity, σS_L, decrease as pressure increases. On the other hand, the product $\beta\,(\mathrm{Le}_{\mathrm{eff}} - 1)$ becomes more negative. Therefore, the increase of the acceleration rate in the first phase of flame propagation could be attributed to the variation of thermo-diffusive parameters. As the flame becomes faster, a leading shock wave is formed: the precompression of the gas ahead of the flame is directly proportional to the initial pressure (see Figure 10.7a). This effect may, therefore, compensate the decrease in the laminar burning velocity and, combined with flame-shock interaction, effectively promote FA.
A spike in the velocity profile, corresponding to detonation initiation, appears for all the investigated cases. However, it occurs at different locations along the tube: for $p_0 = 0.6$, the maximum velocity is measured at $x/D \simeq 18$; for $p_0 = 1$ bar, detonation initiation takes place at $17 < x/D < 18$ depending on the test; while, for $p_0 = 2$ bar, the peak is anticipated at $x/D \simeq 15$. Nevertheless, for all the tests, detonation fails rapidly. As expected, since the thermodynamic properties of the mixtures do not vary with pressure, the asymptotic condition is the same for all the considered cases.
In Figures 10.7 and 10.8 pressure signals recorded by PP6 and PP9 dynamic pressure sensors are shown. For the sake of clarity only filtered signals are plotted (f_c = 4500 Hz). As previously described, signals are synchronized on the basis of flame ToA at the

corresponding PMT. In consistency with the signals presented in the previous section (Figures 10.4 and 10.5), the amplitude of the acoustic waves is strongly reduced for lower initial pressure. As expected, for 15 % hydrogen mixture the pressure increase is much sharper than the one obtained from the combustion of the leaner mixture (due to the higher Mach number). Also in this case the overpressure due to combustion is proportional to p_0. Note that in Figure 10.7b, for the test case with $p_0 = 1$ bar, a higher pressure peak is recorded: this discrepancy is due to the fact that detonation occurs close to PP6.

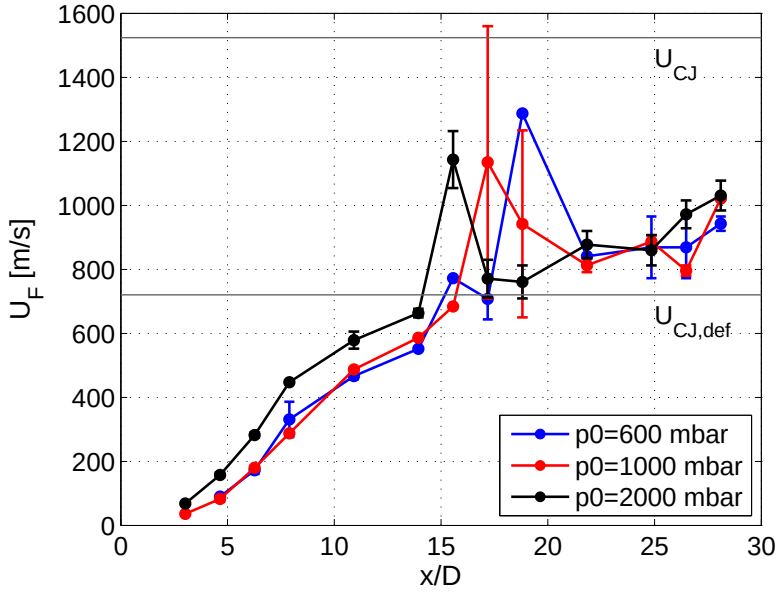

Figure 10.6: Flame tip velocity along the tube axis for 15 %vol hydrogen mixtures as a function of the initial pressure.

10.4 Conclusion

The effect of the initial pressure on flame acceleration for lean hydrogen/air mixtures was experimentally investigated. The initial pressure was varied in the range 0.6-4 bar abs. For very lean mixtures ($X_{H2} \simeq 0.11$), in the early stages of flame acceleration, no significant changes were observed. In the central section of the combustion tube, where the velocity increase is almost constant, a wide data dispersion was noticed. However, this spread is similar to the one encountered in the sensitivity study of Figure 9.2. Moreover, even though the laminar burning velocity decreases of almost one order of magnitude from 0.6 to 4 bar (see Figure 10.1), this seems to have little influence on the first phase of flame acceleration. The decrease of the product σS_L is probably compensated by the variation of the Zeldovich number which governs thermal instabilities. As the flame becomes faster, the precompression of the gas ahead of the flame induced by the leading shock wave may also contribute in promoting FA.
As the initial pressure was increased, we observed a decrease in the flame tip velocity close to the end of the tube. The reason of this flame slowdown is mainly due to the interaction

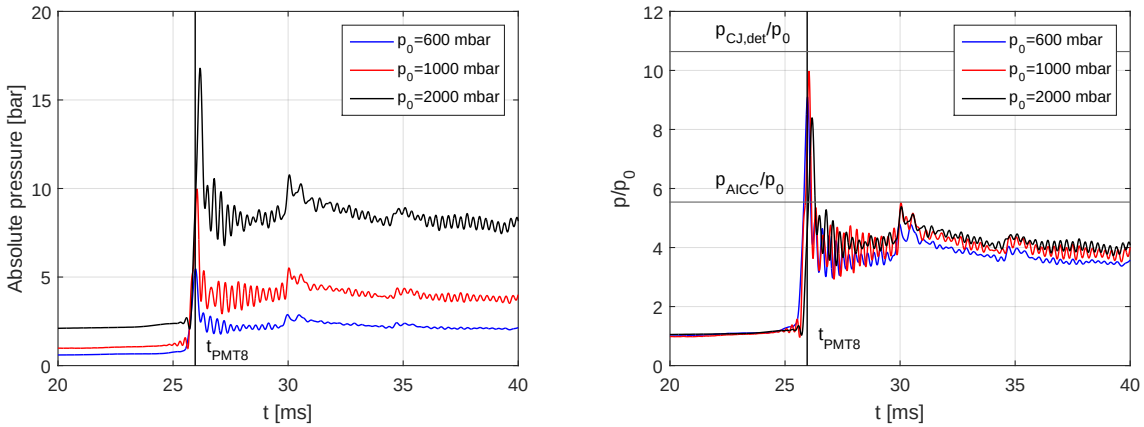

(a) **(b)**

Figure 10.7: Influence of the initial pressure p_0 on the pressure peaks recorded by PP6 (f_c = 4500 Hz): (a) absolute pressure; (b) absolute pressure to initial pressure ratio.

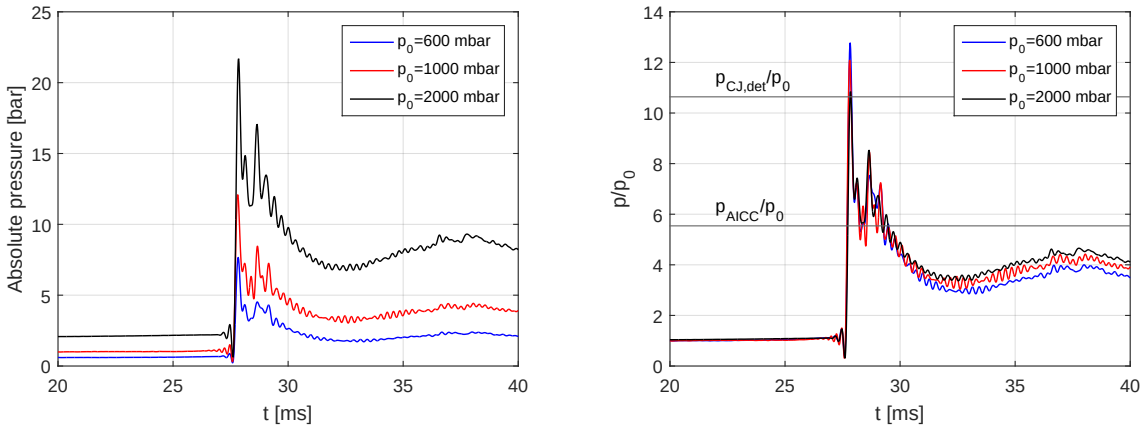

(a) **(b)**

Figure 10.8: Influence of the initial pressure p_0 on the pressure peaks recorded by PP9 (f_c = 4500 Hz): (a) absolute pressure; (b) absolute pressure to initial pressure ratio.

between the reflected shock wave and the flame. Figure 10.4b and Figure 10.5b show that the overpressure due to the combustion is directly proportional to the initial pressure. Therefore, as pressure increases, the hydrodynamic force generated by the reflected shock wave and acting on the flame becomes stronger, slowing it down in its propagation along the tube.
For hydrogen/air mixture with 15 % H2, an increase in the initial pressure results in a higher acceleration rate. A shorter run-up distance is therefore measured for $p_0 = 2$ bar. The increase of the acceleration rate may be related to the development of flame cellularity ($\beta\,(\mathrm{Le}_{\mathrm{eff}} - 1)$ becomes more negative as pressure increases). A recent numerical and experimental study performed at TUM [65] showed that the enhancement of flame wrinkling due to pressure collapses after a short distance from the ignition. Therefore, the effect of thermo-diffusive instabilities should be important only in the first phase of flame propagation. Then, flame-shock interaction should take over.
In terms of combustion generated loads, an increase of p_0 results in a linear increase of the pressure on structures. Moreover, since for highly reactive mixtures the acceleration rate increases with pressure, fluid inertia ($\propto dU/dt$) and drag forces ($\propto \rho U^2$) become more important. As a consequence, in terms of severe accident management, the risk of structural damages due to hydrogen explosions occurring at high pressure inside the reactor containment shall be carefully considered in the safety analysis.

Chapter 11

Effect nitrogen dilution on flame acceleration process

In the present chapter we focus our attention to hydrogen/oxygen/nitrogen mixtures. BWR (Boiling Water Reactors) containments of type MARK-I and MARK-II are inerted with nitrogen in order to reduce the risk of hydrogen explosions in case of severe accidents. This is the main reason why flame acceleration mechanisms of nitrogen-diluted H2/air mixtures have been investigated in the literature [82, 86].
Moreover, in this study nitrogen was chosen as dilutant in order to modify some combustion parameters of hydrogen/air flames. The objective is to replace part of the oxygen with nitrogen in order to study its influence in flame acceleration mechanisms. The hydrogen content in the investigated mixtures was kept constant and equal to 15 %vol, while the nitrogen-to-oxygen ratio was increased from 3.76 (synthetic air) to 8.44. This corresponds to an increase of the equivalence ratio from 0.42 to 0.83 (near stoichiometric condition). Three over four sections of the combustion tube were used to perform this experimental campaign. An array of uniformly distributed annular obstacles with BR= 0.3 was placed inside the tube. Sensors location is detailed in Table 10.4.

11.1 Fundamental combustion properties of the investigated mixtures

In Table 11.1 combustion fundamental parameters are listed as a function of the equivalence ratio ϕ. Since oxygen and nitrogen have similar physical and transport properties, by varying the ratio $X_{\mathrm{N2}}/X_{\mathrm{O2}}$ in the mixture, combustion thermodynamic properties are almost conserved. Less than 10% difference in the fundamental burning velocity was found varying the equivalence ratio from $\phi = 0.42$ to $\phi = 0.83$. On the other hand, those parameters that govern flame thermo-diffusive instabilities strongly vary: the product $\beta(\mathrm{Le}_{\mathrm{eff}} - 1)$ becomes less negative as the equivalence ratio increases. As a result, nitrogen dilution tends to stabilize hydrogen/air flames.
As shown in Chapter 10, the increase of the initial pressure has an effect on both the laminar flame velocity and the product $\beta(\mathrm{Le}_{\mathrm{eff}} - 1)$; therefore, it is difficult to infer *a priori* which phenomenon has a greater impact on flame acceleration. In this case, instead, the variation of the the laminar burning velocity is milder and therefore any changes in flame

propagation are more likely due to thermo-diffusive parameters.

Table 11.1: Fundamental combustion properties for 15% H2/O2/N2 mixtures as a function of the equivalence ratio ϕ, at $T_0 = 300$ K and $p_0 = 1$ bar.

$\boldsymbol{\phi}$	**0.42**	**0.60**	**0.83**
X_{O2}	0.18	0.12	0.09
$X_{\mathrm{N2}}/X_{\mathrm{O2}}$	3.76	5.85	8.44
σ	4.54	4.55	4.56
T_b [K]	1474	1477	1479
c_{su} [m/s]	375.1	376.8	377.8
p_{AICC} [bar]	5.54	5.56	5.57
p_{CJ} [bar]	10.64	10.68	10.70
U_{CJ} [m/s]	1524	1534	1540
$U_{\mathrm{CJ,def}}$ [m/s]	719.9	724.1	726.9
S_L [cm/s]	24.10	23.16	21.75
δ_L^{th} [mm]	0.62	0.67	0.78
δ_L^{h} [mm]	0.32	0.34	0.36
L_T/δ_L^h	375.9	354.8	333.9
σS_L [cm/s]	109.5	105.5	99.21
E_a/R [K]	19357	17565	14959
β	10.46	9.48	8.06
$\mathrm{Le_{eff}}$	0.44	0.51	0.68
$\beta(\mathrm{Le_{eff}} - 1)$	−5.89	−4.68	−2.60

11.2 Results and discussion

As shown in Figure 11.1, by varying the ratio $X_{\mathrm{N2}}/X_{\mathrm{O2}}$, in the early stages of flame propagation no significant changes can be observed. Moreover, flame velocity profiles of nitrogen diluted mixtures are almost coincident all along the combustion process. A different behavior is, instead, observed for hydrogen/air mixtures as $x/D > 7$. In particular, detonation initiation and failure is observed in the central zone of the combustion tube. In the last section of the device a saturation velocity above the CJ deflagration velocity is reached. All the investigated mixtures show a similar behavior in this zone.
In nitrogen-diluted mixtures detonation initiation and failure did not occur, in agreement with the findings of [82] for mixtures with 13 %vol hydrogen (see Figure 11.2). On the other hand, in contrast with the experimental results of [82], in the present study the increase of the run-up distance with the nitrogen content is less pronounced. From the comparison of the fundamental combustion properties of 13 %vol and 15 %vol H2/air mixtures, given in Table 11.2, we can see that the Zeldovich number β is greater for the leaner mixture, whereas the effective Lewis number only slightly varies.
From Figures 11.1 and 11.2, it can be noted that, as the product $\beta(\mathrm{Le_{eff}} - 1)$ becomes more negative, thermo-diffusive instabilities tend to promote flame acceleration. As a

Table 11.2: Fundamental combustion properties of 13 %vol and 15 %vol H2/air mixtures at $T_0 = 298$ K, $p_0 = 1$ bar

X_{H2}	13 vol%	15 vol%
T_b [K]	1323.5	1472.1
σ	4.15	4.57
S_L^0 [m/s]	0.1092	0.2396
c_{su} [m/s]	369.9	373.8
δ_L^{th} [mm]	0.98	0.60
E_a/R [K]	21144	19357
n	0.47	1.09
β	12.36	10.58
$\mathrm{Le_{eff}}$	0.403	0.437
$\beta\,(\mathrm{Le_{eff}} - 1)$	-7.4	-6.0

result, the acceleration rate increases and the run-up distance decreases. Nevertheless, a non-linear behavior is observed: for low values of $|\beta(\mathrm{Le_{eff}} - 1)|$, the acceleration rate seems to be less sensitive to variations in the thermo-diffusive parameters.
In Figures 11.3 and 11.4, pressure signals recorded by Kistler sensors PP6 and PP9 are presented. Here, three tests with different nitrogen-to-oxygen ratio are compared. Signals are synchronized on the basis of flame ToA measured by the adjacent photomultiplier tube (vertical line in Figure 11.3). In the left-hand side of Figures 11.3 and 11.4 raw signals are presented, while in the right-hand side filtered signals ($f_c = 4500$ Hz) are shown. Clearly, filtered signals are useful to qualitatively analyze sensor responses.
Starting from Figure 11.4, we can see that pressure signals perfectly match in terms of pressure amplitude, frequency and phase. This result is coherent with data presented in Table 11.1, since the thermodynamic properties of the three mixtures are similar. In terms of combustion generated loads, the three mixtures give the same loading process at the end of the tube, where the choked flame regime is reached.
On the other hand, in the central zone of the combustion tube pressure loads are more important for the case in which hydrogen is mixed with air. In this case, in fact, as described above, detonation initiation and failure is observed. As a result, the corresponding pressure signal is much steeper and the pressure peak is greater. In fact, a detonation-like load with a strong discontinuity across the leading shock wave is observed in Figure 11.3 for the hydrogen/air mixture, while for the nitrogen-diluted mixtures a smoother pressure increase, typical of fast turbulent flames, is obtained.

11.3 Conclusions

The effect of nitrogen dilution for a 15% hydrogen/air mixture has been investigated. Results show that diluted mixtures do not incur detonation initiation and failure, in contrast to pure hydrogen/air mixtures. Similar results were also obtained by Kuznetsov et al. [82]. As expected, the final phase of flame propagation, governed only by thermodynamics, is similar for all the investigated mixtures since thermodynamic parameters are only slightly varied. On the other hand, a difference is observed between the results of [82] and those

of the present study concerning the first phase of flame acceleration. As a matter of fact, in our case only slight changes can be noticed in FA by diluting the flammable mixture with nitrogen, even though β increases. In Figure 11.2, instead, a strong decrease in the acceleration rate is observed. A possible explanation for this difference may be found in a non-linear effect of the product $\beta(\mathrm{Le}-1)$: if $\beta(\mathrm{Le}-1) \gtrsim -5$, thermo-diffusive phenomena seem not to affect FA mechanisms, in coherence with the results of Chapter 10.
For a deeper knowledge on nitrogen-diluted hydrogen/air mixtures, flame surface visualization at different stages of FA would be advisable. In this way, it would be possible to monitor the evolution in time of the flame cellular structure. By comparing the flame surface area with the flame velocity or acceleration in the region $x/D < 5$, it is possible to determine when and where thermo-diffusive phenomena are predominant. Whereas, an optical access to the region $15 < x/D < 20$ may allow a more detailed analysis on the phenomena associated with detonation initiation and failure.

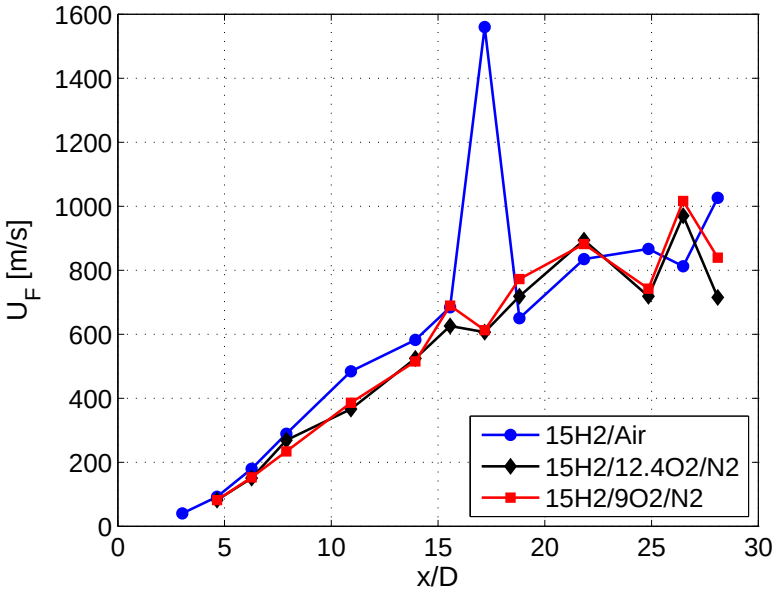

Figure 11.1: Flame speed profile along the tube axis for flammable mixtures with 15 %vol hydrogen and BR= 0.3: effect of the variation of the ratio N_2/O_2.

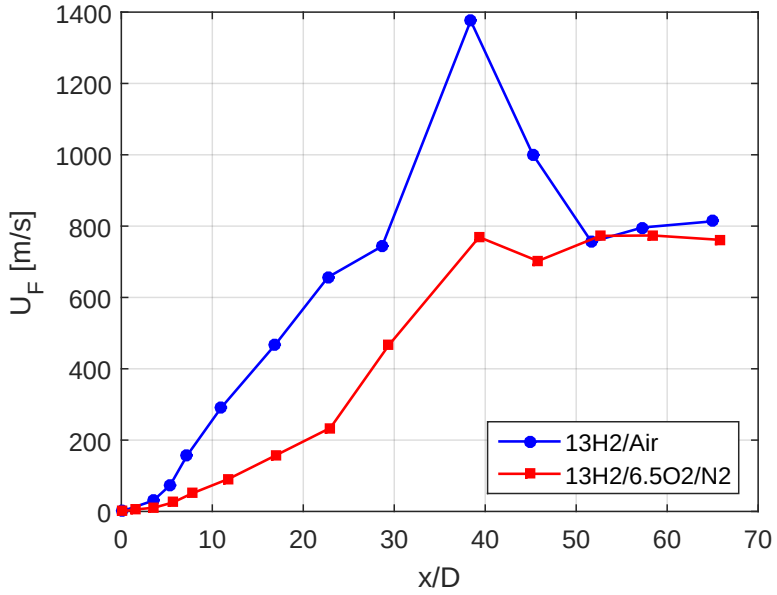

Figure 11.2: Experimental results of [82] with 13 %vol hydrogen and BR= 0.3: effect of the variation of the ratio N_2/O_2.

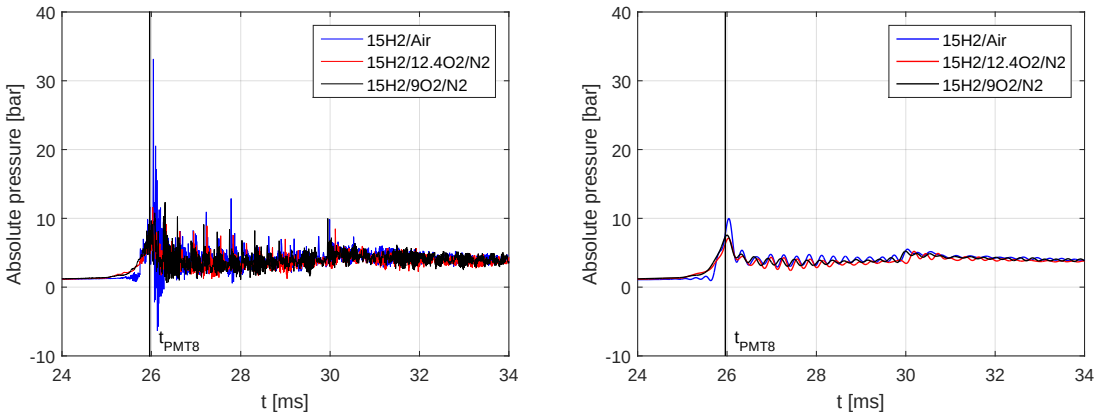

(a) Raw signals. **(b)** Filtered signals, $f_c = 4500$ Hz.

Figure 11.3: Influence of the ratio N_2/O_2 on the pressure signals recorded by PP6.

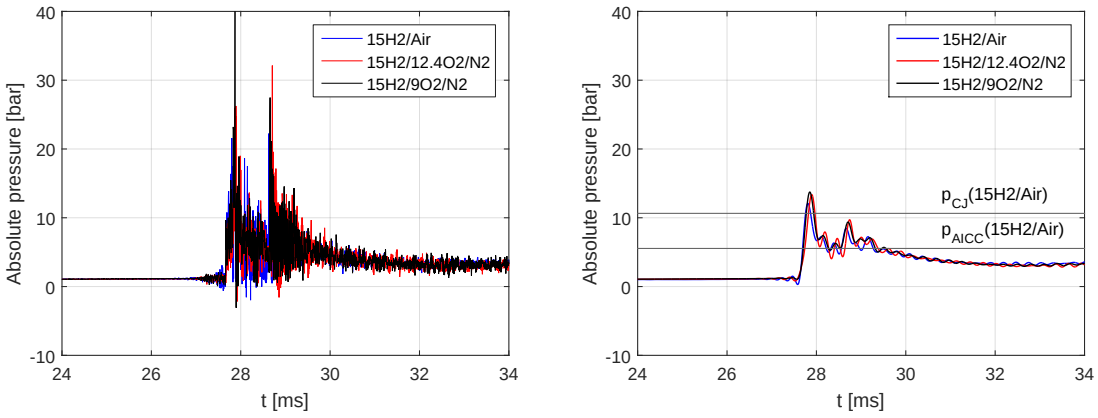

(a) Raw signals. **(b)** Filtered signals, $f_c = 4500$ Hz.

Figure 11.4: Influence of the ratio N_2/O_2 on the pressure signals recorded by PP9.

Part IV

Feasibility study of a new technique for flame front tracking measurements

Chapter 12

Feasibility study of a new technique for flame front tracking measurements

In the previous chapters, the flame front velocity was obtained from the post-processing of photomultiplier tubes output signal. These sensors allow the detection of the combustion wave at different points along the tube axis. The velocity of the reflection wave is obtained at the average value between two consecutive sensors. Despite its robustness, this technique is able to capture only the mono-dimensional behavior of the flame front propagation. Moreover, only a coarse representation of the flame acceleration profile can be achieved.
The increasing demand for a deeper knowledge of flame acceleration mechanisms has pushed towards more accurate and sophisticated experimental techniques. An example of these improvements are visualization sections [71, 20]. Associated with Schlieren techniques and even with rapid field measurement techniques, such as Laser Doppler Velocimetry (LDV), Particle Image Velocimetry (PIV) or Planar Laser Induced Fluorescence (PLIF), they provide detailed and exhaustive data for the improvement and the validation process of numerical models.
However, due to the brittleness of windows materials, most of the experiments were generally carried out with lean mixtures or at low initial pressure or even in open ended tubes. Unfortunately, these configuration are not representative of all the accident-related situations. The use of stainless steel tubes equipped with small instrumentation ports and narrow optical accesses remains therefore of great relevance in case of important overpressures. Thereby, the question of how to increase the measurement capabilities of these devices arises.
In the past, [92] performed continuous measurements of the velocity of a detonation wave in smooth copper tubes by using microwave Doppler interferometry technique. Previous attempts were also made by [84] who used a single photo-diode towards the tube axis to identify the transition time from deflagration to detonation. Oxygen light absorption measurement in detonation tubes, recently implemented by [23] to record variations in the equivalent ratio, constitutes a further example of time-resolved techniques.
In the present chapter we develop a new technique to track the flame front position along the tube. This method consists in performing time-resolved IR absorption measurements by doping the fresh mixture with an alkane. The velocity profile is then derived by measuring the variation of the extension in depth of the unburnt gas along the tube axis.

12.1 Measurement techniques principles

Hydrogen/air mixture are unaffected by IR light; for this reason a small quantity of methane was added to the flammable mixture as tracer. The absorption in the infrared region of the C-H bond at 3.39 μm was then used to monitor the flame front propagation. The advantages of using an alkane as seeding molecule are (1) the small discrete region of absorption (C-H bond in "stretching mode" between 2850 and 2960 cm^{-1}) and (2) its presence only in the unburnt gases. The measurement technique foresees the use of a laser beam in the mid-IR region that is attenuated by an absorbing gaseous medium. Gaseous transmittance τ is given by the Beer-Lambert law:

$$\tau = \frac{I}{I_0} = \exp\left(-\frac{s_i X_i p_0 l_t}{R T_0}\right) \tag{12.1}$$

with I the measured intensity, I_0 the light intensity throughout a non-absorbing medium, X_i the molar fraction of the absorbing chemical species, p_0 the total pressure, T_0 the temperature, l_t the length of the seeded zone, s_i the absorption cross-section and R the perfect gas constant. If we suppose that only methane intervenes in absorbing IR light, $X_i \equiv X_{CH_4}$ and $s_i \equiv s_{CH_4}$.
Methane absorption-cross section was determined in our laboratory at ambient temperature and pressure by using the device shown in Figure 12.1 (cf. [102]). The test cell features a stainless steel flanged tube with two sapphire windows at the extremities. The total length of the inner volume is 217 mm. The two windows allow the laser beam to pass through the test section. Helium-Neon Thorlabs H339P2 laser with 2 mW power was used to produce a beam at 3.39 μm. The laser beam is then chopped at 4000 Hz. Gaseous transmittance was recorded by a Thorlabs PDA20H PbSe detector placed at the end of the optical path. To reduce the influence of the environment surrounding the HeNe laser, a second detector (designated as reference detector in Figure 12.1) is used in common-mode-rejection layout. The transmittance is then normalized as follows:

$$\tau = \left.\frac{I}{I_0}\right|_{\text{det}} \cdot \left.\frac{I_0}{I}\right|_{\text{ref}} = \left.\frac{V^{100\%} - V}{V_0^{100\%} - V_0}\right|_{\text{det}} \cdot \left.\frac{V_0^{100\%} - V_0}{V^{100\%} - V}\right|_{\text{ref}} \tag{12.2}$$

where the subscripts "det" and "ref" refer to the measurement detector and the reference one respectively, while the superscript 100% refers to the case when light is completely absorbed, i.e. when the laser is cut by a chopper blade.
An important thing to stress out when interpreting Thorlabs PDA20H PbSe detectors output signal is that 0 V output signal corresponds to the time-averaged light intensity (for steady-state measurements - AC coupled detector). As the laser beam is chopped by a blade, the detector send a positive voltage output. On the other hand, when the sensitive area of the detector is enlightened, a negative voltage is provided. Light intensity is given by the amplitude of the oscillating wave response.
Results are given in Table 12.1 and Figure 12.2. They were found to be in accordance with the data existing in the literature [52, 111, 149, 139, 78]. Dependence of s_{CH_4} on the total pressure was derived as well, as shown in Figure 12.2.
The uncertainty related to the measure of methane absorption cross section can be derived

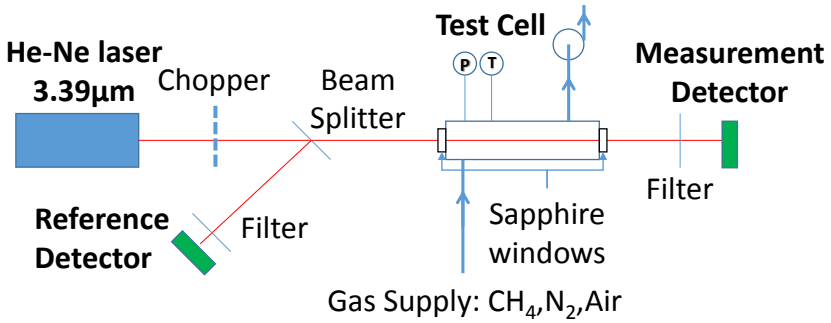

Figure 12.1: Test cell used to evaluate methane absorption cross-section.

Table 12.1: Comparison of $s_{CH_4}/(RT_0)$ at 3.39μm, $p_0 = 1$ atm.

Reference	$\frac{s_{CH_4}}{RT_0}$ [cm.atm]$^{-1}$	T_0 [K]
[52]	8.0	298
[111]	9.2	293
[149]	9.9	298
[139]	9.6	300
[78]	8.2	302
This work	8.2	298

from equation (12.1):

$$\frac{u(s_{CH_4})}{s_{CH_4}} = \sqrt{\left(\frac{u(l)}{l}\right)^2 + \left(\frac{u(\chi_{CH_4})}{\chi_{CH_4}}\right)^2 + \left(\frac{u(p_0)}{p_0}\right)^2 + \left[\left(\frac{u(I_a)}{I_a}\right)^2 + \left(\frac{u(I_0)}{I_0}\right)^2\right]\left(\frac{1}{\ln\frac{I_a}{I_0}}\right)^2}. \tag{12.3}$$

Since all the measurements were performed at constant room temperature, the uncertainty related to the path length can be neglected (no dilatation effects). A value of 6% was obtained for the uncertainty of methane absorption cross section.

12.2 Experimental apparatus

For this R&D study, the combustion tube tube is composed of three sections with a total length of $L = 3930$ mm. It is equipped with annular obstacles (blockage ratio BR = 0.3) located at one diameter distance along the path of the flame. For the IR absorption measurement, two sapphire windows 5 mm thick were installed at both ends of the acceleration tube (see Figure 12.3). Laser optical scheme foresees the same elements described in FIG. 12.1. In addition, a second chopper was installed in front of the measurement detector to deal with flame light emission (as detailed in Chapter 12.3). The initial length of the absorption zone section is $l_t = L = 3930$ mm.
In order to have access to the center line for IR measurements, the electrical spark used to ignite the mixture was moved upward (45 mm from the tube axis), on the gas injection line. Once ignited, the flame propagates along the obstacle-laden tube separating the fresh mixture from the burnt one. Since the quantity of methane is small compared to the other molecules, we can make the hypothesis that no methane remains in the burnt gas

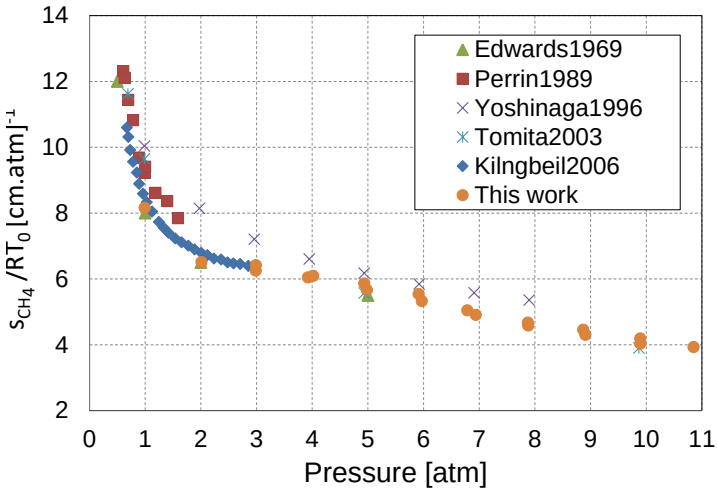

Figure 12.2: Effect of total pressure on methane absorption cross-section at 3.39μm.

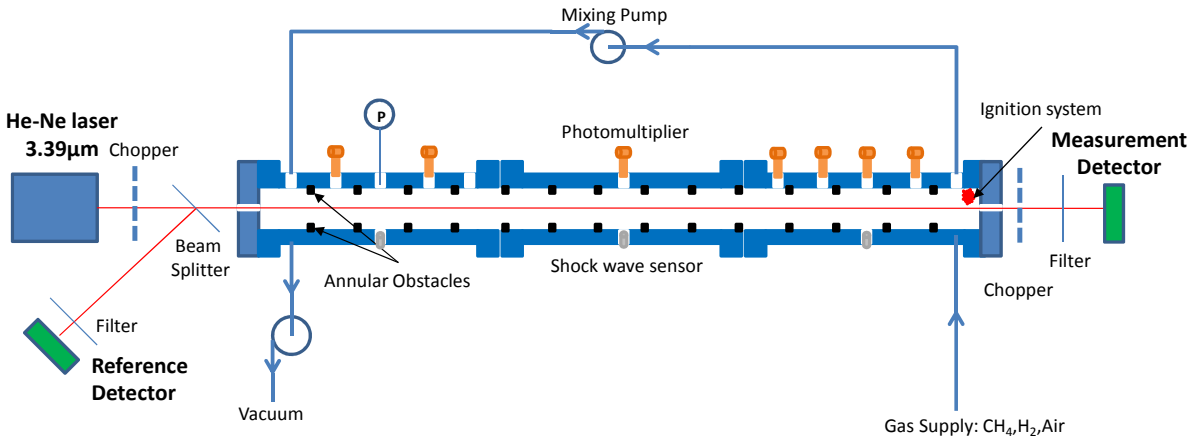

Figure 12.3: Schematic description of the SSEXHY facility for the IR absorption measurements.

(complete combustion of methane). Only lean mixtures ($\phi < 1$) were tested to ensure the latter condition. As a result, while methane is consumed by the flame, the absorbing path decreases and the transmittance across the tube increases. By applying equation (12.1) to time-resolved IR absorption measurement, we obtain the variation of the depth of the fresh mixture in time, as:

$$l(t) = -\frac{RT(t)}{s_{\mathrm{CH_4}}(P(t),T(t))X_{\mathrm{CH_4}}P(t)} \ln\left(\left.\frac{V^{100\%}-V(t)}{V_0^{100\%}-V_0}\right|_{\mathrm{det}} \cdot \left.\frac{V_0^{100\%}-V_0}{V^{100\%}-V(t)}\right|_{\mathrm{ref}}\right). \quad (12.4)$$

The flame tip propagation velocity is obtained deriving equation (12.4) in time:

$$U_{f,\mathrm{tip}} = \frac{\mathrm{d}x(t)}{\mathrm{d}t} = \frac{\mathrm{d}\left[l_t - l(t)\right]}{\mathrm{d}t}, \quad (12.5)$$

where $x(t)$ is the distance from the ignition point. Since we are mostly interested in the early stages of flame propagation, when compressible effects as well as temperature changes in the fresh mixture can be neglected, we can simplify equation (12.4) assuming

$p(t) = p(t_0) = p_0$ and $T(t) = T(t_0) = T_0$. This assumption is valid until either the ratio of burnt/fresh gas volumes exceeds few percents or a leading shock is formed ahead the reaction front. Beyond that, proper correction factors must be used to take into account pressure and temperature variations.

12.3 Experimental results and discussions

IR absorption technique was applied to to two lean hydrogen/air combustion: 23 and 15 vol% of hydrogen in dry air. The former flame is more stable than the latter one in terms of laminar flame stability analysis and, therefore, it presents less cellular structures in the flame front (see pictures of [61]). Combustion fundamental properties of the two mixtures are summarized in Table 12.2.

Table 12.2: Combustion parameters for hydrogen/air mixtures at room temperature and pressure.

Parameter	$X_{H_2} = 15$ %vol	$X_{H_2} = 23$ %vol
S_L [m/s]	0.24	1.11
σ	4.57	6.06
c_{su} [m/s]	374	391
c_{sb} [m/s]	767	914
$U_{\mathrm{CJ,def}}$ [m/s]	720	897
U_{CJ} [m/s]	1524	1812
ν [m^2/s]	1.82×10^{-5}	1.98×10^{-5}

Before performing the tests, several issues were investigated.
First, the effect of methane addition on the flame propagation along the tube was studied. By conducting two tests with and without methane, the results presented in Figure 12.4 show that the small quantity of methane added to the mixture had negligible effects. In Figure 12.4, experimental results are given in terms of average values over three shots. Error bars identify maximum and minimum values of the shots.
The second important issue was the assumption of constant pressure and temperature during the early stage of flame propagation. For the two mixtures without methane addition, the pressure evolution was measured during the beginning of the flame propagation. Results are shown in Figure 12.5. For the 15 %vol hydrogen/air mixture, the pressure increase can be neglected up to PMT2 (see Figure 12.5a). For the 23 %vol hydrogen/air mixture, instead, the overpressure reaches 0.5 barg when the flame approaches PMT2. In this case, the effective methane absorption cross-section decreases in the fresh gas in front of the flame, but this decrease corresponds approximately to the uncertainty on the value of the cross-section. Pressure influence is therefore neglected for the early stages of flame propagation.
Then, the light emitted by the flame itself at 3.39μm was measured. The emission spectrum of hydrogen flames was recently published for a wide range of wavelengths in [8]. According to them, maximum flame irradiance occurs in the mid-infrared. In our experiences, flame emission was measured by turning off HeNe laser and recording $I_e(t)$ during the shot (the subscript e stand for light emission). Results for the 15 %vol and 23 %

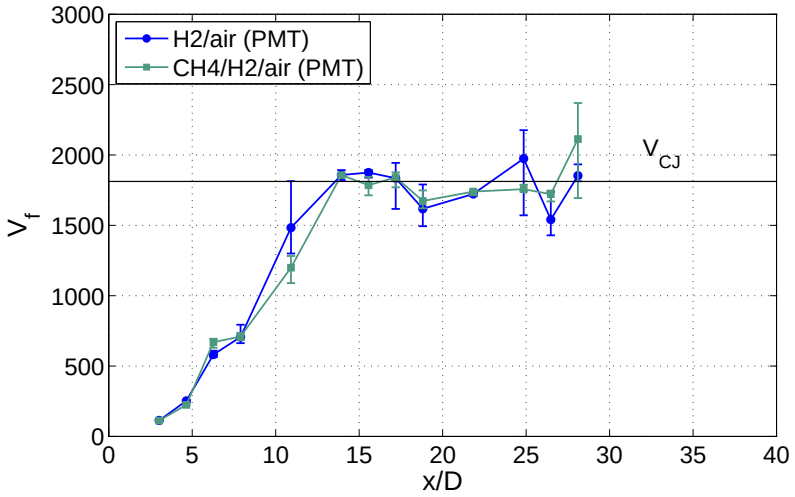

Figure 12.4: Effect of methane seeding on the flame acceleration process for $X_{H2} = 23$ %vol.

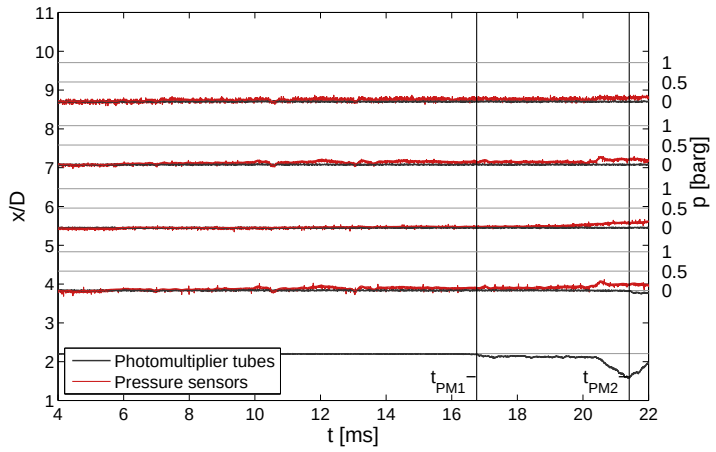

(a) 15 vol% H2.

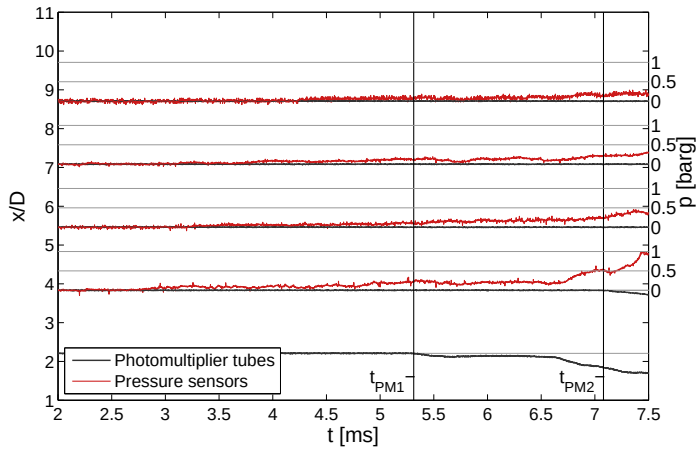

(b) 23 vol% H2.

Figure 12.5: Pressure evolution during the early stages of flame propagation: $x - t$ diagrams of flame propagation.

vol hydrogen/air mixtures without methane seeding are shown in Figure 12.6a and Figure 12.6b. Here, an increase of intensity of the light emitted by the flame as it propagates along the tube was observed. To easily compare the two cases, the same scale for the ordinates was used to present the results. As expected, higher values were measured for the 23 vol% hydrogen flame. Figure 12.8a and Figure 12.8b show the intensity of flame emission with and without methane seeding for the 23 vol% hydrogen mixture. From their comparison, we can state that methane addition had a negligible effect.
The next important issue was the stability of the laser beam in the presence of a propagating flame. For these tests, methane was not added and the laser was in operation. In the absence of any disturbing phenomena and besides flame light emission, the light intensity at the measurement detector was expected to be constant and equal to that one measured in vacuum conditions (no absorbing species). The propagation of an unstable flame (15 vol%) leads to large oscillations of the detector output signal as shown in Figure 12.6c. Laser beam deflection by non normal density gradients in the flame front can be a possible explanation of this behavior. These oscillations were largely reduced by increasing the hydrogen content in the mixture (23 vol%). As a result, the flame is less corrugated and the laser beam is not deflected (see Figure 12.6d). Consequently, for this feasibility test we restricted our attention to the 23 %vol hydrogen mixture.
The last issue concerns the light absorption by the burnt gases. Water molecules at room temperature and pressure do not absorb light at 3.39μm. As the temperature increases, mid-IR peaks become broader due to the Doppler effect. At the adiabatic flame temperature, mid-IR peaks overlaps the 3.39μm wavelength. Nevertheless, studies on hydrogen jet flames [56] showed that water absorption at 3.39μm can be neglected. By referring to HITRAN 2008 database [117], it was estimated that the absorption of 50 cm water column at adiabatic flame temperature and ambient pressure was less then 0.1%. Experimentally, water absorption was determined by subtracting the signal recorded during the “laser OFF" test case (flame emission) from that one recorded during the “laser ON" test case (laser transmission and flame emission), without methane seeding. The result, for the 23 vol% mixture, is shown in Figure 12.7. Here t^* identify the time at which the flame front intersects the laser beam. As expected, the initial value (before the flame is formed, $t < t^*$) for the laser beam transmission was retrieved, proving that water vapor absorption at 3.39μm can be neglected (sporadic deviation of τ in Figure 12.7 may be attributed to laser beam oscillations due non-normal density gradients).
The same procedure described in the above paragraph was applied to the mixture seeded with methane in order to perform front tracking measurements. The evolution in time of the transmittance so obtained is shown in Figure 12.8d.
Due to the geometrical configuration described in the previous chapter, the flame originates 45 mm away from the tube axis. Then it is forced to move downward due to the

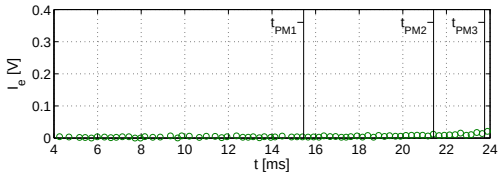

(a) 15 vol% H2. Laser OFF: Flame emission.

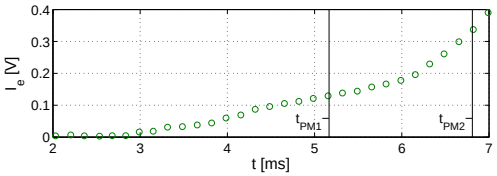

(b) 23 vol% H2. Laser OFF: Flame emission.

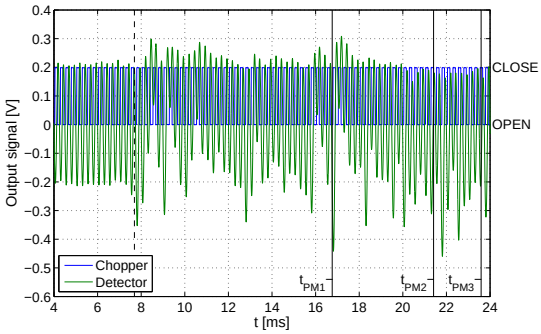

(c) 15 vol% H2. Laser ON.

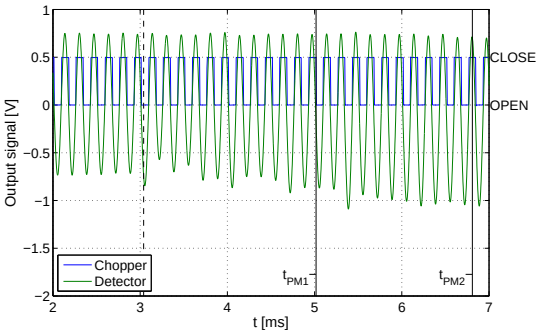

(d) 23 vol% H2. Laser ON.

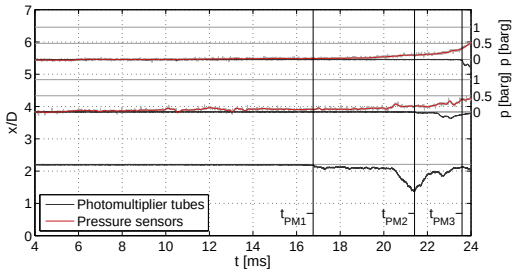

(e) 15 vol% H2. $x-t$ diagram of flame propagation.

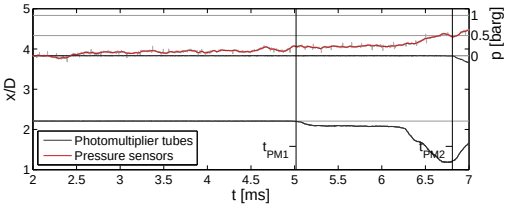

(f) 23 vol% H2. $x-t$ diagram of flame propagation..

Figure 12.6: Flame light emission and laser beam deflection at 3.39μm for 15 and 23 vol% mixtures without methane addition. Tests are synchronized on PM2 flame time-of-arrival.

presence of the first annular obstacle, located 3 mm away from the flange [1]. The intersection with the tube axis, and therefore with the laser beam, is most likely to happen at $x > 0$. The bias so introduced made difficult to use equation (12.4) to determine $l(t)$. A logarithmic fitting was then used to correlate $\tau(t)$ to $l(t)$. The perfect match between photomultiplier tubes signals and IR detector response was imposed to compute regression coefficients. The result, in terms of $x(t)$, is shown in Figure 12.9.
A regression function was then used to fit the experimental data in order to derive a

[1] The flame Froud number, computed as [27]:

$$\mathrm{Fr} = \frac{(\sigma S_L)^2}{2gR_f}$$

can be used to judge whether or not buoyancy effects are important during the early stages flame propagation. By imposing $R_f = 0.6$ m, that corresponds to the tube radius and considering the fundamental combustion properties listed in Table 12.2, we obtain $\mathrm{Fr}(X_{\mathrm{H2}} = 15\%) = 1.02$ and $\mathrm{Fr}(X_{\mathrm{H2}} = 15\%) = 38.4$. For the two mixtures $Fr > Fr^* = 0.11$ found in [27]. Buoyancy effects can therefore be neglected.

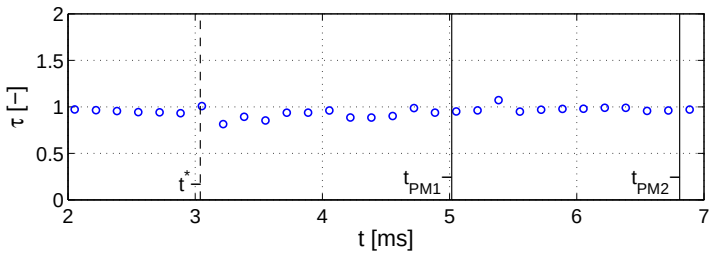

Figure 12.7: Laser beam transmission in time for the 23 vol% H2 mixture without methane.

flame velocity profile. An exponential law (the solid blue line in Figure 12.9) was chosen according to the analytical models of Clanet and Searby [41] and Bychkov et al. [29]:

$$x_f(t) \propto \exp(\vartheta t) \ . \tag{12.6}$$

where ϑ is the acceleration rate. The exponential law matches well the behavior of the flame tip except in the region $t_{\mathrm{PM1}} < t < t_{\mathrm{PM2}}$. Repeating the experience the same trend was observed. As shown in the right hand of Figure 12.9, this flame stagnation may be caused by the flame radial expansion inside the combustion chamber delimited by the third and the fourth obstacles. Further investigations are foreseen to clarify this point.
The velocity profiles for both 15 vol% and 23 vol% mixtures are presented in Figure 12.10. Experimental results are given in terms of average values over three shots. Error bars identify maximum and minimum values of the shots. Flame acceleration profiles are consistent with those found in [82] (see also Chapter 9). A chocked flame regime was reached at about 15 diameters from the ignition point for 15 vol% mixture. For 23 vol% mixture, the flame velocity reached a saturation value close to the CJ detonation velocity. A zoom on the early stages of flame propagation for the 23 vol% mixture is shown in Figure 12.11. Here, IR measurements are compared to those given by photomultiplier tubes. In addition, the analytical expression for the flame tip velocity (3.14) for axisymmetrical geometries (acceleration rate of equation (3.16)) derived by Valiev et al. [141] is also presented (gray solid line). Dashed lines in Figure 12.10 and Figure 12.11 refer to equation (3.18).
Finally, a numerical model for flame acceleration dedicated to large geometries was developed [143, 14]. This simple model is based on the resolution of the Euler equations coupled to a diffuse interface propagation equation. Flame acceleration process is supplied by an algebraic equation for turbulent flame velocity. The application of this model to the present experiments is also given in Figure 12.10 and Figure 12.11 (violet line, RDEM model). Numerical results agree quite well with the experimental ones.

12.4 Conclusions

A feasibility study was performed on a non intrusive technique to record the propagation of a premixed flame. It allows to track the flame front along the tube axis in a quasi-continuous way.
The method demonstrated its capabilities in the early stages of flame propagation for a 23 vol% hydrogen in air mixture. For the moment, results must be interpreted in a

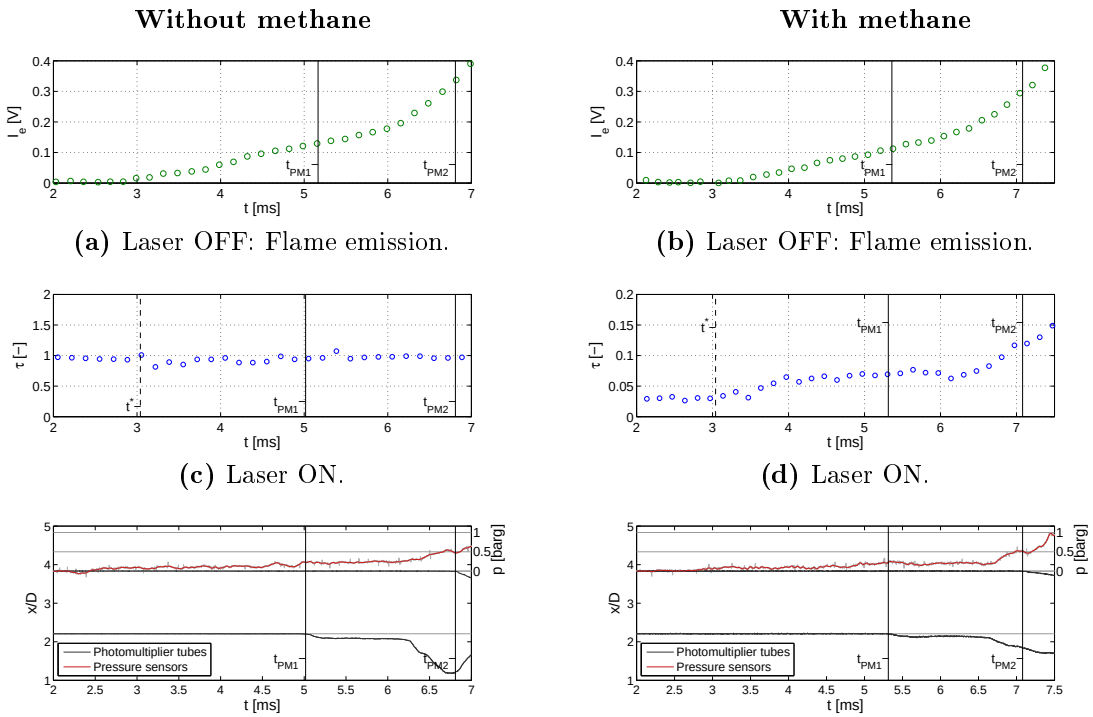

(a) Laser OFF: Flame emission.

(b) Laser OFF: Flame emission.

(c) Laser ON.

(d) Laser ON.

(e) $x-t$ diagram of flame propagation.

(f) $x-t$ diagram of flame propagation..

Figure 12.8: Flame light emission and laser transmission at 3.39μm for a 23 vol% hydrogen/air mixture, with and without methane mixture seeding. Tests are synchronized on PM2 flame time-of-arrival.

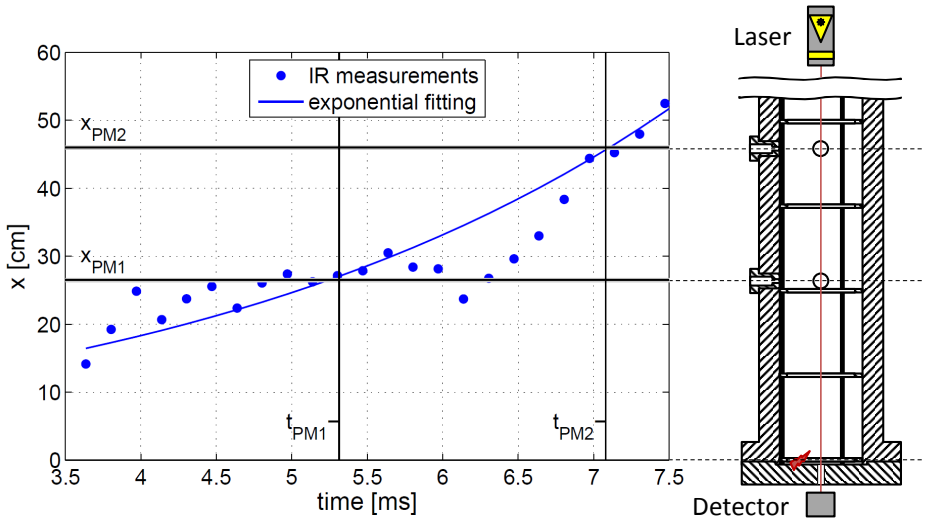

Figure 12.9: Flame tip position in time. $x_{\mathrm{PM}i}$, position of the i-th PMT; $t_{\mathrm{PM}i}$, flame time-of-arrival.

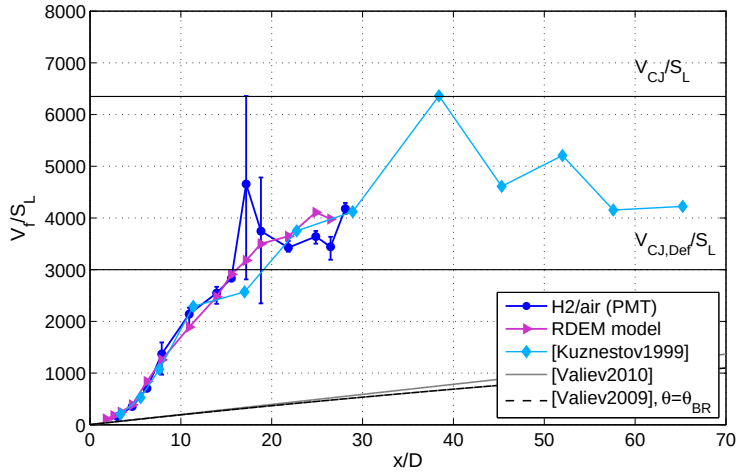

(a) 15 vol% H2, BR= 0.3.

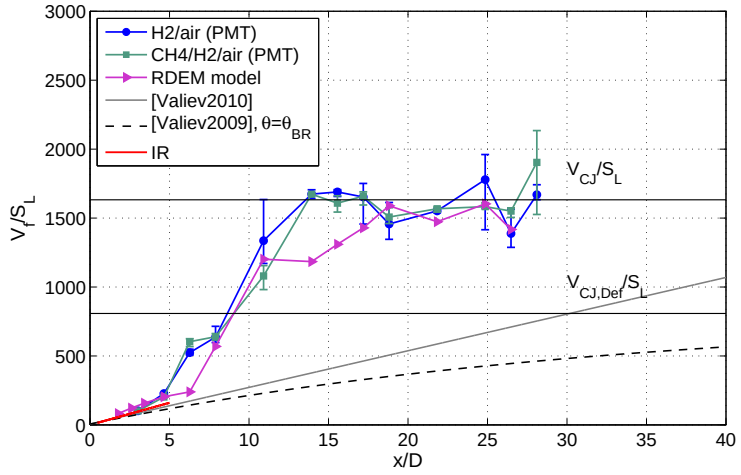

(b) 23 vol% H2, BR= 0.3.

Figure 12.10: Velocity profile along the tube.

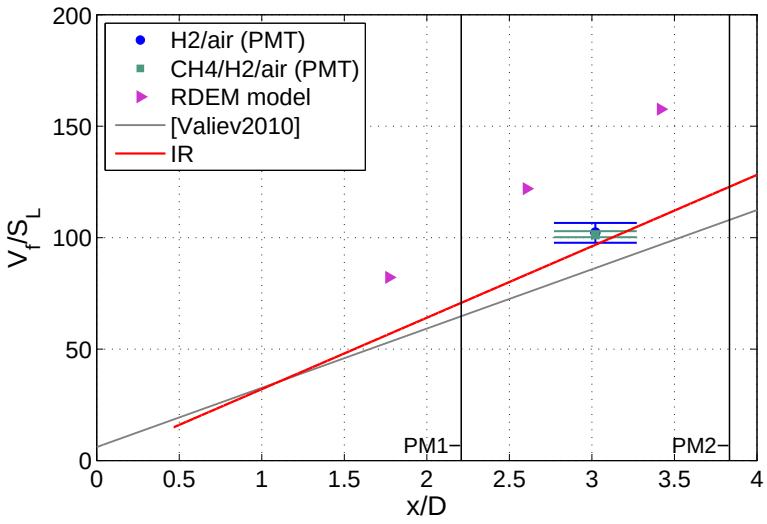

Figure 12.11: Flame tip velocity along the tube for 23 vol% mixture.

qualitative way. For leaner mixtures, improvements are needed to reduce the effect of laser beam deflection by the flame. Nitrogen dilution is foreseen in order to diminish the cellular structures on the flame surface.
Moreover, laser-chopper-detector time response has to be increased to perform proper time resolved measurements. For the moment the acquisition frequency is limited by detector rise time and chopper angular velocity. Additionally, faster optical systems allow the measurement of flame light emission and laser transmission within the same shot. A schematic representation of choppers synchronization for these measurements is shown in Figure 12.12 (here f identifies the chopper frequency).
For rich flames, a seeding molecule in the oxidizer, or the oxidizer itself, will be more relevant. Oxygen absorption at 761 nm can be a good candidate for further investigations because of the low emission of hydrogen flames at this specific wavelength (on-going activity).

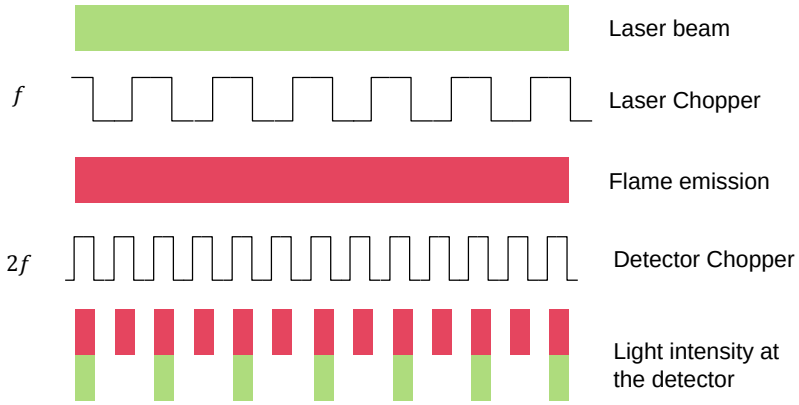

Figure 12.12: Choppers synchronization method to allow flame emission and laser transmission measurements within the same shot.

Part V

Structure response to combustion generated loads

Chapter 13

Design tests at static pressure

In the present Chapter, preliminary results on the static behavior of circular plates are discussed.
These test were performed by placing the specimen (circular plate) at the end of the combustion tube. The intermediate flange, described in Chapter 5.2, was not used to fix the plate during these preliminary tests. As a matter of fact, their aim was to provide experimental data for the design of the structural module and, in particular, for the specimen handling and fixation system.
First, the experimental set-up used for these tests is described. Then, the results in terms of plate static response to pressure loads are presented. Eventually, the main features of the final design of the FSI module are drawn.

13.1 Description of the device

For this experimental campaign, 304L stainless steel circular plates of 0.48 mm uniform thickness and Φ174.5 mm were used. Plates were clamped between two flanges, as shown in figure 13.1. The first flange (the dark one in the picture) corresponds to the terminal flange of the fourth section of the combustion tube. The external surface of this flange presents a $\Phi 175 \times 4.5$ mm recess that, in the normal operating condition, serves to center the end sealing flange. This recess allows us to install the plate in the vertical position. A second flange is then fixed to properly clamp the plate. As a result, the free surface of the plate is reduced to Φ120 mm that corresponds to the inner diameter of the combustion tube. A series of 8 studs assures the rigidity of the assembly. The couter-flange presents a 4.5 mm large and 2.5 mm deep circular groove at Φ133.4 mm that hosts an O-ring. Once the nuts are tighten on the studs, this ring assures the sealing.
Once the apparatus is assembled, the tube presents the same geometry of the configuration for flame acceleration. The pressure inside tube can be controlled though the injection/purge lines. By adjusting the air flow rate entering into the tube or the one towards the vacuum pump it is possible to increase or decrease quasi-statically the pressure loads acting on the plate. Pressure measurements are given by 3 pressure transmitters installed at the end of tube near the location of the plate. Since the original end-flange is replaced by the circulate plate, the purge line is connected to an instrumentation port located at the end of the tube. This allows the inertization and venting of the combustion tube atmosphere.

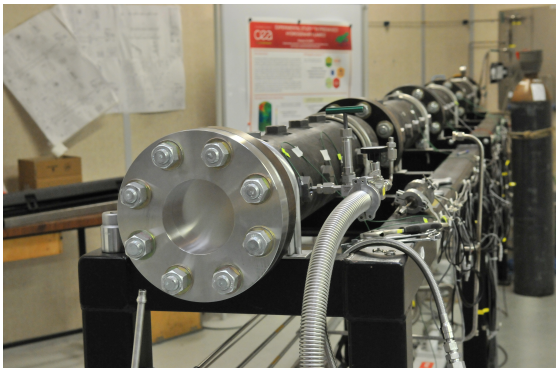

(a) Circular plate clamped between two flanges.

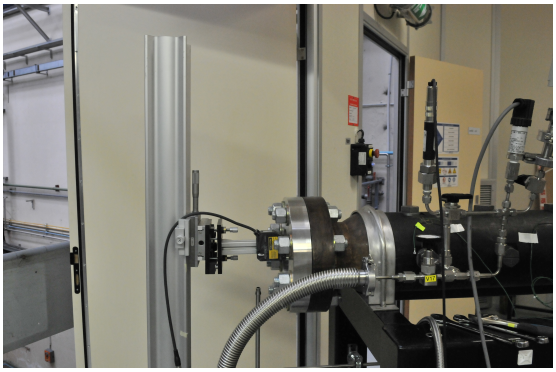

(b) Laser support for displacement measurements.

Figure 13.1: Views of the experimental facility SSEXHY. The current configuration, with the substitution of the terminal sealing flange with a bored Φ120 mm one, allows to perform plates deformation tests.

13.2 Diagnostics

A KEYENCE LK-H082 displacement sensor [76] was used to measure the displacement of the loaded plate.
The sensor was installed on a vertical support in order to meet the height of the experimental facility, as shown in Figures 13.1b and 13.2a. Two sliding boards have been inserted between the vertical support an the sensor to ensure two degrees of freedom for sensor manipulation. The first board allows to shift the sensor along the x-direction (parallel to the ground) in a 95 mm range, while the second one, mounted at 90-degree angle with respect to the other (y-direction), has a 40 mm stroke. The laser can then be moved on the xy-plane using two micrometric screws.
The LK-H082 sensor is able to measure a displacement in the z-direction of ± 18 mm from the reference distance. According to the sensor data sheet, the repeatability of the instrument is 0.1 μm while the linearity is 0.02% FS, thus 7.2 μm.

13.3 Experimental set-up

Once the plate is installed the laser is switched on, in order to proceed with the beam alignment. First of all, the center of the Φ120 mm free surface is traced on the plate. This procedure needs to be performed after having assembled all the parts since the axis of the tube may not coincide with the center of the Φ175 mm disc (due to the lash between the flange hole and the plate). Then the sensor is placed at a distance $\simeq$ 80 mm from the plate (reference distance for diffuse reflection measurements). The thin red light of the laser allows us to properly center the origin of the xy axes of the sensor reference frame (see Figure 13.2b).
A particular care shall be taken while mounting the sensor because of the flange shoulder: the reflected beam needed for the triangulation can be stopped by the flange as the sensor approaches the plate clamped edge. To avoid this problem, the sensor has been tighten to the vertical support to allow the displacement in the x-axis towards the positive direction

up to the edge ($0-60$ mm stroke), while in the other direction the displacement has been limited to 35 mm. The 40 mm range in the y-direction spanning on the origin enables us to verify the axis-symmetric deformation of the plate.

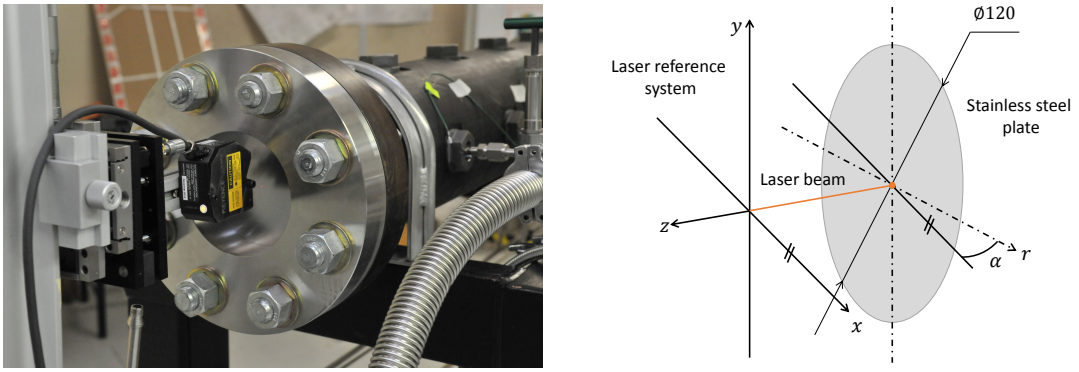

(a) **(b)**

Figure 13.2: Displacement sensor: (a) zoom on the laser support for displacement measurements; (b) schematic representation of the laser reference frame.

Since the laser support is not an integral part of the tube support, the parallelism between the plate and the laser frame is not guaranteed. A small angle can be formed between the two planes as shown in Figure 13.2 b. For sake of clarity, in the picture we have represented only the rotation around y-axis; nothing prevents having a rotation also around x-axis, for example due to a slope on the ground where the laser support lies.
Before measuring the plate deformation under pressure loads, the surface of the plate is scanned in the unloaded configuration. This preliminary measurement is crucial for the following aspects:

1. to verify if the plate is not deformed when unloaded;
2. to evaluate the slope between the laser frame and the plate one;
3. to identify the presence of defects on the plate surface (such as scratch and flaws produced during the forming process).

Since the plate may be deformed under the action of the tightening torque, the verification of point (1) of the list is imperative in order to compare the experimental results with the linear theory (ref. Chapter 4.3). The value of the applied torque must be balanced in order to guarantee that (a) the plate does not slide at the edge and (b) the sealing for vacuum is preserved, and that, at the same time, (c) the related stress does not induce any deformation on the plate.
Point (2) is required to project the displacement measurement on the plate frame, obtaining the true displacement profile. Eventually, point (3) can be helpful to discriminate if the measurement bias is linked to the plate roughness or not.

13.4 Test configurations

Several test have been performed in different configurations in order to verify the associated boundary conditions. The test matrix is presented in Table 13.1.

Table 13.1: Test matrix.

Test #	Configuration
1	Original configuration (single O-ring, torque $T = 200$ Nm)
2	Single O-ring, lower torque ($T = 100$ Nm)
3	Double ring shaped sheet gasket, $T = 100$ Nm
4	Without gaskets, $T = 100$ Nm

The tightening torque was tested first. The plate has been installed keeping a single O-ring on the external flange. The normal operating torque of 200 Nm was applied on the 8 pairs of stud/nuts. As a result the plate was strongly deformed even if no pressure loads were applied. A second test has been performed on a new plate (the previous one has undergone non-reversible plastic deformation) decreasing the value of the torque up to 100 Nm. The displacement on the z-direction was diminished but still not negligible. We blamed the non-symmetrical clamping for this deformation since, as the pressure was slightly increased inside the tube, the concavity of the plate has been immediately reversed.
For this reason two rings with Φ174.8 mm external diameter and Φ120.5 mm internal diameter were cut from a sheet gasket. In this configuration the plate is installed between the two gaskets, so the torque is uniformly distributed from both sides. From the preliminary plate scan no sign of deformation was observed.
In the last experiment we have tested the impact of the gasket on the plate deformation. The gaskets have been removed and the results have been compared with the previous case (Test 3).

13.5 Loading process

Due o the presence of sensors on the combustion tube wall, experiments were not performed under hydraulic pressure. For safety reasons tests were therefore performed with synthetic air in sub-atmospheric conditions so that the pressure of the volume of air contained inside the tube does never exceed the external atmospheric pressure. This condition assures that, in case of plate failure, no missiles will be projected outside the tube, preventing any damages (including damages on the laser-head). Even if plate failure is not foreseen, precautionary measures were taken to avoid any unexpected material flaws. The primary vacuum pump was used to decrease slowly the pressure inside the tube. The loading process is controlled through pressure transmitters and manually operated valves. As mentioned before, one of the main goals of these was to verify that the stainless steel plate does deform according to linear theory. In particular, we want to verify that the constraint at the plate edge corresponds to the ideal clamping one. Eventually, the plastic behavior of the plate was investigated.
The loading process consists in a slow depressurization of the tube up to a chosen testing pressure. Once the displacement of the central point of the plate is stabilized, the deformation profile is recorded. Then the venting valve is gradually opened to restore the atmospheric condition inside the tube.
This process is sequentially repeated by increasing the pressure difference through the

plate thickness at each time. Plasticity occurs when in the unloaded configuration a residual non-negligible displacement is measured at the center of the plate.

13.6 Results and discussion

In this paragraph the results of the Tests 3 and 4 are presented. In Figure 13.3 the comparison of the central displacement measured in the two cases is shown as a function of the pressure load. A quite different behavior can be noted in the first part of the plot. We can allegedly state that this difference is mostly due to the gasket which is only used in Test 3: the tightening torque has only partially deformed the glass-fiber sheet gasket making further deformations possible.

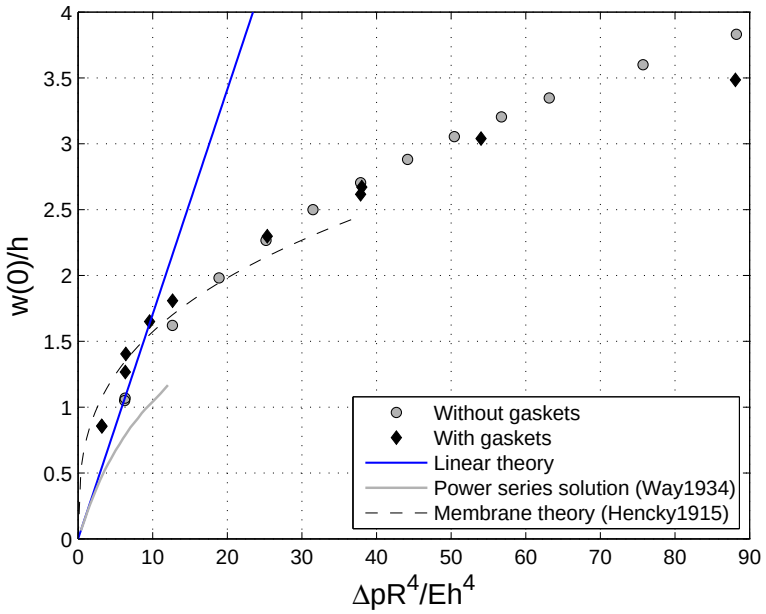

Figure 13.3: Displacement of the central point of the plate as a function of the non-dimensional pressure load. Comparison of the experimental data of Tests 3 and 4 and the theoretical models.

The difference between the two test cases can be better observed in Figure 13.4, where displacement profiles for $\Delta p = 0.005$ MPa are presented. The central displacement of the plate in Figure 13.4a (Test4, no gasket) is greater than the other one in 13.4b (Test 3). For both cases, we can see that the profile shape agrees with the theoretical one of a circular plate with clamped edge under uniform loads.
The profile along y-axis matches perfectly the one in the x-direction: the deformation is perfectly axis-symmetric and the plate response does not vary along θ as predicted by the theory. The error band due to the displacement sensor is also presented in the plots. It has been evaluated as follows supposing a normal distribution for the measurements :

$$u^2(w^*) = u^2(w) + u^2(w_{p0}) \tag{13.1}$$

where w^* is the real displacement in z-direction computed as the difference between the measured displacement w and the initial one in the unloaded configuration w_{p0}, due to the slope between the laser and the plate (see Figure 13.2).

Imperfections of the plate surface are also visible in our measurements: in the left-hand graph we can clearly see a groove at $y \simeq -20$ mm, while a growth appears at $x = 20$ mm. Thus, plate roughness strongly affect our measurements and should be considered while computing the global uncertainty.
The solid line identifies the solution of the linear theory (see equation (4.69)). Material properties, such as the Young's modulus and the Poisson coefficient, were taken from Table 5.3.

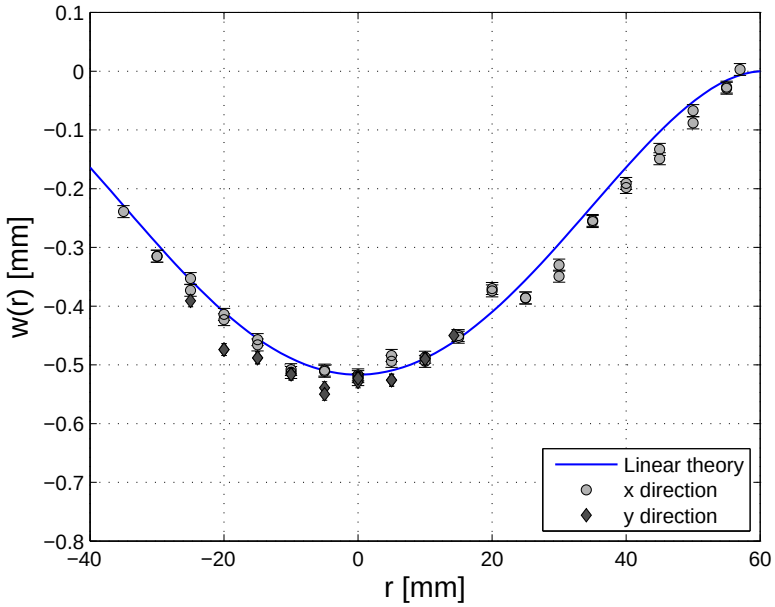

(a) Test 3 (with gaskets).

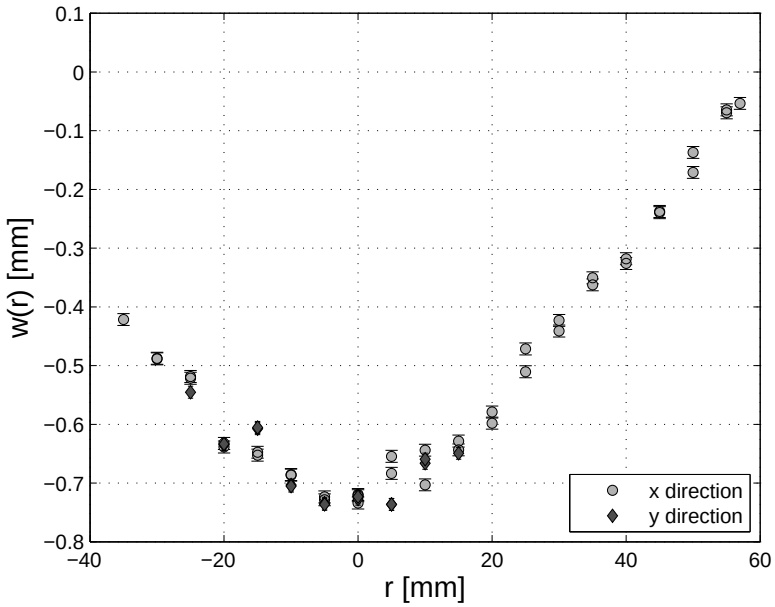

(b) Test 4 (without gaskets).

Figure 13.4: Displacement of the plate in z-direction. $\Delta p = 0.005$ MPa ($\Delta p R^4/Eh^4 \simeq= 6.7$).

For the above considered pressure load ($\Delta p = 0.005$ MPa) the theory of thin plates is no longer valid. According to [147], equation (4.70) should better predict plate central

displacement. On the other hand, if we observe the profiles presented in Figure 13.4, we can note that in our experiments plate deformation seams to better agree with the membrane theory for $w(0)/h \gtrsim 1.5$.
Further analysis can be performed by means of strain gauges. In fact, by installing two strain gauges in a specular way on the plate intrados and extrados, the difference in their response can be used to discriminate the state of tension of the plate. In this way, the transition from the flexural state to the membrane one can be investigated.
To conclude, in Figure 13.5 the behavior of the plate in the plastic domain is shown. A pressure load of $\Delta p = 0.07$ MPa has been applied to both Test 3 and Test 4; the resulting profiles are shown in the plot. We can note that near the edge the two plates behave similarly, while at the center the displacement is greater for the case with gaskets. Here, the shape of the profile differs from that one predicted by the linear elastic theory and it assumes a parabolic profile.

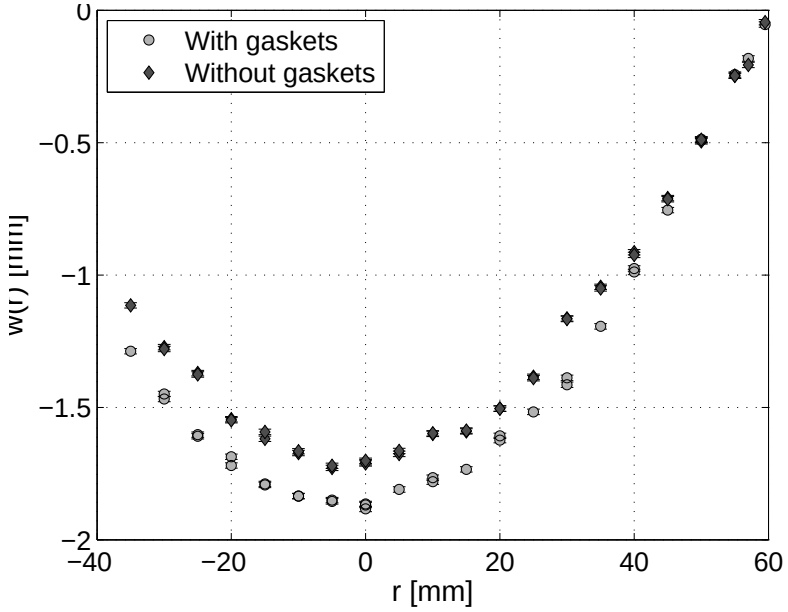

Figure 13.5: Displacement profile for $\Delta p = 0.07$ MPa. Comparison between Test 3 and Test 4.

Another thing to take into account is that plasticity seems to occur for $\Delta p = 0.04$ MPa. This value is much greater than the yield load associated to the Tresca or the Von Mises criteria (5.3) and (5.4) ($p(\sigma_T) = 0.0154$ and $p(\sigma_{VM}) = 0.0173$). Probably this incongrence between experimental results and theoretical model is linked to both the validity of the linear model and the uncertainty in plate central displacement measurements. Further analysis will be performed in a further experimental campaign to better understand the transition from the elastic behavior to the plastic one thus clarifying this point.

13.7 Conclusions

Several tests were preformed to study the behavior of a statically loaded thin circular plate with clamped edge. Results agree quite well with the theoretical models.

Due to the fact that plates are not bolted, the plate may slide between the two flanges as pressure is increased and the initial hypothesis of clamped edge could fail. In this experimental campaign, it was not possible to verify directly whether or not the plate had moved from its original position. At the same time, the plate behavior is consistent with the membrane solution until plasticity takes place (see Figure 13.3). For this theory to be valid, no-slip condition at the edge must be satisfied. Thus we can state indirectly the the plate is supposed not to slide up $\Delta p = 0.03 - 0.04$ MPa.
The regulation on pressure vessel exploitation prohibits the direct contact between moving metal parts, in order to avoid any reduction in thickness due to friction. For this reason, sheet gaskets are foreseen in the final design of the FSI module to seal the connection between the specimens and the flanges. The influence of the sealing gasket on the plate deformation was therefore investigated. By comparing the results from the tests, with and without gaskets, we can see that the structural response in the two cases is different. In light of these results, in order to compare numerical simulations on plate static deformation with the experimental results we recommend to include the gasket into the numerical model.
To summarize, these preliminary studies allowed us to define the experimental approach to investigate plates deformation under static loads, such as the fixation of the specimen (senstivity analysis on gasket shape and toque intensity and verification of the axis-symmetrical response of the plate) and optical diagnostics. The key points for the final design of the FSI module were also indentified. Moreover, this experimental campaign has shown where the measurements need to be increased and which types of technics should be used to better characterize specimens mechanical response (ex. the use of strain gauges to characterize the state of tension of the plate).
A second experimental campaign is foreseen as the FSI module is ready to be installed on the facility. Moreover, the presence of the safety dome allows us to perform the experiments with a positive pressure difference throughout the plate thickness. Since the pressure inside the combustion tube can be increased, failure mechanisms could also be investigated.
In this configuration, the displacement sensor is supposed to be mounted on the same support of the FSI module in order to minimize the influence of the external environment on the measurements (vibrations transmitted by the ground, floor instability, etc.). In particular this may allow more accurate measurements in the linear domain (small deflections) to assure that the plate behavior is consistent with ideal clamping constraint. As a matter of fact, the analysis of specimen deformation under static loads is a key point to characterize/verify plates mechanical behavior. Once this is fully established, then the mechanical response of the specimen under transient loads can be investigated.

Chapter 14

Preliminary analysis on the mechanical response of specimen to dynamic loads

As mentioned in Chapter 4, the structure response to combustion generated loads strongly depends on the combustion regime. Slow deflagrations in closed vessels induce non-uniform pressure loads, that locally can be assumed as quasi-static. The maximum pressure can be conservatively estimated with the Adiabatic Isochoric Complete Combustion (AICC) model. As the the velocity of the flame front increases, pressure loads become more important, while the duration of the load acting on the structure strongly decreases. In the limit of strong detonation, the load can be assumed as purely impulsive. Typical values of AICC and Chapman-Jouguet pressures for hydrogen/air mixtures are listed in Table 14.1 as a function of ϕ, the fuel-to-oxidizer equivalence ratio. Other thermal-dynamic variables, such as the speed of sound in the fresh gas and CJ detonation velocity, are also presented. Data are obtained from Cosilab v.3 [77] equilibrium simulations (for more detail on numerical simulations, see Chapter 8.1).

Table 14.1: Thermo-dynamic variables of hydrogen/air mixtures at $p_0 = 1$ bar and $T_0 = 300$ K. Initial mixture composition: $x\mathrm{H2} + \frac{1-x}{n+1}(\mathrm{O_2} + n\mathrm{N_2})$, $n = \frac{79.1}{20.9}$.

x	ϕ	p_{AICC} [bar]	p_{CJ} [bar]	c_{su} [m/s]	U_{CJ} [m/s]	$U_{\mathrm{CJ,def}}$ [m/s]
0.110	0.30	4.52	8.58	367.2	1340	615.2
0.150	0.42	5.55	10.65	375.1	1524	719.9
0.200	0.60	6.65	12.88	385.7	1715	834.7
0.295	1.00	8.00	15.58	408.7	1977	1008
0.400	1.60	7.70	15.01	439.3	2099	1045
0.500	2.39	7.00	13.59	476.0	2177	1060
0.600	3.59	6.14	11.85	523.8	2247	1068

The following discussion is focused on a preliminary analysis of mechanical response of the structure specimens, i.e. stainless steel plates and cylinders described in Chapter 5.2.1. This analysis is based on the evaluation of those variables previously introduced in Chapter 4.

14.1 Circular plates

Natural frequencies of the circular plates are listed in Table 14.2 as a function of the plate radius R and the plate thickness h. These values were evaluated according to equation (4.81) and they can be used as reference values for the comparison of experimental measurements and/or numerical FEM simulation. The use of four types of plates with different geometrical dimensions allows us to cover a wide range of resonance frequencies: $247 < f_{01} < 686$ Hz. According to Table 14.2, the stiffer plate is the $h1 \times R60$ plate, while the more flexible one is the $h1 \times R100$ plate.

Table 14.2: Oscillation frequencies of circular plates with clamped edge.

	Small plates		**Big plates**	
h [mm]	0.5	1	1	2
R [mm]	60	60	100	100
f_{01} [Hz]	343.0	686.0	247.0	493.9
f_{02} [Hz]	712.9	1426	513.3	1027
f_{11} [Hz]	1336	2673	962.2	1924

Moreover, the natural frequency can be used to perform simple 1DOF analysis on plates response to transient loads. An example is shown in Figure 14.1. Here, the pulsation frequency was obtained from the natural frequency f_{01} of the small plate with $h = 0.5$ mm ($f_{01} = 343$ Hz). The characteristic loading time was varied between $1 \cdot 10^{-6} - 5 \cdot 10^{-2}$ s. The plot at the top of Figure 14.1 refers to a pure impulsive load ($\omega\tau_{\text{load}} \ll 1$): the maximum displacement is equal to the pressure impulse ($x_{\max}/x_s = \omega\tau_{\text{load}}$, where x_s is the corresponding static displacement). On the other hand, the plot at the bottom of the figure shows the oscillating behavior of the structure subjected to a quasi-static load: $x_{\max}/x_s = 2$.
The central plot was obtained imposing $\tau_{\text{load}} = 0.1$ ms, that is coherent with a detonation-like load. Also in this case, the structure response corresponds to a impulsive loading. In Figure 14.2, the mass displacement due to a detonation-like load for the $h1 \times R60$ plate (Figure 14.2a) and the $h1 \times R100$ plate (Figure 14.2b) is shown. For the latter case, that corresponds to the plate with lower natural frequency, the loading process can be assumed as pure impulsive. On the other hand, the mechanical response of the stiffest plate ($h1 \times R60$ plate) lies in between of the two asymptotes defined by the pure impulsive load and the quasi-static load.
For pure impulsive loads, the experimental correlation (4.82) can be used to evaluate the maximum plate displacement. In this case plastic deformations are also taken into account. The results, for two hydrogen/air mixtures ($X_{\text{H2}} = 0.150$ and 0.295), are listed in Table 14.3. Here, the impulse was suppose to be $I = p_{\text{CJ}}(\pi R^2)\tau_{\text{load}}$ with $\tau_{\text{load}} = 0.1$ ms.

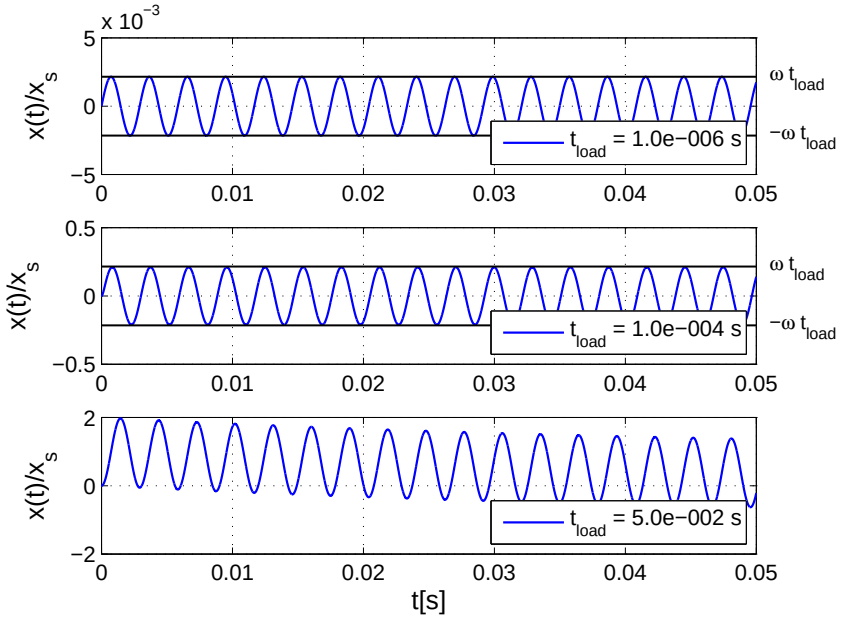

Figure 14.1: Mass displacement in time according to the 1DOF model. Data refers to the $h0.5 \times R60$ plate with $f_{01} = 343$ Hz.

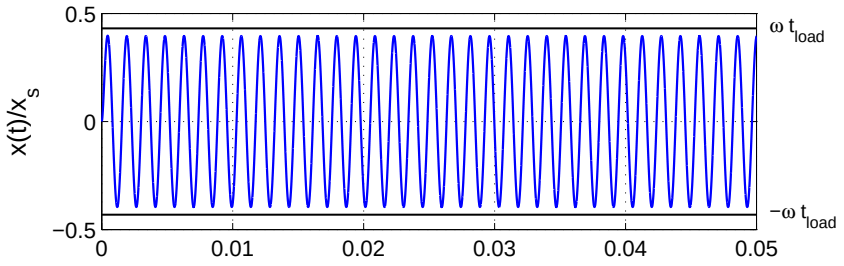

(a) $h1 \times R60$ plate. $f_{01} = 686$ Hz.

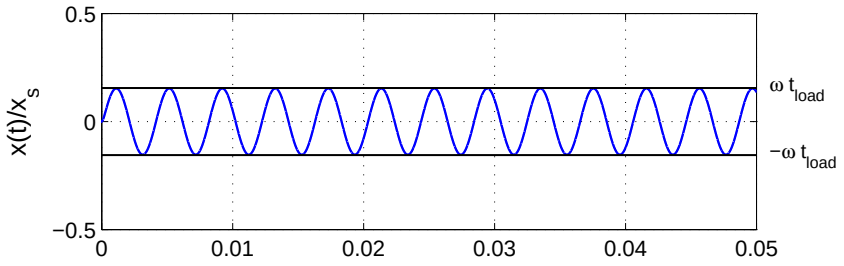

(b) $h1 \times R100$ plate. $f_{01} = 247$ Hz.

Figure 14.2: Mass displacement in time according to the 1DOF model. Comparison between the $h1 \times R60$ plate and the $h1 \times R100$ plate. The characteristic time of load was imposed to be $\tau_{\text{load}} = 0.1$ ms.

Table 14.3: Plate central displacement w_0/h for impulsive loads from equation (4.82). $I = p_{\mathrm{CJ}}(\pi R^2)\tau_{\mathrm{load}}$ with $\tau_{\mathrm{load}} = 0.1$ ms.

	Small plates		**Big plates**	
$h\,[\mathrm{mm}]$	0.5	1	1	2
$R\,[\mathrm{mm}]$	60	60	100	100
$\frac{w_0}{h}(X_{\mathrm{H2}} = 0.150)$	9.09	2.27	3.79	0.95
$\frac{w_0}{h}(X_{\mathrm{H2}} = 0.295)$	13.30	3.33	5.54	1.39

14.2 Thin walled cylinders

With reference to equation (4.30), the fundamental radial frequency of a 304L stainless steel cylinder of infinite length is given in Table 14.4. According to the linear theory of thin cylindrical shells, the average radius R of the cylinder was used to compute f_{00}.

Table 14.4: Fundamental frequency of a 304L stainless steel cylinder of infinite length.

$h\,[\mathrm{mm}]$	2
$R_i\,[\mathrm{mm}]$	60
$R\,[\mathrm{mm}]$	61
$f_{00}\,[\mathrm{Hz}]$	13736

Since the cylindrical specimen is stiffer than the circular plates, we expect a different response to transient loads. By applying the 1DOF analysis to the cylinder, the plots shown in Figure 14.3 are obtained. Here, the values of characteristic time for the dynamic load τ_{load} were the same of Figure 14.1.
The graph in the middle represents the response to a load with $\tau_{\mathrm{load}} = 0.1$ ms. In this case, the ratio τ_{load}/T is greater than 1 and the loading process can be considered as quasi-static. The strain can therefore be computed via equation (4.38). For example, for a steady detonation of a 15 %vol hydrogen/air mixture $\epsilon^{\mathrm{dyn}} = 0.030\%$, while for a stoichiometric mixture we get $\epsilon^{\mathrm{dyn}} = 0.043\%$.
Now, if we refer to the analytical solution proposed by Tang [131], the critical velocities that make the structure to resonate can be determined. In correspondence to these velocities, the dynamic load factor, defined in equation (4.36), presents a singularity. In Table 14.5, the values of the four critical velocities (4.51)-(4.54) for the cylindrical specimen are listed.
The first critical velocity U_{c0}, that separates the dumped oscillatory solution to the pure oscillatory one, is of the order of magnitude of $U_{\mathrm{CJ,def}}$ for lean hydrogen/air mixtures (see Table 14.1). As the velocity of the shock wave approaches this value, the dynamic load factor strongly increases. U_{c1} defines the upper limit of the supercritical solution. According to Table 14.5, U_{c1} corresponds to the detonation velocity in a rich hydrogen/air mixture (see Table 14.1). Therefore, ranging from fast deflagrations ($U_f \simeq U_{\mathrm{CJ,def}}$) to

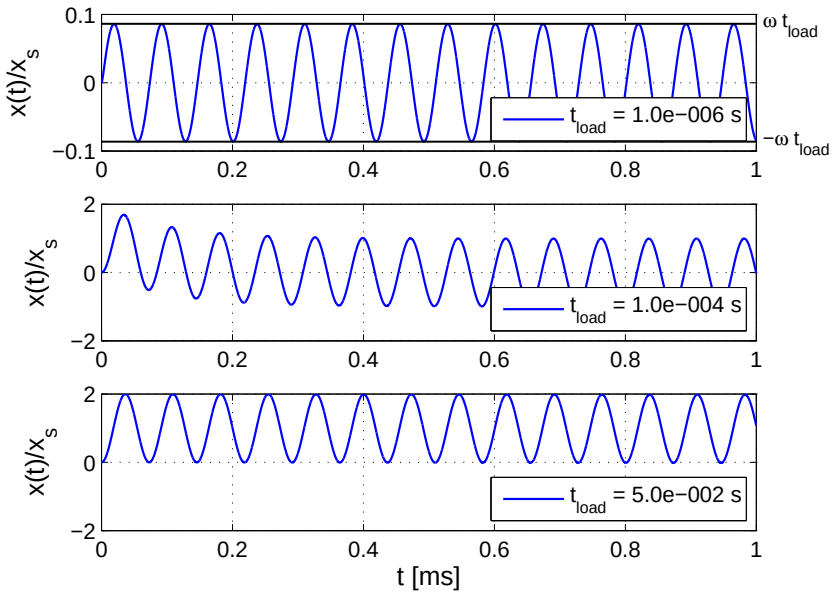

Figure 14.3: Cylinder mass displacement in time according to the 1DOF model.

Table 14.5: Critical velocities predicted by the Tang's model for the cylindrical specimen.

Critical velocity	[m/s]
U_{c0}	664.0
$U_{c1} = U_s$	2198
$U_{c2} = U_{db}$	4713
$U_{c3} = U_d$	4941

steady detonations, the velocity of the reactive wave is in between of U_{c0} and U_{c1}. A pure oscillatory solution is then expected.
Even though for a more realistic prediction of the dynamic load factor, Beltman's [15, 16] and Mirazei's [104] models should be addressed, the analysis proposed by Tang based on the determination of the critical velocities is of great importance in discerning possible structure behavior.

14.3 Conclusions

In the present chapter, a preliminary analysis on the structure response of the stainless steel specimens described in Chapter 5.2.1 was performed. The aim of this study was to provide preliminary analytical results to use as reference for the experimental campaign. They are of great importance not only for the comparison of the experimental results but also for the set-up of the experiments (for the choice of the most suitable diagnostics, the calibration of the sensors in the range of expected deformations, etc.).

For each specimen, the fundamental frequency was determined on the basis of those formula introduced in Chapter 4. With reference to Table 14.2, the choice to use four types of plates with different geometrical dimensions allows us to cover a wide range of resonance frequencies from 247 Hz to 686 Hz. Since their mechanical resistence to pressure loads is different (see Table 5.5), both elastic and plastic regimes can be studied. In case of strong detonations, failure mechanisms may also be investigated.
Cylindrical specimens present a higher mechanical resistence to static loads ($p_{\mathrm{YS}} \simeq 60$ bar) and a higher natural frequency, if compared to planar specimens. In this case, the study will be focused mainly on the structure response to dynamic loads in the elastic region. This allows us to compare the experimental results with the analytical ones predicted by Tang's and Beltman's models.
The application of the 1DOF model was also presented. This simple model allows us to discern whether the loading process can be considered as purely impulsive or quasi-static. Specimen deformation due to dynamic loads can be predicted from equation (4.36). In these two limiting cases, the value of the dynamic load factor is known.
To conclude, these preliminary studies offer a starting point for the analysis of experimental results.

Conclusions and perspectives

In the present study, experimental campaigns were performed with the aim of better understanding the underlying mechanisms of premixed hydrogen/air flame acceleration in obstructed tubes. The main purpose was to provide further details for the improvement of large scale combustion models and, in particular, to determine which parameters play a key role in the acceleration process. Moreover, preliminary analyses on the structural response of stainless steel specimens to dynamic loads have been performed to obtain reference results for the set-up of the future experimental campaign.
Experiments were performed in a circular tube with closed ends, 5 m long, with an internal diameter of 12 cm. An array of equally distributed annular obstacles was placed inside the tube in order to promote flame acceleration. The embedded combustion diagnostic features dynamic pressure sensors, shock sensors and photomultiplier tubes: while the first ones are used to measure the overpressure due to combustion, the latter are used to determine the flame time of arrival and to trace the velocity profile. At this stage, only the mono-dimensional behavior of the propagating flame was analyzed.
Since the experimental device was used for the first time during the present research work, some repeatability and reproducibility tests were carried out. A good accordance with experiments performed in similar geometrical configurations was found. Moreover, results are consistent with the criteria for flame acceleration and DDT provided in the literature.
Most of the experiments on FA and DDT available in the literature were carried out at atmospheric or sub-atmospheric conditions. These conditions are not representative of severe accident scenarios, where the high release rate of steam and non-condensable gases can lead to a pressure increase up to 5 bar abs inside the reactor containment. For this reason, the effect of higher initial pressures (between 0.6 and 4 bar abs) on the flame acceleration has been studied. Results showed that, for very lean mixtures (11% H2), an increase in the initial pressure does not affect the early stages of flame acceleration. However, a decrease in the flame tip velocity towards the tube end was observed in tests performed at higher initial pressures: the reason of this slowdown lies in the interaction between the reflected shock wave and the flame. For slightly richer mixtures (15% H2), instead, a higher initial pressure results in a higher acceleration rate: this effect could be attributed to thermo-diffusive instabilities, in the first stages of the acceleration, and to flame-shock interaction in the last ones. Additionally, for all studied mixtures, the overpressure due to combustion was directly proportional to the initial pressure; the amplitude of the acoustic waves seems to follow the same behavior.
The effect of the nitrogen dilution on the flame acceleration process was also investigated in the present work. Since nitrogen concentration only slightly affects thermo-dynamic and combustion parameters of the mixture, this study also allowed us to perform a sensitivity analysis on the influence of thermo-diffusive parameters on FA. The results obtained for a

15% H2/air mixture showed that, in consistency with the literature, diluted mixture are less susceptible to incur detonation initiation and failure. Moreover, a non-linear effect of the product ($\beta(\mathrm{Le}-1)$) on the first phase of flame acceleration was observed: for values of the product higher than -5, thermo-diffusive phenomena seemed not to affect FA mechanisms. Further experimental campaigns are required to confirm these results and to extend the validity of these findings.
Eventually, these studies are important to identify the key parameters for FA. As a matter of fact, in the analytical models derived by Bychkov et al. [32], Valiev et al. [141] and Veser et al. [144] (see Table 3.1 and equation (3.20)) the acceleration rate is a function of the expansion rate σ, the burning velocity S_L and the turbulence integral length scale L_T (through the blockage ratio), but other parameters, such as Lewis and Zeldovich numbers, are not taken into account. Therefore, according to these analytical models, nitrogen dilution would not affect flame acceleration, which is clearly in contrast with the experimental results.
A feasibility study on a new technique to track the flame position along the tube has been carried out in order to obtain a finer representation of the flame velocity profile. The method consists in performing time-resolved IR absorption measurements by doping the fresh mixture with an alkane. The velocity profile is then derived by measuring the variation of the extension in depth of the unburnt gas along the tube axis. Even though further improvements are needed to finalize the technique, first results showed the capability of the method in capturing flame speed evolution in time for a 23% hydrogen in air mixture. For the moment, measurements are restricted to the early stages of flame propagation, where we can assume that the absorption cross section of fresh gas is not affected by any changes in temperature and pressure. This hypothesis fails as a leading shock wave is formed ahead of the flame; correction factors must be therefore taken into account to evaluate the variation in time and space of the absorption cross section. Further solutions are currently under study to widen the field of application of the technique. For example, nitrogen dilution is foreseen to dampen the effect of the cellular structure on the laser beam deflection for very lean hydrogen/air mixtures. With regard to rich mixtures, instead, a seeding molecule in the oxidizer, or the oxidizer itself, would be more relevant. Ongoing and future activities are in fact devoted to the study of oxygen absorption at 761 nm. Besides, hydrogen/air flames are characterized by low emission at this wave length, making it a good candidate to deal with measurement noises. The increase of diagnostics performances in terms of acquisition frequency also allows improving the accuracy of the technique.
The last part of this thesis report is devoted to the analysis of combustion generated loads. A second experimental device connected to the combustion tube at its flanged end was designed with the aim of studying the effects of dynamic loads on simple structures and of providing further information on fluid-structure interaction phenomena. As a matter of fact, the propagation of a shock wave in a confined volume is influenced by the rigidity of the vessel walls. When a shock wave travels into a pipe, it may induce changes in its geometry. Depending on wall stiffness, the structure may oscillate around a fixed position or deform. In case of plastic deformation, part of the energy released by the shock wave is absorbed by the structure.
Combustion generated loads may vary from quasi-static to dynamic ones depending on flame propagation regimes and structure characteristics. In case of deflagration, low speed

turbulent flames cause a slow pressurization of the combustion chamber, while detonations, characterized by supersonic waves, result in a non-uniform dynamic structural loading. For steady-state detonation, the mechanical response of the structure can be locally determined by considering the dynamic load resulting from a mono-dimensional Chapman-Jouguet detonation. In case of flame acceleration and deflagration-to-detonation transition (DDT) in long tubes with closed ends, the pressure load acting on structures strongly varies in time. In the first phase, the gas ahead of the flame is pre-compressed by the leading shock wave; then, as the run-up distance for DDT is attained, an over-driven detonation occurs. Therefore, cumulative effects of shock waves reflection and detonation occurrence make the problem more and more complex from a structural point of view.
In the present work a preliminary analysis on the dynamic response of circular plates and cylindrical tubes has been performed. Specimens are made of 304L austenitic stainless steel, which is one of the most commonly used in the nuclear industry. Moreover, this type of steel has been widely studied at CEA, from both experimental and numerical point of view. Appropriate specimen support systems were designed to fix the specimen to the combustion tube. Specimens geometry and thickness were chosen on the basis of the material yield strength and the structure natural frequency in order to study the mechanical behavior in both the elastic and plastic domain as a function of the characteristic loading time.
This preliminary study offers a starting point for the set-up of the experiments (for the choice of the most suitable diagnostics, the calibration of the sensors in the range of expected deformations, etc.) as well as for the analysis of the results of the future experimental campaigns. The final purpose is to provide a rich experimental database for the validation of the Fluid-Structure Interaction models currently under development for the EUROPLEXUS code.
In the next few months, a visualization section will be available to improve combustion diagnostics. This module can replace one of the existing sections of the combustion tube. Moreover, it has been designed to provide access to the whole diameter of the tube in order to examine the interaction between the flow and the boundary layers as well. For this purpose, the geometry of the apparatus has been locally modified: the circular cross section of the tube is gradually converted into a square one, hosting quartz windows on three sides. As already mentioned in the previous chapters, the access to the flame surface may clarify some open issue not fully covered in the present work, such as the mitigating effect of nitrogen dilution in detonation initiation and the role of thermo-diffusive instabilities. Moreover it may provide experimental results to corroborate and validate IR absorption technique.

Bibliography

[1] R. G. Abdel-Gayed and D. Bradley. Criteria for turbulent propagation limits of premixed flames. *Combustion and Flame*, 62:61–68, 1985.

[2] R. G. Abdel-Gayed, D. Bradley, and F. K. K. Lung. Combustion regimes and the straining of turbulent premixed flames. *Combustion and Flame*, 76:213–218, 1989.

[3] R. Addabbo, J. K. Bechtold, and M. Matalon. Wrinkling of spherically expanding flames. *Proceedings of the Combustion Institute*, 29(2):1527–1535, 2002.

[4] International Atomic Energy Agency. The fukushima daiichi accident. Technical report, IAEA, Vienna International Centre, 2015.

[5] V. Akkerman, V. Bychkov, A. Petchenko, and L. E. Eriksson. Accelerating flames in cylindrical tubes with nonslip at the walls. *Combustion and Flame*, 145:206–219, 2006.

[6] W. Ambrosini. Lecture notes on Thermalfluid-dynamics and CFD, A.Y. 2010-2011. BSc course in Nuclear Engineering, University of Pisa.

[7] R. Andreotti, M. Colombo, A. Guardone, P. Martinelli, G. Riganti, and M. di Prisco. Performance of a shock tube facility for impact respose of structures. *International Journal of Non-Linear Mechanics*, 72:53–66, 2015.

[8] E. E. Arens, R. C. Youngquist, and S. O. Starr. Intensity calibrated hydrogen flame spectrum. *International Journal of Hydrogen Energy*, 39:9545, 2014.

[9] ASME. Case 2564 - Impulsively loaded Pressure Vessels - Supplement 4 of ASME B & PV Code Cases: Boilers and Pressure Vessels. Technical report, The American Society of Mechanical Engineers, New York, NY, 2008.

[10] V. Aune, E. Fagerholt, K. O. Hauge, M. Langseth, and T. Borvik. Experimental study on the response of thin alluminium and steel plates subjected to airblast loading. *International Journal of Impact Engineering*, 90:106–121, 2016.

[11] V. Aune, E. Fagerholt, K. O. Hauge, M. Langseth, and T. Borvik. A shock tube facility to generate blast loading on structures. *International Journal of Protective Structures*, 7:340–366, 2016.

[12] H. Babaei and A. Darvizeh. Analytical study of plastic deformation of clamped circular plates subjected to impulsive loading. *Journal of Mechanics of Materials and Structures*, 7:309–322, 2012.

[13] W. E. Baker, P. A. Cox, P. S. Westine, J. J. Kulesz, and R. A. Strehlow. *Explosion hazards and evaluation*. Elsevier Scientific Publishing Company, 1983.

[14] A. Beccantini and E. Studer. The reactive Riemann problem for thermally perfect gases at all combustion regimes. *International Journal for Numerical Methods in Fluids*, 76:662, 2009.

[15] W. M. Beltman, E. N. Burcsu, J: E: Shepherd, and L. Zuhal. The structural response of cylindrical shells to internal shock loading. *Journal of pressure vessel technology*, 121:315–322, 1999.

[16] W. M. Beltman and J. E. Shepherd. Linear elastic response of tubes to internal detonation loading. *Journal of sound and vibration*, 252:617–655, 2002.

[17] W. B. Benedick and J. H. S. Knystautas, R. and. Lee. Large-scale experiments on the transmission of fuel-air detonations from two-dimensional channels. *Progress in Astronautics and Aeronautics*, 94:546–555, 1984.

[18] R. A. Benham and T. A. Duffey. Experimental-theoretical correlation on the containment of explosions in closed cylindrical vessels. *Int. J. Mech. Sci.*, 16:549–558, 1974.

[19] R. D. Blevins. *Formulas for dynamics, acoustics and vibration*. John Wiley & Sons, 2016.

[20] L. R. Boeck, R. Mével, T. Fiala, J. Hasslberger, and T. Sattelmayer. High-speed oh-plif imaging of deflagration-to-detonation transition in h2–air mixtures. *Exp. Fluids*, 57:105, 2016.

[21] R. Borghi. *Recent advances in the aerospace science (edited by C. Casci)*, chapter 7, pages 117–138. Plenum Press, 1985.

[22] R. Borghi and M. Destriau. *Combustion and Flames*. Ed́itions TECHNIP, 1998.

[23] S. Boulal, P. Vidal, and R. Zitoun. Experimental investigation of detonation quenching in non-uniform compositions. *Combustion and Flame*, 172:222, 2016.

[24] D. Bradley, A. C. K. Law, and M. Lawes. Flame stretch rate as a determinant of turbulent burning velocity. *Phil. Trans. Roy. Soc. London*, A338:359–387, 1992.

[25] D. Bradley, M. Lawes, and K. Liu. Turbulent flame speeds in ducts and deflagration/detonation transition. *Combustion and Flame*, 154:96–108, 2008.

[26] J. N. Bradley. *Shock waves in chemistry and physics*. Methuen & Co LTD, 1962.

[27] W. Breitung, C. Chan, S. B. Dorofeev, A. Eder, B. Gelfand, M. Heitsch, R. Klein, A. Malliakos, E. Shepherd, E. Studer, and P. Thibault. State-of-the-art report on flame acceleration and deflagration-to-detonation transition in nuclear safety. Technical report, Nuclear Energy Agency, 2000.

[28] J. Brossard and N. Charpentier de Coysevox. Effets d'un confinement souple sur la détonation des mélanges gazeux. *Acta Astronautica*, 3:971–981, 1976.

[29] V. Bychkov, V. Akkerman, G. Fru, A. Petchenko, and L. E. Eriksson. Flame acceleration in the early stages of burning in tubes. *Combustion and Flame*, 150:263–276, 2007.

[30] V. Bychkov, V. Akkerman, D. Valiev, and C. K. Law. Influence of gas compression on flame acceleration in channels with obstacles. *Combustion and Flame*, 157:2008–2011, 2010.

[31] V. Bychkov, A. Petchenko, V. Akkerman, and L. E. Eriksson. Theory and modeling of accelerating flames in tubes. *Physical Review*, 72, 2005.

[32] V. Bychkov, D. Valiev, and L. E. Eriksson. Physical mechanism of ultrafast flame acceleration. *Physical Review Letters*, 101(164501), 2008.

[33] J. Chao and J. H. S. Lee. The propagation mechanism of high speed turbulent deflagrations. *Shock Waves*, 12:277–289, 2003.

[34] T. W. Chao and J. E. Shepherd. Fracture response of externally flowed aluminium cylindrical shells under internal gaseous detonation loading. *International Journal of Fracture*, 134(1):59–90, 2005.

[35] G. Cheng, P. Bauer, and R. Zitoun. Effect of the initial pressure on the characteristics of the flame propagation in hydrogen-propane-air mixtures. *The European Physical Journal of Applied Physics*, 67:20901, 2014.

[36] A. R. K. Chennamsetty, J. LeBlanc, S. Abotula, P. Naik Parrikar, and A. Shukla. Dynamic response of hastelloy$^{\text{trademark}}$ x plates under oblique shocks: Experimental and numerical studies. *International Journal of Impact Engineering*, 92:75–88, 2016.

[37] R. S. Chue, J. F. Clarke, and J. H. Lee. "chapman-jouguet deflagration". *Proceedings of the Royal Society of London Series a-Mathematical Physical and Engineering Sciences*, 441(1913):607–623, 1993.

[38] G. Ciccarelli and S. B. Dorofeev. Flame acceleration and transition to detonation in ducts. *Progress in Energy and Combustion Science*, 34:499–550, 2008.

[39] G. Ciccarelli, C. J. Fowler, and M. Bardon. Effect of obstacle size and spacing on the initial stage of flame acceleration in a rough tube. *Shock Waves*, 14(3):161–166, 2005.

[40] G. Ciccarelli, T. Ginsberg, J. Boccio, C. Economos, K. Sato, and M. Kinoshita. Detonation cell size measurements and predictions in hydrogen-air-steam mixtures at elevated temperatures. *Combustion and Flame*, 99(2):212–220, 1994.

[41] C. Clanet and G. Searby. On the "Tulip Flame" phenomenon. *Combustion and Flame*, 105:225–238, 1996.

[42] G. Darrieus. Propagation d'une fronte de flamme. Unpublished work presented at La Technique Moderne, 1938.

[43] Yu.N. Denisov and Ya.K. Troshin. On the mechanism of detonative combustion. *Eighth Symposium (International) on Combustion*, 8(1):600 – 610, 1961.

[44] W. Döring. On detonation processes in gases. *Ann. Phys*, 43(421-436):9, 1943.

[45] S. B. Dorofeev. Thermal quenching and re-ignition of mixed pockets of reactants and products in gas explosions. *Proceedings of the Combustion Institute*, 31:2371–2379, 2007.

[46] S. B. Dorofeev. Flame acceleration and explosion safety applications. *Proceedings of the Combustion Institute*, 33:2161–2175, 2011.

[47] S. B. Dorofeev, M. S. Kuznetsov, V. I. Alekseev, A. Efimenko, and W. Breitung. Evaluation of limits for effective flame acceleration in hydrogen mixtures. *Journal of Loss Prevention in the Process Industries*, 14:583–589, 2001.

[48] S. B. Dorofeev, M. S. Kuznetsov, V. I. Alekseev, A.A. Efimenko, A. V. Bezmelnitsyn, Yu. G. Yankin, and W. Breitung. Effect of scale and mixture properties on behavior of turbulent flames in obstructed areas. FZKA 6268 IAE-6127/3, Forschungszentrum Karlsruhe, Technik und Umwelt, 1999.

[49] T. A. Duffey, E. A. Rodriguez, and C. Romero. Detonation-induced dynamic pressure loading in containment vessels. Technical Report LA-UR-03-0741, Los Alamos National Laboratories, 2003.

[50] D. Dunn-Rankin and R. F. Sawyer. Tulip flames: changes in shape of premixed flames propagating in closed tubes. *Experiments in Fluids*, 24:130–140, 1998.

[51] W. P. Eaton, F. Bitsie, J. h. Smith, and D. W. Plummer. A new analytical solution for diaphragm deflection and its application to a surface-micromachined pressure sensor. In *2nd International Conference On Modeling And Simulation Of Microsystems*, pages 640–643. Computational Publications, 1999.

[52] B.N. Edwards and D.E. Burch. Absorption of 3.39-micron helium-neon laser emission by methane in the atmosphere. *Journal of the Optical Society of America*, 55:174–177, 1965.

[53] F. N. Egolfopoulos and C. K. Law. Chain mechanisms in the overall rection orders in laminar flame propagation. *Combustion and Flame*, 80:7–16, 1990.

[54] F. Ettner, K. G. Vollmer, and T. Sattelmayer. Numerical simulation of the deflagration-to-detonation transition in inhomogeneous mixtures. *Journal of Combustion*, 2014.

[55] W. B. Fichter. Some solutions for the large deflections of uniformly loaded circular membranes. Technical Paper 3658, NASA, 1997.

[56] J. H. Frank, R. S. Barlow, and C. Lundquist. Radiation and nitric oxide formation in turbulent non-premixed jet flames. *Proceeding of the Combustion Institute*, 28:447, 2000.

[57] A. I. Gavrikov, A. A. Efimenko, and S. B. Dorofeev. A model for detonation cell size prediction from chemical kinetics. *Combustion and Flame*, 120:19–33, 2000.

[58] A. G. Gaydon. *The Spectroscopy of Flames*, chapter Hydrogen Flames, pages 99–126. Springer, Dordrecht, 1974.

[59] R.J. Gibert. *Vibrations des structures: interactions avec les fluides, sources d'excitation aléatoires*. Collection de la Direction des études et recherces d'Électricité de France. Eyrolles, 1988.

[60] I. Glassman and R. A. Yetter. *Combustion*. Elsevier, 4th ed. edition, 2008.

[61] J. Goulier, A. Comandini, F. Halter, and N. Chaumeix. Experimental study on turbulent expanding flames of lean hydrogen/air mixtures. *Proceedings of the Combustion Institute*, 36:2823, 2017.

[62] H. Guénoche. Chapter e - flame propagation in tubes and in closed vessels. In GEORGE H. MARKSTEIN, editor, *Nonsteady Flame Propagation*, volume 75 of *{AGARDograph}*, pages 107 – 181. Elsevier, 1964.

[63] C. M. Guirao, R. Knystautas, and J. H. S. Lee. *A summary of hydrogen-air detonation experiments*. Division of Systems Research, Office of Nuclear Regulatory Research, US Nuclear Regulatory Commission, 1989.

[64] C.M. Guirao, R. Knystautas, J.H. Lee, W. Benedick, and M. Berman. Hydrogen-air detonations. *Nineteenth Symposium (International) on Combustion*, 19(1):583 – 590, 1982.

[65] J. Hasslberger, P. Katzy, and T. Sattelmayer. On the effect of pressure on intrinsic flame instabilities in lean hydrogen-air mixtures – part i: Detailed chemistry based direct numerical simulation. In *26th International Colloquium on the Dynamics of Explosions and Reactive Systems*, Boston, 2017.

[66] H. Hencky. Über den Spannungszustand in kreisrunden Platten mit verschwindender Biegesteifigkeit. *Zeitschrif für Mathematik und Physik*, 63:113–117, 1915.

[67] E. O. Hulburt. The reflecting power of metals in the Ultra-Violet region of the spectrum. *Astrophysical Journal*, 42:205, 1915.

[68] IRSN. Le projet mithygéne. `http://www.irsn.fr/FR/Larecherche/Organisation/Programmes/projet-Mithygene/Pages/projet-Mithygene.aspx#.Wf7iP1vWzIV`, Last visit: September, 2017.

[69] M. F. Ivanov, A. D. Kiverin, I. S. Yakovenko, and M. A. Liberman. Hydrogen-oxygen flame acceleration and deflagration-to-detonation transition in three-dimensional rectangular channels with no-slip walls. *International Journal of Hydrogen Energy*, 38:16427–16440, 2013.

[70] JCGM 100:2008. Evaluation of measurement data – Guide to the expression of uncertainty in measurements (GUM 1995 with minor corrections). Standard, BIPM Joint Committee for Guides in Metrology, Paris, September 2008.

[71] C. T. Johansen and G. Ciccarelli. Visualization of the unburned gas flow field ahead of an accelerating flame in a obstructed square channel. *Combustion and Flame*, 156:405–416, 2009.

[72] Hamamatsu Photonics K. K. *Photomultiplier tubes, Photomultiplier tubes and related products*. Japan, 2008.

[73] N. Kambouchev, L. Noels, and R. Radovitzky. Numerical simulation of the fluid-structure interaction between air blast waves and free-standing plates. *Computers and Structures*, 85:923–931, 2007.

[74] R. J. Kee, F. M. Rupley, and J. A. Miller. A Fortran chemical kinetics package for the analysis of gas-phase chemical kinetics. Report SAND89-8009, Sandia National Laboratories, 1989.

[75] M. Kellenberger and G. Ciccarelli. Propagation mechanisms of supersonic combustion waves. In *Proceedings of the Combustion Institute.*, volume http://dx.dot.org/10.1016/j.proci.2014.08.002, 2014.

[76] KEYENCE Corporation. *High precision measurement general catalogue*, 2013.

[77] Rotexo-Cosilab GmbH & Co. KG. COSILAB Version 3. `http://www.rotexo.com`, 2010. Bad Zwischenahn, Ger- many.

[78] A.E. Klingbeil, J.B. Jeffries, and R.K. Hanson. Temperature- and pressure-dependent absorption cross sections of gaseous hhydrocarbon at 3.39 μm. *Measurement Science and Technology*, 17:1950–1957, 2006.

[79] R. Knystautas, J. H. Lee, and C. M. Guirao. The critical tube diameter for detonation failure in hydrocarbon-air mixtures. *Combustion and Flame*, 48:63–83, 1982.

[80] A. Kotchourko, A. Lelyakin, and T. Jordan. Modeling of hydrogen flame dynamics in narrow gap with bendable walls. In *Proceedings of 7th International Conference on Hydrogen Safety (ICHS2017)*, pages 388–399, Hamburg, Germany, September 2017. International Association for Hydrogen Safety.

[81] K. K. Kuo. *Principles of Combustion*. John Wiley & Sons, 1986.

[82] M. Kuznetsov, V. Alekseev, A. V. Bezmelnitsyn, W. Breitung, S. B. Dorofeev, I. Matsukov, A. Vaser, and Y. G. Yankin. Effect of obstacle geometry on behaviour of turbulent flames. FZKA 6328 IAE-6137/3, Forschungszentrum Karlsruhe, Technik und Umwelt, 1999.

[83] M. Kuznetsov, V. Alekseev, I. Matsukov, J. Jo Upendra Rohatgi, and T. Kim. Effect of pressure and temperature on flame acceleration and ddt limits for methane-air mixture. In *Proceedings of the European Combustion Meeting*, 2005.

[84] M. Kuznetsov, G. Ciccarelli, S.B. Dorofeev, V. Alekseev, Y. Yankin, and T.H. Kim. DDT in methane-air mixtures. *Shock waves*, 12:215, 2002.

[85] M. Kuznetsov and J. Grune. Experiments of flame acceleration and ddt for stoichiometric hydrogen/air mixture in a thin layer geometry. In *Proceedings of 7th International Conference on Hydrogen Safety (ICHS2017)*, pages 166–176, Hamburg, Germany, September 2017. International Association for Hydrogen Safety.

[86] M. Kuznetsov, A. Lelyakin, W. Breitung, J. Grune, K. Sempert, and A. Friedrich. Dynamic effects under gaseous detonation and mechanical response of piping structures. In *Proceeding of the 2009 ASME International Mechanical Engineering Congress & Exposition*, 2009.

[87] L. Landau. On the theory of slow combustion. *Acta Physicochimica U.R.R.S.*, 19(1), 1944.

[88] L. D. Landau and E. M. Lifshitz. *Fluid mechanics*, volume 6. Elsevier, Course of Theoretical Physics, Institute of Physical Problems, USSR Academy of Science, Moscow, 2nd edition, 2004.

[89] C. K. Law. Propagation, structure, and limit phenomena of laminar flames at elevated pressures. *Combustion Science and Technology*, 178:335–360, 2006.

[90] J. H. Lee, R. Knystautas, and C. K. Chan. Turbulent flame propagation in obstacle-filled tubes. *Twentieth Symposium (International) on Combustion*, pages 1663–1672, 1984.

[91] J. H. Lee, R. Knystautas, and N. Yoshikawa. Photochemical initiation of gaseous detonation. *Acta Astronautica*, 5:971–982, 1978.

[92] J. J. Lee, G. Dupré, R. Knystautas, and J. H. Lee. Doppler interferometry study of unstable detonations. *Shock waves*, 5:175–181, 1995.

[93] B. Lewis and G. von Elbe. *Combustion, Flames and Explosions of Gases*. Academic Press, 3rd edition, 1987.

[94] Q. Li, J. Lieh, and A. Mayer. Large deflection of laminated circular plates with clamped edge and uniform loading. *Journal of Process Mechanical Engineering*, 219:83–88, 2005.

[95] M. A. Liberman, M. F. Ivanov, Kiverin A. D., Kuznetsov M. S., Chukalovsky A. A., and Rakhimova T. V. Deflagration-to-detonation transition in highly reactive combustible mixtures. *Acta Astronautica*, 67:688 – 701, 2010.

[96] F. Malet. *Etude expérimentale et numérique de la propagation de flammes prémelangées tuturbulent dans une atmosphère pauvre en hydrogène et humide*. PhD thesis, Université d'Orléans, 2005.

[97] E. Mallard and H. L. Le Chatelier. *Annales des Mines*, volume 4. Dunod, 1883.

[98] G. H. Markstein. Experimental and thoretical study of flame front stability. *J. Aero. Sci.*, 18, 1951.

[99] G. H. Markstein. *Non-steady flame propagation*. Pergamon Press, 1964.

[100] MATLAB. *version 8.6 (R2015b)*. The MathWorks Inc., Natick, Massachusetts, 2015.

[101] C. Meneveau and T. Poinsot. Stretching and quenching of flamelets in premixed turbulent combustion. *Combustion and Flame*, 86(4):311 – 332, 1991.

[102] R. Mevel, P.A. Boettcher, and J.E. Shepherd. Absorption cross section at 3.39μm of alkanes, aromatics and substituted hydrocarbons. *Chemical Physics Letters*, 531:22, 2012.

[103] R. Mével, S. Javoy, F. Lafosse, N. Chaumeix, G. Dupré, and C.-E. Paillard. Hydrogen-nitrous oxide delay times: Schok tube experimental study and kinetic modelling. *Proceedings of the Combustion Institute*, 32:359–366, 2009.

[104] M. Mirazei, K. Mazaheri, and H. Biglari. Analytical modeling of the elastic structural response of tubes to internal detonation loading. *International Journal of Pressure Vessel and Piping*, 82:883–895, 2005.

[105] M. Mirzaei. Finite element analysis of deformation and fracture of cylindrical tubes under internal moving pressures. In *Finite Element Analysis*. InTech, 2010.

[106] I. O. Moen, Donato M., and R. Knystautas. Flame acceleration due to turbulence produced by obstacles. *Combustion and Flame*, 39:21–32, 1980.

[107] I.O. Moen, M. Donato, R. Knystautas, and J.H. Lee. The influence of confinement on the propagation of detonations near the detonability limits. *Eighteenth Symposium (International) on Combustion*, 18(1):1615 – 1622, 1981.

[108] G. N. Nurik and J. B. Martin. Deformation of thin plates subjected to impulsive loading - a review. part i: Theoretical considerations. *International Journal of Impact Engineering*, 8(2):159–170, 1989.

[109] G. N. Nurik and J. B. Martin. Deformation of thin plates subjected to impulsive loading - a review. part ii: Experimental studies. *International Journal of Impact Engineering*, 8(2):171–186, 1989.

[110] M. O'Connaire, H J. Curran, J. M. Simmie, W. J. Pitz, and C.K. Westbrook. A comprehensive modeling study of hydrogen oxidation. *International Journal of Chemical Kinetics*, 36:603–622, 2004.

[111] M.Y. Perrin and J.M. Hartmann. High temperature adsorption of the 3.39μm He-Ne laser line by methane. *J. Quant. Spectrosc. Radiat. Transfer.*, 42(6):459, 1989.

[112] G. Petrangeli. *Nuclear Safety*. Elsevier Butterworth-Heinemann, 1st edition, 2006.

[113] J. Pionteck and G. Wypych, editors. *Handbook of antistatic*. ChemTech, 2nd edition, 2016.

[114] T. Poinsot and D. Veynante. *Theoretical and numerical combustion*. Edwards, 2nd ed. edition, 2005.

[115] T. Poinsot, D. Veynante, and S. Candel. Quenching processes and premixed turbulent combustion diagrams. *Journal of Fluid Mechanics*, 228:561–606, 1991.

[116] S. B. Pope. *Turbulent Flows*. Cambridge University Press, 2000.

[117] L.S. et al. Rothman. The hitran 2008 molecularspectroscopicdatabase. *JQSRT*, 110:533, 2009.

[118] D.A. Rotman and A.K. Oppenheim. Aerothermodynamic properties of stretched flames in enclosures. *Symposium (International) on Combustion*, 21(1):1303 – 1312, 1988. Twenty-First Symposuim (International on Combustion).

[119] G.D. Salamandra, T.V. Bazhenova, and I.M. Naboko. Formation of detonation wave during combustion of gas in combustion tube. *Symposium (International) on Combustion*, 7(1):851 – 855, 1958.

[120] R. Scarpa. Numerical analysis of the diffusion process of chemical species in a closed volume characterized by a stratified atmosphere. Master's thesis, Engineering School, University of Pisa, 3 March 2014.

[121] K. I Shelkin. On combustion in a turbulent flow. *Journal of Technical Physics*, 1943.

[122] K. I. Shelkin and Y. K. Troshin. *Gasdynamics of combustion*. MONO BOOK CORP., 1965.

[123] J. E. Shepherd. Chemical kinetics of hydrogen-air-diluent detonation. *Progress in Astronautics and Aeronautics*, 106:263–293, 1986.

[124] J. E. Shepherd. Structural response of piping to internal gas detonation. *Journal of Pressure Vessel Technology*, 131, 2009.

[125] J. E. Shepherd and K. Inaba. *Shock Loading and Failure of Fluid-filled Tubular Structures*, chapter 6, pages 153–190. Springer US, 2010.

[126] M. Silvestrini, B. Genova, G. Parisi, and F. J. Leon Trujillo. Flame acceleration and DDT run-up distance for smooth and obstacles filled tubes. *Journal of loss prevention in the process industries*, 21:555–562, 2008.

[127] R. A. Strehlow and A. J. Crooker. The structure of marginal detonation waves. *Acta Astronautica*, 1:303–315, 1974.

[128] E. Studer, S. Kudriakov, and A. Beccantini. Combustion et explosion de prémélanges gazeux - application à la surêté nucléaire, 2013.

[129] M. Summerfield, S. H. Reiter, V. Kebely, and R. W. Mascolo. The structure and propagation mechanism of turbulent flames in high speed flow. *Jet Propulsion*, 25(8):377–384, 1955.

[130] C. J. Sun, C. J. Sung, L. He, and C. K. Law. Dynamics of weakly stretched flames: quantitative description and extraction of global flame parameters. *Combustion and Flame*, 118:108–128, 1999.

[131] S. Tang. Dynamic response of a tube under moving pressure. In *Proceeding of the American Society of Civil Engineers*, volume 5, pages 97–122. Engineering Mechanics Division, 1965.

[132] A. Teodorczyk and J. H. S. Lee. Detonation attenuation by foams and wire meshes lining the walls. *Shock Waves*, 4:225–236, 1995.

[133] The Steel Construction Institute. *Protection of piping systems subject to fires and explosions.* Health&Safety Executive, 2005.

[134] P. Thibault, Y. K. Liu, C. Chan, J. H. Lee, R. Knystautas, C. Guirao, B. Hjertager, and K. Fuhre. Transmission of an explosion through an orifice. *Nineteenth Symposium (International) on Combustion*, pages 599–606, 1982.

[135] S. R. Tieszen. Effect of initial conditions on combustion generated loads. *Nuclear Engineering and Design*, 140:81–94, 1993.

[136] S.R. Tieszen, M.P. Sherman, W.B. Benedick, R. Shepherd, J.E. Knystautas, and J.H.S. Lee. Detonation cell size measurements in hydrogen-air-steam mixtures. *Progress in Astronautics and Aeronautics*, 106:205–219, 1986.

[137] S. Timoshenko and S. Woinowsky-Krieger. *Theory of plates and shells.* McGraw Hill, 1959.

[138] N. E. Todreas and M. S. Kazimi. *Nuclear Systems I: Thermal Hydraulic and Fundamentals.* Taylor and Francis Group, 1990.

[139] E. Tomita, N. Kawahara, M Shigenaga, A. Nishiyama, and RW Dibble. In situ measurement of hydrocarbon fuel concentration near a spark plug in an engine cylinder using the 3.392μm infrared laser absorption: discussions and applicability with a homogeneous methane-air mixture. *Measurement science and technology.*, 14:1350, 2003.

[140] D. Valiev, V. Bychkov, V. Akkerman, and L. E. Eriksson. Different stages of flame acceleration from slow burning to Chapman-Jouguet deflagration. *Physical Review*, 80(036317), 2009.

[141] D. Valiev, V. Bychkov, V. Akkerman, C. K. Law, and L. E. Eriksson. Flame acceleration in channels with obstacle in the deflagration-to-detonation transition. *Combustion and Flame*, 157:1012–1021, 2010.

[142] S. van Herwaarden. *Thermal Conductivity Gauge, TCG-3880*, 2007.

[143] A. Velikorodny, E. Studer, S. Kudriakov, and A. Beccantini. Combustion modeling in large scale volumes using EUROPLEXUS code. *Journal of Loss Prevention in the Process Industries*, 35:104, 2015.

[144] A. Veser, W. Breitung, and S. B. Dorofeev. Run-up distances to supersonic flames in obstacle-laden tubes. *J. Phys. IV France*, 2002.

[145] B. V. Voitsekhovskii, V. V. Mitrofanov, and M. E. Topchiyan. Structure of the detonation front in gases (survey). *Combustion, Explosion and Shock Waves*, 5(3):267–273, 1969.

[146] J. von Neuman. Progress report on theory of detonation waves. Technical Report 549, National defense research commitee of the office of scientific research and developpement, 1942.

[147] S. Way. Bending of circular plates. *Transactions of the American Society of Mechanical Engineers*, 56, 1934.

[148] C. K. Westbrook and P. A. Urtiew. Chemical kinetics prediction of critical parameters in gaseous detonations. *Nineteenth Symposium (International) on Combustion*, pages 615–623, 1982.

[149] S. Yoshiyama, Y. Hamamoto, E. Tomita, and K.I. Minami. Measurement of hydrocarbon fuel concentration by means of infrared absorption technique with 3.39μm He-Ne laser. *JSAE Review*, 17:339, 1996.

[150] Y B Zeldovich. On the theory of the propagation of detonation in gaseous systems. NACA Technical Memorandum NACA-TM-1261, National Advisory Committee for Aeronautics, Washington, DC, United States, 1950.

[151] B Zel'dovich Ya. Classification of regimes of exothermic reaction in accordance with initial conditions. *Combustion and Flame*, 39:211–214, 1980.

[152] V. L. Zimont. Theory of turbulent combustion of a homogeneous fuel mixture at high reynolds number. *Translated from Fizika Goreniya i Vzryva*, 15(3):23–32, 1979.

Roberta SCARPA

Mécanisme d'accélération d'une flamme de prémélange hydrogène/air et effets sur les structures

Résumé :
Le risque d'explosion des mélanges H2/air revêt toujours une importance cruciale pour la gestion des accidents graves dans les centrales nucléaires. Des critères expérimentaux ont été proposés dans les années 2000 par Dorofeev et al. afin de déterminer les conditions nécessaires à l'accélération de flamme et à la TDD. Ce travail de thèse a l'objectif de mieux comprendre les mécanismes d'accélération des flammes de prémélange H2/air et de fournir une solide base de données expérimentales pour la validation des codes utilisés pour les études de sûreté. Les expériences ont été menées dans un tube muni d'obstacles (taux de blocage entre 0.3 et 0.6) avec un diamètre interne de 12 cm et une longueur d'environ 5 m. Les effets de la pression initiale et de la dilution en azote sur des mélanges pauvres en H2 ont été étudiés. Les résultats montrent que la pression favorise l'accélération seulement pour les mélanges les plus réactifs et que la surpression induite par la combustion est directement proportionnelle à la pression initiale. Les interactions flamme-choc ainsi que les instabilités thermo-diffusives jouent un rôle important sur la propagation de flamme. Une nouvelle technique a été développée dans le but d'obtenir une représentation plus fine du profil de vitesse de flamme. Des mesures d'absorption IR résolues dans le temps ont été effectuées en dopant le mélange avec un alcane. Le profil de vitesse a été obtenu en mesurant la variation d'extension du gaz frais pendant l'avancement de la flamme. Enfin, des analyses préliminaires ont été menées pour la conception d'un nouveau dispositif expérimental pour l'étude des effets de la combustion sur des structures en acier inox.
Mots clés : Risque hydrogène, Flamme de prémélange hydrogène/air, Accélération de flamme, TDD, Efforts dynamiques sur les structures, Absorption IR

Flame propagation mechanisms of premixed hydrogen/air mixtures and effects of combustion generated loads on structures

Abstract:
Flame acceleration and explosion of hydrogen/air mixtures remain key issues for severe accident management in nuclear power plants. Empirical criteria were developed in the early 2000s by Dorofeev and colleagues providing effective tools to discern possible FA or DDT scenarios. The objectives of the present work are to better understand the mechanisms of acceleration for premixed H2/air flames and to provide a solid base of experimental data for the validation of the codes used for safety analyses. The experiments were performed in an obstacles-laden tube (blockage ratio between 0.3 and 0.6) with 120 mm internal diameter and about 5 m length. The effects of the initial pressure and the nitrogen dilution on lean H2 mixtures have been studied. The results show that pressure promote flame acceleration only for highly reactive mixtures. Moreover, the overpressure induced by the combustion is directly proportional to the initial pressure. Besides, flame-shock interactions and thermo-diffusive instabilities play an important role in flame acceleration. A new technique to track the flame position along the tube has been developed in order to obtain a finer representation of the flame velocity profile. The method consists in performing time-resolved IR absorption measurements by doping the mixture with an alkane. The velocity profile is then derived by measuring the variation of the extension in depth of the unburnt gas along the tube axis. Finally, analyses on the effects of combustion generated loads on stainless steel structures were performed in order to provide preliminary results for the design of a new experimental device.
Keywords: Hydrogen safety, Premixed hydrogen/air flames, Flame acceleration, DDT, Combustion generated loads, IR absorption measurements

DEN/DANS/DM2S/STMF/LIEFT,
CEA Paris-Saclay

ICARE, CNRS-Orléans